2.15 Soft Chemistry Synthesis of Oxides

M Hayward, University of Oxford, Oxford, UK

2.15.1 Introduction

Complex transition-metal oxides are of wide and enduring interest due to the complex structural chemistry and broad range of physical behavior these phases exhibit. The synthesis of complex oxides has therefore been the subject of extensive study (**Chapters 2.01** and **4.03**).

In contrast to gas-phase or solution-phase chemistry, where the diffusion and mixing of reagents are relatively low-energy processes, a characteristic feature of chemical reactions in the solid state is the low mobility of chemical species. This is especially true in the synthesis of metal oxides. As demonstrated by the high lattice energies and melting points of metal-oxide phases, there are strong bonding interactions between small, highly charged oxide ions and metal cations. These interactions act to resist the motion of chemical species within the extended lattices of metal oxides and thus present large energetic barriers to the diffusion of reagents.

Typical 'ceramic' synthesis strategies applied to the preparation of complex oxide phases involve heating mixtures of binary metal oxides and/or metal oxy-acid salts (carbonates, nitrates, etc.) at high temperature. Rapid reaction occurs initially at the contact point between component phases and then proceeds by slow interdiffusion between reactant particles to form product phases. Reactions of this form therefore require ionic diffusion over length scales defined by the particle size of reactants (typically 1–10 μm) in order to form homogeneous products. While reaction rates can be increased by regular grinding to expose fresh reagents and by compressing samples to increase the degree of inter-grain contact, the intrinsically poor ionic diffusion in metal-oxide phases means that overall reaction rates are slow and reactions require multiple heating

periods (typically measured in days) at elevated temperature ($T > 1000\,^{\circ}C$) to reach completion. However, even after prolonged heat treatment, the homogeneity of samples prepared by ceramic processes can often be poor. For example, the reaction between two component oxides AO and BO_2 will form not only the desired ABO_3 product, but also A_2BO_4 or AB_2O_5 depending on the local stoichiometry of the reaction mixture. Thus extensive heating and grinding can be required for samples to reach equilibrium, and the contamination of samples with low levels of impurity phases is common. In addition, the extensive physical processing of materials required by ceramic synthesis (grinding, ball milling, and compression) can also introduce impurities into samples. Thus, it can be seen that ceramic routes are not optimal if high levels of sample purity and homogeneity are required.

A second potentially undesirable feature of high-temperature ceramic synthesis relates to product selection. As noted above, there are considerable barriers to diffusion in solid oxide systems. These barriers are in fact so large that mass transport contributions account for the majority of the activation energy of a typical solid–solid reaction. Given that the motion of chemical species is a feature common to all solid–solid reactions, it follows that the activation energies of competing solid–solid reactions tend to be comparable. Thus at the elevated synthesis temperatures required to overcome these activation barriers, the products of these competing reactions are all energetically accessible, and enter an equilibrium with each other resulting in the formation of the most thermodynamically stable phase or mixture of phases. Thus we can see that, as a consequence of the large energetic barriers to diffusion in solids, solid–solid reactions are generally performed under the influence of thermodynamic product selection. As a result, a large number of metastable product phases are synthetically inaccessible by this route.

Motivated by the undesirable features of high-temperature solid-state synthesis, there has been a concerted effort to 'soften' the reaction conditions (lower the reaction temperatures) required for the synthesis of complex oxides by applying a *chimie douce* approach.[1–4]

Strategies can be split into three major strands:

1. Methods that reduce the length scale over which solid–solid diffusion must occur, by improving the mixing of reactant species and/or reducing the particle size of reagent phases.
2. Methods which lower the barriers to diffusion by utilizing an external medium or solvent to circumvent the need for extensive solid–solid reaction.
3. Low-temperature topochemical reactions which exploit the high mobility of particular components within extended oxide phases, to bring about structure-conserving reactions which form metastable phases.

2.15.2 Synthesis from Precursors

As noted above, ceramic synthesis routes involve reacting mixtures of binary metal oxides and metal oxo-acid salts (carbonates and nitrates). Even after extensive mechanical processing, these mixtures are extremely inhomogeneous on the length scale of a typical mixed-oxide structural repeat unit (5–20 Å), and as a result extensive long-range diffusion of species is required to form homogeneous products.

An obvious strategy for reducing reaction times and lowering reaction temperatures is to prepare more homogeneous mixtures of reagents. For example, if the homogeneity and intermixing of a solution of metal cations could be trapped in a solid precursor, so that metal cations were mixed on an atomic length scale, much softer reaction conditions could be used to prepare homogeneous materials. However, simply drying a solution of metal salts will not prepare such a precursor due to the propensity of metal salts to crystallize into binary phases rather than solid solutions. Thus, for example, a mixed solution of metal nitrates will crystallize into a mixture of binary nitrate crystals when the solvent is driven off. While this mixture of small crystals may be more homogeneous than a mechanically ground sample, it is still far from homogeneous on the atomic length scale. More elaborate procedures are therefore required to form suitable precursor materials.

2.15.2.1 Co-Precipitation Precursor Routes

Rapid co-precipitation of metal cations from solution offers one method for preparing intimately mixed precursor phases. In the simplest case, rapid precipitation leads to the formation of very small particles of binary metal salts in suspension. If these precipitated phases are sufficiently insoluble in the liquid from which they were precipitated, the suspended particles will not ripen and grow, and a finely divided mixture of reagent phases can be separated by filtration for subsequent heat treatment.

More homogeneous precursor phases can be prepared if the reagent metal cations can be precipitated to form a solid-solution salt. For example, it has been observed that many binary carbonates of divalent metals adopt calcite-type structures related to that of $CaCO_3$.[5] The lattice parameters of these carbonate phases show little variation with the identity of the metal cation, suggesting a high degree of cation miscibility between phases and further suggesting that materials containing cation solid solutions can be formed.[6] Thus, for example, if $(NH_4)_2CO_3$ is added to a solution containing $Ca(NO_3)_2$ and $Mn(NO_3)_2$, a $Ca_{1-x}Mn_xCO_3$ solid-solution phase is precipitated in which calcium and manganese cations are statistically distributed over the metal cation sites of the calcite lattice and are therefore homogeneously mixed on a unit cell length scale.[7] Decomposition of this mixed-metal carbonate readily yields highly homogeneous calcium manganese oxide phases as no long-range cation diffusion is required during the sintering process.

Similar procedures can be utilized to prepare mixed-metal hydroxide precursor phases. Thus, for example, $La_{0.5}M_{0.5}(OH)_3$ (M = Al, Cr, Fe, Co) precursor phases precipitated from solution can be readily transformed into the corresponding $LaMO_3$ perovskite phases at low temperature (600–700 °C).[8] In this case, there is some choice of precipitating agent. Sodium hydroxide and potassium hydroxide have been widely used as agents to precipitate mixed-metal hydroxides. However, this usually requires that the sodium and potassium cations are removed, typically by washing in hot water, after precipitation is complete and prior to thermal treatment. Therefore, the bases of nonmetal cations such as ammonium or substituted variants are usually

preferred as these can be burned out of samples during the sintering process leaving samples uncontaminated. Subsequent sintering of co-precipitated precursor phases to yield highly crystalline, homogeneous samples can be performed at much lower temperatures than that would be required for ceramic syntheses.

2.15.2.2 Sol–Gel Precursor Routes

The preparation of homogeneous precursor phases containing more than two or three different cations can be extremely challenging via co-precipitation routes. However by utilizing sol–gel chemistry, precursor phases which have homogeneous distributions of large numbers of different cations can be readily prepared.[9,10] The term 'sol' is generally used to refer to a suspension or dispersion of colloidal particles. A 'gel' is a highly viscous fluid consisting of a polymer network which contains large amounts of liquid within its structure. Thus, precursor materials prepared by sol–gel chemistry consist of intimately mixed arrays of coordinated metal cations or colloidal particles, trapped within an extended polymer matrix, such that when the precursor phase is dried, the homogeneous mixture of metal cations present in solution/suspension is retained in the resulting material.

Sol–gel precursor phases can be split into two broad classes: inorganic polymeric materials and organic polymeric materials.

2.15.2.2.1 Inorganic polymer sol–gel precursors

Sol–gel precursor phases based on inorganic polymers contain continuous networks of M–O–M–O–M polymers, such that the polymer chain is made from the 'trapped' metal cations which will ultimately form the product metal-oxide phase. Such inorganic polymer sol–gel precursors can be prepared by two principal routes: the hydrolysis of metal alkoxides and the slow hydrolysis of strongly chelated metal cations.

2.15.2.2.1.1 Alkoxide hydrolysis

Metal alkoxides of the general formula $M(OR)_n$, where R is an alkyl group, are readily hydrolyzed as shown in reaction [1] (**Chapter 2.16**). Hydrolysis can then be followed by dehydration or dealcholation to form condensed M–O–M links as shown in reactions [2] and [3].[11] Repeated hydrolysis steps can be used to build up extended polymeric oxide networks:

$$M(OR)_n + xH_2O \rightarrow M(OH)_x(OR)_{n-x} + xROH \quad [1]$$

$$-M-OH + HO-M \rightarrow M-O-M + H_2O \quad [2]$$

$$-M-OH + RO-M- \rightarrow -M-O-M- + ROH \quad [3]$$

In order to prepare homogeneous precursor phases which contain different types of metal cations, it is necessary to perform cross-hydrolysis reactions to incorporate all the metal cations present in solution into the inorganic polymer chains. This requires that the alkoxides of the different metal cations present have similar hydrolysis rates, which can be a significant obstacle to the formation of complex oxide phases by this route. For example, rare earth alkoxides are much more readily hydrolyzed than copper alkoxide complexes. Therefore, the introduction of water into a mixture of rare earth and copper alkoxides would result in the preferential hydrolysis of the rare earth alkoxides resulting in a highly inhomogeneous precursor phase. The relative rates of alkoxide hydrolysis can be modified by using substituted alkoxide ligands. Thus by using the appropriate metal alkoxide complexes a wide range of mixed-metal oxides can be prepared via this precursor route.

An alternative strategy is to prepare mixed-metal alkoxide phases which can be hydrolyzed directly to form sol–gel precursor phases. For example, a mixture of $Ba(OCH_2CH_2OCH_3)_2$ and $Ti(OCH_2CH_2OCH_3)_4$ in 2-methoxyethanol ($HOCH_2CH_2OCH_3$) leads to the formation of the mixed-metal alkoxide $BaTi(OCH_2CH_2OCH_3)_6$.[12] Hydrolysis with excess water readily yields a sol–gel precursor phase which can be used to prepare $BaTiO_3$ at only 400 °C, compared to the 1100 °C required for ceramic synthesis.[13]

2.15.2.2.1.2 Metal chelate gels

As noted above, metal complexes, particularly those in aqueous solution, are prone to hydrolysis and condensation polymerization. The addition of base to a solution of metal cations can catalyze the rapid hydrolysis of the metal complexes present. However, this generally results in the precipitation of binary metal hydroxide particles, rather than the formation of inorganic polymers. The rate of cation hydrolysis can be slowed significantly if the metal centers are bound strongly to chelating ligands, allowing a polymeric network to form. For example, the complexation of Fe(III) cations with ethylenediamine tetraacetic acid (EDTA) can lower the equilibrium constant of hydrolysis by 22 orders of magnitude as shown in reactions [4] and [5][14]:

$$Fe(H_2O)_6^{3+} + H_2O \leftrightarrow Fe(OH)(H_2O)_5^{2+} + H_3O^+ \quad K = 10^{-3} \quad [4]$$

$$[Fe(H_2O)_2EDTA]^- + H_2O \leftrightarrow [Fe(OH)(H_2O)EDTA]^{2-} + H_3O^+ \quad K = 10^{-25} \quad [5]$$

Utilizing this approach, precursor phases which incorporate large numbers of different metal cations can be prepared. For example, sol–gel precursors suitable for the formation of the high-T_c superconducting copper oxide phase $Bi_2Sr_2CaCu_2O_{8+x}$ can be readily prepared by adding EDTA to an aqueous solution of the corresponding metal nitrates, to achieve a cation:EDTA ratio of 1:1. Addition of ammonia to adjust the acidity of the solution to pH 5, followed by gentle heating to drive off water, leads to the formation of a glassy sol–gel precursor material, which can then be thermally treated to form the target $Bi_2Sr_2CaCu_2O_{8+x}$ phase.[15]

2.15.2.2.1 Organic polymer sol–gel precursors

A further strategy for the preparation of sol–gel precursor phases is the use of organic polymers to form a highly connected, extended, semi-rigid network containing a homogeneous distribution of metal cations immobilized within coordination sites. The inorganic–organic hybrid precursor can then be sintered into a homogeneous complex oxide phase by burning out the organic framework.

The most direct way of preparing such a precursor is the addition of a water-soluble organic polymer, such as polyacrylic acid $[CH_2CH(COOH)]_n$ or polyvinyl alcohol $[CH_2CH(OH)]_n$, to a solution of metal cations.[10] Complexation of the metal cations by the acid or alcohol residues of the organic polymer chain leads to crosslinking and immobilization of metal cations within the precursor polymer network. Thus if a 10% solution of polyacrylic acid is added to a mixed solution of yttrium, barium, and copper cations, a viscous gel is formed as the solution is concentrated by evaporation, which then sets into an amorphous glassy precursor. Subsequent sintering of this precursor yields $YBa_2Cu_3O_z$.[16]

In order to ensure that highly homogeneous precursor materials are prepared by this method, the polymer chains must have a uniform complexing affinity for the different metal cations present in solution. This requirement can be readily achieved by the use of polymers with strong polydentate coordination sites, such as EDTA–ethylene diamine polyamide, that show a strong affinity for almost all metal cations.[17]

Organic polymer sol–gel precursors can also be prepared by the *in situ* polymerization of organic ligands which are chelating metal centers. The most common chemical system used in such processes is a combination of citric acid and ethylene glycol, first described in the Pechini process.[18] Citric acid is a tridentate ligand which binds strongly to a wide variety of metal cations. Reaction with ethylene glycol leads to a rapid esterification reaction, which can drive an efficient condensation polymerization reaction of the citric acid units. Thus if an aqueous solution of citric acid, ethylene glycol, and metal salts is concentrated by heating to favor condensation polymerization, a polyester network is formed trapping a homogeneous array of coordinated metal cations. The resulting precursor phase can be readily dried and sintered at low temperature to form homogeneous complex oxide phases.

Citric acid and related polymerizable organic ligands form strong bonds to a very wide variety of metal cations. This makes the 'citrate gel' precursor route suitable for the synthesis of a large number of complex oxide phases which contain a variety of different metal cations.[19,20] This broad applicability is particularly valuable for the synthesis of phases which contain solid solutions of metal cations in which the physical properties of the materials are decisively dependent on sample homogeneity.

2.15.3 Synthesis in Solvents and Fluxes

The conventional ceramic synthesis of mixed-metal-oxide phases requires cations to diffuse in the solid state over length scales defined by the particle size of the reagent materials. The tight binding of metal cations within extended oxide lattices means that in general the rate of solid-state cation diffusion in oxides is low, necessitating high reaction temperatures for ceramic synthesis procedures. Rapid low-temperature synthesis of complex oxide phases can be facilitated if the diffusion of species occurs in a fluid medium, rather than in the solid state. Thus by the use of molten fluxes or liquid solvents, in which the diffusing species are 'soluble,' the synthetic conditions for oxide synthesis can be softened. An additional advantage of such a synthetic approach is that the dissolution process is reversible, facilitating the control of particle size and crystal growth.

2.15.3.1 Solvothermal Synthesis

Solvothermal reactions, in which a solvent is used as a reaction medium in a sealed apparatus above its boiling point, have been utilized to prepare an extensive range of complex oxide phases.[21,22] Such reactions utilize the autogeneous pressure which is generated under such conditions to modify the solvation properties of solvents, and thus favor the dissolution of 'insoluble' oxide reagent phases. Taking water as an example, the viscosity of this solvent decreases dramatically with increasing temperature, facilitating the diffusion of dissolved species.[23] In addition, the ionic product and dielectric constant of water are also strongly temperature dependent. These changes have dramatic consequences on the solubility of metal oxides in the temperature range typically employed for synthesis. For example, the solubility of the rutile polymorph of TiO_2 increases by two orders of magnitude on heating to 300 °C.[24] Thus, the products of solvothermal synthesis routes are often strongly dependent on the synthesis temperature and pressure.

2.15.3.1.1 Early transition-metal oxides

Hydrothermal synthesis has been used widely to prepare dielectric oxide phases containing early transition metals in their group oxidation states (Ti^{IV}, Nb^{V}, and Ta^{V}). One of the most extensively studied phases is the ferroelectric $BaTiO_3$. Conventional preparation of this phase via a ceramic synthesis route involves the repeated heating of mixtures of $BaCO_3$ and TiO_2 at 1100 °C.[13] In contrast, the ferroelectric tetragonal polymorph of $BaTiO_3$ can be readily prepared by the hydrothermal reaction of $BaCl_2$, TiO_2, and NaOH at 200 °C.[25] The much lower reaction temperature employed clearly demonstrates the utility of water as a solvent to facilitate the diffusion of reacting species.

Interestingly, if $Ba(OH)_2$ is used as the barium source in this reaction rather than $BaCl_2$, the cubic polymorph of $BaTiO_3$ is prepared. It has been hypothesized that chloride ions facilitate the nucleation of $BaTiO_3$ crystals in some manner. This enhances the crystal size of the hydrothermal product sufficiently to stabilize the structural transition to the low-temperature tetragonal polymorph of $BaTiO_3$.[25] Such interactions and effects demonstrate the sensitivity of hydrothermal reactions to subtle influences from 'spectator' species. This has motivated many detailed studies of the mechanisms of this class of reaction in order to utilize and control these features of solvothermal chemistry.

Cation-substituted phases and solid solutions can also be readily prepared by solvothermal methods. For example, phases across the entire $Ba_{1-x}Sr_xTiO_3$ compositional range can be synthesized under the appropriate conditions.[26] The rapid diffusion and intimate mixing of reagents in solution leads to products of high homogeneity with compositions which are in good agreement with the ratio of reagents used.

Group 5 AMO_3 (A = Na, K; M = Nb, Ta) perovskite phases can also be readily prepared via solvothermal routes.[27–35] For example, direct reaction between Nb_2O_5 and sodium hydroxide solutions readily yields crystals of the cubic perovskite-phase

$NaNbO_3$ with a cubic habit, at much lower temperatures than that required for solid-state single-crystal growth. By lowering the pH of the reaction, a metastable polymorph of $NaNbO_3$ with the ilmenite structure is formed after 3 h.[36] This further emphasizes the sensitivity of solvothermal synthesis to the specific conditions employed. Indeed in this instance the reaction is so sensitive to conditions that either raising the concentration of NaOH in the reaction mixture (raising pH), or increasing the reaction time, leads to the formation of the perovskite polymorph of $NaNbO_3$ in increasing quantities.

The sensitivity of solvothermal synthesis to pH and other reaction conditions can also be seen in the solvothermal preparation of the pyrochlore-phase $Pb_2Ti_2O_6$.[37] Reaction of Pb(II) acetate and titanium *n*-butoxide in aqueous KOH yields $Pb_2Ti_2O_6$, an anion-deficient pyrochlore phase in which the O′ anion site of the $A_2B_2O_6O'$ lattice is vacant. When the concentration of potassium hydroxide in this synthesis is high, products are formed in which the Pb^{II} and Ti^{IV} cations are ordered on the A- and B-cation sites of the pyrochlore lattice, respectively. However, synthesis at lower KOH concentrations yields products in which the cations are statistically disordered over both cation sites demonstrating the influence of pH on the synthesis. Heating either anion-deficient pyrochlore product above 500 °C leads to a transformation to a perovskite structure, demonstrating the ability of solvothermal reactions to prepare metastable phases.

2.15.3.1.2 Complex manganese oxides

The solvothermal synthesis of complex manganese oxides has been extensively studied due to the varied magnetic and electronic properties these phases exhibit[38] (Chapter 4.03 and 4.11). The synthesis of complex manganese oxides under solvothermal conditions is more complicated than that of the early transition-metal oxides, due to the range of oxidation states (Mn^{II}–Mn^{IV}) and nonstoichiometry (cation and anion deficiency) exhibited by the manganate phases. In high-temperature ceramic syntheses, the average manganese oxidation state present in product phases is controlled via the partial pressure of oxygen in equilibrium with the solid-state reaction. In the analogous solvothermal syntheses, manganese oxidation states are controlled by the comproportionation of a Mn(II) salt and the Mn(VII) permanganate ion. Thus, for example, the reaction of $Ho(NO_3)_3$, $KMnO_4$, and $MnCl_2$ in alkaline solution readily yields the Mn(III) perovskite-phase $HoMnO_3$ according to reaction [6].[39] By utilizing this approach, crystals of a wide range of $REMnO_3$ (RE = Sm–Ho) cubic-type perovskite phases have been prepared[39–41]:

$$5Ho(NO_3)_3 + KMnO_4 + 4MnCl_2 + 22KOH \rightarrow 5HoMnO_3 + 15KNO_3 + 8KCl + 11H_2O \quad [6]$$

Reactions of the smaller rare earths (Er–Ly+Y) at higher temperature, utilizing Mn_2O_3 as a source of manganese, yield 'hexagonal' $REMnO_3$ phases which adopt structures consisting of sheets of apex-linked MnO_5 trigonal bipyramids (Figure 1).[42] The high reaction temperatures of these syntheses are required to decompose $RE(OH)_3$ to the more reactive REO(OH) as reflected by the variation in reaction temperature required for $LuMnO_3$ (175 °C) compared with $YMnO_3$ (350 °C).

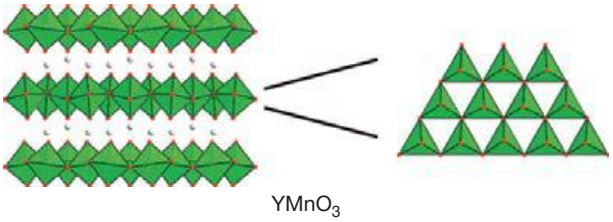

Figure 1 The layered structure of hexagonal $YMnO_3$ consists of sheets of apex-linked MnO_5 trigonal bipyramids.

The decisive role that the average manganese oxidation state in the reaction medium plays in the solvothermal synthesis of complex manganese oxides can be demonstrated by tuning this parameter. For example, if the Mn^{II}:MnO_4^- ratio is adjusted to yield an average oxidation state of $Mn^{3.5+}$, $REMn_2O_5$ phases are produced rather than Mn(III) perovskite phases. Thus, for example, $TbMn_2O_5$ can be prepared according to reaction [7][41,43]:

$$5Tb(NO_3)_3 + 3KMnO_4 + 7MnCl_2 + 26KOH \rightarrow 5TbMn_2O_5 + 15KNO_3 + 14KCl + 13H_2O \quad [7]$$

Following the same strategy of manganese oxidation state tuning, the Mn(IV) hexagonal perovskite phases 2H–$BaMnO_3$ and 4H–$SrMnO_3$ can be readily prepared from a 4:3 ratio of $KMnO_4$:$MnSO_4$ in the presence of basic solutions of $BaCl_2$ and $SrSO_4$, respectively.[44,45] In the case of 2H–$BaMnO_3$, this leads to a much more rapid synthesis than the extended ceramic process required to prepare this phase.[46] By raising the temperature during the synthesis of $BaMnO_3$ to 420 °C, and thus the autogeneous pressure to 600 atm, the high-pressure 9R polymorph of the material is prepared,[44] demonstrating a further parameter by which solvothermal synthesis reactions can be controlled.

A wide range of mixed-valence $Mn^{III/IV}$ $RE_{1-x}A_xMnO_3$ perovskite phases can also be prepared via this method.[45,47–50] For example by heating the appropriate mixture of Mn^{II} and Mn^{IV} salts in a basic solution containing $Pr(NO_3)_3$ and $Ca(NO_3)_2$, $Pr_{1-x}Ca_xMnO_3$ phases with $x = 0.39$, 0.46, 0.7, and 0.76 have been prepared.[51] This again demonstrates that the oxidation state of the mixed-valent manganate product is directly defined by the comproportionation of Mn^{II} and Mn^{VII} species.

The majority of manganese perovskite product phases produced by solvothermal routes appear to be directly comparable, both structurally and in terms of magnetic behavior, to analogous phases produced by the ceramic method. However, there are some exceptions. For example, the ceramic synthesis of the $Mn^{III/IV}$-phase $La_{0.5}Ba_{0.5}MnO_3$ yields a simple cubic perovskite phase in which the La^{3+} and Ba^{2+} cations are statistically distributed over the A-cation site of the perovskite lattice.[52] However, the solvothermal preparation of $La_{0.5}Ba_{0.5}MnO_3$ from a 7:3:5:5 ratio of Mn^{2+}:Mn^{7+}:Ba^{2+}:La^{3+} in basic solution yields a tetragonally distorted perovskite phase in which the La^{3+} and Ba^{2+} cations are ordered into layers.[53,54] This A-cation-ordered phase can be prepared via ceramic routes,[52] but only in a two-step process in which an A-cation-ordered, anion-deficient-phase $LaBaMn_2O_5$ is prepared first and then topochemically oxidized as described in Section 2.15.4.4.1.2, to form the metastable cation-ordered, oxygen-stoichiometric material.

2.15.3.2 Flux Synthesis

Metal salts with low melting points can also be used as fluid media in which to perform low-temperature solid-state reactions. An enormous variety of salt fluxes have been utilized, with a particular emphasis of crystal growth from these media.[55] However, by far the most useful class of flux for oxide synthesis are the hydroxides of group 1 and 2 metals.[56] Simple binary hydroxides have melting points ranging from 272 (CsOH) to 512 °C ($Sr(OH)_2$) and readily form eutectic mixtures with melting points in the range 160–325 °C,[57] and so can act as molten fluxes even at modest reaction temperatures as demonstrated by the synthesis of $La_{2-x}M_xCuO_4$ (M = Na, K) from a NaOH/KOH flux at 300 °C.[58]

The extensive and adjustable acid–base chemistry of molten hydroxides makes them among the best solvent systems for oxide phases. When molten, the auto-ionization equilibrium described in reaction [8] is established, in which H_2O can be considered an acid and O^{2-} a base.

$$2OH^- \leftrightarrow H_2O + O^{2-} \qquad [8]$$

By analogy to the auto-ionization constant of water, K_w, the dissociation constant of hydroxide melts, K_d, is defined as $K_d = [H_2O][O^{2-}]$, with $pH_2O = -\log_{10}[H_2O]$ being a measure of acidity in hydroxide fluxes analogous to pH in aqueous systems. The dissociation constant K_d is observed to be strongly dependent on temperature and on the identity of the metal cations present, with cations of high charge density favoring greater dissociation. Thus, the pH_2O (acidity) of a hydroxide flux can be controlled by selecting an appropriate reaction temperature and metal counterions and then by adjusting the level of hydration of the melt, by adding water or removing it by evaporation.

This acidity adjustment is often decisive to the success of syntheses as the solubility of metal cations in hydroxide fluxes is strongly dependent on the pH_2O of the melt. By carefully controlling this parameter, initially to dissolve the reagent cations and then to precipitate (crystallize) them as ternary and quaternary phases, a wide range of complex oxides can be prepared, many of which are metastable and unattainable by ceramic methods.[56]

A particularly useful aspect of flux synthesis, with regard to soft chemistry, is the preparation of highly oxidized phases from metal hydroxide fluxes. As noted in Section 2.15.4.3.1, at elevated temperatures complex oxides are in equilibrium with the oxygen partial pressure in the atmosphere in contact with their surfaces according to reaction [31]. Due to the favorable entropy change on oxygen release, the oxygen content of product phases tends to decline as the synthesis temperature rises. As a result, the preparation of complex metal oxides containing transition metals in elevated oxidation states can be extremely challenging if the reagent phases are highly refractory and thus only reactive at high temperature.

The use of metal hydroxide fluxes can alleviate these problems in two ways. First, by acting as a fluid transport medium and increasing the rate of cation diffusion, metal hydroxide fluxes lower the required reaction temperature, favoring more oxidized products. Second, hydroxide fluxes can react with atmospheric oxygen to form peroxides (reaction [9]) and superoxides (reaction [10]), which act as oxidizing agents within the melt[59]:

$$2MOH + \frac{1}{2}O_2 \rightarrow M_2O_2 + H_2O \qquad [9]$$

$$2MOH + \frac{3}{2}O_2 \rightarrow 2MO_2 + H_2O \qquad [10]$$

As a result, molten hydroxide fluxes can be employed to prepare metal oxides containing highly oxidized transition-metal centers under ambient oxygen partial pressures. For example, by heating a mixture of Nd_2O_3 and elemental iridium at 550 °C within a KOH flux, the Ir(VI)-phase $Nd_2K_2IrO_7$ is formed, which contains isolated $Ir^{VI}O_6$ octahedra imbedded within a neodymium–potassium-oxide matrix.[60] By comparison, the preparation of the Ir(VI) double perovskite-phase Sr_2CaIrO_6 via a ceramic route requires an applied oxygen pressure of 600 atm in order to stabilize the Ir^{6+} cation.[61] By utilizing a strontium hydroxide flux, crystals of the highly oxidized Rh(V) phases Sr_3ARhO_6 (A = Li, Na) can be grown from melts containing RhO_2 and the corresponding AOH hydroxide.[62] The Sr_3ARhO_6 phases adopt K_4CdCl_6-type structures and represent the first Rh(V) oxides prepared.

Hydroxide fluxes can also be used to prepare oxide phases containing highly oxidized 3d transition-metal centers. For example, the Fe(IV)-containing $RE_{0.5}Sr_{1.5}FeO_4$ (RE = Nd, Sm, Eu) phases can be readily prepared from the corresponding lanthanide oxide, strontium hydroxide, and iron oxide in a KOH flux.[63] Similarly, the Ni(IV)-containing phases $Ba_6Ni_5O_{15}$ and $BaNiO_3$ can be prepared from nickel oxide and barium carbonate in a KOH flux.[64,65] The ceramic synthesis of complex oxide phases containing Fe(IV) or Ni(IV) centers usually requires high oxygen pressures.[66,67]

Thus by employing hydroxide fluxes as strongly oxidizing environments for low-temperature synthesis, an extensive range of complex oxides containing highly oxidized transition-metal centers can be prepared.[56]

2.15.4 Low-Temperature Topochemical Synthesis

Solid-state reactions performed at low temperature can utilize large differences between the rates of solid–solid diffusion of the different ions present in complex oxides, to prepare novel metastable phases. For example, in certain complex oxides particular classes of ion are observed to be significantly more mobile, at a given temperature, than the remainder of the host phase in which they reside. As a result, these highly mobile species can be inserted into, or removed from, host phases under conditions in which the remaining constituents of the host lattice are effectively immobile. The resulting chemical transformations are described as 'topochemical' because they conserve the basic topology of the parent complex oxide phase. The term 'topotactic' is often used interchangeably with topochemical; however, it should be noted that 'topotactic' has a more crystallographic meaning, as it also requires the orientation of crystallites in the product phase to be correlated with those of the starting material. The conservation of structure observed in low-temperature topochemical reactions is in stark contrast to conventional high-temperature ceramic synthesis, in which there is generally no relation between the

structures of reagents and products. By utilizing this structural conservation and carefully selecting the initial complex oxide phase, topochemical reactions enable a degree of synthesis planning and product targeting unavailable in high-temperature synthesis routes.

The large difference in mobility between the mobile species and the host lattice observed under soft chemical conditions corresponds to a large difference in reactivity. This difference in reactivity can be exploited to enable some kinetic control to be exerted over the outcome of solid-state reactions. By performing reactions at temperatures where there is insufficient thermal energy for the host lattice to respond to changes in the composition or structure of the overall phase, solid-state reactions can be performed in which the products are those which form fastest, rather than those which have the most thermodynamically stable structures and/or compositions. The resulting product phases are metastable and generally synthetically inaccessible by conventional high-temperature synthesis routes. Thus, it can be seen that in contrast to the soft chemical synthesis routes described above, topochemical syntheses do not attempt to overcome the intrinsically poor rates of solid–solid diffusion in the reactions of complex oxides. Instead, these synthetic strategies make use of the refractory nature of the complex oxide host lattices to set up a situation in which one component of a complex oxide phase is much more reactive than the remainder, to facilitate the preparation of metastable complex oxide phases.

The low-temperature topochemical chemistry of complex oxides described below is organized with respect to the identity of the mobile species. It should be noted, however, that the species added or removed from the parent oxide phase must be electrically neutral to conserve the electroneutrality of the product. Thus, the addition of a cation or removal of an anion will reduce the host phase and conversely the addition of an anion or removal of a cation will lead to a formal oxidation.

2.15.4.1 Cation-Insertion Reactions

In order to effectively insert cations into metal-oxide host lattices in a topochemical manner, a number of conditions need to be met.

1. There must be intercalation sites within the host framework which can accommodate the inserted cations. These sites can either be existing vacant sites within a close-packed anion framework, or cation sites between weakly bound structural layers.
2. The host lattice must contain reducible metal centers. The insertion process is accompanied by a reduction of the host lattice as shown in reaction [11]. Formally, a neutral species is inserted into the metal-oxide host which auto-ionizes to yield a cation, donating the resultant electron to the framework, which it formally reduces:

$$A \rightarrow A^{n+} + ne^{-} \qquad [11]$$

3. There must be ample mobility of both the inserted cation and the donated electron to allow penetration of the bulk solid, not just the surface.

2.15.4.1.1 Intercalation into framework oxide phases

Transition-metal cations in high oxidation states form strong networks of metal–oxygen covalent bonds in the binary oxides they form. As a result, these phases tend to adopt structures which optimize the geometry of these metal–oxygen interactions at the expense of more conventional nondirectional, Coulombic, close-packing considerations. In addition, the high cation charge of the transition-metal centers strongly disfavors face-sharing and edge-sharing connectivity between neighboring metal–oxygen polyhedra, driving the prevalence of corner-sharing MO_x polyhedral networks. As a consequence of these factors, the binary oxides of highly oxidized transition metals often exhibit quite open structures which include large numbers of vacant coordination sites. Intercalation of cations into these sites allows the topochemical reduction of the host phases to form metastable intercalation compounds.

2.15.4.1.1.1 ReO_3-type hosts

Small electropositive cations can be readily intercalated into dense oxide host phases which contain suitable cation vacancies within their extended frameworks. ReO_3 adopts a structure consisting of a three-dimensional (3D) network of corner-sharing ReO_6 octahedra (**Figure 2**).[5] This framework is topologically identical to the TiO_6 network in the mineral perovskite, $CaTiO_3$ (**Figure 2**). As such the structure of ReO_3 contains large vacant cation sites which would be occupied by the A-cations in ABO_3 perovskite phases. These empty sites will readily host inserted cations as demonstrated by the reaction of ReO_3 with lithium iodide which results in the formation of $Li_{0.2}ReO_3$ as shown in reaction [12][68]:

$$xLiI + ReO_3 \rightarrow Li_xReO_3 + \frac{x}{2}I_2 (0 < x < 0.2) \qquad [12]$$

Using the more powerful reducing agent *n*-butyllithium, greater levels of lithiation can be achieved, ultimately leading

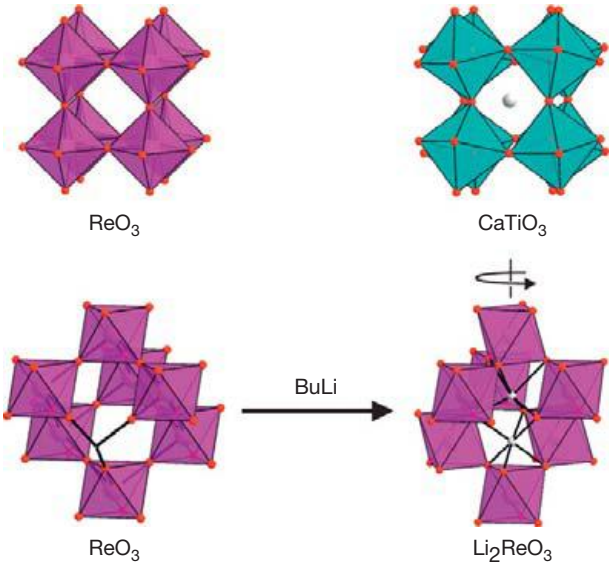

Figure 2 The structures of ReO_3 and $CaTiO_3$ perovskite. Insertion of lithium into ReO_3 drives a cooperative rotation of the ReO_6 polyhedra to convert the 12-coordinate A-site into a pair of 6-coordinate sites occupied by lithium.

to the Re(IV)-phase Li_2ReO_3.[69,70] Subsequent oxidation with ethanol can partially delithiate the material, allowing the preparation of $LiReO_3$ and $Li_{0.35}ReO_3$. Neutron powder diffraction studies have revealed that the lithium inserted into the ReO_3 network is accommodated within octahedral sites within the highly distorted ReO_3 framework. The ReO_6 octahedra undergo a cooperative rotation around the ⟨111⟩ body diagonal of the cubic unit cell, to convert the 12-coordinate cavity in the ReO_3 network into two edge-sharing octahedral interstitial sites as shown in **Figure 2**.[71] Formation of Li_2ReO_3 fills both of these sites to form a structure consisting of chains of face-sharing MO_6 octahedra which share edges. Partial delithiation to form $LiReO_3$ results in an ordered arrangement of Re(V), Li (I), and vacancies within the same anion framework.

Lithium intercalated into the homologous oxide WO_3 is accommodated in a different manner. Reaction of WO_3 with *n*-butyllithium allows the preparation of Li_xWO_3 ($0 \le x \le 0.67$) at ambient temperature.[72] In the resulting materials, the WO_3 host lattice undergoes a cooperative distortion which converts 75% of the large 12-coordinate A-cation sites into 4-coordinate rectangular planar sites which are occupied by lithium (**Figure 3**).[68] Full occupation of these fourfold sites would result in materials of composition $Li_{0.75}WO_3$ suggesting that the low level of lithium insertion which can be achieved for WO_3, compared to ReO_3, has a structural origin.

In contrast, Na_xWO_3 ($0 \le x \le 0.9$) phases prepared at high temperature accommodate sodium ions within the 12-coordinate cation sites of the host lattice with a minimum of distortion to the WO_3 network, consistent with the larger size of the sodium cation.[73] This undistorted lattice can accommodate sodium cations up to a composition of $Na_{0.9}WO_3$. Thus, rather counter-intuitively, it is possible to insert a higher concentration of large sodium ions than small lithium ions into the WO_3 network, due to the large lattice distortion required in the latter case.

In addition to metal cations, hydrogen can also be intercalated into metal-oxide lattices. Reaction at high temperature leads to the removal of oxygen from the extended metal–oxygen lattice as described in detail in Section 2.15.4.3. However, at low temperatures reductive intercalation reactions are possible.

Insertion of hydrogen into ReO_3 is achieved simply by boiling in water, according to reaction [13].[74,75] The resulting gold lustrous material is thought to have a limiting composition of $H_{0.4}ReO_3$:

$$1 + xReO_3 + xH_2O \rightarrow H_xReO_3 + xHReO_4 \qquad [13]$$

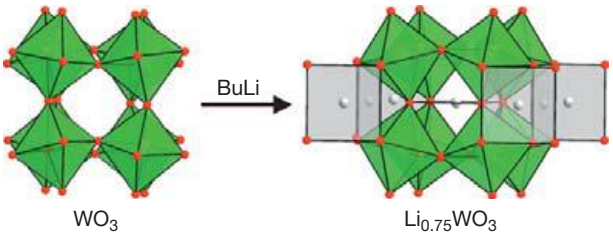

Figure 3 Reaction with BuLi inserts lithium into four-coordinate sites within the structure of WO_3.

Larger levels of hydrogen insertion are achieved using the 'spill-over' method.[76] In this process, small particles of platinum are added to the sample. On exposure to hydrogen gas at room temperature, these particles catalyze the cleavage of the H–H bond in H_2 and so act as a source of atomic hydrogen, which is then inserted into the ReO_3 lattice. Using this technique, compositions in the range H_xReO_3 ($0 < x < 1.36$) have been prepared. After auto-ionization, the hydrogen is incorporated into the structure of ReO_3 as hydroxide ions, which drive a significant cooperative tilting distortion of the $Re(O,OH)_6$ octahedra.[76] Nuclear magnetic resonance (NMR) studies at low temperature suggest that the inserted protons are mobile at temperatures above $T > 235$ K.[77]

Hydrogen can also be readily inserted into WO_3 using zinc in hydrochloric acid as a reducing agent according to reaction [14].[78,79] Compositions in the range H_xWO_3 ($0 < x < 0.6$) can be prepared in this way, which can be considered as mixed-oxide/hydroxide phases like H_xReO_3:

$$WO_3 + \frac{x}{2}Zn + xHCl \rightarrow H_xWO_3 + \frac{x}{2}ZnCl_2 \qquad [14]$$

2.15.4.1.1.2 MO_2 rutile-type hosts

The structure of the rutile polymorph of TiO_2 is widely adopted by the dioxides of other tetravalent transition metals. The structure can be described as a hexagonally close-packed array of oxide ions with the M^{4+} transition-metal cations occupying half of the octahedral coordination sites in this framework to form an edge-sharing network of MO_6 octahedra (**Figure 4**).[5] While the rutile structure is based on close packing, it still contains a large number of available coordination sites, into which additional cations can be inserted. Most notably there are still large numbers of vacant octahedral and tetrahedral sites, which form chains parallel to the crystallographic *c*-axis of the structure. Thus, it is no surprise that reaction with

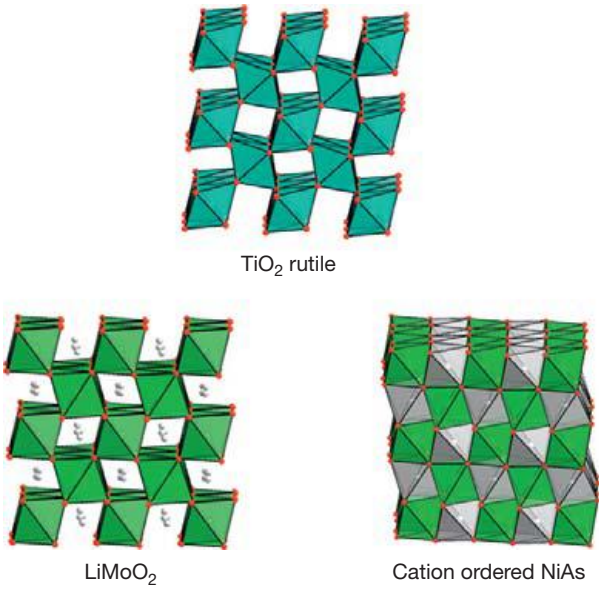

Figure 4 The rutile polymorph of TiO_2. Lithiation of MoO_2 inserts lithium into octahedral sites to form a cation-ordered variant of the NiAs structure.

n-butyllithium leads to the reductive intercalation of lithium into MO_2 (M = Mo, Ru, Os, Ir) rutile phases.[80] While initial reports indicated that lithiation was possible up to composition of Li_xMO_2 ($x = 1.3$–1.5) for these host phases, in subsequent structural studies only limited compositions with $x < 1$ are reported. Detailed structural analysis of $LiMoO_2$[81] and $Li_{0.9}RuO_2$[82] reveals that the lithium in these materials is accommodated exclusively within octahedral coordination sites, and that at a composition of $LiMO_2$ the resulting structure can be related to a cation-ordered variant of the NiAs structure shown in **Figure 4**.

Lithiation of rutile-type WO_2 cannot be achieved using chemical intercalating agents; however, lithium insertion is possible electrochemically,[80] suggesting that the chemical agents employed are not sufficiently reducing. The rutile phases of VO_2, NbO_2, and ReO_2 however show no reactivity either chemically or electrochemically to lithium intercalation. It has been observed that the rutile phases which do undergo lithium-insertion reactions are all metallic. This has prompted the hypothesis that metallic conductivity is a necessary prerequisite for reactivity, as a metallic host lattice can readily transport the reducing electron and also efficiently screen the polarizing influence of the Li^+ cations. However, lithiation-insertion reactions performed at temperatures above the metal–insulator transition of VO_2 (67 °C) did not incorporate lithium either, suggesting that metallic conductivity may be a necessary but not sufficient condition of lithium intercalation into rutile phases.

TiO_2, MnO_2, and CrO_2 exhibit only modest lithiation. Reaction with *n*-butyl lithium yields limiting compositions of $Li_{0.3}TiO_2$, $Li_{0.2}MnO_2$, and $Li_{0.8}CrO_2$. It has been postulated that the smaller size of these first-row transition-metal cations leads to smaller, less flexible host structures which cannot accommodate the lattice expansions and distortions which occur on cation insertion.

2.15.4.1.1.3 AB_2O_4 spinel-type hosts

In contrast to the ReO_3 and rutile host lattices, which contain transition metals in high oxidation states, compounds which adopt structures related to that of the mineral spinel, $MgAl_2O_4$, typically contain metals in lower oxidation states consistent with the increased degree of face-sharing between MO_x coordination polyhedra in this structure type.[5]

The spinel structure is rather complex and based on close packing (**Figure 5**). Described in the face-centered cubic (FCC) space group $Fd\bar{3}m$, the structure consists of a cubic close-packed array of oxide ions with Al^{3+} cations occupying 1/2 of the 32 octahedral interstitial sites (16 per cell, assigned the symmetry label 16d) and Mg^{2+} cations occupying 1/8 of the 64 tetrahedral sites (eight per cell, symmetry 8a) in each unit cell. Therefore, it follows that in each unit cell there are 16 empty octahedral sites (16c) and 56 empty tetrahedral sites (which are split on symmetry grounds into two sets 8b and 48f) into which small cations can be inserted.

A large variety of oxide phases adopt spinel structures including the binary oxides Mn_3O_4, Fe_3O_4, and Co_3O_4. Fe_3O_4 adopts the inverse spinel structure in which, due to crystal field effects, Fe^{III} centers are located on the 8a tetrahedral sites and a 1:1 mixture of Fe^{II} and Fe^{III} centers is located on the 16d octahedral sites. Reaction with *n*-butyllithium readily inserts

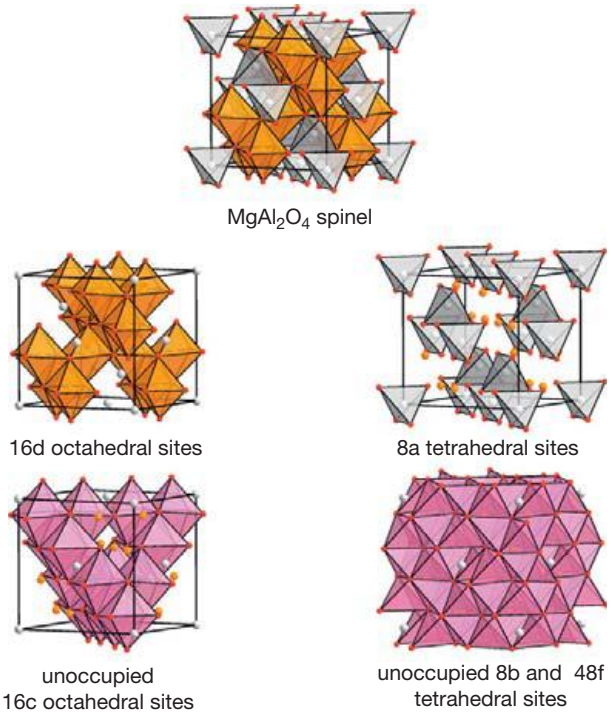

Figure 5 The occupied and unoccupied cation-coordination sites in the $MgAl_2O_4$ spinel structure.

lithium into the spinel host phase, up to a limiting composition of $Li_{1.3}Fe_3O_4$, while electrochemical insertion can add further lithium to produce the Fe(II)-phase $Li_2Fe_3O_4$.[83]

The lithium-insertion process in spinels is not entirely topochemical. Lithium is inserted into the 16c octahedral coordination sites in Fe_3O_4. Associated with this insertion, there is a migration of iron cations from the 8a tetrahedral sites to the 16c octahedral sites within the host lattice. As a result, materials of composition $LiFe_3O_4$ have a partially ordered rock salt structure with iron cations on the 16d sites and a 1:1 disordered array of lithium and iron cations on the 16c sites.[83] Thus, lithiation proceeds according to reaction [15]. It should be noted that the $[Fe_2]_{16d}O_4$ framework is retained throughout the insertion process:

$$\left(Fe^{3+}\right)_{8a}\left[Fe_2{}^{2+/3+}\right]_{16d}O_4 + xLi \rightarrow \left(Li_xFe^{2+/3+}\right)_{16c}\left[Fe_2{}^{2+/3+}\right]_{16d}O_4 \qquad [15]$$

Further lithiation to form phases of composition $Li_xFe_3O_4$ ($1 < x < 2$) proceeds via insertion of lithium ions into the 8b and 48f tetrahedral coordination sites, to yield materials with both octahedrally and tetrahedrally coordinated lithium cations.[83] Lithium insertion into Mn_3O_4[84] and Co_3O_4[85] proceeds via a similar mechanism.

Ternary oxides such as LiM_2O_4 (M = Ti, V, Mn) also adopt spinel structures in which the transition-metal cations are accommodated within the 16d octahedral sites and the small lithium cations in the 8a tetrahedral sites. The lithium-insertion mechanism adopted by these phases is dependent on the identity of the transition-metal ion. Lithiation of $LiTi_2O_4$ follows a mechanism similar to that of the M_3O_4 (M = Mn, Fe, Co) phases. Lithium insertion into the octahedral

16c sites is accompanied by cation migration from the tetrahedral 8a to the octahedral 16c coordination sites.[86] As a result, $Li_{1+x}Ti_2O_4$ ($x>0$) phases adopt cation-ordered rock salt-like structures. In contrast, lithium insertion into $LiMn_2O_4$ occurs without cation migration. Thus, $Li_2Mn_2O_4$ contains lithium cations in both 8a tetrahedral and 16c octahedral coordination sites[84,87] despite the potential for unfavorable Columbic interactions between lithium cations in these two coordination sites.

LiV_2O_4 exhibits a lithiation mechanism which is intermediate between that of $LiTi_2O_4$ and $LiMn_2O_4$. At low levels of lithiation, cations are inserted into the 16d octahedral sites of $Li_{1+x}V_2O_4$ ($0<x<0.5$) with no accompanying migration.[88] However as the lithium content rises above $Li_{1.5}V_2O_4$, cation migration does occur to yield a cation-ordered rock salt structure for the V(III)-phase $Li_2V_2O_4$.

The cation migration observed during the lithiation of spinel phases can be attributed to structural features of the host lattice. As noted above, cations within the ReO_3 and rutile structures are in high oxidation states and, as a result, are tightly bound within octahedral coordination sites so the activation energy for cation migration is extremely high. In contrast, the cations located within the tetrahedral sites of the spinel structure are in lower oxidation states and are located within coordination polyhedra which share faces with empty interstitial sites. Consequently, the barriers to cation migration are lower for the tetrahedral cations, and these cations can move through the host lattice at room temperature. Thus, we can see a general synthetic strategy for preparing metastable materials by utilizing the facile migration of some of the cations within a structure, in combination with reductive intercalation, to induce cation order into extended oxide phases.

2.15.4.1.2 Intercalation into layered binary oxide phases

In addition to the framework oxide hosts described above, it is also possible to reductively intercalate cations into layered oxide host phases to facilitate the preparation of metastable phases. Binary oxide phases of transition metals in high oxidation states can adopt layered structures consisting of sheets of linked MO_x polyhedra. These sheets are then stacked within the material. As a result, there is a strong network of covalent metal–oxygen bonds within each neutrally charged metal-oxide layer. However, the only interlayer interactions present are weak van der Waals forces which are destabilized by electrostatic repulsions between the negatively charged oxide ions. As a result, the intercalation of cationic species into these 'van der Waals gaps' is favored.

2.15.4.1.2.1 α-MoO_3

α-MoO_3, which is typical of this type of host phase, has a structure consisting of $Mo^{IV}O_6$ octahedra which are linked through edges and corners into charge neutral sheets, which stack as shown in Figure 6.[5] Reaction of α-MoO_3 with sodium dithionite (a reducing agent) leads to the reductive intercalation of hydrated sodium ions according to reaction [16][89]:

$$Na_2S_2O_4 + MoO_3 + yH_2O \rightarrow \left[Na^+(H_2O)_n\right]_xMoO_3 + xSO_2 \qquad [16]$$

Diffraction studies reveal that the hydrated sodium ions are inserted topochemically into the van der Waals gap of α-MoO_3

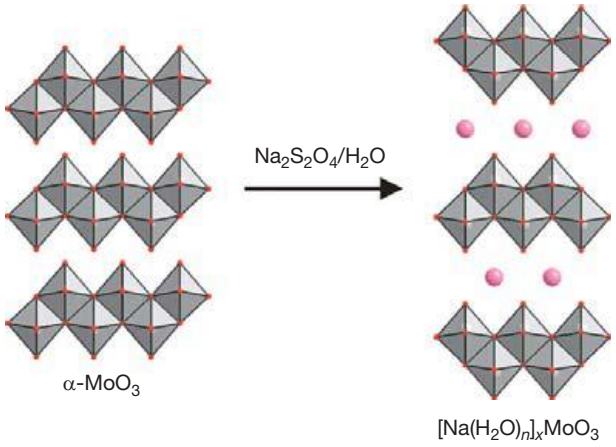

Figure 6 Reaction with sodium dithionite reductively intercalates hydrated sodium ions into α-MoO_3.

as demonstrated by the large expansion in the interlayer spacing on intercalation as shown in Figure 6. Lithium, potassium, rubidium, magnesium, and calcium analogs can also be prepared, either by cation exchange as described in Section 2.15.4.5.1.2, or by electrochemical insertion from solutions of the corresponding cations. Intercalation of unsolvated cations can be achieved via electrochemical reduction reactions in suitable nonaqueous solvents such as dimethoxyethane or dimethylsulfoxide.[89]

The layered nature of the structure of α-MoO_3 means that large cations can be inserted into this phase. By electrochemical reduction, large organic cations such as methylammonium or propylpyridinium can also be inserted to form layered inorganic/organic hybrid phases.[90] The reductive nature of the insertion reactions is demonstrated by a change in the color of the material from white to dark metallic blue, which is accompanied by a large increase in electrical conductivity. All intercalated phases react with strong oxidizing agents such as MnO_4^- and NO_2^- to recover unintercalated α-MoO_3.[89]

The hydrogen-insertion chemistry of α-MoO_3 is extensive. H_xMoO_3 ($0<x<2$) phases can be readily prepared by reaction with Zn/HCl,[91,92] or by electrochemical insertion.[89] H_2MoO_3 has a deep green color, with less hydrogenated samples exhibiting deep red ($1.55<x<1.7$) and deep blue ($0.93<x<0.28$) colors.[91] Intercalated phases are good metallic conductors and exhibit temperature-independent paramagnetism and no electron spin resonance (ESR) signal, consistent with the insertion of the reducing electrons into the d-bands of the MoO_3 host, rather than residing in localized states.[93,94]

Detailed structural studies show that the insertion of hydrogen into α-MoO_3 is topochemical. At low concentrations, the inserted protons bind to oxide ions which bridge between molybdenum centers within the metal-oxide layers.[95] At higher concentration, the protons are bound as $-OH_2$ units to the terminal oxide ions on the outside of the metal-oxide sheets.[96] The shift in binding site is attributed to changes in Mo–Mo bonding as the level of hydrogen in the phases increases. NMR studies indicate that H_xMoO_3 phases with $x\sim1.7$ exhibit proton conductivity at room temperature,[97] while phases with lower hydrogen concentrations do not. This is consistent with a proton-transport mechanism which involves hopping within the van der Waals gap of the α-MoO_3 host phase.

2.15.4.1.2.2 V_2O_5

V_2O_5 can be considered intermediate between the framework oxides such as ReO_3 and RuO_2 and the layered oxides such as α-MoO_3. The structure of V_2O_5 can be considered either as an array of square-based pyramidal VO_5 units which share edges and corners to form a layered 2D structure, or as a three-dimensionally connected network of VO_6 octahedra (Figure 7).[5] The different structural views depend on whether the extended V–O interlayer interaction is considered to be within the coordination sphere of vanadium or not. Regardless of the semantics of the bonding in V_2O_5, it is clear that the extended V–O contact has a significant influence on the intercalation chemistry of V_2O_5 as it prevents the delamination of the structure and thus the intercalation of large cations. As a result, V_2O_5 behaves much like the framework host structures and only intercalates small cations.

Lithium can be intercalated into V_2O_5 either electrochemically or via reaction with *n*-butyllithium or lithium iodide.[98] Phases in the range $Li_xV_2O_5$ $(0<x<1)$ are crystalline, while those with $x>1$ become amorphous. The phase diagram of $Li_xV_2O_5$ contains a number of different phases in which the Li^+ cations are intercalated into coordination sites within the van der Waals gap of the host material, resulting in subtle distortions to the host lattice.[99] Despite these distortions, the 'interlayer' V–O bond, which makes the vanadium centers pseudo-octahedral, is retained. However, if V_2O_5 is reacted with an excess of lithium iodide at room temperature, δ-LiV_2O_5 is formed. In this material the vanadium oxide sheets shift relative to each other to accommodate the lithium cations in more regular tetrahedral sites.[100] This breaks the interlayer V–O bond. δ-LiV_2O_5 has a rather small compositional stability range and only forms at ambient temperature, suggesting that it is a kinetically stabilized phase.

V_2O_5 can readily intercalate large amounts of hydrogen via the spill-over route.[101] Extended reaction at room temperature results in the preparation of $H_{3.8}V_2O_5$, a black material which has an amorphous structure and contains vanadium in an average oxidation state of V+3.1.[102] Lower levels of hydrogenation $(0<x<0.5)$ yield a series of green materials which are isostructural with the V_2O_5 host phase and exhibit semiconducting behavior.[103]

2.15.4.1.3 Intercalation into layered perovskite structures

There are a number of structure types which are commonly adopted by complex oxide phases, which can be considered as layered variants of the ABO_3 cubic perovskite structure (Chapter 2.03). Among the most common are the $A_{n+1}B_nO_{3n+1}$ Ruddlesden–Popper structures. As shown in Figure 8, this family of structures can be thought of as a regular stacked intergrowth of (ABO_3) perovskite blocks and (AO) rock salt layers. Thus, the value of *n* in the compositional formula $(AO)(ABO_3)_n = A_{n+1}B_nO_{3n+1}$ indicates the number of perovskite sheets which are stacked between adjacent AO rock salt layers. Compounds which exhibit $n=1$ or $n=2$ structures are common, while the materials with larger values of *n* are less so. It can be seen in Figure 8 that Ruddlesden–Popper structures with $n\geq 2$ exhibit two distinct A-cation-coordination sites: a 12-coordinate site analogous to that in cubic perovskite phases and a nine-coordinate site which resides within the rock salt layers of the structure. Typically, alkaline earth (Ca, Sr, Ba) or lanthanide cations can be accommodated within the A-cation sites of Ruddlesden–Popper phases, with ordering between the 9- and 12-coordinate sites possible in mixed cation systems where the two A-cations have significantly different charges and/or radii.

Layered perovskite phases which contain large alkali metals (K, Rb, Cs) tend to adopt $A'A_{n-1}B_nO_{3n+1}$ Dion–Jacobson structures. In this structural family, the large monovalent A′-cations reside between the perovskite blocks in eight-coordinate pseudo-cubic coordination sites (Figure 9). It should be noted that the low formal charge on the A′-cations means that in order to charge-balance the $A'A_{n-1}B_nO_{3n+1}$ composition of Dion–Jacobson phases, the B-cations must be tetravalent or pentavalent transition metals. Such high oxidation states appear to provide a good electrochemical driving force for reductive cation-insertion reactions.

2.15.4.1.3.1 Dion–Jacobson phases

While it may appear that there are no obvious vacant coordination sites suitable to host intercalated cations within the Dion–Jacobson family of structures, it has been demonstrated that lithium can be inserted into $A'Ca_2Nb_3O_{10}$ (A′=K, Rb, Cs) or $A'Sr_2Nb_3O_{10}$ phases by exposure to *n*-butyllithium, in a very slow process that can take several weeks, or by electrochemical reduction which is significantly faster.[104,105] The structures of the resulting $Li_xA'A_2Nb_3O_{10}$ $(0<x<0.6)$ phases are not well studied; however, it is clear that the only significant change to x-ray diffraction data collected after intercalation is an expansion of the *c*-lattice parameter, suggesting that the lithium cations are inserted, in a topochemical manner, into the

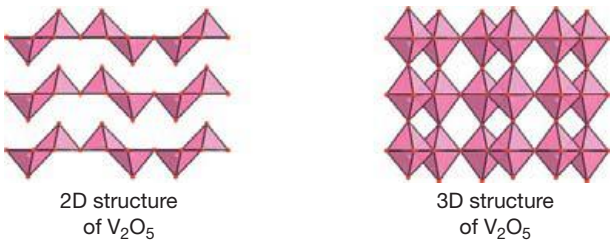

Figure 7 The 2D and 3D representations of the structure of V_2O_5.

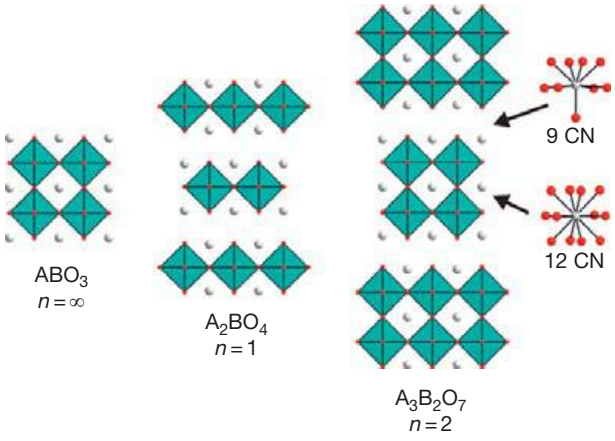

Figure 8 The $A_{n+1}B_nO_{3n+1}$ Ruddlesden–Popper phases.

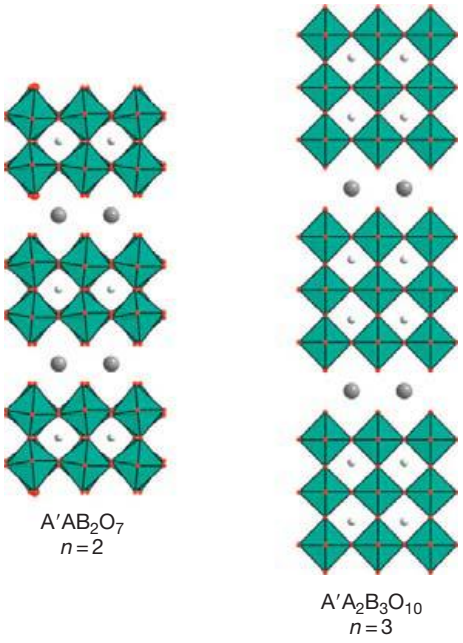

Figure 9 The $A'A_{n-1}B_nO_{3n+1}$ Dion–Jacobson phases.

A′-cation layers which lie between the perovskite blocks in the Dion–Jacobson phases.[106]

On lithium intercalation, the $Li_xA'A_2Nb_3O_{10}$ materials change from white to black, consistent with the reduction of Nb(v). Magnetization data indicate that these phases are superconductors at low temperature,[104] with the highest $T_c = 7$ K observed for $Li_{0.1}CsSr_2Nb_3O_{10}$.[107] Detailed studies suggest that the materials are only superconductors over a small compositional range ($0.1 \leq x \leq 0.15$) and that there is a correlation between the in-plane lattice parameter of a $Li_xA'A_2Nb_3O_{10}$ phase and the maximum superconducting transition temperature observed for that material.

Intercalation of larger cations into Dion–Jacobson phases drives a structural change. On heating $RbLaNb_2O_7$ in the presence of a controlled amount of rubidium vapor, $Rb_2LaNb_2O_7$ is formed.[108] Associated with the insertion of rubidium, there is a change in the stacking of the perovskite blocks from an $A'AB_2O_7$ Dion–Jacobson arrangement in which the A′ rubidium cations are located in eight-coordinate pseudo-cubic sites, to an $A_3B_2O_7$ Ruddlesden–Popper-type stacking arrangement in which the two rubidium cations are located in nine-coordinate sites within the rock salt layer of the structure and adjacent perovskite blocks have a staggered relationship to each other (**Figure 10**). Similarly, exposure of $CsLaNb_2O_7$ to cesium vapor induces an analogous reductive intercalation of cesium to yield the $n = 2$ Ruddlesden–Popper-phase $Cs_2LaNb_2O_7$.[109]

A similar transformation is observed on insertion of sodium into the $n = 3$ Dion–Jacobson-phase $RbCa_2Nb_3O_{10}$.[110] Heating in sodium vapor yields $RbNa_{0.83}Ca_2Nb_3O_{10}$ which adopts a structure in which adjacent perovskite blocks are arranged in a 'staggered' manner consistent with a Ruddlesden–Popper-type structure. The sodium and rubidium cations in the rock salt layers of this phase are situated in highly distorted coordination

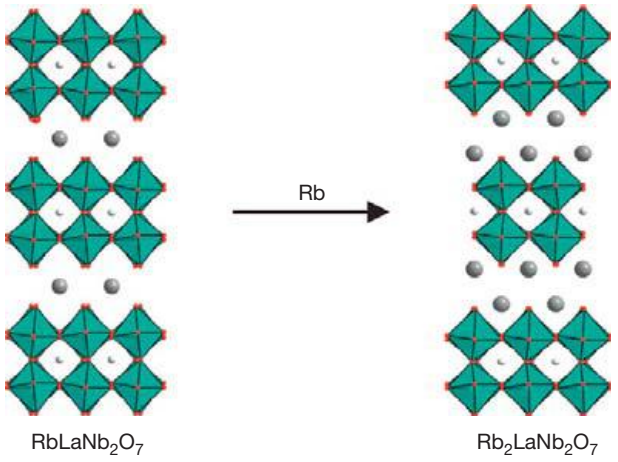

Figure 10 Reductive intercalation of rubidium into the Dion–Jacobson-phase $RbLaNb_2O_7$ drives a structural change to for the Ruddlesden–Popper-phase $Rb_2LaNb_2O_7$.

sites, presumably due to the large mismatch in ionic radii between Na^+ and Rb^+, which drives a significant buckling of the perovskite framework.

The reactions above demonstrate that even though there are no obvious intercalation sites for large cations within Dion–Jacobson structures, a small shift in the relative position of the perovskite layers can create suitable sites. This change in the perovskite stacking sequence, and the ready intercalation of large cationic species, demonstrates the relatively weak binding between the A′-cations and the perovskite blocks in Dion–Jacobson-type structures and is somewhat reminiscent of the layered oxides MoO_3 and V_2O_5. Indeed, this weak interlayer coupling in Dion–Jacobson phases is often exploited in their extensive cation-substitution chemistry described in Section 2.15.4.5.1.3.

2.15.4.1.3.2 Cation-deficient Ruddlesden–Popper Phases

Cation-deficient Ruddlesden–Popper phases can be prepared by exploiting the extensive cation-substitution chemistry of materials which adopt Dion–Jacobson-type structures (Section 2.15.4.5.1.3). Thus, the reaction of $RbCa_2Nb_3O_{10}$ with $LiNO_3$ or $NaNO_3$ yields the cation-deficient Ruddlesden–Popper phases $ACa_2Ta_3O_{10}$ (A = Li, Na) in which the small alkali metal cations are accommodated within partially filled tetrahedral coordination sites between the triple-layer perovskite blocks (**Figure 11**).[111–113] Reaction of $LiCa_2Ta_3O_{10}$ with *n*-butyllithium leads to the reductive intercalation of lithium, to completely fill the remaining tetrahedral coordination sites and form $Li_2Ca_2Ta_3O_{10}$, in which the lithium cations adopt an anti-fluorite-type arrangement between the apical oxide ions of the perovskite sheets (**Figure 11**).[111] In contrast, the reaction of $NaCa_2Ta_3O_{10}$ with NaN_3 inserts sodium into the oxide host and drives a migration of sodium cations from tetrahedral to nine-coordinate sites, so that the resulting phase, $Na_2Ca_2Ta_3O_{10}$, adopts a conventional Ruddlesden–Popper structure with sodium cations located within rock salt layers (**Figure 11**).[112] The intercalated $ACa_2Ta_3O_{10}$ phases exhibit a deep blue color and Pauli paramagnetic responses, consistent with metallic behavior. Similar lithium intercalation reactions have been performed on

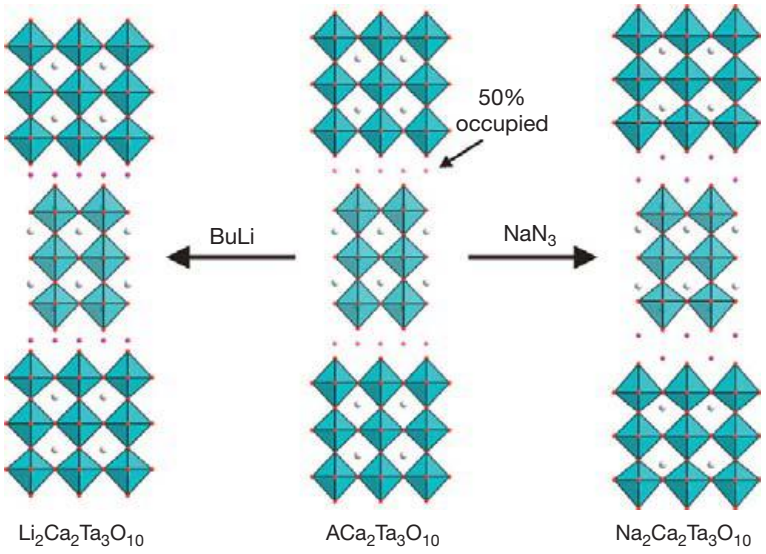

Figure 11 Reductive intercalation of $ACa_2Ta_3O_{10}$ (A = Li, Na) yields phases with structures that depend on the size of the intercalated cation.

the cation-deficient $n = 2$ Ruddlesden–Popper phases $LiLaNb_2O_7$ and $LiLaTa_2O_7$.[111,114]

Cation-deficient Ruddlesden–Popper phases can also be prepared by direct, redox-neutral, cation exchange in which one divalent cation replaces two monovalent cations, to create a cation vacancy (Section 2.15.4.5.1.4). Thus, reaction of the A-cation-ordered Ruddlesden–Popper-phase $NaLaTiO_4$ with $Ca(NO_3)_2$ yields $Na_{0.13}Ca_{0.43}\square_{0.47}TiO_4$ (where □ represents a cation vacancy). On reaction with sodium vapor, $Na_{0.51}Ca_{0.53}LaTiO_4$, a phase with an average titanium oxidation state of Ti + 3.63, is formed.[115]

2.15.4.1.3.3 Aurivillius phases

$Bi_2A_{n-1}B_nO_{3n+3}$ Aurivillius phases can be described as layered intergrowths between $(Bi_2O_2)^{2+}$ blocks with fluorite-like structures and $(A_{n-1}B_nO_{3n+1})$ perovskite blocks. It has been demonstrated that despite the apparently close-packed nature of this structural family, lithium can be inserted into the Bi_2O_2 fluorite layers with concomitant reduction of the transition-metal centers. Thus, the reaction of $Bi_4Ti_3O_{10}$ with *n*-butyllithium yields $Li_2Bi_4Ti_3O_{10}$. Neutron diffraction data indicate that the lithium cations reside within pseudo-square-planar coordination sites between the Bi_2O_2 blocks and perovskite layers.[116]

2.15.4.2 Cation Deintercalation Reactions

The cation deintercalation chemistry of complex transition-metal oxides which contain small monovalent cations (Li, Na) has been widely studied as this is the chemical transformation which occurs during the charging of lithium-ion batteries (Chapter 4.03). From the perspective of soft chemical synthesis, low-temperature cation deintercalation reactions allow the preparation of oxidized, metastable complex oxide phases which exhibit metal–oxygen frameworks which cannot be prepared directly by ceramic routes.

In order to effectively deintercalate cations from metal-oxide host lattices in a topochemical manner, a number of conditions need to be met.

1. There must be suitable highly mobile cations present in the parent phase and their mobility must be significantly higher than that of the host lattice. This generally restricts this type of reaction to phases which contain monovalent cations, typically lithium, sodium, or silver.
2. The removal of cations must leave a kinetically stable phase. Deintercalation of cations from a complex oxide phase can lead to unscreened, unfavorable Columbic interactions between oxide ions in the host lattice. These interactions can limit the level of cation deintercalation which can be achieved.
3. The deintercalation of cations formally oxidizes the host phase as the metal cations are removed as neutral atoms. Thus, the host phase must contain readily oxidizable metal centers, and the oxidizing agent, or electrochemical driving force, used must be of sufficient strength to bring about the reaction.

2.15.4.2.1 α-$NaFeO_2$-type phases

2.15.4.2.1.1 $LiCoO_2$

$LiCoO_2$ is a thermodynamically stable phase which is readily prepared by heating a combination of Li_2CoO_3 and Co_3O_4 under flowing oxygen. The resulting Co(III) oxide adopts a structure analogous to α-$NaFeO_2$ which can be considered as a cation-ordered variant of the NaCl rock salt structure in which Co^{3+} and Li^+ cations are arranged into layers of edge-sharing MO_6 octahedra within the distorted FCC oxide ion lattice as shown in Figure 12. The layered nature of this structure, and the large number of additional interstitial sites available to the lithium cations within each layer, lead to good lithium-ion mobility. This high mobility can be utilized to bring about the oxidative deintercalation of lithium ions to form phases of composition $Li_{1-x}CoO_2$.[117] The degree of deintercalation which can be achieved depends on the strength of the oxidant used, as the deintercalation of lithium is

accompanied by the oxidation of Co^{3+} centers to Co^{4+}.[118] This is exemplified by the reactions with the halogens as shown in reaction [17]:

$$2LiCoO_2 + xX_2 \rightarrow 2Li_{1-x}CoO_2 + 2xLiX \quad [17]$$

$$LiCoO_2 + xH^+ \rightarrow Li_{1-x}CoO_2 + xLi^+ + \frac{x}{2}H_2 \quad [18]$$

Reaction with I_2, Br_2, or Cl_2 yields $Li_{1-x}CoO_2$ phases with $x = 0.09$, 0.53, and 0.69 respectively, broadly in line with the electrochemical reduction potentials of the halogens.[118] Alternatively, strong acids such as HCl or H_2SO_4 can be used to deintercalate lithium from $LiCoO_2$. Treating single crystals of $LiCoO_2$ with HCl for 7 days yields $Li_{0.35}CoO_2$ as shown in reaction [18].[119] In contrast, if powder samples of $LiCoO_2$ are treated with H_2SO_4, delithiation occurs via a combination of disproportionation and proton-exchange processes as shown in reactions [19] and [20], respectively[118]:

$$LiCoO_2 + 2xH_2SO_4 \rightarrow Li_{1-2x}CoO_{2-2x} + xLi_2SO_4 + xCoSO_4 + 2xH_2O \quad [19]$$

$$LiCoO_2 + 0.5xH_2SO_4 \rightarrow Li_{1-x}H_xCoO_{2-2x} + 0.5xLi_2SO_4 \quad [20]$$

Complete deintercalation of lithium can be achieved electrochemically.[120,121] The resulting metastable Co(IV)-phase, CoO_2, is highly oxidizing, reacting rapidly with moisture to form CoOOH according to eqn [21].[120] However if materials are kept under appropriate conditions, a combination of chemical and electrochemical oxidation allows the entire $Li_{1-x}CoO_2$ ($0 \leq x \leq 1$) composition range to be prepared:

$$4CoO_2 + 2H_2O \rightarrow 4CoOOH + O_2 \quad [21]$$

The deintercalation of lithium from $LiCoO_2$ is strictly topochemical in the composition range $0.12 \leq x \leq 1$. Removal of lithium ions leads to vacancies within the planes of lithium cations (Figure 12) which adopt a disordered arrangement over most of the compositional range. Magnetic anomalies provide some evidence for lithium vacancy ordering in compositions close to $x = 0.7$; however, these ordered states appear fragile and are easily disrupted by small compositional changes and so are as yet uncharacterized.[122,123] Compositions close to $x = 0.5$ however exhibit robust 1:1 ordering of lithium and lithium vacancies which is associated with Co(III)/Co(IV) charge order as described below.[119,124]

Complete removal of all the lithium ions from $LiCoO_2$ drives a change to the structure, in which the $[CoO_2]$ planes shift relative to each other such that the Co(IV)-phase CoO_2 adopts the CdI_2 structure as shown in Figure 12.[120] At compositions close to $x = 0.12$, a hybrid structure is adopted which includes both the cubic and the hexagonal stacking of $[CoO_2]$ planes.[125,126]

2.15.4.2.1.2 $NaCoO_2$

Similar deintercalation reactions can be performed on the analogous layered Na_xCoO_2 phases. However in this instance the situation is more complex because there are four different thermodynamically stable layered Na_xCoO_2 phases which can be prepared by conventional high-temperature synthesis routes: the α phase ($0.9 \leq x \leq 1$) which adopts the O3 structure of $NaFeO_2$, the α′ phase ($x = 0.75$) which exhibits an O1 structure, the γ phase ($x \sim 0.7$) which adopts a P2 structure, and the β phase ($0.55 \leq x \leq 0.60$) which adopts a P1 structure as shown in Figure 13.[127,128]

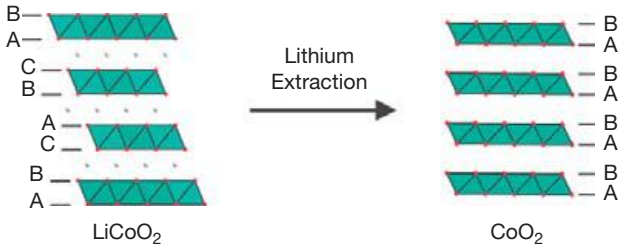

Figure 12 Extraction of lithium drives a change from the ABCABC cubic stacking present in $LiCoO_2$ to ABAB hexagonal stacking in CoO_2.

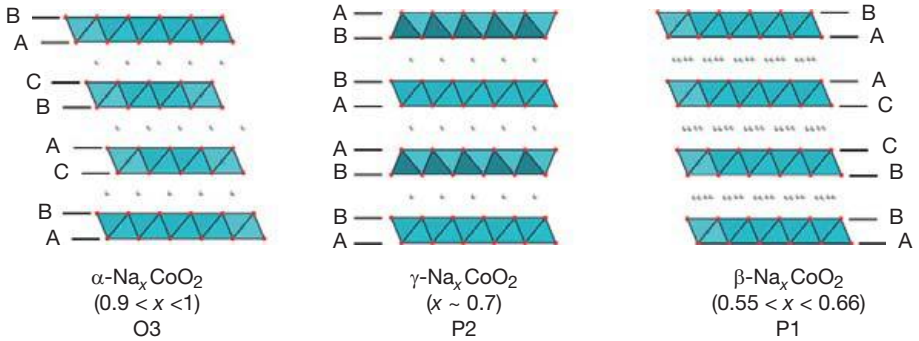

Figure 13 The thermodynamically stable structures of Na_xCoO_2.

Oxidative deintercalation reactions performed on the α phase of Na_xCoO_2, which like $LiCoO_2$ adopts the α-$NaFeO_2$ structure, reveal that the sodium phases are more easily oxidized than the lithium-containing analogs. Thus oxidation of $Na_{0.92}CoO_2$ with excess iodine or bromine in acetonitrile yields $Na_{0.5}CoO_2$ and $Na_{0.3}CoO_2$, respectively, compared with $Li_{0.81}CoO_2$ and $Li_{0.47}CoO_2$ as described above.[118,128] $Na_{0.3}CoO_2$ prepared in this way retains the O3 structure of the α-Na_xCoO_2 parent phase. In contrast, $Na_{0.5}CoO_2$ prepared by the oxidative deintercalation of $Na_{0.92}CoO_2$ adopts the P1-type structure of thermodynamically stable β-Na_xCoO_2 (**Figure 13**).[128] Given that $Na_{0.5}CoO_2$ has a composition which is very similar to the stability range of β-Na_xCoO_2, this suggests that the change in $[CoO_2]$ layer stacking observed on chemical oxidation of α-type $Na_{0.92}CoO_2$ to β-type $Na_{0.5}CoO_2$ is under thermodynamic control to some extent. Similar changes to the stacking sequence of the $[CoO_2]$ sheets are observed during the electrochemical oxidation of α-Na_xCoO_2.[129]

The intercalation/deintercalation chemistry of the double-layer γ-phase $Na_{0.7}CoO_2$ has been very extensively studied. Sodium can be readily deintercalated from this phase using bromine or iodine in a manner similar to that employed on other Na_xCoO_2 compounds.[130] Sodium concentrations as low as $Na_{0.34}CoO_2$ are also achievable by employing NO_2PF_6 as an oxidant. Additional sodium has been intercalated into γ-$Na_{0.7}CoO_2$ by gentle heating in tetrahydrofuran in which elemental sodium and benzophenone had been dissolved. Thus by utilizing both oxidative deintercalation and reductive intercalation 2-layer, γ-type phases can be prepared over the composition range Na_xCoO_2 ($0.34 \leq x \leq 0.89$).[130]

In contrast to the Na_xCoO_2 phases derived from α-$Na_{0.92}CoO_2$, products of the low-temperature intercalation/deintercalation of γ-$Na_{0.7}CoO_2$ are isostructural with respect to the parent phase in that the $[CoO_2]$ layers retain their AABBAA stacking sequence across the whole available composition range.[130] This suggests that this stacking sequence is kinetically stabilized under the reaction conditions employed. This kinetic stability of the P2 structure of γ-type Na_xCoO_2 is also observed during electrochemical oxidation.[129]

One structural feature, which does change across the γ-Na_xCoO_2 compositional range, is the coordination site occupied by the sodium ions. The sodium cations are located in prismatic coordination sites within the 2P structure of γ-Na_xCoO_2. There are two crystallographically distinct prismatic coordination sites created by the stacking of the $[CoO_2]$ layers. The distribution of sodium between these two sites changes sharply as a function of sodium content, suggesting that the configuration of the sodium layers is coupled to the complex electronic configuration of the triangular CoO_2 lattice.[130]

2.15.4.2.1.3 Physical properties of $A_{1-x}CoO_2$

The extensive investigation of the cation deintercalation chemistry of A_xCoO_2 phases described above has been motivated by the useful and exotic properties they exhibit. In addition to the widespread utilization of Li_xCoO_2 phases as cathode materials in secondary lithium-ion batteries, A_xCoO_2 phases have received significant attention because the cobalt centers in the $[CoO_2]$ sheets within these materials are arranged into triangular lattices. This unusual lattice symmetry, combined with the ability to change the electron count (oxidation state) of the cobalt centers directly by simply changing the alkali metal concentration,[131,132] makes the A_xCoO_2-layered cobaltates an ideal set of materials for the study of correlated electronic interactions.

Taking Li_xCoO_2 and the different polymorphs of Na_xCoO_2 as a whole, it has been observed that for phases with high alkali metal concentrations, where Co^{3+} is the predominant cobalt oxidation state ($x > 0.5$), an unusual 'Curie–Weiss metallic state' is observed.[122,123,130,132,133] Samples exhibit metallic conductivity (resistivities of the order of 1 mΩ cm) and simultaneously have magnetic responses which are indicative of localized electronic behavior. In the specific case of Na_xCoO_2 ($x \sim 0.7$), this combination of localized magnetic spins and metallic conductivity is thought to be responsible for the highly enhanced thermopower observed in the materials ($\sim 100\ \mu V\ K^{-1}$ at 300 K).[134,135] Lowering the alkali metal content to $x = 0.5$ induces cation order within the vacant sheets of lithium and sodium cations.[119,136] This is rather unexpected as a 1:1 order of cations and vacancies appears to be incompatible with the threefold symmetry of the $[CoO_2]$ sheets. Detailed studies, particularly of γ-type $Na_{0.5}CoO_2$, have revealed that the observed cation order is assisted by partial Co(III)/Co(IV) charge order which breaks the triangular symmetry of the CoO_2 planes and leads to insulating behavior at this composition.[136] The interplay between the electronic configuration of the $[CoO_2]$ sheets and the dispositions of the sodium cations further confirms that these two features of the material are strongly coupled.

As the alkali metal concentration declines further, the Curie–Weiss-like magnetic behavior diminishes, so that for A_xCoO_2 phases with $x < 0.5$ temperature-independent paramagnetism more typical of metallic systems is observed.[123,130,133] However, the most striking physical behavior in the A_xCoO_2 system appears after a further piece of soft chemistry. If two-layer γ-type Na_xCoO_2 phases with $x \sim 0.3$ are exposed to water, they readily absorb water molecules into the partially occupied sodium layers to form phases of approximate composition $Na_{0.3}CoO_2 \cdot 1.3H_2O$, with greatly expanded interlayer separations as shown in **Figure 14**. The resulting material, when cooled below 4.5 K, exhibits bulk superconductivity.[137] Studies have shown that the presence of water in this phase is critical for the appearance of superconductivity as even partial dehydration to a composition of $Na_{0.3}CoO_2 \cdot 0.6H_2O$ is sufficient to suppress the superconducting state.[138] However, the exact role of water in inducing superconductivity into $Na_{0.3}CoO_2$ is not clear. The large increase in separation between the $[CoO_2]$ layers in superconducting $Na_{0.3}CoO_2 \cdot 1.3H_2O$ (9.8 Å)[137] compared with nonsuperconducting $Na_{0.3}CoO_2 \cdot 0.6H_2O$ (6.9 Å)[138] and $Na_{0.3}CoO_2$ (5.6 Å),[130] and the observation that the superconducting critical temperature, T_c, decreases under pressure,[139] suggest the isolation of the $[CoO_2]$ sheets, and the more 2D character of the superconducting phases is important. Preparation of hydrated phases with a range of sodium contents reveals that superconductivity is only supported over a small compositional range ($Na_xCoO_2 \cdot 1.3H_2O$ ($0.25 \leq x \leq 0.35$)) with a maximum T_c at $x \sim 0.3$ and a 'dome' like dependence of T_c on the $[CoO_2]$ layer electron count.[140]

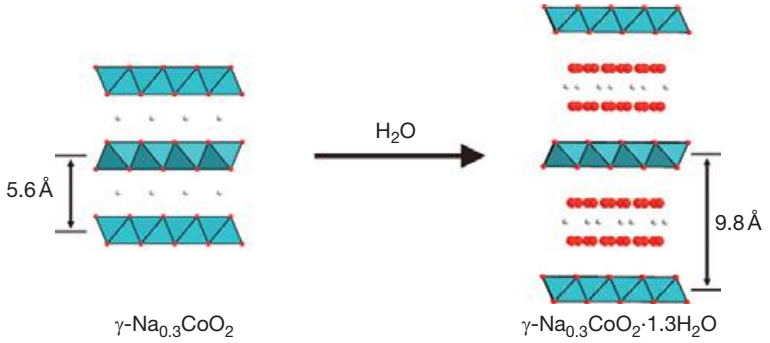

Figure 14 γ-$Na_{0.3}CoO_2$ intercalates water to form the superconducting phase γ-$Na_{0.3}CoO_2 \cdot 1.3H_2O$.

2.15.4.2.1.4 A_xNiO_2

Analogous deintercalation reactions can be performed on layered A_xNiO_2 (A = Li, Na) phases which also adopt α-$NaFeO_2$-type structures. Compared to the oxidations of the A_xCoO_2 materials, the oxidation of A_xNiO_2 phases requires more powerful oxidizing agents, consistent with the greater electronegativity of nickel compared to cobalt. Partial delithiation can be achieved by reaction with H_2SO_4 via a disproportionation route to generate $Li_{1-x}NiO_2$ and Ni^{2+} as shown in reaction [22][141]:

$$LiNiO_2 + 4\gamma H^+ \rightarrow (1-\gamma)Li_{(1-2\gamma)/(1-\gamma)}NiO_2 + \gamma Ni^{2+} + 2\gamma Li^+ + 2\gamma H_2O \quad [22]$$

Complete delithiation of $LiNiO_2$ to form NiO_2 is possible electrochemically.[142] From a structural perspective, the delithiation of $LiNiO_2$ is complicated by the possibility of $Li_{1-z}Ni_{1+z}O_2$ nonstoichiometry which substitutes some of the lithium centers with nickel ions. In the absence of this nonstoichiometry, lithium deintercalation proceeds in a topochemical manner until a low lithium concentration is achieved. There is then a structural reorganization, like that observed during the delithiation of $LiCoO_2$, such that the Ni(IV)-phase NiO_2 adopts a hexagonal, CdI_2-type structure.[143] However in samples with appreciable nonstoichiometry ($Li_{1-z}Ni_{1+z}O_2$ ($z > 0.07$)), the presence of nickel ions on interlayer coordination sites prevents the shift of $[NiO_2]$ sheets. As a result, the oxidative deintercalation is topochemical over the entire composition range. NiO_2 prepared from such a sample has a $CdCl_2$-type structure in which the cubic stacking of the oxide ions in $LiNiO_2$ is retained.[142] These structural complications and the highly oxidizing nature of A_xNiO_2 phases have to date prevented a detailed study of their physical properties.

2.15.4.2.1.5 $LiVO_2$

$LiVO_2$ also adopts an α-$NaFeO_2$-type ordered rock salt structure. Reaction with bromine in chloromethane leads to the oxidative deintercalation of lithium and the formation of cation-deficient $Li_{1-x}VO_2$ phases over the compositional range $0 \leq x \leq 1$.[144] In contrast to the cobaltates and nickelates described above, the deintercalation reactions of $LiVO_2$ are not topochemical.[145,146] In $Li_{1-x}VO_2$ phases where $x > 0.3$, vanadium cations are observed to diffuse into octahedral sites made vacant by the removal of lithium, to help stabilize the structure of the cation-deficient phase. As a result, a significant degree of disorder is introduced into the layered, ordered rock salt structure of the $LiVO_2$ parent phase. For example, it is observed that $Li_{1-x}VO_2$ phases with $x \sim 0.7$ have one-third of the vanadium cations located in the 'wrong' cation sites. It is proposed that vanadium cations diffuse between octahedral coordination sites via a network of face-sharing tetrahedral sites which exist within the cubic close-packed lattice of the host phase. The vanadium diffusion is further facilitated by the disproportionation of V^{4+} and the preference of V^{5+} for tetrahedral coordination as shown in reactions [23] and [24]:

$$2V^{4+}{}_{\text{octahedral}} \rightarrow V^{3+}{}_{\text{octahedral}} + V^{5+}{}_{\text{tetrahedral}} \quad [23]$$

$$V^{3+}{}_{\text{octahedral}} + V^{5+}{}_{\text{tetrahedral}} \rightarrow 2V^{4+}{}_{\text{octahedral}} \quad [24]$$

The metastability of $Li_{1-x}VO_2$ phases is exemplified by the observation that if $Li_{0.5}VO_2$ is heated above 300 °C, it transforms to the spinel LiV_2O_4, with lithium cations located on the 8a tetrahedral sites and vanadium on 16d octahedral sites.[147]

2.15.4.2.2 Lithium manganese oxides

Manganese dioxide is known to adopt a number of different polymorphs, the most thermodynamically stable of which is the mineral pyrolusite (β-MnO_2) which has the same structure as the rutile polymorph of TiO_2.[5] Reaction of manganese oxides with lithium leads to the formation of three principal phases – Li_2MnO_3, $LiMn_2O_4$, and $LiMnO_2$ – which adopt different manganese–oxygen frameworks in order to accommodate the lithium cations in phases with average manganese oxidations states of +4, +3.5, and +3, respectively.

All three lithium manganese oxide phases can be delithiated in acidic solutions. On exposure to acid, Li_2MnO_3 decomposes into known polymorphs of MnO_2 by what is thought to be a dissolution/precipitation mechanism.[148] However, as described below, the more reduced lithium manganese oxide phases undergo oxidative lithium deintercalation reactions to form novel MnO_2 frameworks.

$LiMn_2O_4$ adopts a spinel-type structure in which lithium cations are located on the 8c tetrahedral sites and manganese cations accommodated within 16d octahedral sites (**Figure 15**). Reaction with acid brings about the delithiation/disproportionation reaction described in reaction [25] to yield a new polymorph of manganese dioxide, λ-MnO_2.[149] The delithiation reaction is topochemical such that λ-MnO_2 retains the manganese–oxygen framework of the spinel parent phase (**Figure 15**). The novel MnO_2 framework has been observed to exhibit complex magnetic frustration and good activity as a

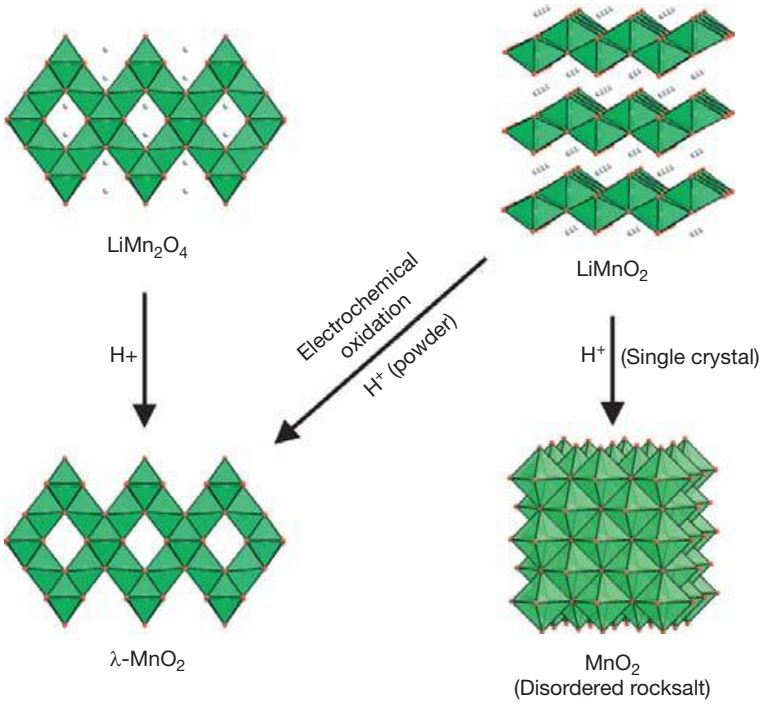

Figure 15 Delithiation of $LiMn_2O_4$ and $LiMnO_2$ leads to the formation of new metastable polymorphs of MnO_2.

water-oxidation catalyst.[150,151] On heating λ-MnO_2 to 300 °C, it is observed to transform to β-MnO_2, demonstrating the metastability of the delithiated phase[149]:

$$2LiMn_2O_4 + 4H^+ \rightarrow 3MnO_2 + 2Li^+ + Mn^{2+} + 2H_2O \quad [25]$$

Orthorhombic $LiMnO_2$ adopts an ordered rock salt structure consisting of zigzag sheets of edge-sharing MnO_6 octahedra, separated by octahedrally coordinated lithium ions (Figure 15). In common with $LiCoO_2$ (Section 2.15.4.2.1.1), the delithiation reactions which occur between orthorhombic $LiMnO_2$ and acid depend on the physical form of the material. On exposure to acid, a single crystal of $LiMnO_2$ was observed to undergo a delithiation reaction as described in reaction [26] to form a phase of composition MnO_2[152]:

$$2LiMnO_2 + 2H^+ \rightarrow MnO_2 + 2Li^+ + H_2 \quad [26]$$

The extraction of lithium from $LiMnO_2$ drives a structural transition in which some of the manganese cations diffuse into octahedral sites vacated by the lithium cations. As a result, the MnO_2 phase formed by acid delithiation of $LiMnO_2$ has a rock salt structure in which Mn^{4+} cations are randomly distributed over half the available octahedral sites (Figure 15).

In contrast, the reaction between powder samples of orthorhombic $LiMnO_2$ and acid proceed via a combination of disproportionation and ion exchange as shown in reactions [27] and [28].[153] In this case, the deintercalation reaction drives a migration of the manganese cations so that they adopt the λ-MnO_2 network of delithiated $LiMn_2O_4$, which shares a common oxide ion lattice with the rock salt structure. Electrochemical delithiation of orthorhombic $LiMnO_2$ also results in the formation of λ-MnO_2.[154] The observation that both $LiMn_2O_4$ and orthorhombic $LiMnO_2$ (under the correct conditions) are delithiated to form λ-MnO_2 suggests that this phase has good kinetic stability.

$$3LiMnO_2 + 4\gamma H^+ \rightarrow Li_{3-2\gamma}Mn_{3-\gamma}O_{6-2\gamma} + \gamma Mn^{2+} + 2\gamma Li^+ + 2\gamma H_2O \quad [27]$$

$$LiMnO_2 + xH^+ \rightarrow Li_{1-x}H_xMnO_2 + xH^+ \quad [28]$$

2.15.4.2.2 Titanates

There are three common polymorphs of titanium dioxide – rutile, anatase, and brookite – which all adopt structures consisting of connected TiO_6 octahedra.[5] It is possible to prepare further metastable polymorphs of TiO_2 by the low-temperature oxidative deintercalation of cations from A_xTiO_2 phases.

2.15.4.2.2.1 TiO_2(R)

Reaction of a 1:2 molar ratio of lithium metal and TiO_2 at 1200 °C yields $Li_{0.5}TiO_2$ which adopts a structure in which TiO_6 octahedra are arranged into a corner and edge-sharing network analogous to that of the ramsdellite polymorph of MnO_2.[155] The lithium cations are located in approximately tetrahedral sites within this TiO_2 network, as shown in Figure 16. On exposure to air, lithium is topochemically deintercalated, such that Li_xTiO_2 phases with $x = 0.41$, 0.16, and 0.14 are formed after a couple of days, 1 month, and 1 year, respectively. Reaction with HCl enables the complete removal of all the lithium from $Li_{0.5}TiO_2$ according to reaction [29][156]:

$$Li_{0.5}TiO_2 + 0.5HCl \rightarrow TiO_2 + 0.5LiCl + 0.25H_2 \quad [29]$$

As shown in Figure 16, the deintercalation of lithium from $Li_{0.5}TiO_2$ is topochemical and thus enables the preparation of a new metastable polymorph of TiO_2 with the ramsdellite

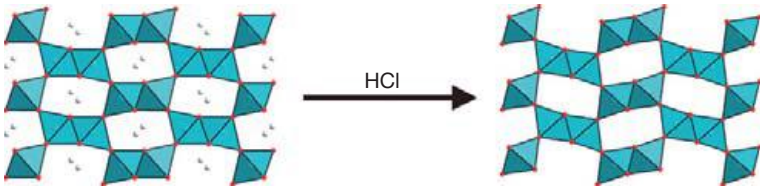

Figure 16 Oxidative deintercalation of lithium from the ramsdellite-phase $Li_{0.5}TiO_2$ yields a metastable polymorph of titanium dioxide, TiO_2(R).

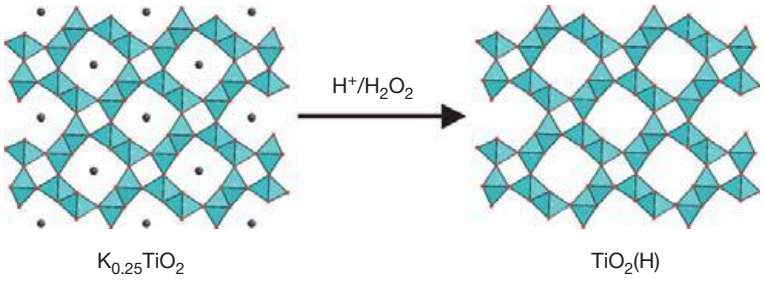

Figure 17 Oxidative deintercalation of potassium from the hollandite-phase $K_{0.25}TiO_2$ yields a metastable polymorph of titanium dioxide, TiO_2(H).

structure, referred to as TiO_2(R). The metastability of the TiO_2(R) polymorph can be seen by observing that it transforms to the brookite polymorph of TiO_2 on heating above 370 °C.[157]

2.15.4.2.2.2 TiO_2(H)

$K_{0.25}TiO_2$ can be readily prepared by heating the appropriate ratio of metallic potassium and titanium dioxide in a sealed nickel tube at approximately 1000 °C. The phase formed adopts a structure analogous to that of the mineral $BaMn_8O_{16}$ hollandite, which consists of double chains of edge-sharing TiO_6 octahedra which share edges to form wide tunnels occupied by potassium ions as shown in **Figure 17**.[158]

Reaction between $K_{0.25}TiO_2$ and an acidic solution of hydrogen peroxide leads to the deintercalation of potassium in a topochemical manner to yield a new metastable hollandite polymorph of titanium dioxide, TiO_2(H), as shown in **Figure 17**. TiO_2(H) has the lowest density of any of the TiO_2 polymorphs reported to date.[158,159] On heating TiO_2(H) above 410 °C, a structural transition occurs to form the more stable anatase polymorph of TiO_2, emphasizing the metastability of the deintercalated phase.

2.15.4.3 Anion Deintercalation Reactions

The topochemical deintercalation of oxide ions from complex transition-metal oxides can be utilized to prepare a large number of metastable phases which contain transition-metal centers in unusual oxidation states and coordination geometries. In order for anion extraction reactions to be effective, a number of conditions must be met:

1. The mobility of the anion lattice must be much greater than the cation lattice at the temperature of reaction, if anions are to be removed from a host phase without disruption or rearrangement of the cation framework.
2. The removal of anions must leave a kinetically stable phase. The removal of anions from a complex oxide will tend to lower the coordination number of the metal cations present. The anions within complex oxides act to screen the unfavorable Columbic repulsions between highly charged metal cations; therefore, anion deintercalation is only possible if any unfavorable cation–cation interactions in the resulting phase are small. This generally requires the transition-metal cations in host phases suitable for topochemical reduction to initially reside in sites of high coordination number ($CN \geq 5$).
3. The deintercalation of oxide ions formally reduces the transition-metal centers within the host phase. The reducing agent or method used must therefore have sufficient 'reducing power' at the temperature of reaction to bring about the reduction.

2.15.4.3.1 'Cubic' perovskite phases

The anion deintercalation chemistry of phases which adopt the cubic perovskite structure, or distorted variants of this structure, has been widely studied due to the ability of phases with this structure type to accommodate large numbers of anion vacancies with minimal energetic penalties.[160] This is particularly true of host phases which contain late, first-row transition-metal centers (Mn, Fe, Co, Ni) within their MO_6 octahedral coordination sites.

For example, the reaction of the perovskite-phase $CaMnO_3$ with hydrogen at 300 °C yields the topochemically reduced phase $CaMnO_{2.5}$,[161] in which the $Mn^{IV}O_6$ octahedra of the host phase have been converted into an ordered array of $Mn^{III}O_5$ square pyramids in the reduced product (**Figure 18**).[162] The reduction proceeds by the reaction of hydrogen with $CaMnO_3$ to form a reduced $CaMnO_{3-x}$ phase and water vapor, according to reaction [30]:

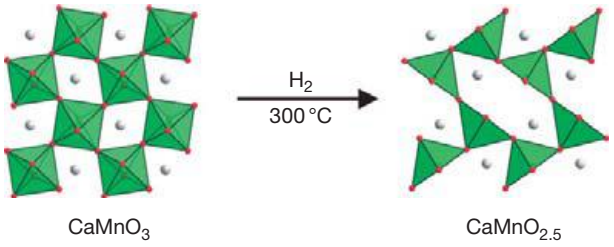

Figure 18 The topochemical reduction of $CaMnO_3$ yields $CaMnO_{2.5}$.

$$CaMnO_3 + xH_2 \rightarrow CaMnO_{3-x} + xH_2O \quad [30]$$

The reaction is spontaneous ($\Delta G < 0$) due to the formation of water. However, the reduction reaction is readily reversible so the equilibrium position (level of anion deintercalation) can be controlled by adjusting the partial pressure of water in the reacting system allowing the controlled synthesis of phases in the composition range $CaMnO_{3-x}$ ($0 \leq x \leq 0.5$).[163]

The physical behavior of $CaMnO_{3-x}$ phases reveals a feature common to many topochemically reduced materials. On reduction, the coordination number of the transition-metal cation being reduced, in this case manganese, is lowered. As a result, it is not only the electron count (oxidation state) of the metal center which is changed on anion deintercalation, but also the relative energies of the different partially filled metal d-orbitals, as these are sensitive to the local symmetry of the cation-coordination site. This change in the cation-coordination number and d-orbital energy has a tendency to localize the electrons added to the system on reduction at the low-coordinate metal centers, often leading to insulating behavior in topochemically reduced phases. This insulating behavior is often in contrast with the behavior of analogous cation-doped phases. For example, phases in the compositional series $La_xCa_{1-x}MnO_3$ ($0 \leq x \leq 1$) adopt distorted perovskite structures[164] and span the manganese oxidation state ranging from Mn^{4+} at $x = 0$ to Mn^{3+} at $x = 1$, in an analogous manner to the anion-deficient series $CaMnO_{3-x}$ ($0 \leq x \leq 0.5$) which spans the same oxidation state range. $CaMnO_3$, the $x = 0$ member of both series, is an antiferromagnetic insulator.[165] Substitution of calcium with lanthanum to form mixed-valent $Mn^{3+/4+}$ $La_xCa_{1-x}MnO_3$ phases induces metallic behavior and complex magnetism at low temperature.[166] In contrast, topochemically reduced $CaMnO_{3-x}$ phases remain insulated across the whole composition range due to the localization of electrons at five-coordinate Mn^{III} centers.[161]

An alternate reduction method widely applied to transition-metal perovskite phases utilizes metals as oxygen getters. At temperatures where there is appreciable anion mobility, the oxygen content of a complex metal oxide is in equilibrium with the partial pressure of oxygen in contact with the surface of the solid phase according to reaction [31]:

$$MO_n \leftrightarrow MnO_{n-2x} + xO_2 \quad [31]$$

The position of the equilibrium is a balance between the lattice energy released on oxygen incorporation (oxidation of Mn_{n-2x} to MO_n) and the entropy increase of reduction, due to the release of oxygen. This equilibrium can be driven to the right by taking advantage of the favorable entropy change on reduction and simply raising the reaction temperature. Alternatively, the reduction of the complex oxide phase can be favored by artificially lowering the oxygen partial pressure in the system, either by pumping the oxygen away or purging with an inert atmosphere or by the use of a highly electropositive metal such as titanium or zirconium. In this latter case, the metals will react rapidly with the low partial pressure of oxygen in the system 'gettering' the oxygen away and thus driving the reduction of the complex oxide phase. Thus if the cubic perovskite $LaCoO_3$ is heated to 400 °C in the presence of zirconium, a deintercalation reaction occurs according to reaction [32], to yield the Co(II)-phase $La_2Co_2O_5$[167]:

$$LaCoO_3 \leftrightarrow LaCoO_{3-2x} + xO_2 + Zr \rightarrow LaCoO_{2.5} + ZrO_y \quad [32]$$

The oxygen removed from the complex oxide passes through the gas phase. As a result, the substrate oxide and the metal getter (Zr in this case) need to be in close proximity, but do not need to be in contact, so the reduced product need not be contaminated with ZrO_y byproducts. In addition because the substrate oxide and metal getter can be physically separated, the getter can be heated to a higher temperature than the substrate to facilitate rapid oxygen scavenging and a faster reaction.

The reduced phase produced via getter reduction of $LaCoO_3$, $La_2Co_2O_5$, adopts the brownmillerite structure. This is one of the most common anion-deficient variants of the perovskite structure and consists of sheets of $Co^{II}O_6$ octahedra stacked in an alternating sequence with sheets of $Co^{II}O_4$ tetrahedra (**Figure 19**).[167] The material is an electronic insulator which adopts an antiferromagnetically ordered structure below $T_N \sim 300$ K. In principle, it should be possible to tune the level of reduction in getter reactions by adjusting the temperature of the substrate phase to shift the position of the equilibrium in reaction [32]. However, in practice this is extremely challenging so $LaCoO_{3-x}$ phases of intermediate composition are most easily prepared by the controlled partial oxidation of $La_2Co_2O_5$.[168]

The two reduction strategies discussed thus far, hydrogen reduction and metal getters, operate at moderate temperatures. In the case of hydrogen reduction, a reasonable amount of thermal energy is required to overcome appreciable activation barriers associated with the strength of the H–H bond of the hydrogen gas reductant. Likewise metal getter reactions must operate at reasonably high temperatures due to the entropy-driven nature of the oxygen-release process. As a result, these two reduction techniques preclude the formation of the most metastable phases because, at their temperature of operation ($T \geq 300$ °C), the cations in the most metastable phases are mobile, and therefore reduction reactions lead to the formation of thermodynamic products – typically binary oxide phases – rather than metastable topochemically reduced phases.

In order to address this problem, binary metal hydrides such as NaH,[169] CaH_2,[170] and LiH[171] have been utilized as solid-state reducing agents. The topochemical reduction of the Ni(III) perovskite-phase $LaNiO_3$, via a zirconium getter reaction at 400 °C, results in the formation of $La_2Ni_2O_5$.[172] This Ni(II) phase adopts a unique structure consisting of stacked chequerboard layers of $Ni^{II}O_6$ octahedra and $Ni^{II}O_4$ square planes. Attempts to decrease the oxygen content of the $LaNiO_{3-x}$

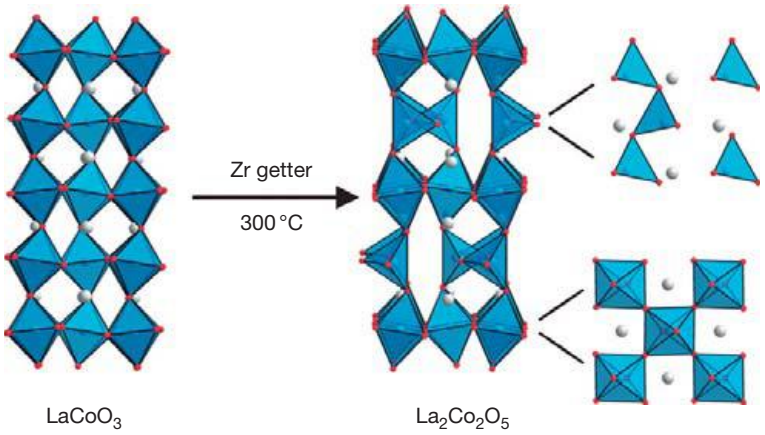

Figure 19 The topochemical getter reduction of $LaCoO_3$ with zirconium yields the brownmillerite-phase $La_2Co_2O_5$.

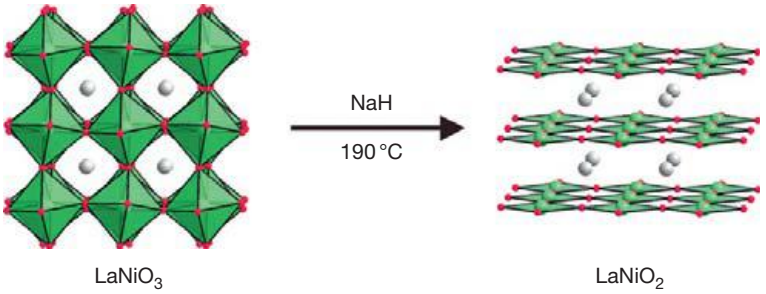

Figure 20 The topochemical reduction of $LaNiO_3$ with NaH yields the infinite layer phase $LaNiO_2$.

phase further by raising the temperature of the getter reaction result in sample decomposition to La_2O_3 and elemental nickel. However if an intimate mixture of $LaNiO_3$ and NaH is heated at 190 °C under vacuum within a sealed glass ampoule, a topochemical reduction of the substrate phase occurs to from $LaNiO_2$,[169] driven by the formation of NaOH according to reaction [33]:

$$LaNiO_3 + NaH \rightarrow LaNiO_2 + NaOH \qquad [33]$$

The extremely low reaction temperature demonstrates that there are no large activation barriers in the reduction process. When combined with a large thermodynamic driving force provided by the formation of NaOH, this allows the highly metastable Ni(I)-phase $LaNiO_2$ to be isolated ($T_{decomposition}$ of $LaNiO_2 \sim 225$ °C). In order to act as an effective reducing agent, sodium hydride must be in close physical contact with the phase to be reduced. As a result, the reduced product phases are contaminated with a mixture of NaOH byproducts and unused NaH reducing agent. These can be readily removed by reaction/dissolution in a weak acid such as methanol.[169]

$LaNiO_2$ adopts an infinite layer structure consisting of sheets of apex-sharing Ni^IO_4 square planes which are stacked in an alternating sequence with sheets of La^{3+} cations (Figure 20). As a result, the phase is isoelectronic and isostructural with $Sr_{1-x}Ca_xCuO_2$ which is considered to be the parent structure of all the layered high-T_c superconducting cuprates.[173] Despite the structural and electronic similarity of $LaNiO_2$ to the corresponding copper oxide phases, the nickel compound does not exhibit superconductivity. This is attributed to insufficient mixing of the Ni 3d and oxygen 2p orbitals in this material.[174]

In contrast to sodium hydride, which acts as a two-electron reducing agent, formally converting H^- into H^+, calcium hydride and lithium hydride act as one-electron reducing agents converting H^- into H^0 according to reactions [34] and [35][175,176]:

$$Sr_7Mn_4O_{15} + 2CaH_2 \rightarrow Sr_7Mn_4O_{13} + 2CaO + 2H_2 \qquad [34]$$

$$BaMnO_3 + 2LiH \rightarrow BaMnO_2 + Li_2O + H_2 \qquad [35]$$

The oxide byproducts of these reactions can be readily removed by dissolution in a weak acid such as NH_4Cl in methanol.[170,171] However under some circumstances this is not possible due to the acid sensitivity of the topochemically reduced phase.[177] The choice of reducing agent therefore becomes a compromise between the synthetic simplicity of hydrogen or getter reactions and the reducing power and chemical compatibility of hydride reducing agents.

The utility of hydride reducing agents can be seen in the preparation of mixed-valent $Mn^{II/III}$ oxide phases. A very large number of studies have investigated the reduction chemistry of $La_{1-x}A_xMnO_3$ (A = Ca, Sr, Ba) perovskite phases in order to prepare anion-deficient materials with average manganese oxidation states between Mn(II) and Mn(III).[178–181] The majority

of these studies have utilized hydrogen as a reducing agent. However, this synthetic route appears to be limited to preparing phases with a minimum average oxidation state of $Mn^{2.5+}$. Thus, for example, reaction of $La_{0.5}A_{0.5}MnO_3$ (A = Ca, Sr) with hydrogen at 600 °C yields the respective $La_{0.5}A_{0.5}MnO_{2.5}$ brownmillerite phases[182,183] and the analogous reduction of $LaMnO_3$ yields $LaMnO_{2.75}$.[184,185] In contrast, reaction of $La_{1-x}A_xMnO_3$ (A = Ca, Sr; $0.2 \leq x \leq 0.4$) phases with NaH at 190 °C yields the corresponding $La_{1-x}A_xMnO_{2.5}$ brownmillerite phases with manganese oxidation states which span the range 2.2–2.4.[69,186]

Topochemical reduction reactions can also be used to prepare extended oxide phases which contain transition-metal cations in highly unusual coordination environments. $SrFeO_{3-\delta}$ can be readily reduced to the Fe(III) brownmillerite-phase $Sr_2Fe_2O_5$ with a wide range of reducing agents. Further reaction of $Sr_2Fe_2O_5$ with CaH_2 leads to an anion deintercalation reaction which drives a large-scale reorganization of the host anion lattice to yield the Fe(II)-phase $SrFeO_2$.[187,188] This phase adopts an infinite layer structure like $LaNiO_2$[169] (Figure 21) in which Fe(II) centers are located within square-planar $Fe^{II}O_4$ coordination sites.

The stabilization of a phase containing iron in square-planar coordination sites is highly unusual. Square-planar coordination sites are generally only occupied by transition-metal centers which have d-electron counts which can provide some electronic stabilization in D_{4h} symmetry (e.g., d^8 Ni^{2+}, Pt^{2+}; d^9 Cu^{2+}). However, the high-spin d^6 electronic configuration of the Fe(II) centers in $SrFeO_2$, determined from neutron diffraction data and Mössbauer spectra,[187] provides no obvious electronic stabilization in a square-planar coordination geometry, making their existence a bit of a puzzle. There is, however, some evidence for a more complex stabilization of the square-planar geometry by the Fe(II) centers as substitution of greater than 30% of the iron centers with manganese or cobalt leads to the formation of a different structure type on reduction.[189]

$SrFeO_2$ is an antiferromagnetic insulator with an ordering temperature of 473 K.[187] On the application of pressures greater than 40 GPa, the material undergoes a spin transition to a highly unusual $S = 1$ intermediate spin state accompanied by a change in physical behavior from an antiferromagnetic insulator to a ferromagnetic conductor.[190] This pressure-induced insulator to metal transition again highlights the large on-site repulsion effects which typically localize the valence electrons in topochemically reduced phases.

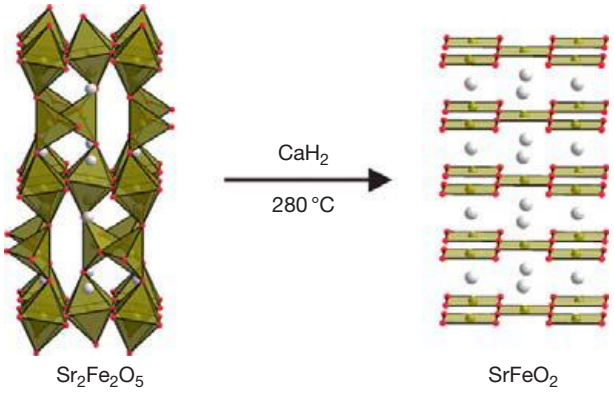

Figure 21 The topochemical reduction of $Sr_2Fe_2O_5$ yields the infinite layer phase $SrFeO_2$.

2.15.4.3.2 Ruddlesden–Popper phases

Complex oxides which adopt layered Ruddlesden–Popper-type structures also readily exhibit oxygen nonstoichiometry and so can act as good substrate phases for oxygen deintercalation reactions. The reduction chemistry of $A_{n+1}B_nO_{3n+1}$ phases where the transition-metal B-cation is manganese has been particularly well studied, and is typical of the reduction chemistry of phases of this structure type.

The reaction of the $n = 1$ Ruddlesden–Popper-phase Ca_2MnO_4 with hydrogen at 300 °C readily yields the Mn(III)-phase $Ca_2MnO_{3.5}$.[161] On reduction oxide ions are deintercalated from 'equatorial' sites within the MnO_2 sheets of the host phase to form sheets of composition $MnO_{1.5}$ which have an identical anion-vacancy arrangement as that present in $CaMnO_{2.5}$ (Figure 22) with the manganese centers located within $Mn^{III}O_5$ square-based pyramids.[191] Topochemical reduction of the structurally analogous phase $Sr_2MnO_{4-\delta}$ readily forms $Sr_2MnO_{3.5}$, again by the removal of oxide ions from the equatorial MnO_2 sheets within the host phase. However, the arrangement of anion vacancies in $Sr_2MnO_{3.5}$ is such that the $Mn^{III}O_5$ units formed on reduction are arranged into tetramers which then share corners (Figure 22) in a strong contrast to the anion-vacancy ordering present in $Ca_2MnO_{3.5}$.[192]

Utilizing the more powerful reducing agent CaH_2, the $n = 1$ phases $LaSrMnO_4$ and $LaBaMnO_4$ can be reduced to the respective Mn(II) phases $LaSrMnO_{3.5}$ and $LaBaMnO_{3.5}$, consistent with the greater low-temperature reducing powder of the hydride reagent.[193] Oxide ions are again deintercalated from the equatorial sheets of the substrate phases, but in this instance the arrangement of anion vacancies is disordered within this plane.

The topochemical reduction of cobalt-based Ruddlesden–Popper phases can also be achieved. Reduction of the $n = 3$ phase $La_4Co_3O_{10}$ using a zirconium getter reaction readily yields the Co(II)-phase $La_4Co_3O_9$.[194] During the reduction process, anions are deintercalated from the central CoO_2 sheet of the host phase to form an anion-deficient CoO layer which adopts an anion-vacancy-ordered arrangement analogous to that present in the mineral brownmillerite.

Reaction of the $n = 1$ cobaltate $LaSrCoO_4$ with hydrogen readily yields Co(II)-phase $LaSrCoO_{3.5}$ in which the anion vacancies are accommodated in a disordered arrangement within equatorial $CoO_{1.5}$ sheets.[195] Reaction with the more powerful reducing agent NaH yields the more oxygen-deficient-phase $LaSrCoO_{3.38}$ which has an average cobalt oxidation state of $Co^{1.76+}$ indicating that approximately one-quarter of the cobalt centers in the phase are monovalent.[195]

In contrast to the reaction with NaH, the reaction between $LaSrCoO_4$ and CaH_2 at slightly higher temperature proceeds via a two-step process. In the first step, $LaSrCoO_4$ is reduced to $LaSrCoO_{3.35}$ according to reaction [36]. There then follows an anion-substitution reaction in which one oxide ion is exchanged with two hydride ions, to form an oxide-hydride-phase $LaSrCoO_3H_{0.7}$ according to reaction [37][170,196]:

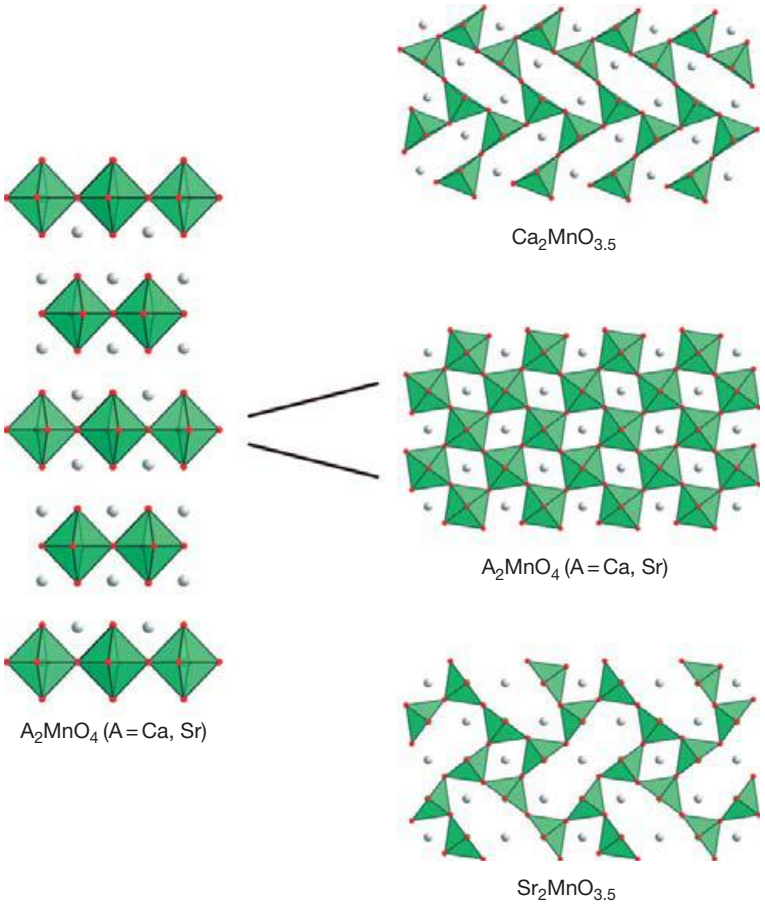

Figure 22 The reduction of A_2MnO_4 Ruddlesden–Popper phases yields products with anion-vacancy-ordering schemes which are dependent on the identity of the A-cation.

$$LaSrCoO_4 + 0.65CaH_2 \rightarrow LaSrCoO_{3.35} + 0.65CaO + 0.375H_2 \quad [36]$$

$$LaSrCoO_{3.35} + 0.35CaH_2 \rightarrow LaSrCoO_3H_{0.7} + 0.35CaO \quad [37]$$

Computational studies have revealed that this highly metastable oxide-hydride phase is stabilized by strong hybridization between Co 3d, oxygen 2p, and hydrogen 1s orbitals.[196] The high-temperature antiferromagnetic order observed in $LaSrCoO_3H_{0.7}$ ($T_N = 380$ K) has also been attributed to this hybridization. Similar reactions with CaH_2 to form oxide-hydride phases have also been observed for $PrSrCoO_4$, $NdSrCoO_4$,[197] and the $n = 2$ phase $Sr_3Co_2O_{7-x}$.[177]

In contrast to the simple anion deintercalations observed on the reduction of manganates and cobaltates, the low-temperature reduction of Ruddlesden–Popper phases containing iron or nickel occurs in association with large-scale rearrangements of the anion lattices of the host phases, resulting in reduced products which contain transition-metal centers in square-planar coordination sites. The $n = 2$ Ruddlesden–Popper-phase $Sr_3Fe_2O_{7-\delta}$ is readily reduced to $Sr_3Fe_2O_6$.[198] This Fe(III) phase adopts an anion-deficient structure in which the anion vacancies are located within the central 'bridging' anion site of the $n = 2$ Ruddlesden–Popper lattice (Figure 23)

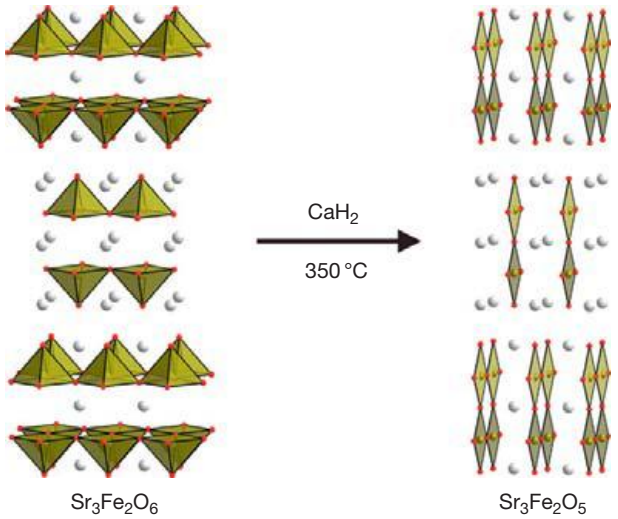

Figure 23 Low-temperature reduction of $Sr_3Fe_2O_6$ drives a rearrangement of the anion lattice to yield $Sr_3Fe_2O_5$ which contains corner-linked FeO_4 square planes.

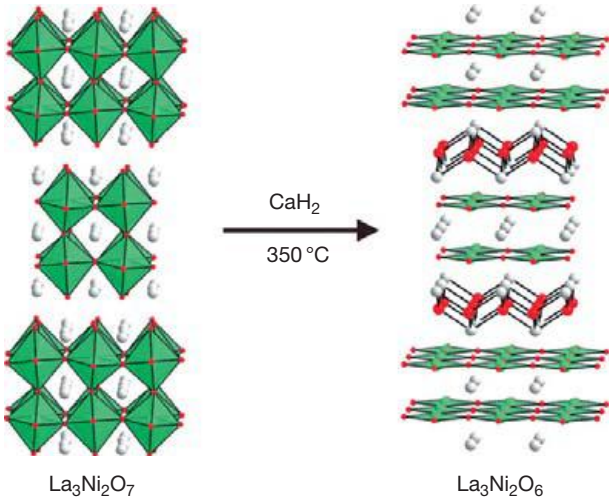

Figure 24 Reduction of $La_3Ni_2O_7$ drives a rearrangement of the anion lattice to yield $La_3Ni_2O_6$ containing sheets of corner-linked NiO_4 square planes.

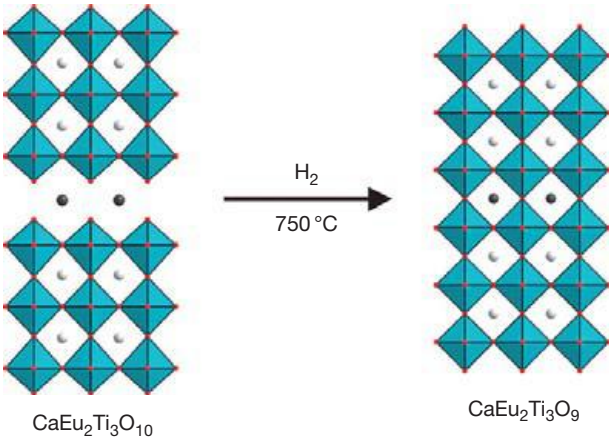

Figure 25 Reduction of the $n=3$ Dion–Jacobson-phase $CaEu^{III}{}_2Ti_3O_{10}$ leads to a fusion of adjacent TiO_6 octahedra and the formation of an A-cation-ordered perovskite-phase $CaEu^{II}{}_2Ti_3O_9$.

such that the iron centers are located within square-based pyramidal coordination sites. Reaction with calcium hydride leads to the deintercalation of anions from $Sr_3Fe_2O_6$ to yield the Fe(II)-phase $Sr_3Fe_2O_5$[199] in which the anion lattice has undergone a reorganization, similar to that observed in the reduction of $Sr_2Fe_2O_5$ to $SrFeO_2$[187] (Section 2.15.4.3.1), resulting in a square-planar coordination for the iron centers in the product phase (Figure 23).

Reduction of the $n=2$ nickelate $La_3Ni_2O_7$ induces a different anion reorganization. Reaction with CaH_2 at 350 °C yields the mixed-valent Ni(I/II)-phase $La_3Ni_2O_6$[200] which adopts a structure related to the T′-structure of Nd_2CuO_4. During the reduction of $La_3Ni_2O_7$, the 'apical' oxide ions, which reside within rock salt layers of the host phase, migrate into coordination sites analogous to those adopted by fluoride ions in the fluorite structure.[5] As a result, the nickel cations in the reduced product are located within apex-linked NiO_4 square planes (Figure 24) in a manner analogous to that of the infinite layer phase $LaNiO_2$, described in Section 2.15.4.3.1.

2.15.4.3.3 Reductive fusion of perovskite sheets

The anion deintercalation reactions described above are all associated with the reduction of transition-metal cations. However, there are a number of lanthanides, most notably europium, which exhibit multiple stable oxidation states in extended oxides. When present in transition-metal-oxide phases which contain early transition metals in high oxidation states, these lanthanide cations are reduced in preference to the transition metals. As the transition-metal oxidation state is unchanged during the reaction, the reduction of lanthanide A-cations is associated with lattice rearrangements which preserve the local coordination geometry of the oxophilic transition-metal centers. Thus, for example, the reduction of the $n=3$ Dion–Jacobson-phase $CaEu^{III}{}_2Ti_3O_{10}$ (prepared via cation exchange as described in Section 2.15.4.5.1.3) with hydrogen yields the perovskite-phase $CaEu^{II}{}_2Ti_3O_9$ according to reaction [38]:

$$CaEu_2Ti_3O_{10} + H_2 \rightarrow CaEu_2Ti_3O_9 + H_2O \qquad [38]$$

The low-temperature nature of the oxygen deintercalation reaction limits the rate of cation diffusion and thus the perovskite product retains the calcium–europium cation order of the original Dion–Jacobson phase as shown in Figure 25. An analogous reaction can be observed on reduction of $Ca_{0.5}Eu^{III}TiO_4$, which forms the $n=2$ Ruddlesden–Popper-phase $CaEu^{II}{}_2Ti_2O_7$ when heated in hydrogen. In both of the reactions described, the retention of the TiO_6 coordination polyhedra leads to a fusion of separated perovskite sheets to form either perovskite phases, or layered phases of higher order, on oxygen deintercalation.

2.15.4.3.4 Structural selectivity

The variety of anion-vacancy-ordered structures adopted by anion-deficient phases indicates that there are a number of factors which direct the structural selectivity of topochemical deintercalation reactions. For example, the anion-deficient perovskite phases $Ca_2Mn_2O_5$, $La_2Co_2O_5$, and $La_2Ni_2O_5$ all adopt different anion-vacancy-ordered structures in which the transition-metal cations reside within coordination sites of differing coordination number and geometry: $Ca_2Mn_2O_5$–$Mn^{III}O_5$ square-based pyramids[162]; $La_2Co_2O_5$–$Co^{II}O_6$ octahedra and $Co^{II}O_4$ tetrahedra[167]; and $La_2Ni_2O_5$–$Ni^{II}O_6$ octahedra and $Ni^{II}O_4$ square planes.[172] In these three examples, the structures adopted by these $A_2B_2O_5$ phases can be rationalized by considering the respective coordination preferences of the Mn^{3+}, Co^{2+}, and Ni^{2+} cations as directed by the crystal field stabilization provided to cations in coordination sites of different geometry. However, the different anion-vacancy-ordering schemes adopted by the two Mn(III), $n=1$ Ruddlesden–Popper phases $Ca_2MnO_{3.5}$ and $Sr_2MnO_{3.5}$ (Figure 22) demonstrate that the coordination preferences of the transition-metal cations are not the only factor to consider. Instead, the anion-vacancy distributions in topochemically reduced phases are best considered as being due to the coordination 'preferences' of all the cations in the host phase. As a result, changes to the identity of the A-cations within a host phase can lead to striking changes to the anion-vacancy-

ordered structure and oxygen stoichiometry of topochemically reduced products. For example, the $n=2$ Ruddlesden–Popper-phase $YSr_2Mn_2O_7$ can be readily reduced with sodium hydride to yield the Mn(II)-phase $YSr_2Mn_2O_{5.5}$ in which oxide ions have been deintercalated from the equatorial MnO_2 sheets of the host phase.[201] In contrast, hydrogen reduction of $NdSr_2Mn_2O_7$, which differs from $YSr_2Mn_2O_7$ by the simple aliovalent substitution of Nd^{3+} for Y^{3+}, removes oxide ions from the central bridging oxide site in the $n=2$ Ruddlesden–Popper lattice,[202] demonstrating the structure directing role of the 'spectator' A-cations.

A more dramatic change can be observed as a function of A-cation identity, in the reduction reactions of $REBaCo_2O_5$ phases. Phases of composition $REBaM_2O_5$ (RE = lanthanide, Y; M = Mn, Fe, Co) adopt structures in which the strong 'preference' of the large Ba^{2+} cation for 12-coordination drives the simultaneous ordering of both the A-cations and anion vacancies to yield the anion-deficient cation-ordered perovskite structure shown in **Figure 26** (see Section 2.15.4.4.1.2).[203–207] Reduction of $YBaCo_2O_5$ with sodium hydride leads to the formation of $YBaCo_2O_{4.5}$. Deintercalation of oxide ions from the 'equatorial' anions sites of the host lattice yields a Co(II) phase which contains cobalt centers located in four- and five-coordinate sites as shown in **Figure 26**.[208] In contrast, reduction of the isoelectronic and isostructural lanthanum-substituted analog, $LaBaCo_2O_5$, with sodium hydride yields $LaBaCo_2O_{4.25}$. This mixed-valent Co(I/II) phase adopts a dramatically different anion-vacancy-ordering pattern resulting in a structure which contains $Co^{II}O_5$ square-based pyramids, $Co^{II}O_4$ tetrahedra, and $Co^{I}O_4$ square planes.[208] This dramatic change in the reduction product of $REBaCo_2O_5$ phases on the substitution of yttrium with lanthanum further demonstrates the important structure directing role the A-cations play in topochemical reduction reactions.

2.15.4.4 Anion-Insertion Reactions

In order to effectively insert anions into metal-oxide host lattices in a topochemical manner, a number of conditions need to be met.

1. There must be intercalation sites within the host framework which can accommodate the inserted anions. These can be anion 'vacancies' which already exist within the close-packed host frameworks, unoccupied interstitial anion sites, or anion-insertion sites that can be formed by minor rearrangements of the host oxide lattice.
2. The host lattice must contain oxidizable centers. The insertion process is formally an oxidation in which a neutral species is inserted into the host material (for example, an oxygen atom); this species becomes reduced (to an O^{2-} oxide ion for example), thus oxidizing the host phase. In order for the insertion process to proceed, the oxidation needs to be thermodynamically favorable under the 'soft' conditions applied. Therefore, the lattice/bond energy released during the oxidation must be larger than the energetic cost of the electron transfer required to form the cation–anion pair.
3. There must be sufficient anion mobility to allow the inserted species to diffuse into the 'interior' of the host material, rather than just remain at the surface. In addition, there must be sufficient electronic mobility to enable the motion of charge associated with the oxidation process.

2.15.4.4.1 Anion-deficient perovskites

The ABO_3 cubic perovskite structure contains no obvious sites into which additional anions can be inserted. When phases which are 'over-stoichiometric' in oxygen adopt cubic perovskite structures, the elevated anion contents are

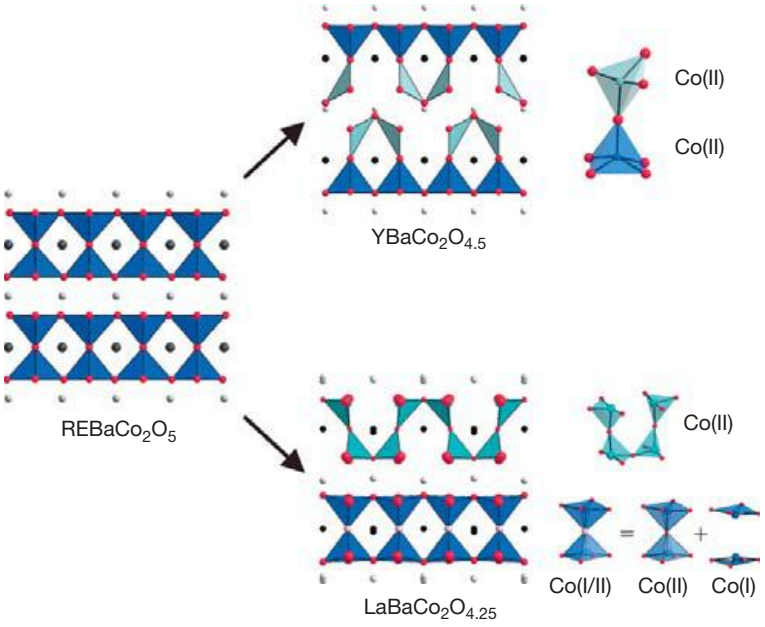

Figure 26 Topochemical reduction of $REBaCoO_5$ results in product phases with anion-vacancy-ordering schemes directed by the identity of the RE cations.

accommodated through cation deficiency. Thus, the over-stoichiometric composition $LaMnO_{3+\delta}$ is realized through lanthanum and manganese cation vacancies and is better written as $La_{1-\delta}Mn_{1-\delta}O_3$.[209] However as noted in Section 2.15.4.3.1, phases which adopt the perovskite structure can accommodate large numbers of anion vacancies without incurring significant energetic penalties. As a result, the oxygen content of perovskite phases is particularly sensitive to the preparative conditions employed for their synthesis, and anion-deficient perovskite phases are easily prepared. The anion deficiency can then be readily tuned or removed by low-temperature topochemical oxidation reactions.

2.15.4.4.1.1 Structural stabilization

The ABO_3 cubic perovskite structure, and its distorted variants, is almost ubiquitous in ternary transition-metal-oxide chemistry, due to the large number of cation combinations it can host. This chemical diversity is attributable to the wide range of A:B cation radius ratios which can be accommodated. As shown in Figure 27, the large A-cations reside in 12-cordinate sites, while the smaller transition-metal cations are located in six-coordinate octahedral sites within the perovskite lattice. If the unit cell is a perfect cube, it can be seen that the A–O and B–O bond lengths must be in the ratio: $(A\text{–}O)/(\sqrt{2}\times(B\text{–}O))=1$, which is defined as the structural tolerance factor, t. This apparently restrictive geometric requirement can be eased by a series of cooperative twisting and tilting distortions of the BO_6 octahedra, which lower the average A–O bond length while maintaining the B–O bond length. This allows compositions with small A-cations ($t<1$) to adopt distorted perovskite structures, significantly extending the stability range of this structure type. There are however a significant number of ABO_3 compositions which have tolerance factors greater than 1, indicating that the A-cation is too large for the 12-coordinate site of a cubic perovskite framework. These phases tend to adopt hexagonal perovskite structures which incorporate face-sharing links into the connectivity of BO_6 octahedra, to accommodate these larger A-cations. A small subset of these hexagonal perovskite phases can be induced to adopt cubic-type perovskite structures by synthesizing them with anion-deficient compositions. The ABO_{3-x} phases thus prepared will contain transition-metal B-cations in lower oxidation states than present in oxygen-stoichiometric ABO_3 formulations. This B-cation reduction will tend to increase the average B–O bond length, reducing the tolerance factor and moving the material into the cubic perovskite stability field. The anion-deficient phases can then be oxidized to stoichiometric ABO_3 compositions. If this oxidation is performed at a suitably low temperature, there will be insufficient cation mobility for the material to adopt the thermodynamically stable hexagonal perovskite structure, and the metastable, oxygen-stoichiometric, cubic phase will be kinetically trapped. Thus, for example, $SrMnO_3$, which crystallizes as a 4H hexagonal perovskite,[210,211] can be converted into a cubic perovskite-phase $SrMnO_{2.72}$ by heating in air at high temperature.[210] Subsequent reaction in oxygen below 500 °C yields $SrMnO_{3.00}$, which retains the cubic perovskite structure of the anion-deficient phase.[212]

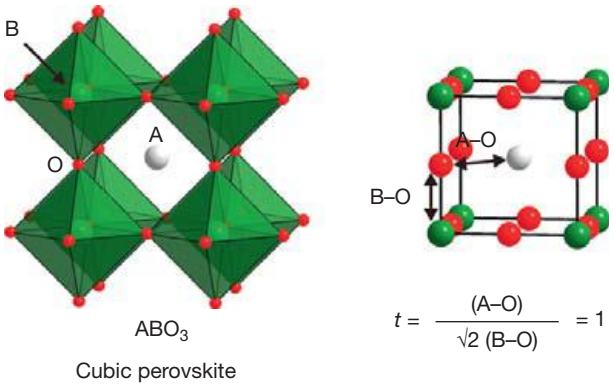

Figure 27 The structural tolerance factor of ABO_3 perovskite phases.

The oxidation of cubic $SrMnO_{3-x}$ can also be achieved with fluorine. $SrMnO_{2.5}$,[213] prepared in a manner analogous to that described for $CaMnO_{2.5}$ in Section 2.15.4.3.1, reacts readily with XeF_2 – a convenient fluorine source – to yield $SrMnO_{2.5-x}F_{0.5+x}$, a mixed-valent Mn(III)/Mn(IV) phase as shown in reaction [39].[214] In addition to the simple fluorine insertion, the highly oxidizing nature of fluorine leads to an accompanying anion displacement reaction in which fluorine displaces oxygen to yield $SrMnO_{2.5-x}F_{0.5+x}$ rather than $SrMnO_{2.5}F_{0.5}$:

$$SrMnO_{2.5}+\frac{0.5+x}{2}XeF_2 \rightarrow SrMnO_{2.5-x}O_{0.5+x}+\frac{x}{2}O_2+\frac{0.5+x}{2}Xe \qquad [39]$$

$SrFeO_{3-x}$ phases adopting cubic perovskite-derived structures can be prepared in a similar way. Reaction of the brownmillerite-phase $Sr_2Fe_2O_5$ at low temperature with oxygen partial pressures of up to 500 atm allows phases of composition $SrFeO_{2.5+x}$ $(0<x<0.5)$ to be synthesized.[215] These materials exhibit a number of anion-vacancy-ordered intermediate phases which can be described by the compositional series $Sr_nFe_nO_{3n-1}$ $(n=2,\ 4,\ 8,\ \infty)$.[216] Oxidative insertion of anions into $SrFeO_{3-x}$ can also be performed electrochemically by electrolyzing samples in KOH to yield highly crystalline $SrFeO_3$.[217] The anion-deficient lattice of $SrFeO_{3-x}$ phases also enables fluorine insertion. Reaction of $SrFeO_{2.88}$ with poly (vinylidene fluoride), $[CH_2CF_2]_n$, leads to an anion-insertion/displacement reaction and the formation of $SrFeO_2F$.[218] In contrast to the fluorination of $Sr_2Mn_2O_5$, the fluorination of $SrFeO_{3-x}$ proceeds with the reduction of the iron oxidation state from $Fe^{3.76+}$ to Fe^{3+} indicating that the oxidizing nature of Fe^{4+} centers leads to a significant substitutive component to the anion-insertion reaction.

2.15.4.4.1.2 Cation-ordered phases

Anion-deficient cubic perovskite phases are often prepared to encourage cation ordering. In general, entropy strongly favors the formation of cation-disordered perovskite phases. Thus, an $AA'B_2O_6$ double perovskite composition will tend to adopt a structure with a statistically disordered arrangement of A- and A′-cations over the available 12-coordinate cation sites of the perovskite framework. However, the introduction of anion deficiency can lead to the synergic ordering of anion vacancies and cations. As shown in Figure 28, $LaBaMn_2O_5$ adopts a structure based on that of a cubic perovskite, in which the anion vacancies order to yield two distinct A-cation sites: a 12-coordinate site occupied by Ba^{2+} and a smaller 8-coordinate site occupied by La^{3+}.[52] The simultaneous ordering

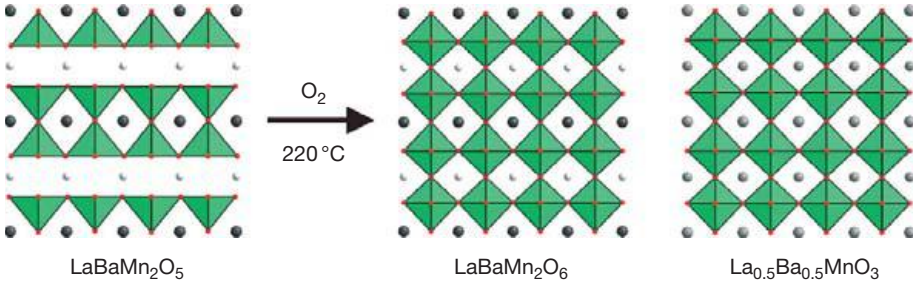

Figure 28 Low-temperature oxidation of $LaBaMn_2O_5$ leads to the formation of the metastable A-cation-ordered perovskite-phase $LaBaMn_2O_6$ rather than the more thermodynamically stable cation-disordered phase $La_{0.5}Ba_{0.5}MnO_3$.

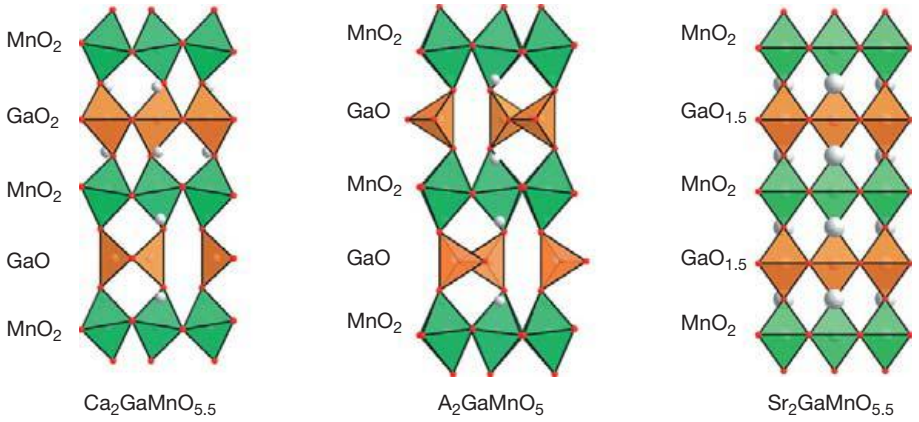

Figure 29 Oxidation of A_2GaMnO_5 (A = Ca, Sr) brownmillerite phases yields products with anion-vacancy distributions which depend on the identity of the A-cations.

of anion vacancies and cations is driven by the differing coordination preferences of the large barium and smaller lanthanum cations. Subsequent low-temperature oxidation yields metastable, cation-ordered $LaBaMn_2O_6$ which exhibits an elevated magnetic ordering temperature ($T_N = 335$ K) compared to the cation-disordered phase $La_{0.5}Ba_{0.5}MnO_3$ ($T_N = 270$ K) which is prepared directly at high temperature.[52] Similar behavior is observed for $LaBaCo_2O_5$ which can be readily oxidized to A-cation-ordered $LaBaCo_2O_6$.[219]

Anion deficiency can also be used to prepare B-cation-ordered perovskite phases. As noted in Section 2.15.4.3.1, the anion-deficient $A_2B_2O_5$ brownmillerite structure is adopted by a large number of anion-deficient perovskite phases. The octahedral and tetrahedral coordination sites within brownmillerite-type structures (Figure 29) can be used to segregate and order different B-cations on the basis of their stability in these two coordination geometries, to yield cation-ordered $A_2BB'O_5$ phases. Subsequent low-temperature anion-insertion reactions can then be utilized to tune the oxygen content of materials.

A widely studied group of cation-ordered brownmillerite oxides are the $A_2BMn^{III}O_5$ (A = Ca, Sr; B = Al, Ga) phases in which cation ordering in these materials is particularly robust due to the favorable location of the Jahn–Teller-active Mn^{III} cations within an octahedral coordination site. Oxidation of these materials to Mn^{IV}-containing A_2BMnO_{5+x} compositions leads to the insertion of oxide ions into the vacant anion sites which reside within the layers of apex-linked BO_4 tetrahedra, converting them to BO_6 octahedra. However, the manner in which these inserted anions are arranged depends on the size of the A-cations.

When the A-cation is small, Ca^{2+} for example, oxide ions are inserted into alternate layers of tetrahedra, changing the OTOT stacking sequence of octahedra (O) and tetrahedra (T) in the brownmillerite host phase into an OOOTOOOT sequence. Thus, the oxidation of Ca_2GaMnO_5 to $Ca_2GaMnO_{5.4}$ yields a phase in which approximately half the Ga^{3+} cations are in octahedral coordination sites and half in tetrahedral coordination sties (Figure 29).[220,221] When the A-cations are larger, oxidation follows a different pattern. Reaction of Sr_2GaMnO_5 with oxygen forms the Mn^{IV}-phase $Sr_2GaMnO_{5.5}$ in which the additional anions have been inserted evenly into all the sheets of tetrahedra within the brownmillerite structure, oxidizing the anion-deficient GaO layers to a composition of $GaO_{1.5}$ (Figure 29).[222–224] As a result, the gallium cations have an average coordination number of 5. It is argued that the differences in oxidation behavior are driven by the differing ability of the two $A_2BMnO_{5.5}$ structures to accommodate small A-cations through cooperative twisting of polyhedra.[225]

2.15.4.4.2 Ruddlesden–Popper phases

2.15.4.4.2.1 Oxygen-insertion reactions

In common with the perovskite phases described above, it is possible to stabilize Ruddlesden–Popper structures, particularly

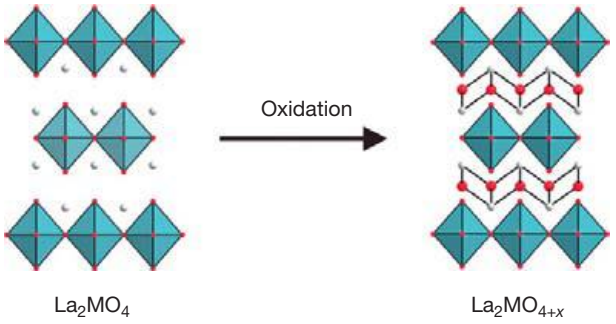

Figure 30 Oxidation of La_2MO_4 (M = Co, Ni, Cu) inserts additional anions into tetrahedral coordination sites between the sheets of MO_6 corner-sharing octahedra.

$n = 2$ members, by the formation of anion-deficient phases. For example, the reaction of a 3:2 molar ratio of $SrCO_3$ and MnO_2, which would be expected to form the $n = 2$ Ruddlesden–Popper-phase $Sr_3Mn_2O_7$, actually results in the formation of $Sr_7Mn_4O_{15}$ and MnO_2.[226] However if prepared at high temperature (1650 °C) to favor anion deficiency, and then quenched to room temperature with dry ice, the $n = 2$ Ruddlesden–Popper-phase $Sr_3Mn_2O_{6.55}$ is formed, which can then be readily oxidized to the Mn^{IV}-phase $Sr_3Mn_2O_7$.[227] Likewise $Sr_3Co_2O_{7-x}$ can be stabilized with respect to a mixture of competing phases, by lowering the oxygen concentration of the material.[228] In this instance, reaction with oxygen only facilitates oxidation to $Sr_3Co_2O_{6.60}$,[229] consistent with the increased difficulty in stabilizing the highly oxidizing Co^{4+} oxidation state.

In addition to the oxidative insertion of anions into vacant sites within anion-deficient Ruddlesden–Popper phases, it is also possible to insert anions into interstitial sites within the rock salt layers of phases of this structure type. Thus, oxidation of La_2MO_4 (M = Co, Ni, Cu) yields phases of composition $La_2MO_{4+\delta}$ ($\delta \lesssim 0.15$) in which the additional oxide ions are inserted into interstitial tetrahedral sites within the rock salt layers of these $n = 1$ Ruddlesden–Popper phases (**Figure 30**).[230–233] Oxidation of these phases can be achieved either by heating in oxygen gas or electrochemically in a KOH electrolyte.

An unusual feature of these topochemical oxidations is that the anions are inserted into locations within the host phase which are not within the coordination spheres of the transition-metal cations being oxidized. As a result, the oxidation state of the transition metal is changed (raised) while the local coordination at that transition-metal site, and thus the d-orbital energies of the metal center, remain largely unchanged. Modification of the electron count in this structurally independent, isolated manner is much more typical of cation insertion or substitution, than manipulation of the anion lattice which tends to insert or remove anions from within the coordination spheres of the redox active transition-metal centers. Therefore, these 'remote' anion insertions into rock salt layers of Ruddlesden–Popper phases can be thought of as almost pure electronic doping processes.

2.15.4.4.2.2 Fluorination reactions

Extensive investigations of the soft fluorination chemistry of Ruddlesden–Popper phases[234,235] have revealed that fluoride ions can be oxidatively inserted into interstitial sites between

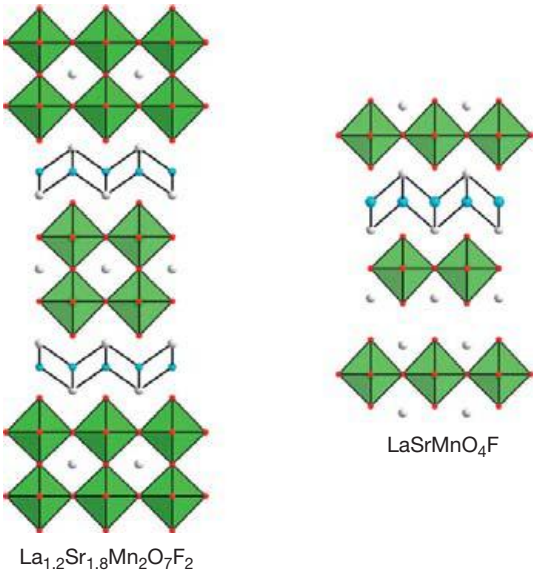

Figure 31 Fluorination of Ruddlesden–Popper phases inserts fluoride ions into tetrahedral interstitial sites.

the perovskite blocks of this structural family, to form structures similar to those of the $La_2MO_{4+\delta}$ phases described above. For example, reaction of the mixed-valent $Mn^{3+/4+}$ $n = 2$ Ruddlesden–Popper-phase $RE_{1.2}Sr_{1.8}Mn_2O_7$ (RE = La, Pr, Nd, Sm, Eu, Gd) with dilute fluorine gas or poly(vinylidene fluoride) yields $RE_{1.2}Sr_{1.8}Mn_2O_7F_2$.[236,237] Fluoride ions are inserted into four-coordinate sites within the rock salt layers of the host phase, to form an arrangement reminiscent of the fluorite structure (**Figure 31**). Similar reactions with the $n = 1$ phase $LaSrMnO_4$ lead to the formation of $LaSrMnO_4F_{1.7}$ in which the analogous interstitial sites are only partially filled.[236] The level of intercalation is presumably limited in this case by the ability to stabilize the higher oxidation states of manganese. If $LaSrMnO_4F_{1.7}$ is heated with the appropriate amount of $LaSrMnO_4$, the Mn(IV)-phase $LaSrMnO_4F$ can be formed via the thermal equilibration of the fluorine concentration. The resulting oxyfluoride phase adopts a novel-staged structure in which the anion intercalation sites in alternate layers are either full or empty (**Figure 31**).[238] This staging behavior suggests that there is a large energy penalty associated with expanding the rock salt layers to make them suitable for anion intercalation and that this 'penalty' is only worth paying if all the anion intercalation sites within a layer are filled, in a situation strongly reminiscent of some cation intercalation reactions of layered host phases. It should be noted that these fluorination reactions must be performed with the rigorous exclusion of water to prevent the formation of large quantities of binary metal fluoride impurities such as SrF_2.

In an attempt to simplify the often elaborate experimental setups required to handle and perform reactions with fluorine, a number of other fluorinating strategies have been investigated. For example, binary metal fluorides of late transition metals (MF_2: M = Ni, Cu, Zn, Ag) have been used to good effect to fluorinate Ruddlesden–Popper phases.[239] For example, heating a 1:1 mixture of the $n = 2$ Ruddlesden–Popper-phase $Sr_3Ru_2O_7$ with CuF_2 in air at temperatures up to 300 °C yields

the Ru(IV)-phase $Sr_3Ru_2O_7F_2$ and CuO.[240] It is postulated that the metal fluorides act as an *in situ* source of fluorine through reaction with atmospheric oxygen according to reaction [40],[241] and that this fluorine then rapidly reacts with the host phase to give the overall reaction [41].

$$MF_2 + \frac{1}{2}O_2 \rightarrow MO + F_2 \qquad [40]$$

$$Sr_3Ru_2O_7 + CuF_2 + \frac{1}{2}O_2 \rightarrow Sr_3Ru_2O_7F_2 + CuO \qquad [41]$$

It can be seen from these reaction schemes that the atmospheric oxygen is acting as the oxidant and the metal fluoride only acts as a fluorine source. The use of metal fluorides as fluorinating agents not only eases the practical difficulties associated with handling fluorine, it is also observed to produce lower levels of binary fluoride impurities than reactions with elemental fluorine. However, it should be noted that samples fluorinated in this manner almost inevitably become contaminated with the binary oxide byproducts of the reaction, which are often hard to remove.

Soft fluorination chemistry has also been used extensively to tune the electronic behavior of complex copper oxide phases to induce superconductivity.[241] The structural selectivity of the anion-insertion/substitution reactions of these phases appears to be directed by a strong energetic preference for the retention of CuO_4 square-planar motifs. Thus, for example, the fluorination of Sr_2CuO_3 to form $Sr_2CuO_2F_{2+x}$ via a combination of anion insertion and anion exchange leads to a large-scale rearrangement of the anion lattice. As a result, the majority of the fluoride ions within the product phase are located in axial coordination sites with a small minority located within interlayer interstitial sites (**Figure 32**).[241–243] Thus, the SrO–SrO–CuO–SrO–SrO– stacking of the host phase is converted into SrF–F_x–SrF–CuO_2–SrF–F_x–SrF– in the product. While it is intrinsically difficult to determine the oxygen–fluorine distribution in a mixed oxyfluoride by diffraction due to the similarity of both the x-ray and neutron scattering lengths of the two anions, Madelung energy calculations provide strong support for the structural model presented. The observed large-scale reorganization of the anion lattice also clearly demonstrates that there is high anion mobility in the host phase.

Fluorination of Ca_2CuO_3, which is isostructural and isoelectronic with Sr_2CuO_3, leads to a subtly different structure.[244] Reaction of Ca_2CuO_3 with fluorine gas yields $Ca_2CuO_2F_{2+x}$ in which the majority of the inserted fluoride ions now reside within interlayer interstitial sites, with a small minority of fluoride ions located in sites which bond axially to the copper centers (**Figure 32**). The structure of $Ca_2CuO_2F_{2+x}$ is therefore more closely related to the T′ structure of Nd_2CuO_4 than that of the parent Ruddlesden–Popper phase. The different distribution of fluoride ions over the two coordination sites in $A_2Cu_2O_2F_{2+x}$ to yield a Ruddlesden–Popper phase when A = Sr and a T′ phase when A = Ca is consistent with the small size of Ca^{2+} stabilizing the T′ structure.

2.15.4.4.2.3 Chlorine-insertion reactions

In general, chloride ions are too large to be inserted into vacant oxide ion-coordination sites. However, chlorine can be inserted into the interlayer region of Ruddlesden–Popper phases which contain large A-cations. As noted in Section 2.15.4.1.3.1, exposure of $A'LaNb_2O_7$ (A′ = Rb, Cs) Dion–Jacobson phases to cesium or rubidium vapor leads to the formation of $A'_2LaNb_2O_7$ (A′ = Cs, Rb) Ruddlesden–Popper phases via reductive intercalation.[108,109] The A′-cations in these phase are sufficiently large to facilitate the oxidative insertion of chlorine, to yield phases of composition $(A'_2Cl)LaNb_2O_7$ (A′ = Cs, Rb).[109] The $(A'_2Cl)^+$ layers thus formed adopt a CsCl-type structure in which the A′-cations are located within eight-coordinate $A'O_4Cl_4$ sites, facilitated by a relative shift in the position of the $LaNb_2O_7$ perovskite blocks from a centered stacking to a primitive stacking as shown in **Figure 33**.

2.15.4.4.2.4 Iodine-insertion reactions

The weak oxidizing potential of iodine means that in general it does not intercalate into complex oxides in an oxidative manner. It has been observed however that iodine can intercalate into bismuth-containing oxides. Thus, for example, the reaction of the high-temperature superconducting phase $Bi_2Sr_2CaCu_2O_{8-x}$ with elemental iodine yields $IBi_2Sr_2CaCu_2O_{8-x}$, in which iodine has been inserted into the Bi_2O_2 layers of the host phase driving a change in the stacking sequence of the phase from centered to

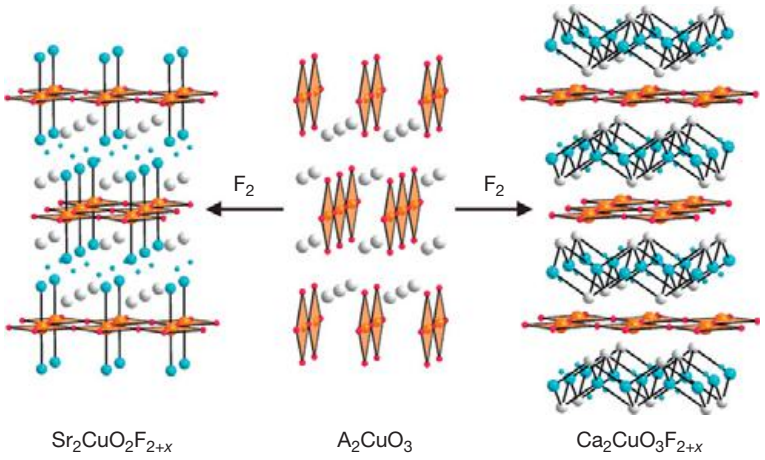

Figure 32 Fluorination of A_2CuO_3 (A = Ca, Sr) phases leads to a rearrangement of the anion lattice and the retention of sheets of apex-linked CuO_4 square planes.

primitive (Figure 34).[245] Raman spectroscopy data collected from intercalated samples are consistent with the presence of I_3^- molecular anions, demonstrating the oxidative nature of the insertion process.[246] Analogous insertion reactions have been observed to occur in $A_xBi_{9-x}O_{(27-x)/2}$ (A = Ba, Sr) phases, in which the insertion of iodine leads to the partial oxidation of bismuth.[247,248]

2.15.4.5 Redox-Neutral Topochemical Reactions

The topochemical reactions described in the previous sections occur with concomitant oxidation or reduction of the complex oxide host lattice. However, it is possible to insert, extract, or exchange chemical species from complex oxide phases in redox-neutral processes. In order for such redox-neutral processes to proceed, a number of general conditions must be met:

1. The species to be intercalated and/or extracted must have significant mobility within the host lattice at the reaction temperature.
2. The product phase produced must be kinetically stable. Thus, there must be suitable intercalation sites for insertion reactions, or minimal unfavorable-like ion interactions in the resulting product phase in the case of deintercalation reactions.
3. The redox-neutral reactions must be spontaneous ($\Delta G < 0$). Unlike the redox active reactions which are generally driven by thermodynamically favorable electron-transfer processes, redox-neutral reactions need to be driven by other favorable reaction steps, such as increase in product lattice energy (due to exchange of large cations for smaller cations for example) or acid neutralization or the formation of highly thermodynamically stable byproduct phases (e.g., water) in the case of deintercalation reactions.

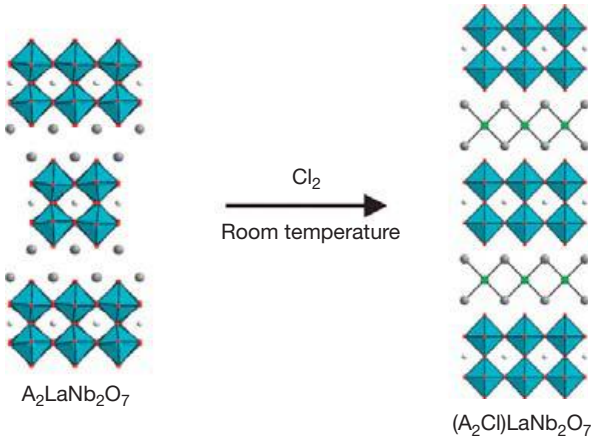

Figure 33 Chlorination of $A_2LaNb_2O_7$ (A = Cs, Rb) leads to the insertion of chloride ions into eight-coordinate cubic sites formed by a relative shift in the position of the perovskite double layers.

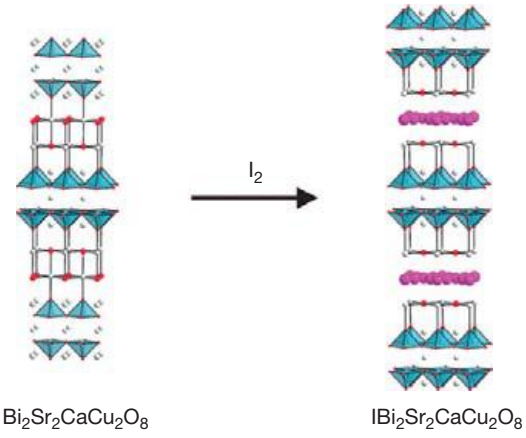

Figure 34 Reaction of $Bi_2Sr_2CaCu_2O_8$ with iodine oxidatively inserts I_3^- ions into the Bi_2O_2 layers of the cuprate phase to yield $IBi_2Sr_2CaCu_2O_8$.

2.15.4.5.1 Cation-substitution reactions

The majority of transition-metal cations in complex oxide phases are tightly bound within oxide coordination polyhedra. As a result, they are effectively immobile under 'soft' chemical conditions. In contrast, large, low-valent cations residing in sites of low coordination number within the interlayer regions of complex oxide structures can be readily exchanged at modest temperatures. By utilizing the low-temperature mobility of this class of cation, a wide range of topochemical reactions can be performed.

2.15.4.5.1.1 $NaFeO_2$-type phases

The high ionic mobility which facilitates the rapid extraction and reintercalation of cations into phases which adopt α-$NaFeO_2$-type structures also enables numerous low-temperature cation-exchange reactions to be performed.[249] For example, reaction of α-$NaFeO_2$ with lithium chloride in a potassium chloride flux brings about a topochemical cation exchange according to reaction [42]. The metastable phase, $LiFeO_2$, thus formed retains the ordering of lithium and iron cations within the rock salt lattice of the parent phase (the thermodynamically stable form of $LiFeO_2$ has a disordered rock salt structure) consistent with the differential mobility of the monovalent cations (Na, Li) compared to Fe^{3+}[250]:

$$NaFeO_2 + LiCl \rightarrow LiFeO_2 + NaCl \qquad [42]$$

However if α-$NaFeO_2$-type phases of composition $LiMO_2$ (M = Cr, Co, Rh) are reacted with silver nitrate in a potassium nitrate flux, the resulting cation-exchange reactions drive a change to the structure of the host lattice so the product $AgMO_2$ phases adopt delafossite-type structures in which the inserted silver cations occupy linear coordination sites, as shown in Figure 35.[251]

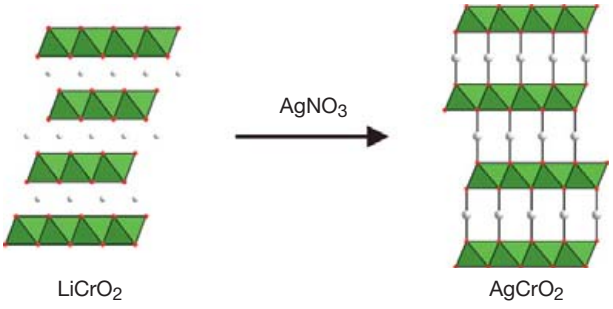

Figure 35 Exchange of silver for lithium drives a change from an ordered rock salt structure to a delafossite structure with silver ions in a linear coordination geometry.

The structural transition is presumably driven by the coordination preferences of the Ag^{I} cation.

Analogous cation-exchange reactions to form delafossite phases are also observed when α-$NaFeO_2$-type $LiMO_2$ (M = Cr, Rh) phases are reacted with a mixture of palladium and palladium dichloride, in a process which involves the comproportionation of Pd^0 and Pd^{II} according to reaction [43][251]:

$$2LiMO_2 + Pd + PdCl_2 \rightarrow 2PdMO_2 + 2LiCl \qquad [43]$$

It is also possible to substitute divalent cations into α-$NaFeO_2$-type phases in redox-neutral processes which exchange two monovalent cations for a single divalent cation. For example, the reaction of Na_xCoO_2 with anhydrous calcium nitrate readily yields $Ca_{x/2}CoO_2$ phases according to reaction [44][252,253]:

$$Na_xCoO_2 + \frac{x}{2}Ca(NO_3)_2 \rightarrow Ca_{x/2}CoO_2 + xNaNO_3 \qquad [44]$$

The cation-exchange reactions of Na_xCoO_2 phases with low values of x are topochemical. Thus, γ-$Na_{0.5}CoO_2$, which adopts a P2-type structure as described in Section 2.15.4.2.1.2, forms γ-$Ca_{0.25}CoO_2$, and β-$Na_{0.5}CoO_2$, which has a P1-type structure, forms β-$Ca_{0.25}CoO_2$ on cation exchange. However, Na_xCoO_2 phases with large values of x undergo structural changes similar to those observed on sodium deintercalation. Thus, for example, reaction of α-$NaCoO_2$ with anhydrous calcium nitrate forms $Ca_{0.5}CoO_2$ with the β-type P1 structure of the most thermodynamically stable form of $Na_{0.5}CoO_2$ (see Section 2.15.4.2.1.2), suggesting that the change in structure is driven by the declining A-cation concentration in the A_xCoO_2 (A = Na, Ca) phases rather than a change in the identity of the A-cation.

Reaction between α-$NaFeO_2$ and nickel nitrate or nickel chloride leads to a further class of cation-exchange reactions, in which the sodium and some of the iron cations are replaced by nickel according to reaction [45] to yield a $Ni_{1+x}Fe_{2-x}O_4$ spinel-type phase[254,255]:

$$2NaFeO_2 + (1+x)NiCl_2 \rightarrow Ni_{1+x}Fe_{2-(2x/3)}O_4 + 2NaCl + \frac{2x}{3}FeCl_3 \qquad [45]$$

Detailed structural analysis reveals that despite the common oxide ion lattice shared by the ordered rock salt structure of $NaFeO_2$ and the spinel structure, there is significant cation rearrangement associated with the exchange reaction as half the iron centers are displaced from octahedral sites in $NaFeO_2$ to tetrahedral sites in the $Ni_{1+x}Fe_{2-(2x/3)}O_4$ product.

2.15.4.5.1.2 Layered binary and ternary oxides

Layered binary oxide phases which contain monovalent cations in between sheets of connected transition-metal coordination polyhedra exhibit extensive cation-substitution chemistry. For example, as noted in Section 2.15.4.1.1.2, the layered structure of α-MoO_3 enables a wide range of intercalation reactions to be performed due to the high mobility of cations located between the MoO_3 layers. This high cation mobility also facilitates a wide range of cation-exchange reactions, Thus, exposure of $[Na(H_2O)_2]_{0.25}MoO_3$ to a solution containing potassium chloride leads to rapid and complete cation exchange and the formation of $[K(H_2O)_n]_xMoO_3$ phases.[256]

Layered structures are also observed for a wide range of ternary oxides. For example, there is an extensive series of ternary titanium oxides of composition $A_2Ti_nO_{2n+1}$ (A = monovalent cation) which adopt structures consisting of arrays of edge-sharing TiO_6 octahedra separated by layers of A-cations, as shown in **Figure 36**. The open structures adopted by these phases enable a wide range of cation-substitution chemistry to be performed.[257,258] For example, the $n = 4$ phase $TlTi_4O_9$ has been shown to undergo substitution reactions with a very wide range of MCl metal monochlorides (M = Li, Na, K, Rb, Cs, Ag) to yield substituted phases according to reaction [46][259]:

$$Tl_2Ti_4O_9 + 2MCl \rightarrow M_2Ti_4O_9 + 2TlCl \qquad [46]$$

This family of phases has also been observed to react with mineral acids to form proton-exchanged solid-acid phases. For example, $Na_2Ti_3O_7$, $K_2Ti_4O_9$, and $Cs_2Ti_5O_{11}$ all react with hydrochloric acid to form the analogous $H_2Ti_nO_{2n+1}$ phases.[260]

2.15.4.5.1.3 Dion–Jacobson phases

The large monovalent interlayer A′-cations present in $A'A_{n-1}B_nO_{3n+1}$ Dion–Jacobson phases are relatively mobile under 'soft' synthesis conditions, due to the low charge density of the ions and the large sites of low coordination number they occupy. As a result, these cations can be readily exchanged for cations of smaller size in reactions which are driven by the increased lattice energies of the substituted products. Thus, for example, the reaction of the $n = 2$ Dion–Jacobson phases $A'LaNb_2O_7$ (A′ = K, Rb, Cs) with fused $LiNO_3$ or $NaNO_3$ yields A′-cation-substituted phases (**Figure 37**) and $A'NO_3$ according to reaction [47][261,262]:

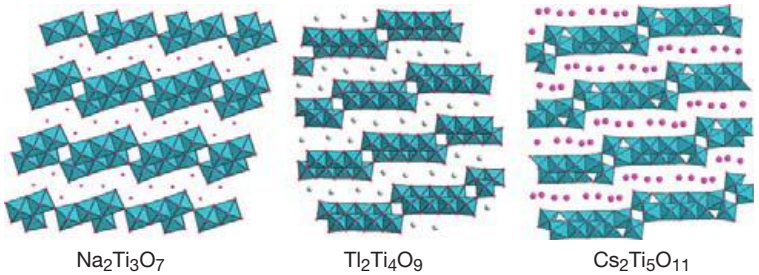

Figure 36 The layered structures of $Na_2Ti_3O_7$, $Tl_2Ti_4O_9$, and $Cs_2Ti_5O_{11}$.

$$A'LaNb_2O_7 + MNO_3 \rightarrow MLaNb_2O_7 + A'NO_3 \qquad [47]$$

If the exchanged cations are small (Li^+, Na^+), their introduction drives a structural change in which the perovskite sheets shift from the primitive stacking of the Dion–Jacobson phases to the staggered stacking of the Ruddlesden–Popper structural series. This structural change leads to the formation of small tetrahedral sites which can better accommodate the small monovalent cations as shown in **Figure 37**. Analogous cation-exchange reactions can be performed on Dion–Jacobson tantalates to yield a wide range of cation-substituted phases,[263] including $AgLaTa_2O_7$ and $AgCa_2Ta_3O_{10}$[264] which exhibit appreciable Ag^+ cation mobility at high temperature.

The A′-cations in Dion–Jacobson phases can also be replaced by divalent cations to yield cation-deficient phases. Thus, reaction of $RbCa_2Nb_3O_{10}$ with $Sr(NO_3)_2$ or $Ba(NO_3)_2$ leads to the formation of $Rb_{0.55}Sr_{0.23}\square_{0.24}Ca_2Nb_3O_{10}$ and $Rb_{0.45}Ba_{0.27}\square_{0.27}Ca_2Nb_3O_{10}$, respectively,[265] where □ represents a vacancy on the A′-cation site of the Dion–Jacobson structure.

The large A′-cations in Dion–Jacobson phases can also be readily exchanged for protons by treatment with mineral acid, resulting in the formation of solid-acid phases.[266–269] For example, reaction of the $n=3$ $A'Ca_2Nb_3O_{10}$ or $n=2$ $A'LaNb_2O_7$ (A = K, Rb, Cs) phases with 6 M HCl readily yields the solid-acid phases $HCa_2Nb_3O_{10}$ and $HLaNb_2O_7$ respectively according to reaction [48][266,269]:

$$KCa_2Nb_3O_{10} + HCl \rightarrow HCa_2Nb_3O_{10} + KCl \qquad [48]$$

In addition to simple cation-exchange reactions, the A′-cations in Dion–Jacobson phases can be replaced by charged layers of other metal salts. Thus if the $n=2$ Ruddlesden–Popper-phase $RbLaNb_2O_7$ is heated in the presence of $CuCl_2$, an exchange reaction occurs to replace the large Rb^+ cations with a sheet of stoichiometry $(CuCl)^+$ according to reaction [49][270]:

$$RbLaNb_2O_7 + CuCl_2 \rightarrow (CuCl)LaNb_2O_7 + RbCl \qquad [49]$$

The resulting phase consists of double blocks of corner-sharing NbO_6 octahedra stacked with sheets of edge-sharing $Cu^{II}O_2Cl_4$ octahedra as shown in **Figure 38**.[270,271] By use of the appropriate dichloride, similar exchange reactions can be performed to insert other $(MCl)^+$ (M = Cr, Mn, Fe, Co) layers into Dion–Jacobson phases in a directly analogous manner.[272–274] The $(MCl)LaMb_2O_7$ phases thus formed can also undergo cation substitution reactions. Reaction of $(CuCl)LaNb_2O_7$ with *n*-butyllithium results in the insertion/exchange of lithium and the excretion of elemental copper according to reaction [50], to yield $(Li_xCl)LaNb_2O_7$, typically with $x>2$. Subsequent exposure to iodine can readily remove the displaced copper and any excess lithium to yield $(Li_2Cl)LaNb_2O_7$ as shown in reaction [51][275]:

$$(CuCl)LaNb_2O_7 + xC_4H_9Li \rightarrow (Li_xCl)LaNb_2O_7 + \frac{x}{2}C_8H_{18} + Cu \qquad [50]$$

$$(Li_xCl)LaNb_2O_7 + Cu + \frac{x-1}{2}I_2 \rightarrow (Li_2Cl)LaNb_2O_7 + CuI + (x-2)LiI \qquad [51]$$

The $(Li_2Cl)^+$ layer inserted between the perovskite blocks in $(Li_2Cl)LaNb_2O_7$ adopts an anti-fluorite structure in which the lithium cations are located within LiO_2Cl_2 tetrahedra as shown in **Figure 38**, and thus the exchange of two lithium cations for each Cu^{2+} cation can be considered topochemical.

2.15.4.5.1.4 Ruddlesden–Popper phases

The majority of $A_{n+1}B_nO_{3n+1}$ Ruddlesden–Popper phases contain small, highly charged A-cations such as lanthanides and/or alkaline earth metals which have high charge densities limiting their mobility at low synthesis temperatures. However, when the B-cations present in Ruddlesden–Popper phases are early transition metals in high oxidation states such as Ti^{4+}, Nb^{5+}, or Ta^{5+}, monovalent A-cations can be incorporated into Ruddlesden–Popper phases. Under suitable conditions, these monovalent cations can participate in substitution reactions in which they are replaced by other, smaller, monovalent ions.[276] Thus, for example, the reaction of the $n=3$ Ruddlesden–Popper-phase $Na_2La_2Ti_3O_{10}$ with $LiNO_3$ or $AgNO_3$ yields $Li_2La_2Ti_3O_{10}$ and $Ag_2La_2Ti_3O_{10}$, respectively.[277,278]

The large monovalent A-cations in Ruddlesden–Popper phases can also be readily exchanged for protons to form solid-acid phases.[279–285] For example, the $n=3$ phase

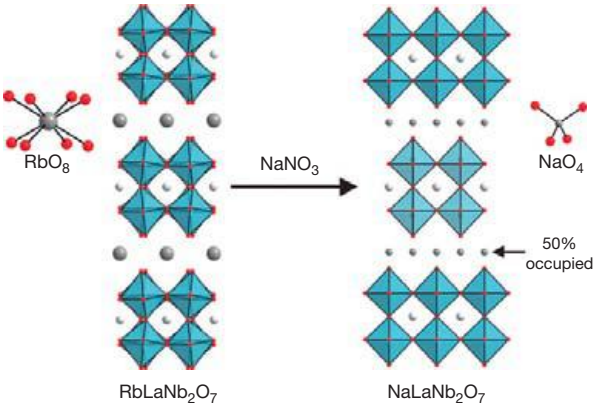

Figure 37 Substitution of sodium for rubidium leads to a shift of the perovskite blocks to form a cation-deficient Ruddlesden–Popper-type phase.

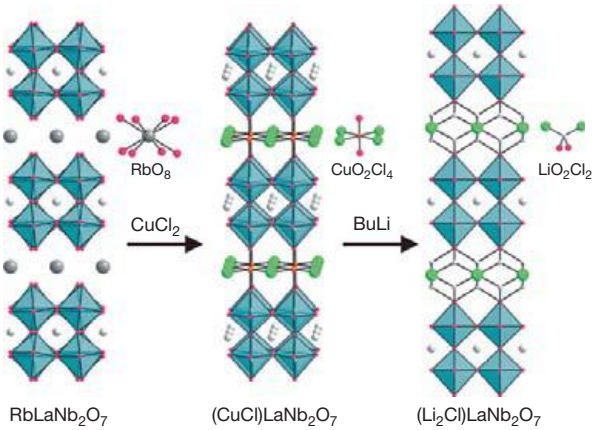

Figure 38 The large rubidium cations in $RbLaNb_2O_7$ can be exchanged for $(CuCl)^+$ salt units which can then undergo cation exchange in which a Cu^{2+} cation is replaced by two Li^+ cations.

$A_2La_2Ti_3O_{10}$ (A = K, Rb) when reacted with nitric acid yields proton-exchanged $H_2LaTi_3O_{10}$ materials.[261] Using these solid-acid phases as precursors, subsequent reactions can replace the incorporated protons with large monovalent cations to yield phases which cannot be made directly. Thus, for example, if the $n = 1$ Ruddlesden–Popper-phase $NaLaTiO_4$ is first treated with nitric acid to form $HLaTiO_4$ and subsequently exposed to KOH, the metastable, cation-substituted phase $KLaTiO_4$ is formed.[285] It should be noted that the protonated intermediate is an essential part of the reaction scheme as $KLaTiO_4$ cannot be made directly from $NaLaTiO_4$ (by reaction with KNO_3 for example) due to the loss of lattice energy on potassium substitution. However, when KOH is reacted with $HLaTiO_4$, the formation of water due to the acid neutralization processes drives the reaction forward as shown in reactions [52] and [53]:

$$NaLaTiO_4 + HNO_3 \rightarrow HLaTiO_4 + NaNO_3 \quad [52]$$

$$HLaTiO_4 + KOH \rightarrow KLaTiO_4 + H_2O \quad [53]$$

By substituting divalent cations for monovalent cations, it is possible to convert $A_{n+1}B_nO_{3n+1}$ Ruddlesden–Pooper phases into $A'A_{n-1}B_nO_{10}$ Dion–Jacobson phases. Thus, the reaction of $K_2Eu_2Ti_3O_{10}$ with $Ca(NO_3)_2$ or $Sr(NO_3)_2$ yields $CaEu_2Ti_3O_{10}$ and $SrEu_2Ti_3O_{10}$ according to reaction [54][286]:

$$K_2Eu_2Ti_3O_{10} + M^{II}(NO_3)_2 \rightarrow M^{II}Eu_2Ti_3O_{10} + 2KNO_3 \quad [54]$$

In this instance the large Ca^{2+} and Sr^{2+} cations drive a shift of the $Eu_2Ti_3O_{10}$ perovskite blocks to adopt a Dion–Jacobson stacking sequence with large eight-coordinate A′ cation sites. However, it is possible to exchange the monovalent cations in Ruddlesden–Popper phases for smaller divalent transition-metal cations with retention of the Ruddlesden–Popper framework. For example, reaction of $Na_2La_2Ti_3O_{10}$ with a 1:1 mixture of $CoCl_2$/KCl forms $Co^{II}La_2Ti_3O_{10}$ according to reaction [55], in which the small Co^{II} cations occupy half the tetrahedral interlayer cation sites as shown in **Figure 39**.[287] Similar reactions can be performed to exchange Cu^{II} or Zn^{II} cations for sodium, in an analogous manner[287]:

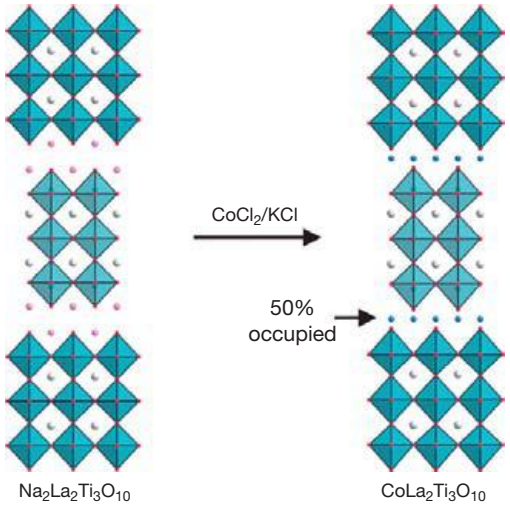

Figure 39 Reaction of the $n = 3$ Ruddlesden–Popper-phase $Na_2La_2Ti_3O_{10}$ with $CoCl_2$ in a KCl flux exchanges the nine-coordinate sodium ions for tetrahedrally coordinated cobalt centers.

$$Na_2La_2Ti_3O_{10} + CoCl_2 \rightarrow Co^{II}La_2Ti_3O_{10} + 2NaCl \quad [55]$$

Charged metal-oxide layers can also be inserted into Ruddlesden–Popper phases via exchange reactions. If the $n = 3$ Ruddlesden–Popper-phase $K_2La_2Ti_3O_{10}$ is reacted with two equivalents of BiOCl, $(Bi_2O_2)^{2+}$ layers are inserted between the $La_2Ti_3O_{10}$ perovskite sheets to yield the Aurivillius-phase $(Bi_2O_2)La_2Ti_3O_{10}$ according to reaction [56][288]:

$$K_2La_2Ti_3O_{10} + 2BiOCl \rightarrow (Bi_2O_2)La_2Ti_3O_{10} + 2KCl \quad [56]$$

By careful selection of the reacting salt, more elaborate metal-oxide layers can be inserted. Thus, the reaction of $K_2La_2Ti_3O_{10}$ with $VOSO_4$ inserts $(VO)^{2+}$ into the host phase with ejection of two potassium cations according to reaction [57][288]:

$$K_2La_2Ti_3O_{10} + VOSO_4{\cdot}3H_2O \rightarrow (VO)La_2Ti_3O_{10} + K_2SO_4 + 3H_2O \quad [57]$$

Thus, it can be seen that when sufficiently mobile cations are present, a wide range of substitution reactions can be performed to prepare metastable phases.

2.15.4.5.2 Deintercalation

2.15.4.5.2.1 Dehydration reactions

The deintercalation of incorporated molecules is a common feature of a wide range of hydrated oxide phases. However, the dehydration reactions of solid-acid oxide phases can be utilized to form new metal–oxygen linkages between existing MO_n metal–oxygen coordination polyhedra. For example, if the solid-acid-phase $HTiNbO_5$ is heated at 300 °C, a dehydration reaction occurs in which water is formed and released from the solid, leading to the synthesis of $Ti_2Nb_2O_9$.[289,290] The dehydration reaction drives the fusion of adjacent $(Ti, Nb)_2O_5$ sheets via the formation of new corner-sharing links between $(Ti, Nb)O_6$ octahedra, resulting in a new 3D metal-oxide network as shown in **Figure 40**. Similar dehydration reactions are observed to occur when proton-exchanged titanates in the $H_2Ti_nO_{2n+1}$ series are heated above 350 °C, forming a metastable polymorph of TiO_2, referred to as TiO_2(B), although it should be noted that the dehydration reactions in this instance are not topochemical.[260,291,292]

Following a similar dehydration strategy, layered double hydroxide phases can be readily converted into dense spinel oxides at low temperature. Thus by heating $Ni_{1/3}Co_{1/3}Al_{1/3}(OH)_2(CO_3)_x(NO_3)_y{\cdot}nH_2O$ at 500 °C, the metastable spinel-phase $NiCoAlO_4$ is formed.[293] On heating above 600 °C, this phase decomposes by expelling NiO, demonstrating the metastability of the spinel phase and further

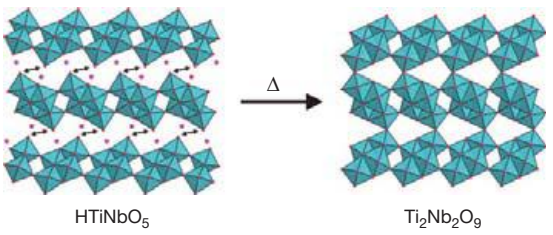

Figure 40 Dehydration of the layered solid-acid $HTiNbO_5$ leads to the formation of the 3D oxide-phase $Ti_2Nb_2O_9$.

emphasizing the ability of low-temperature dehydration reactions to prepare kinetically stabilized phases.

2.15.4.5.2.2 Layer extraction

Under suitable conditions, it is possible to extract charge neutral 'salt' units from extended oxide phases, thus generating new extended lattices. For example, if the $n=3$ Ruddlesden–Popper-phase $K_2La_2Ti_3O_{10}$ is treated with two equivalents of tetraphenylphosphonium bromide (PPh_4Br), K_2O is extracted from the host phase according to reaction [58], to yield $La_2Ti_2O_9$ as shown in **Figure 41**.[294] The potassium cations are extracted from the rock salt layers of the host phase along with oxide ions from within the Ti_3O_{10} blocks:

$$K_2La_2Ti_3O_{10} + 2PPH_4Br \rightarrow La_2Ti_3O_{10} + 2KBr + PPh_3O + PPh_3 + Ph_2 \quad [58]$$

An alternative route for the extraction of layers from extended oxide structures is to utilize the dehydration of solid-acid phases described in Section 2.15.4.5.2.1. For example if the $n=3$ solid-acid-phase $H_2La_2Ti_3O_{10}$ is heated to approximately 600 °C, water is eliminated to yield $La_2Ti_3O_9$.[261] The elimination of water is associated with a structural change in which the TiO_6 octahedra on either side of each 'rock salt' sheet fuse to form an A-cation-deficient perovskite structure, better expressed as $La_{2/3}TiO_3$ (**Figure 42**). The large size of the La^{3+} cations makes them effectively immobile during the dehydration process, and thus the lanthanum cations adopt a layered arrangement within the A-cation sites of the perovskite product, patterned by the cation arrangement of the Ruddlesden–Popper parent phase.

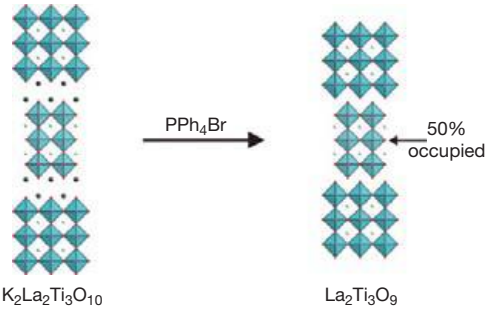

Figure 41 PPh_4Br extracts K_2O topochemically from the structure of $K_2La_2Ti_3O_{10}$ to yield $La_2Ti_3O_9$.

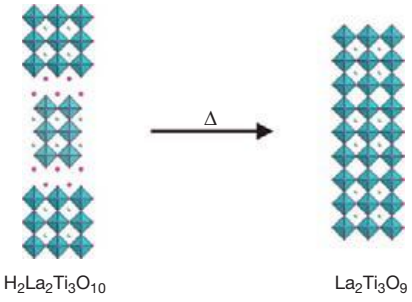

Figure 42 Dehydration of $H_2La_2Ti_3O_{10}$ leads to the formation of the cation-deficient perovskite $La_{2/3}TiO_3$ in which layered arrangement of the La^{3+} of the parent phase is retained.

Thus, it can be seen that two different metastable phases of identical composition, $La_2Ti_3O_9$ (**Figure 41**) and $La_{2/3}TiO_2$ (**Figure 42**), can be formed by performing different sequences of soft chemical reactions on the host $K_2La_2Ti_3O_{10}$ phase.

The analogous $H_2RE_2Ti_3O_{10}$ phases in which RE is a smaller lanthanide (RE = Nd, Sm, Eu, Gd, Dy) do not condense to form perovskite structures on dehydration.[261,280] Instead, the $RE_2Ti_3O_9$ phases formed retain layered structures in which some of the small lanthanide cations have migrated into the region between the perovskite blocks. On heating above 950 °C, these layered dehydrated phases undergo transitions to $RE_2Ti_2O_7$ pyrochlore-type structures, demonstrating their metastability.[261]

The $n=2$ Ruddlesden–Popper-phase $H_2SrTa_2O_7$ also undergoes a dehydration/layer fusion reaction to form the strontium-deficient perovskite-phase $SrTa_2O_6$, in which the strontium cations are distributed randomly over the A-cation sites of the perovskite lattice.[281] On further heating, $SrTa_2O_6$ undergoes a structural reorganization to adopt a tetragonal tungsten bronze structure, further demonstrating the metastability of cation-deficient perovskite phases.

2.15.4.5.3 Redox-neutral intercalation

2.15.4.5.3.1 Salt intercalation reactions

As described in Section 2.15.4.5.1.3, charged salt layers can be substituted for metal cations, residing within layered complex oxide host phases, to yield new hybrid materials. In analogous processes, uncharged salt layers can be inserted into suitable layered hosts in a redox-neutral manner. For example by exploiting the weak interlayer bonding interactions within the Bi_2O_2 layers of Aurivillius and related bismuth-containing superconducting oxide materials, neutral salt fragments can be inserted into $Bi_2Sr_2Ca_{n-1}Cu_nO_y$-type phases. Thus if the layered $n=2$ phase $Bi_2Sr_2CaCu_2O_8$ is heated in the presence of silver and iodine, AgI is readily intercalated within the Bi_2O_2 layers of the cuprate phase to yield $(AgI)Bi_2Sr_2CaCu_2O_8$ according to reaction [59][295]:

$$Bi_2Sr_2CaCu_2O_8 + Ag + \frac{1}{2}I_2 \rightarrow (AgI)Bi_2Sr_2CaCu_2O_8 \quad [59]$$

The composition of the intercalated layer and the oxidation state of silver have been confirmed by x-ray absorption measurements, demonstrating that the intercalation reaction is redox neutral with respect to the host lattice. Similar reactions can be performed to insert HgI_2 or $HgBr_2$ into $Bi_2Sr_2CaCu_2O_8$ by heating the host phase with the appropriate mercury dihalide in the presence of iodine to act as a transport agent.[296] However, x-ray absorption data collected from the resulting $(HgX_2)_{0.5}Bi_2Sr_2CaCu_2O_8$ phases indicate that there is partial charge transfer between the HgX_2 guest layers and $Bi_2Sr_2CaCu_2O_8$ host lattice, so the intercalation is mildly oxidative in this case.[297]

The intercalation reactions of $n=3$ $Bi_2Sr_2Ca_{n-1}Cu_nO_y$ phases are observed to proceed much more slowly than those of $n=2$ and $n=1$ hosts. For example, $Bi_2Sr_2Ca_2Cu_3O_{10}$ is observed not to react with HgI_2. However if $Bi_2Sr_2Ca_2Cu_3O_{10}$ is first reacted with iodine to form $IBi_2Sr_2Ca_2Cu_3O_{10}$ as described in Section 2.15.4.4.2.4, reaction with AgI or HgI_2 proceeds rapidly to yield $(AgI)Bi_2Sr_2Ca_2Cu_3O_{10}$ or $(HgI_2)_{0.5}Bi_2Sr_2Ca_2Cu_3O_{10}$, respectively.[298] Following such a

two-step intercalation route also allows the intercalation of AuI_3 into $Bi_2Sr_2CaCu_2O_8$. Thus if $IBi_2Sr_2CaCu_2O_8$ is heated with a quarter of a mole equivalent of gold powder, $(AuI_3)_{0.25}Bi_2Sr_2CaCu_2O_8$ is formed.[299] Raman spectroscopy indicates that AuI_3 exists as a novel trigonal planar intercalated molecule. Subsequent theoretical analysis suggests that Au^{III} is unstable with respect to a strong Jahn–Teller distortion which favors Y- or T-shaped molecules and that in fact the gold–iodine species is AuI_3^{2-} containing monovalent gold.[300]

2.15.4.5.3.2 Intercalation of organic bases

Proton-exchanged complex oxide phases can act as Brønsted solid acids facilitating the intercalation of organic bases to form organic/inorganic hybrid materials via an acid/base neutralization process. For example, if the proton-exchanged Dion–Jacobson-phases $HCa_2Na_{n-3}Nb_nO_{3n+1}$ $(3 \leq n \leq 7)$ are stirred with *n*-octylamine $(CH_3(CH_2)_7NH_2)$ in hexane, the alkylamine is intercalated into the interlayer region of the oxide host phase, as demonstrated by a constant expansion of the interlayer separation on intercalation, for all phases in the series.[267] Similar base intercalation reactions can occur for a wide range of layered solid-acid phases, if the incorporated protons are sufficiently acidic. For example, the series of $n=3$ Dion–Jacobson-phases $HCa_{2-x}La_xNb_{3-x}Ti_xO_{10}$ $(0<x<2)$ have Brønsted acidities which decrease with increasing *x*, such that the $x=2$ member of the series, $HLa_2Nb_3Ti_2O_{10}$, intercalates very strong bases only sparingly.[279,301]

The stability of the inorganic/organic hybrid phases prepared by the intercalation of long-chain alkylamines is thought to derive from favorable van der Waals forces which arise from the efficient packing of the organic chains. However if short-chain or sterically bulky bases, which do not pack efficiently, are intercalated into layered solid acids, solvent can penetrate the interlayer spaces, leading to the delamination of the oxide host. Thus if $HCa_2Nb_3O_{10}$ is treated with the bulky amine tetra(*n*-butyl)ammonium hydroxide (TBA), sheets of $TBA_xH_{1-x}Ca_2Nb_3O_{10}$ are exfoliated from the host phase and suspended in solution.[302,303] The exfoliated sheets have a net negative charge and can therefore be self-assembled onto a positively charged surface, such as oxidized silicon treated with poly(diallyldimethylammonium chloride) (PDDA). The deposited monolayer, which is charge neutral, can then be treated with PDDA and a further monolayer deposited on top of the first. This second layer need not be based on the same inorganic block as the first, allowing films with complex stacking sequences to be constructed. Thus by careful layer-by-layer synthesis, complex stacking sequences such as $Ca_2Nb_3O_{10}$/$LaNb_2O_7$/$Sr_2Nb_3O_{10}$/$LaNb_2O_7$ (interleaved by organic bases) can be formed.[303] This layer-by-layer deposition method allows the synthesis of films with complex stacking sequences which could not be simply made by other synthesis routes.

2.15.5 Conclusion

In summary, it can be seen that by applying a wide variety of low-temperature topochemical reactions, a large number of metastable complex oxide phases can be prepared, in which the solid structure and metal oxidation states can be carefully tuned and controlled. By applying such topochemical reactions in sequence, the directed synthesis of desired product phases can be undertaken in a much more controllable way than is possible via the high-temperature ceramic synthesis routes traditionally used to prepare complex oxide phases.

References

1. Gopalakrishnan, J. *Chem. Mater.* **1995**, *7*, 1265.
2. Schaak, R. E.; Mallouk, T. E. *Chem. Mater.* **2002**, *14*, 1455.
3. Stein, A.; Keller, S. W.; Mallouk, T. E. *Science* **1993**, *259*, 1558.
4. Disalvo, F. J. *Science* **1990**, *247*, 649.
5. Wells, A. F. *Structural Inorganic Chemistry*. Oxford University Press: Oxford, 1984.
6. Vidyasagar, K.; Gopalakrishnan, J.; Rao, C. N. R. *Inorg. Chem.* **1984**, *23*, 1206.
7. Horowitz, H. S.; Longo, J. M. *Mater. Res. Bull.* **1978**, *13*, 1359.
8. Vidyasagar, K.; Gopalakrishnan, J.; Rao, C. N. R. *J. Solid State Chem.* **1985**, *58*, 29.
9. Livage, J.; Henry, M.; Sanchez, C. *Prog. Solid State Chem.* **1988**, *18*, 259.
10. Kakihana, M. *J. Sol-Gel Sci. Techn.* **1996**, *6*, 7.
11. Chandler, C. D.; Roger, C.; Hampdensmith, M. J. *Chem. Rev.* **1993**, *93*, 1205.
12. Campion, J. F.; Payne, D. A.; Chae, H. K.; Maurin, J. K.; Wilson, S. R. *Inorg. Chem.* **1991**, *30*, 3244.
13. Kwei, G. H.; Lawson, A. C.; Billinge, S. J. L.; Cheong, S. W. *J. Phys. Chem.* **1993**, *97*, 2368.
14. Gustafson, R. L. *J. Chem. Educ.* **1960**, *37*, 603.
15. Fransaer, J.; Roos, J. R.; Delaey, L.; Vanderbiest, O.; Arkens, O.; Celis, J. P. *J. Appl. Phys.* **1989**, *65*, 3277.
16. Catania, P.; Hovnanian, N.; Cot, L. *Mater. Res. Bull.* **1990**, *25*, 1477.
17. Maeda, S.; Tsurusaki, Y.; Tachiyama, Y.; Naka, K.; Ohki, A.; Ohgushi, T.; Takeshita, T. *J. Polym. Sci. Pol. Chem.* **1994**, *32*, 1729.
18. Pechini M.P. (1967) Patent, U. S., Ed. USA, *3*: 697.
19. Fjellvag, H.; Hansteen, O. H.; Tilset, B. G.; Olafsen, A.; Sakai, N.; Seim, H. *Thermochim. Acta* **1995**, *256*, 75.
20. Sale, F. R.; Mahloojchi, F. *Ceram. Int.* **1988**, *14*, 229.
21. Walton, R. I. *Chem. Soc. Rev.* **2002**, *31*, 230.
22. Modeshia, D. R.; Walton, R. I. *Chem. Soc. Rev.* **2010**, *39*, 4303.
23. Rabenau, A. *Angew. Chem. Int. Ed.* **1985**, *24*, 1026.
24. Knauss, K. G.; Dibley, M. J.; Bourcier, W. L.; Shaw, H. F. *Appl. Geochem.* **2001**, *16*, 1115.
25. Dutta, P. K.; Gregg, J. R. *Chem. Mater.* **1992**, *4*, 843.
26. Wei, X.; Xu, G.; Ren, Z. H.; Wang, Y. G.; Shen, G.; Han, G. R. *J. Cryst. Growth* **2008**, *310*, 4132.
27. Ashbrook, S. E.; Le Polles, L.; Gautier, R.; Pickard, C. J.; Walton, R. I. *Phys. Chem. Chem. Phys.* **2006**, *8*, 3423.
28. Goh, G. K. L.; Lange, F. F.; Haile, S. M.; Levi, C. G. *J. Mater. Res.* **2003**, *18*, 338.
29. Goh, G. K. L.; Levi, C. G.; Lange, F. F. *J. Mater. Res.* **2002**, *17*, 2852.
30. He, Y.; Zhu, Y. F.; Wu, N. Z. *J. Solid State Chem.* **2004**, *177*, 3868.
31. He, Y.; Zhu, Y. F.; Wu, N. Z. *J. Solid State Chem.* **2004**, *177*, 2985.
32. Liu, J. W.; Chen, G.; Li, Z. H.; Zhang, Z. G. *Int. J. Hydrogen Energ.* **2007**, *32*, 2269.
33. Santos, I.; Loureiro, L. H.; Silva, M. F. P.; Cavaleiro, A. M. V. *Polyhedron* **2002**, *21*, 2009.
34. Suchanek, W. L. *Chem. Mater.* **2004**, *16*, 1083.
35. Vasco, E.; Magrez, A.; Forro, L.; Setter, N. *J. Phys. Chem. B* **2005**, *109*, 14331.
36. Modeshia, D. R.; Darton, R. J.; Ashbrook, S. E.; Walton, R. I. *Chem. Commun.* **2009**, 68.
37. Ju, J.; Wang, D. J.; Lin, J. H.; Li, G. B.; Chen, J.; You, L. P.; Liao, F. H.; Wu, N. Z.; Huang, H. Z.; Yao, G. Q. *Chem. Mater.* **2003**, *15*, 3530.
38. Rao, C. N. R., Raveau, B., Eds.; In *Colossal Magnetoresistance, Charge Ordering and Related Properties of Manganese Oxides*; World Scientific: Singapore, 1998.
39. Wang, Y. W.; Lu, X. Y.; Chen, Y.; Chi, F. L.; Feng, S. H.; Liu, X. Y. *J. Solid State Chem.* **2005**, *178*, 1317.
40. Chen, Y.; Yuan, H. M.; Li, G. H.; Tian, G.; Feng, S. H. *J. Cryst. Growth* **2007**, *305*, 242.
41. Han, J. T.; Huang, Y. H.; Huang, W.; Goodenough, J. B. *J. Am. Chem. Soc.* **2006**, *128*, 14454.
42. Stampler, E. S.; Sheets, W. C.; Prellier, W.; Marks, T. J.; Poeppelmeier, K. R. *J. Mater. Chem.* **2009**, *19*, 4375.
43. Chen, Y.; Yuan, H. M.; Tian, G.; Zhang, G. H.; Feng, S. H. *J. Solid State Chem.* **2007**, *180*, 1340.
44. Christen, A. N.; Ollivier, G. *J. Solid State Chem.* **1972**, *4*, 131.
45. Spooren, J.; Walton, R. I. *J. Solid State Chem.* **2005**, *178*, 1683.

46. Cussen, E. J.; Battle, P. D. *Chem. Mater.* **2000**, *12*, 831.
47. Li, C. P.; Li, T.; Wang, B.; Yan, H. *J. Cryst. Growth* **2006**, *295*, 137.
48. Liu, J. B.; Wang, H.; Zhu, M. K.; Wang, B.; Yan, H. *Mater. Res. Bull.* **2003**, *38*, 817.
49. Li, J. Q.; Sun, W. A.; Ao, W. Q.; Tang, J. N. *J. Magn. Magn. Mater.* **2006**, *302*, 463.
50. Urban, J. J.; Ouyang, L.; Jo, M. H.; Wang, D. S.; Park, H. *Nano Lett.* **2004**, *4*, 1547.
51. Chen, Y.; Yuan, H. M.; Tian, G.; Zhang, G. H.; Feng, S. H. *J. Solid State Chem.* **2007**, *180*, 167.
52. Millange, F.; Caignaert, V.; Domenges, B.; Raveau, B.; Suard, E. *Chem. Mater.* **1998**, *10*, 1974.
53. Spooren, J.; Rumplecker, A.; Millange, F.; Walton, R. I. *Chem. Mater.* **2003**, *15*, 1401.
54. Spooren, J.; Walton, R. I.; Millange, F. *J. Mater. Chem.* **2005**, *15*, 1542.
55. Laurent, Y. *Rev. Chim. Miner.* **1969**, *6*, 1145.
56. Mugavero, S. J.; Gemmill, W. R.; Roof, I. P.; zur Loye, H. C. *J. Solid State Chem.* **1950**, *2009*, 182.
57. Perry, D. L.; Phillips, S. L. *Hand Book of Inorganic Compounds*. CRC Press: Orinda, CA, 1995.
58. Ham, W. K.; Holland, G. F.; Stacy, A. M. *J. Am. Chem. Soc.* **1988**, *110*, 5214.
59. Lux, H.; Kuhn, R.; Niedermaier, T. *Z. Anorg. Allg. Chem.* **1959**, *298*, 285.
60. Mugavero, S. J.; Smith, M. D.; Yoon, W. S.; zur Loye, H. C. *Angew. Chem. Int. Ed.* **2009**, *48*, 215.
61. Jung, D. Y.; Demazeau, G. *J. Solid State Chem.* **1995**, *115*, 447.
62. Reisner, B. A.; Stacy, A. M. *J. Am. Chem. Soc.* **1998**, *120*, 9682.
63. Zhao, Q. B.; Smith, M. D.; zur Loye, H. C. *J. Chem. Crystallogr.* **2011**, *41*, 674.
64. Campa, J. A.; Gutierrezpuebla, E.; Monge, M. A.; Rasines, I.; Ruizvalero, C. *J. Solid State Chem.* **1994**, *108*, 230.
65. Dicarlo, J.; Yazdi, I.; Jacobson, A. J.; Navrotsky, A. *J. Solid State Chem.* **1994**, *109*, 223.
66. Dann, S. E.; Weller, M. T.; Currie, D. B.; Thomas, M. F.; Alrawwas, A. D. *J. Mater. Chem.* **1993**, *3*, 1231.
67. Takeda, Y.; Shimada, M.; Kanamaru, F.; Koizumi, M.; Yamamoto, N. *Chem. Lett.* **1974**, 107.
68. Cava, R. J.; Santoro, A.; Murphy, D. W.; Zahurak, S. M.; Roth, R. S. *J. Solid State Chem.* **1983**, *50*, 121.
69. Cava, R. J.; Santoro, A.; Murphy, D. W.; Zahurak, S.; Roth, R. S. *Solid State Ionics* **1981**, *5*, 323.
70. Murphy, D. W.; Greenblatt, M.; Cava, R. J.; Zahurak, S. M. *Solid State Ionics* **1981**, *5*, 327.
71. Cava, R. J.; Santoro, A.; Murphy, D. W.; Zahurak, S.; Roth, R. S. *J. Solid State Chem.* **1982**, *42*, 251.
72. Cheng, K. H.; Whittingham, M. S. *Solid State Ionics* **1980**, *1*, 151.
73. Straumanis, M. E. *J. Am. Chem. Soc.* **1949**, *71*, 679.
74. Kimizuka, N.; Akahane, T.; Matsumoto, S.; Yukino, K. *Inorg. Chem.* **1976**, *15*, 3178.
75. Horiuchi, S.; Kimizuka, N.; Yamamoto, A. *Nature* **1979**, *279*, 226.
76. Dickens, P. G.; Weller, M. T. *J. Solid State Chem.* **1983**, *48*, 407.
77. Weller, M. T.; Dickens, P. G. *Solid State Ionics* **1983**, *9–10*, 1081.
78. Dickens, P. G.; Moore, J. H.; Neild, D. J. *J. Solid State Chem.* **1973**, *7*, 241.
79. Wiseman, P. J.; Dickens, P. G. *J. Solid State Chem.* **1973**, *6*, 374.
80. Murphy, D. W.; Disalvo, F. J.; Carides, J. N.; Waszczak, J. V. *Mater. Res. Bull.* **1978**, *13*, 1395.
81. Cox, D. E.; Cava, R. J.; McWhan, D. B.; Murphy, D. W. *J. Phys. Chem. Solids* **1982**, *43*, 657.
82. Davidson, I. J.; Greedan, J. E. *J. Solid State Chem.* **1984**, *51*, 104.
83. Thackeray, M. M.; David, W. I. F.; Goodenough, J. B. *Mater. Res. Bull.* **1982**, *17*, 785.
84. Thackeray, M. M.; David, W. I. F.; Bruce, P. G.; Goodenough, J. B. *Mater. Res. Bull.* **1983**, *18*, 461.
85. Thackeray, M. M.; Baker, S. D.; Adendorff, K. T.; Goodenough, J. B. *Solid State Ionics* **1985**, *17*, 175.
86. Cava, R. J.; Murphy, D. W.; Zahurak, S.; Santoro, A.; Roth, R. S. *J. Solid State Chem.* **1984**, *53*, 64.
87. David, W. I. F.; Thackeray, M. M.; Depicciotto, L. A.; Goodenough, J. B. *J. Solid State Chem.* **1987**, *67*, 316.
88. Depicciotto, L. A.; Thackeray, M. M. *Mater. Res. Bull.* **1985**, *20*, 1409.
89. Schollhorn, R.; Kuhlmann, R.; Besenhard, J. O. *Mater. Res. Bull.* **1976**, *11*, 83.
90. Tagaya, H.; Ara, K.; Kadokawa, J.; Karasu, M.; Chiba, K. *J. Mater. Chem.* **1994**, *4*, 551.
91. Birtill, J. J.; Dickens, P. G. *Mater. Res. Bull.* **1978**, *13*, 311.
92. Glemser, O.; Lutz, G. *Z. Anorg. Allg. Chem.* **1951**, *264*, 17.
93. Schroder, F. A.; Weitzel, H. *Z. Anorg. Allg. Chem.* **1977**, *435*, 247.
94. Tinet, D.; Canesson, P.; Estrade, H.; Fripiat, J. J. *J. Phys. Chem. Solids* **1980**, *41*, 583.
95. Dickens, P. G.; Birtill, J. J.; Wright, C. J. *J. Solid State Chem.* **1979**, *28*, 185.
96. Dickens, P. G.; Short, A. T.; Crouchbaker, S. *Solid State Ionics* **1988**, *28*, 1294.
97. Slade, R. C. T.; Halstead, T. K.; Dickens, P. G. *J. Solid State Chem.* **1980**, *34*, 183.
98. Dickens, P. G.; French, S. J.; Hight, A. T.; Pye, M. F. *Mater. Res. Bull.* **1979**, *14*, 1295.
99. Murphy, D. W.; Christian, P. A.; Disalvo, F. J.; Waszczak, J. V. *Inorg. Chem.* **1979**, *18*, 2800.
100. Cava, R. J.; Santoro, A.; Murphy, D. W.; Zahurak, S. M.; Fleming, R. M.; Marsh, P.; Roth, R. S. *J. Solid State Chem.* **1986**, *65*, 63.
101. Dickens, P. G.; Chippindale, A. M.; Hibble, S. J.; Lancaster, P. *Mater. Res. Bull.* **1984**, *19*, 319.
102. Yoshikawa, A.; Yagisawa, K.; Shimoda, M. *J. Mater. Sci.* **1994**, *29*, 1319.
103. Shimoda, M.; Yoshikawa, A.; Yagisawa, K. *J. Mater. Sci.* **1994**, *29*, 478.
104. Takano, Y.; Takayanagi, S.; Ogawa, S.; Yamadaya, T.; Mori, N. *Solid State Commun.* **1997**, *103*, 215.
105. Nagai, I.; Abe, Y.; Kato, M.; Koike, Y.; Kakihana, M. *Physica C* **2001**, *357*, 393.
106. Nagai, I.; Abe, Y.; Kato, M.; Koike, Y.; Kakihana, A. *Solid State Ionics* **2002**, *151*, 265.
107. Kato, M.; Inoue, A.; Nagai, I.; Kakihana, M.; Sleight, A. W.; Koike, Y. *Physica C* **2003**, *388*, 445.
108. Armstrong, A. R.; Anderson, P. A. *Inorg. Chem.* **1994**, *33*, 4366.
109. Choi, J.; Zhang, X.; Wiley, J. B. *Inorg. Chem.* **2009**, *48*, 4811.
110. Byeon, S. H.; Kim, H. J.; Kim, D. K.; Hur, N. H. *Chem. Mater.* **2003**, *15*, 383.
111. Toda, K.; Takahashi, M.; Teranishi, T.; Ye, Z. G.; Sato, M.; Hinatsu, Y. *J. Mater. Chem.* **1999**, *9*, 799.
112. Toda, K.; Teranishi, T.; Takahashi, M.; Ye, Z. G.; Sato, M. *Solid State Ionics* **1998**, *113*, 501.
113. Toda, K.; Teranishi, T.; Ye, Z. G.; Sato, M.; Hinatsu, Y. *Mater. Res. Bull.* **1999**, *34*, 971.
114. Bohnke, C.; Bohnke, O.; Fourquet, J. L. *J. Electrochem. Soc.* **1997**, *144*, 1151.
115. McIntyre, R. A.; Falster, A. U.; Li, S. C.; Simmons, W. B.; O'Connor, C. J.; Wiley, J. B. *J. Am. Chem. Soc.* **1998**, *120*, 217.
116. Choy, J. H.; Kim, J. Y.; Chung, I. *J. Phys. Chem. B* **2001**, *105*, 7908.
117. Mizushima, K.; Jones, P. C.; Wiseman, P. J.; Goodenough, J. B. *Mater. Res. Bull.* **1980**, *15*, 783.
118. Gupta, R.; Manthiram, A. *J. Solid State Chem.* **1996**, *121*, 483.
119. Takahashi, Y.; Kijima, N.; Tokiwa, K.; Watanabe, T.; Akimoto, J. *J. Phys. Condens. Matter* **2007**, *19*, 436202.
120. Amatucci, G. G.; Tarascon, J. M.; Klein, L. C. *J. Electrochem. Soc.* **1996**, *143*, 1114.
121. Motohashi, T.; Katsumata, Y.; Ono, T.; Kanno, R.; Karppinen, M.; Yamauchi, H. *Chem. Mater.* **2007**, *19*, 5063.
122. Hertz, J. T.; Huang, Q.; McQueen, T.; Klimczuk, T.; Bos, J. W. G.; Viciu, L.; Cava, R. J. *Phys. Rev. B* **2008**, *77*, 075119.
123. Motohashi, T.; Ono, T.; Sugimoto, Y.; Masubuchi, Y.; Kikkawa, S.; Kanno, R.; Karppinen, M.; Yamauchi, H. *Phys. Rev. B* **2009**, *80*, 165114.
124. Reimers, J. N.; Dahn, J. R. *J. Electrochem. Soc.* **1992**, *139*, 2091.
125. Van der Ven, A.; Aydinol, M. K.; Ceder, G. *J. Electrochem. Soc.* **1998**, *145*, 2149.
126. Van der Ven, A.; Aydinol, M. K.; Ceder, G.; Kresse, G.; Hafner, J. *Phys. Rev. B* **1998**, *58*, 2975.
127. Fouassie, C.; Matejka, G.; Reau, J. M.; Hagenmul, P. *J. Solid State Chem.* **1973**, *6*, 532.
128. Viciu, L.; Bos, J. W. G.; Zandbergen, H. W.; Huang, Q.; Foo, M. L.; Ishiwata, S.; Ramirez, A. P.; Lee, M.; Ong, N. P.; Cava, R. J. *Phys. Rev. B* **2006**, *73*, 174104.
129. Delmas, C.; Braconnier, J. J.; Fouassier, C.; Hagenmuller, P. *Solid State Ionics* **1981**, *3–4*, 165.
130. Huang, Q.; Foo, M. L.; Pascal, R. A.; Lynn, J. W.; Toby, B. H.; He, T.; Zandbergen, H. W.; Cava, R. J. *Phys. Rev. B* **2004**, *70*, 184110.
131. Poltavets, V. V.; Croft, M.; Greenblatt, M. Phys. *Rev. B* **2006**, *74*, 125103.
132. Viciu, L.; Huang, Q.; Cava, R. J. *Phys. Rev. B* **2006**, *73*, 212107.
133. Foo, M. L.; Wang, Y. Y.; Watauchi, S.; Zandbergen, H. W.; He, T.; Cava, R. J.; Ong, N. P. *Phys. Rev. Lett.* **2004**, *92*, 247001.
134. Terasaki, I.; Sasago, Y.; Uchinokura, K. *Phys. Rev. B* **1997**, *56*, 12685.
135. Wang, Y. Y.; Rogado, N. S.; Cava, R. J.; Ong, N. P. *Nature* **2003**, *423*, 425.
136. Williams, A. J.; Attfield, J. P.; Foo, M. L.; Viciu, L.; Cava, R. J. *Phys. Rev. B* **2006**, *7*, 134401.
137. Takada, K.; Sakurai, H.; Takayama-Muromachi, E.; Izumi, F.; Dilanian, R. A.; Sasaki, T. *Nature* **2003**, *422*, 53.
138. Foo, M. L.; Schaak, R. E.; Miller, V. L.; Klimczuk, T.; Rogado, N. S.; Wang, Y.; Lau, G. C.; Craley, C.; Zandbergen, H. W.; Ong, N. P.; Cava, R. J. *Solid State Commun.* **2003**, *127*, 33.

139. Lorenz, B.; Cmaidalka, J.; Meng, R. L.; Chu, C. W. *Phys. Rev. B* **2003**, *68*, 014512.
140. Schaak, R. E.; Klimczuk, T.; Foo, M. L.; Cava, R. J. *Nature* **2003**, *424*, 527.
141. Arai, H.; Tsuda, M.; Saito, K.; Hayashi, M.; Takei, K.; Sakurai, Y. *J. Solid State Chem.* **2002**, *163*, 340.
142. Croguennec, L.; Pouillerie, C.; Delmas, C. *Solid State Ionics* **2000**, *135*, 259.
143. Tarascon, J. M.; Vaughan, G.; Chabre, Y.; Seguin, L.; Anne, M.; Strobel, P.; Amatucci, G. *J. Solid State Chem.* **1999**, *147*, 410.
144. Vidyasagar, K.; Gopalakrishnan, J. *J. Solid State Chem.* **1982**, *42*, 217.
145. Depicciotto, L. A.; Thackeray, M. M.; David, W. I. F.; Bruce, P. G.; Goodenough, J. B. *Mater. Res. Bull.* **1984**, *19*, 1497.
146. Thackeray, M. M.; Depicciotto, L. A.; David, W. I. F.; Bruce, P. G.; Goodenough, J. B. *J. Solid State Chem.* **1987**, *67*, 285.
147. Depicciotto, L. A.; Thackeray, M. M. *Mater. Res. Bull.* **1985**, *20*, 187.
148. Shao-Horn, Y.; Ein-Eli, Y.; Robertson, A. D.; Averill, W. F.; Hackney, S. A.; Howard, W. F. *J. Electrochem. Soc.* **1998**, *145*, 16.
149. Hunter, J. C. *J. Solid State Chem.* **1981**, *39*, 142.
150. Greedan, J. E.; Raju, N. P.; Wills, A. S.; Morin, C.; Shaw, S. M.; Reimers, J. N. *Chem. Mater.* **1998**, *10*, 3058.
151. Robinson, D. M.; Go, Y. B.; Greenblatt, M.; Dismukes, G. C. *J. Am. Chem. Soc.* **2010**, *132*, 11467.
152. Akimoto, J.; Takahashi, Y.; Gotoh, Y.; Kawaguchi, K.; Dokko, K.; Uchida, I. *Chem. Mater.* **2003**, *15*, 2984.
153. Tang, W. P.; Kanoh, H.; Ooi, K. *J. Solid State Chem.* **1999**, *142*, 19.
154. Gummow, R. J.; Liles, D. C.; Thackeray, M. M. *Mater. Res. Bull.* **1993**, *28*, 1249.
155. Akimoto, J.; Gotoh, Y.; Sohma, M.; Kawaguchi, K.; Oosawa, Y.; Takei, H. *J. Solid State Chem.* **1994**, *110*, 150.
156. Akimoto, J.; Gotoh, Y.; Oosawa, Y.; Nonose, N.; Kumagai, T.; Aoki, K.; Takei, H. *J. Solid State Chem.* **1994**, *113*, 27.
157. Takahashi, Y.; Kijima, N.; Akimoto, J. *Chem. Mater.* **2006**, *18*, 748.
158. Latroche, M.; Brohan, L.; Marchand, R.; Tournoux, M. *J. Solid State Chem.* **1989**, *81*, 78.
159. Watanabe, M.; Komatsu, Y.; Sasaki, T.; Fujiki, Y. *J. Solid State Chem.* **1991**, *92*, 80.
160. Anderson, M. T.; Vaughey, J. T.; Poeppelmeier, K. R. *Chem. Mater.* **1993**, *5*, 151.
161. Poeppelmeier, K. R.; Leonowicz, M. E.; Longo, J. M. *J. Solid State Chem.* **1982**, *44*, 89.
162. Poeppelmeier, K. R.; Leonowicz, M. E.; Scanlon, J. C.; Longo, J. M.; Yelon, W. B. *J. Solid State Chem.* **1982**, *45*, 71.
163. Chiang, C. C. K.; Poeppelmeier, K. R. *Mater. Lett.* **1991**, *12*, 102.
164. Rorrmark, L.; Wiik, K.; Stolen, S.; Grande, T. *J. Mater. Chem.* **2002**, *12*, 1058.
165. MacChesney, J. B.; Williams, H. J.; Potter, J. F.; Sherwood, R. C. *Phys. Rev.* **1967**, *164*, 779.
166. Schiffer, P.; Ramirez, A. P.; Bao, W.; Cheong, S.-W. *Phys. Rev. Lett.* **1995**, *75*, 3336.
167. Hansteen, O. H.; Fjellvag, H.; Hauback, B. C. *J. Solid State Chem.* **1998**, *141*, 411.
168. Hansteen, O. H.; Fjellvag, H.; Hauback, B. C. *J. Mater. Chem.* **1998**, *8*, 2081.
169. Hayward, M. A.; Green, M. A.; Rosseinsky, M. J.; Sloan, J. *J. Am. Chem. Soc.* **1999**, *121*, 8843.
170. Hayward, M. A.; Cussen, E. J.; Claridge, J. B.; Bieringer, M.; Rosseinsky, M. J.; Kiely, C. J.; Blundell, S. J.; Marshall, I. M.; Pratt, F. L. *Science* **2002**, *295*, 1882.
171. Adkin, J. J.; Hayward, M. A. *Inorg. Chem.* **2008**, *47*, 10959.
172. Alonso, J. A.; Martinez-Lope, M. J. *J. Chem. Soc. Dalton Trans.* **1995**, 2819.
173. Siegrist, T.; Zahurak, S. M.; Murphy, D. W.; Roth, R. S. *Nature* **1988**, *334*, 231.
174. Lee, K. W.; Pickett, W. E. *Phys. Rev. B* **2004**, *70*, 045104.
175. O'Malley, M.; Lockett, M. A.; Hayward, M. A. *J. Solid State Chem.* **2007**, *180*, 2851.
176. Hadermann, J.; Abakumov, A.; Adkin, J. J.; Hayward, M. A. *J. Am. Chem. Soc.* **2009**, *131*, 10598.
177. Helps, R. M.; Rees, N. H.; Hayward, M. A. *Inorg. Chem.* **2010**, *49*, 11062.
178. Suescun, L.; Dabrowski, B.; Mais, J.; Remsen, S.; Richardson, J. W.; ER, M.; Jorgensen, J. D. *Chem. Mater.* **2008**, *20*, 1636.
179. Suescun, L.; Dabrowski, D.; Remsen, S.; Mais, J. *J. Solid State Chem.* **2009**, *182*, 187.
180. Mori, T.; Kamegashira, N. *J. Alloy Compd.* **2006**, *408–412*, 1210.
181. Trukhanov, S. V.; Kasper, N. V.; Troyanchuk, I. O.; Tovar, M.; Szymczak, H.; Barner, K. *J. Solid State Chem.* **2002**, *169*, 85.
182. Gonzalez-Calbet, J. M.; Herrero, E.; Rangavittal, N.; Alonso, J. M.; Martinez, J. L.; Vallet-Regi, M. *J. Solid State Chem.* **1999**, *148*, 158.
183. Cortes-Gil, R.; Ruiz-Gonzalez, M. L.; Alonso, J. M.; Vallet-Regi, M.; Hernando, M.; Gonzalez Calbet, J. M. *Chem.-Eur. J.* **2007**, *13*, 4246.
184. Hansteen, O. H.; Breard, Y.; Fjellvag, H.; Hauback, B. C. *Solid State Sci.* **2004**, *6*, 279.
185. Ruiz-Gonzalez, M. L.; Cortes-Gil, R.; Alonso, J. M.; Hernando, A.; Vallet-Regi, M.; Gonzalez-Calbet, J. M. *Chem. Mater.* **2006**, *18*, 5756.
186. Parsons, T. G.; D'Hondt, H.; Hadermann, J.; Hayward, M. A. *Chem. Mater.* **2009**, *21*, 5527.
187. Tsujimoto, Y.; Tassel, C.; Hayashi, N.; Watanabe, T.; Kageyama, H.; Yoshimura, K.; Takano, M.; Ceretti, M.; Ritter, C.; Paulus, W. *Nature* **2007**, *450*, 1062.
188. Hayward, M. A.; Rosseinsky, M. J. *Nature* **2007**, *450*, 960.
189. Seinberg, L.; Yamamoto, T.; Tassel, C.; Kobayashi, Y.; Hayashi, N.; Kitada, A.; Sumida, Y.; Watanabe, T.; Nishi, M.; Ohoyama, K.; Yoshimura, K.; Takano, M.; Paulus, W.; Kageyama, H. *Inorg. Chem.* **2011**, *50*, 3988.
190. Kawakami, T.; Tsujimoto, Y.; Kageyama, H.; Chen, X. Q.; Fu, C. L.; Tassel, C.; Kitada, A.; Suto, S.; Hirama, K.; Sekiya, Y.; Makino, Y.; Okada, T.; Yagi, T.; Hayashi, N.; Yoshimura, K.; Nasu, S.; Podloucky, R.; Takano, M. *Nat. Chem.* **2009**, *1*, 371.
191. Leonowicz, M. E.; Poeppelmeier, K. R.; Longo, J. M. *J. Solid State Chem.* **1985**, *59*, 71.
192. Gillie, L. J.; Wright, A. J.; Hadermann, J.; Van Tendeloo, G.; Greaves, C. *J. Solid State Chem.* **2002**, *167*, 145.
193. Kitchen, H. J.; Saratovsky, I.; Hayward, M. A. *Dalton Trans.* **2010**, *39*, 6098.
194. Hansteen, O. H.; Fjellvag, H.; Hauback, B. C. *J. Mater. Chem.* **1998**, *8*, 2089.
195. Hayward, M. A.; Rosseinsky, M. J. *Chem. Mater.* **2000**, *12*, 2182.
196. Bridges, C. A.; Darling, G. R.; Hayward, M. A.; Rosseinsky, M. J. *J. Am. Chem. Soc.* **2005**, *127*, 5996.
197. Bowman, A.; Claridge, J. B.; Rosseinsky, M. J. *Chem. Mater.* **2006**, *18*, 3046.
198. Dann, S. E.; Weller, M. T.; Currie, D. B. *J. Solid State Chem.* **1992**, *97*, 179.
199. Kageyama, H.; Watanabe, T.; Tsujimoto, Y.; Kitada, A.; Sumida, Y.; Kanamori, K.; Yoshimura, K.; Hayashi, N.; Muranaka, S.; Takano, M.; Ceretti, M.; Paulus, W.; Ritter, C.; Andre, G. *Angew. Chem.* **2008**, *47*, 5704.
200. Poltavets, V. V.; Lokshin, K. A.; Dikmen, S.; Croft, M.; Egami, T.; Greenblatt, M. *J. Am. Chem. Soc.* **2006**, *128*, 9050.
201. Hayward, M. A. *Chem. Mater.* **2006**, *18*, 321.
202. Millburn, J. E.; Mitchell, J. F. *Chem. Mater.* **2001**, *13*, 1957.
203. Vogt, T.; Woodward, P. M.; Karen, P.; Hunter, B. A.; Henning, P.; Moodenbaugh, A. R. *Phys. Rev. Lett.* **2000**, *84*, 2969.
204. Millange, F.; Suard, E.; Caignaert, V.; Raveau, B. *Mater. Res. Bull.* **1999**, *34*, 1.
205. Caignaert, V.; Millange, F.; Domenges, B.; Raveau, B. *Chem. Mater.* **1999**, *11*, 930.
206. Woodward, P. M.; Karen, P. *Inorg. Chem.* **2003**, *42*, 1121.
207. Karen, P.; Suard, E.; Fauth, F.; Woodward, P. M. *Solid State Sci.* **2004**, *6*, 1195.
208. Seddon, J.; Suard, E.; Hayward, M. A. *J. Am. Chem. Soc.* **2010**, *132*, 2802.
209. Tofield, B. C.; Scott, W. R. *J. Solid State Chem.* **1974**, *10*, 183.
210. Negas, T.; Roth, R. S. *J. Solid State Chem.* **1970**, *1*, 409.
211. Battle, P. D.; Gibb, T. C.; Jones, C. W. *J. Solid State Chem.* **1988**, *74*, 60.
212. Chmaissem, O.; Dabrowski, B.; Kolesnik, S.; Mais, J.; Brown, D. E.; Kruk, R.; Prior, P.; Pyles, B.; Jorgensen, J. D. *Phys. Rev. B* **2001**, *64*, 134412.
213. Caignaert, V.; Nguyen, N.; Hervieu, M.; Raveau, B. *Mater. Res. Bull.* **1985**, *20*, 479.
214. Lobanov, M. V.; Abakumov, A. M.; Sidorova, A. V.; Rozova, M. G.; D'Yachenko, O. G.; Antipov, E. V.; Hadermann, J.; Van Tendeloo, G. *Solid State Sci.* **2002**, *4*, 19.
215. Takeda, Y.; Kanno, K.; Takada, T.; Yamamoto, O.; Takano, M.; Nakayama, N.; Bando, Y. *J. Solid State Chem.* **1986**, *63*, 237.
216. Hodges, J. P.; Short, S.; Jorgensen, J. D.; Xiong, X.; Dabrowski, B.; Mini, S. M.; Kimball, C. W. *J. Solid State Chem.* **2000**, *151*, 190.
217. Wattiaux, A.; Fournes, L.; Demourgues, A.; Bernaben, N.; Grenier, J. C.; Pouchard, M. *Solid State Commun.* **1991**, *77*, 489.
218. Berry, F. J.; Ren, X. L.; Heap, R.; Slater, P.; Thomas, M. F. *Solid State Commun.* **2005**, *134*, 621.
219. Rautama, E. L.; Boullay, P.; Kundu, A. K.; Caignaert, V.; Pralong, V.; Karppinen, M.; Raveau, B. *Chem. Mater.* **2008**, *20*, 2742.
220. Abakumov, A. M.; Rozova, M. G.; Pavlyuk, B. P.; Lobanov, M. V.; Antipov, E. V.; Lebedev, O. I.; Van Tendeloo, G.; Sheptyakov, D. V.; Balagurov, A. M.; Bouree, F. *J. Solid State Chem.* **2001**, *158*, 100.
221. Sheptyakov, D. V.; Abakumov, A. M.; Antipov, E. V.; Balagurov, A. M.; Billinge, S. J. L.; Fischer, P.; Keller, L.; Lobanov, M. V.; Pavlyuk, B. P.; Pomjakushin, V. Y.; Rozova, M. G. *Appl. Phys. A-Mater.* **2002**, *74*, S1734.
222. Abakumov, A. M.; Rozova, M. G.; Pavlyuk, B. P.; Lobanov, M. V.; Antipov, E. V.; Lebedev, O. I.; Van Tendeloo, G.; Ignatchik, O. L.; Ovtchenkov, E. A.; Koksharov, Y. A.; Vasil'ev, A. N. *J. Solid State Chem.* **2001**, *160*, 353.
223. Pomjakushin, V. Y.; Balagurov, A. M.; Elzhov, T. V.; Sheptyakov, D. V.; Fischer, P.; Khomskii, D. I.; Yushankhai, V. Y.; Abakumov, A. M.; Rozova, M. G.; Antipov, E. V.; Lobanov, M. V.; Billinge, S. J. L. *Phys. Rev. B* **2002**, *66*, 184412.

224. Abakumov, A. M.; Rozova, M. G.; Alekseeva, A. M.; Kovba, M. L.; Antipov, E. V.; Lebedev, O. I.; Van Tendeloo, G. *Solid State Sci.* **2003**, *5*, 871.
225. Antipov, E. V.; Abakumov, A. M.; Istomin, S. Y. *Inorg. Chem.* **2008**, *47*, 8543.
226. Vente, J. F.; Kamenev, K. V.; Sokolov, D. A. *Phys. Rev. B* **2001**, *64*, 214403.
227. Mitchell, J. F.; Millburn, J. E.; Medarde, M.; Short, S.; Jorgensen, J. D.; Fernandez-Diaz, M. T. *J. Solid State Chem.* **1998**, *141*, 599.
228. Dann, S. E.; Weller, M. T. *J. Solid State Chem.* **1995**, *115*, 499.
229. Hill, J. M.; Dabrowski, B.; Mitchell, J. F.; Jorgensen, J. D. *Phys. Rev. B* **2006**, *74*, 174417.
230. Girgsdies, F.; Schollhorn, R. *Solid State Commun.* **1994**, *91*, 111.
231. Jorgensen, J. D.; Dabrowski, B.; Pei, S.; Richards, D. R.; Hinks, D. G. *Phys. Rev. B* **1989**, *40*, 2187.
232. Jorgensen, J. D.; Dabrowski, B.; Pei, S. Y.; Hinks, D. G.; Soderholm, L.; Morosin, B.; Schirber, J. E.; Venturini, E. L.; Ginley, D. S. *Phys. Rev. B* **1988**, *38*, 11337.
233. Nemudry, A.; Rudolf, P.; Schollhorn, R. *Solid State Ionics* **1998**, *109*, 213.
234. Greaves, C.; Francesconi, M. G. *Curr. Opin. Solid State Mater. Sci.* **1998**, *3*, 132.
235. McCabe, E. E.; Greaves, C. *J. Fluorine Chem.* **2007**, *128*, 448.
236. Aikens, L. D.; Gillie, L. J.; Li, R. K.; Greaves, C. *J. Mater. Chem.* **2002**, *12*, 264.
237. Sivakumar, T.; Wiley, J. B. *Mater. Res. Bull.* **2009**, *44*, 74.
238. Aikens, L. D.; Li, R. K.; Greaves, C. *Chem. Commun.* **2000**, 2129.
239. Slater, P. R.; Hodges, J. P.; Francesconi, M. G.; Edwards, P. P.; Greaves, C.; Gameson, I.; Slaski, M. *Physica C* **1995**, *253*, 16.
240. Li, R. K.; Greaves, C. *Phys. Rev. B* **2000**, *62*, 3811.
241. Francesconi, M. G.; Slater, P. R.; Hodges, J. P.; Greaves, C.; Edwards, P. P.; Al-Mamouri, M.; Slaski, M. *J. Solid State Chem.* **1998**, *135*, 17.
242. Almamouri, M.; Edwards, P. P.; Greaves, C.; Slaski, M. *Nature* **1994**, *369*, 382.
243. Slater, P. R.; Edwards, P. P.; Greaves, C.; Gameson, I.; Francesconi, M. G.; Hodges, J. P.; Almamouri, M.; Slaski, M. *Physica C* **1995**, *241*, 151.
244. Almamouri, M.; Edwards, P. P.; Greaves, C.; Slater, P. R.; Slaski, M. *J. Mater. Chem.* **1995**, *5*, 913.
245. Xiang, X. D.; McKernan, S.; Vareka, W. A.; Zettl, A.; Corkill, J. L.; Barbee, T. W.; Cohen, M. L. *Nature* **1990**, *348*, 145.
246. Huong, P. V.; Verma, A. L. *Phys. Rev. B* **1993**, *48*, 9869.
247. Scarfe, D. P.; Bhavaraju, S.; Jacobson, A. J. *Chem. Commun.* **1997**, 313.
248. Scarfe, D. P.; Jacobson, A. J. *Chem. Mater.* **1997**, *9*, 3107.
249. England, W. A.; Goodenough, J. B.; Wiseman, P. J. *J. Solid State Chem.* **1983**, *49*, 289.
250. Shirane, T.; Kanno, R.; Kawamoto, Y.; Takeda, Y.; Takano, M.; Kamiyama, T.; Izumi, F. *Solid State Ionics* **1995**, *79*, 227.
251. Shannon, R. D.; Rogers, D. B.; Prewitt, C. T. *Inorg. Chem.* **1971**, *10*, 713.
252. Cushing, B. L.; Falster, A. U.; Simmons, W. B.; Wiley, J. B. *Chem. Commun.* **1996**, 2635.
253. Cushing, B. L.; Wiley, J. B. *J. Solid State Chem.* **1998**, *141*, 385.
254. Blesa, M. C.; Amador, U.; Moran, E.; Menendez, N.; Tornero, J. D.; Rodriguezcarvajal, J. *Solid State Ionics* **1993**, *63–5*, 429.
255. Blesa, M. C.; Moran, E.; Amador, U.; Andersen, N. H. *J. Solid State Chem.* **1997**, *129*, 123.
256. Eda, K.; Suzuki, M.; Hatayama, F.; Sotani, N. *J. Mater. Chem.* **1997**, *7*, 821.
257. Izawa, H.; Kikkawa, S.; Koizumi, M. *J. Phys. Chem.* **1982**, *86*, 5023.
258. Marchand, R.; Brohan, L.; Tournoux, M. *Mater. Res. Bull.* **1980**, *15*, 1129.
259. Dion, M.; Piffard, Y.; Tournoux, M. *J. Inorg. Nucl. Chem.* **1978**, *40*, 917.
260. Feist, T. P.; Davies, P. K. *J. Solid State Chem.* **1992**, *101*, 275.
261. Gopalakrishnan, J.; Bhat, V. *Inorg. Chem.* **1987**, *26*, 4299.
262. Gopalakrishnan, J.; Bhat, V.; Raveau, B. *Mater. Res. Bull.* **1987**, *22*, 413.
263. Toda, K.; Sato, M. *J. Mater. Chem.* **1996**, *6*, 1067.
264. Toda, K.; Suzuki, T.; Sato, M. *Solid State Ionics* **1996**, *93*, 177.
265. Mahler, C. H.; Cushing, B. L.; Lalena, J. N.; Wiley, J. B. *Mater. Res. Bull.* **1998**, *33*, 1581.
266. Jacobson, A. J.; Lewandowski, J. T.; Johnson, J. W. *J. Less-Common Met.* **1986**, *116*, 137.
267. Jacobson, A. J.; Johnson, J. W.; Lewandowski, J. T. *Inorg. Chem.* **1985**, *24*, 3727.
268. Uma, S.; Gopalakrishnan, J. *Chem. Mater.* **1994**, *6*, 907.
269. Palacin, M. R.; Lira, M.; Garcia, J. L.; Caldes, M. T.; CasanPastor, N.; Fuertes, A.; GomezRomero, P. *Mater. Res. Bull.* **1996**, *31*, 217.
270. Kodenkandath, T. A.; Lalena, J. N.; Zhou, W. L. L.; Carpenter, E. E.; Sangregorio, C.; Falster, A. U.; Simmons, W. B.; O'Connor, C. J.; Wiley, J. B. *J. Am. Chem. Soc.* **1999**, *121*, 10743.
271. Kodenkandath, T. A.; Kumbhar, A. S.; Zhou, W. L.; Wiley, J. B. *Inorg. Chem.* **2001**, *40*, 710.
272. Viciu, L.; Caruntu, G.; Royant, N.; Koenig, J.; Zhou, W. L. L.; Kodenkandath, T. A.; Wiley, J. B. *Inorg. Chem.* **2002**, *41*, 3385.
273. Viciu, L.; Golub, V. O.; Wiley, J. B. *J. Solid State Chem.* **2003**, *175*, 88.
274. Viciu, L.; Koenig, J.; Spinu, L.; Zhou, W. L.; Wiley, J. B. *Chem. Mater.* **2003**, *15*, 1480.
275. Viciu, L.; Kodenkandath, T. A.; Wiley, J. B. *J. Solid State Chem.* **2007**, *180*, 583.
276. Gondrand, M.; Joubert, J. C. *Rev. Chim. Miner.* **1987**, *24*, 33.
277. Toda, K.; Watanabe, J.; Sato, M. *Solid State Ionics* **1996**, *90*, 15.
278. Toda, K.; Watanabe, J.; Sato, M. *Mater. Res. Bull.* **1996**, *31*, 1427.
279. Gopalakrishnan, J.; Uma, S.; Bhat, V. *Chem. Mater.* **1993**, *5*, 132.
280. Richard, M.; Brohan, L.; Tournoux, M. *J. Solid State Chem.* **1994**, *112*, 345.
281. Ollivier, P. J.; Mallouk, T. E. *Chem. Mater.* **1998**, *10*, 2585.
282. Bhuvanesh, N. S. P.; Crosnier-Lopez, M. P.; Duroy, H.; Fourquet, J. L. *J. Mater. Chem.* **2000**, *10*, 1685.
283. Schaak, R. E.; Mallouk, T. E. *J. Solid State Chem.* **2000**, *155*, 46.
284. Crosnier-Lopez, M. P.; Le Berre, F.; Fourquet, J. L. *J. Mater. Chem.* **2001**, *11*, 1146.
285. Schaak, R. E.; Mallouk, T. E. *J. Solid State Chem.* **2001**, *161*, 225.
286. Schaak, R. E.; Mallouk, T. E. *J. Am. Chem. Soc.* **2000**, *122*, 2798.
287. Hyeon, K. A.; Byeon, S. H. *Chem. Mater.* **1999**, *11*, 352.
288. Gopalakrishnan, J.; Sivakumar, T.; Ramesha, K.; Thangadurai, V.; Subbanna, G. N. *J. Am. Chem. Soc.* **2000**, *122*, 6237.
289. Rebbah, H.; Desgardin, G.; Raveau, B. *Mater. Res. Bull.* **1979**, *14*, 1125.
290. Rebbah, H.; Pannetier, J.; Raveau, B. *J. Solid State Chem.* **1982**, *41*, 57.
291. Feist, T. P.; Mocarski, S. J.; Davies, P. K.; Jacobson, A. J.; Lewandowski, J. T. *Solid State Ionics* **1988**, *28*, 1338.
292. Tournoux, M.; Marchand, R.; Brohan, L. *Prog. Solid State Chem.* **1986**, *17*, 33.
293. Kobayashi, Y.; Ke, X.; Hata, H.; Schiffer, P.; Mallouk, T. E. *Chem. Mater.* **2008**, *20*, 2374.
294. Gonen, Z. S.; Paluchowski, D.; Zavalij, P.; Eichhorn, B. W.; Gopalakrishnan, J. *Inorg. Chem.* **2006**, *45*, 8736.
295. Choy, J. H.; Kim, D. K.; Hwang, S. J.; Hwang, S. H.; Hur, N. H. *Physica C* **1994**, *235*, 1023.
296. Choy, J. H.; Park, N. G.; Hwang, S. J.; Kim, D. H.; Hur, N. H. *J. Am. Chem. Soc.* **1994**, *116*, 11564.
297. Choy, J. H.; Hwang, S. J.; Park, N. G. *J. Am. Chem. Soc.* **1997**, *119*, 1624.
298. Choy, J. H.; Kwon, S. J.; Hwang, S. J.; Kim, Y. I.; Jang, E. S. *Int. J. Inorg. Mater.* **2001**, *3*, 253.
299. Choy, J. H.; Kim, Y. I.; Hwang, S. J.; Huong, P. V. *J. Phys. Chem. B* **2000**, *104*, 7273.
300. Munzarova, M. L.; Hoffmann, R. *J. Am. Chem. Soc.* **2002**, *124*, 5542.
301. Uma, S.; Raju, A. R.; Gopalakrishnan, J. *J. Mater. Chem.* **1993**, *3*, 709.
302. Fang, M. M.; Kim, C. H.; Saupe, G. B.; Kim, H. N.; Waraksa, C. C.; Miwa, T.; Fujishima, A.; Mallouk, T. E. *Chem. Mater.* **1999**, *11*, 1526.
303. Schaak, R. E.; Mallouk, T. E. *Chem. Mater.* **2000**, *12*, 2513.

This page intentionally left blank

2.16 Alkoxides and Alkoxosynthesis

VG Kessler, Swedish University of Agricultural Sciences, Uppsala, Sweden

Nomenclature

Ac	MeCO
acac	Ac_2CH^-
Alk	Alkyl, C_nH_{2n+1}
Am	Amine
Cp*	Pentamethyl-cyclopentadienyl
Dec	Decomposition
Dig	Diglyme
Dipy	2,2′Dipyridyl
Hc	Hydrocarbon
Hex	Hexane

2.16.1 Introduction

Metal alkoxides, salts of alcohols – extremely weak and, most often, volatile organic acids – as a class of compounds have earned a special status in inorganic chemistry. Their high sensitivity to hydrolysis and, very often, rather poor thermal stability made them highly attractive as, on the one hand, molecular precursors of inorganic materials – oxides, sulfides, and also metals and alloys – and, on the other hand, as reactants in fine inorganic and organic synthesis and as homogeneous catalysts.

The identification of this family of metal derivatives dates from the beginning of the systematic studies of the chemistry of elements with the works of Lamy[1] and Demarcay,[2] who described the isolation of alkoxide complexes of thallium, TlOR, and titanium, $Ti(OR)_4$, respectively, in the second half of the nineteenth century. Recognition of the potential of metal alkoxides as homogeneous catalysts came at the very beginning of the twentieth century, with fundamental works of Vyacheslav Tishchenko on the catalytic transformations of aldehydes and ketones in the presence of aluminum alkoxides, the Tishchenko reaction,[3] and with a series of publications and patents produced by Marcel Guerbet, who discovered that highly basic, in the first hand, alkali and alkaline-earth alkoxides catalyze β-hydrogen substitution with the formation of a new C–C bond, Guerbet reaction.[4] However, it took another 50 years until the potential of metal alkoxides as precursors for solution and gas-phase deposition processes for the preparation of coatings and thin films received truly broad recognition, which, to a great extent, was due to systematic studies led

by Donald C. Bradley,[5] who is recognized today as the founder of this branch of chemistry in its modern form. Bradley had even discovered one more principal reaction pathway for metal alkoxides, the nonhydrolytic transformations with elimination of alkyl halides[6] and dialkyl ethers, the Bradley reaction,[7,8] that results in the formation of oxo-complexes and, as further studies revealed, can lead even to the direct formation of metal-oxide nanoparticles under rather mild conditions, an application that has attracted huge interest during recent years. Further development of the synthetic approaches to transition-metal derivatives owes a lot to the works of Ram C. Mehrotra[9] and Nataliya Turova.[10] Structural and physical chemistry of alkoxides made huge progress in the 1990s, facilitated by the principally improved availability and performance of X-ray single-crystal studies[11,12] and nuclear magnetic resonance.[13,14] The modern concepts concerning principles in the structure and reactivity of transition-metal alkoxides are, however, even more recent, dating from the beginning of the twenty-first century.[15,16]

Different aspects in the chemistry of metal and, specifically, transition-metal alkoxides have been presented in a number of contemporary review articles focusing in particular on oxo-alkoxides,[17] derivatives of branched alcohols,[18] nucleation and growth mechanisms in sol–gel,[19] and nonhydrolytic solution transformations.[20] Truly complete overviews of the work done before 2000 can be found in the latest books on the topic.[9,10]

2.16.2 Synthetic Approaches to Metal Alkoxides

When planning synthetic procedures for the preparation of representatives of this class of compounds, it is necessary to bear in mind that appropriate measures have to be taken to ensure application of anhydrous solvents, which today are normally available commercially, and of dry and mostly oxygen-free atmosphere, if not the opposite, is directly required by the reaction conditions. To provide the proper atmosphere, the synthesis is carried out using dry nitrogen (or even argon) in a dry box or using a Schlenk line (parallel vacuum–inert gas installation). In extreme cases when low-valent derivatives have to be obtained, the use of solvents freshly distilled from drying agents – aluminum or alkaline-earth metal alkoxides for alcohols and lithium–aluminum hydride, $LiAlH_4$, for hydrocarbons – may be preferable. Heavy (butanol, pentanols) and functional (amino- and alkoxy-) alcohols as well as carboxylic acids or β-diketo compounds for chemical modification have to be stored over dried molecular sieves to protect them from the uptake of moisture.

2.16.2.1 Interaction of Metals with Alcohols

Dissolution in alcohols as acids with the evolution of hydrogen gas is characteristic of only the most electropositive metals, such as alkaline metals and strontium or barium:

$$M + n\mathrm{ROH} \longrightarrow M(\mathrm{OR})_n + \frac{n}{2}H_2(g) \qquad [1]$$

The reaction is facile in the most acidic alcohols, such as MeOH, EtOH, and ^{i}PrOH, and some functional ones, for example, 2-methoxyethanol. Even for the efficient dissolution of calcium, magnesium, and aluminum, one has to apply catalysts such as iodine to initiate this reaction. The role of iodine consists partly in increasing the acidity of alcohols through the formation of solvate complexes but primarily in cleaning the metal surfaces. For the activation of barium metal, the bubbling of ammonia gas also has been applied successfully.[21,22] It is important to note that the traces of water in alcohols lead to the formation of protective oxide layers on the surface of metal pieces and efficiently quench the reaction, which means that truly dry alcohols are required for the successful implementation of this approach. To accomplish the reaction, one normally has to carry it out on reflux. Often, solvents with higher boiling points, such as toluene, are added in quantities of 50 vol% or more to both increase the reaction temperature and improve the solubility of the produced alkoxides. Among the transition metals, only rare earth (RE) metals can be dissolved directly in alcohols (^{i}PrOH or functional ones in this case because solubility of the product and self-cleaning of the metal surface are prerequisites for completion of the reaction). Initiation of the reaction for RE metals is normally achieved by the addition of a small amount of mercury chloride ($HgCl_2$), producing a surface amalgam layer and preventing the formation of oxides that in this case hinder dissolution. In the view of the hazardous nature of this additive, the application of this approach is strictly limited for RE metals to laboratory conditions, while industrial synthesis of their derivatives is carried out using halide metathesis (see Section 2.16.2.4). It is interesting that the reaction is facilitated for RE metals by the presence of (nonreducible) alkoxides of other elements, forming stable and soluble bimetallic complexes,[23] for example,

$$\mathrm{La(chips)} + \mathrm{exc.}^i\mathrm{PrOH/toluene} + \mathrm{Al(O^iPr)_3} \longrightarrow \tfrac{1}{2}\mathrm{La_2Al_2(O^iPr)_{12}(^iPrOH)_2} \qquad [2]$$

Harsh reflux conditions often facilitate partial decomposition of the initially formed species (often, solvates with alcohols in this case,[24,25] with at least partial transformation into oxo-alkoxides), such as $Ln_5O(OPr^i)_{13}$, for the RE elements.[26]

The application of solvothermal conditions for reaction with higher boiling point and functional alcohols, in particular, aminoalcohols, has recently been shown to open the possibility to apply direct dissolution, even for the synthesis of derivatives of heavy main-group metals, for example, tin[27]:

$$\mathrm{Sn(powder)} + 2\mathrm{ROH} \longrightarrow \mathrm{Sn(OR)_2} + H_2; \quad \mathrm{R} = \mathrm{Bu}^n,\ \mathrm{Me_2NC_2H_4OH} \qquad [3]$$

An alternative pathway for the interaction with alcohols is offered via oxidation by atmospheric oxygen. The byproduct of this reaction is not hydrogen, but water, and the resulting species have to be hydrolysis-stable under reaction conditions or form easily separable oxo- or hydroxo-derivatives[28,29]:

$$\mathrm{Cu} + \mathrm{exc.ROH} + \tfrac{1}{2}O_2 \longrightarrow \mathrm{Cu(OR)_2} + H_2O \qquad [4]$$

$$2\mathrm{Tl} + \mathrm{EtOH} + \tfrac{1}{2}O_2 \longrightarrow \mathrm{TlOEt} + \mathrm{TlOH} \qquad [5]$$

2.16.2.2 Anodic Oxidation of Metals

The electrochemical processes in alcohol media are considerably different from those in water, because, on the one hand,

the produced alkoxide species often are not electrochemically active, and, also, because the dissolution processes are not always exclusively of electrochemical nature. The modern view on the involved pathways permits to identify three principal types of reactions typical for different families of metal elements:

1. The chemically most active metals, such as RE ones, require just initiation of the reaction, which is provided by applying an anodic potential. The yields very often exceed 100%, indicating a high extent of parallel chemical dissolution. The major implication in carrying out the reaction in this case is that poorly conductive low-polarity alcohols, i-propanol in particular, are used, because they offer soluble RE complexes. This requires the use of high potential (normally over 30 V) and of relatively high concentrations of conductive additives, LiCl or LiBr, and results in contamination of the product with halides. Multiple recrystallization steps in hydrocarbon solvents are then required in order to remove these impurities.
2. The reaction pathways for the least chemically active late-transition metals are, to a considerable extent, analogous to those in aqueous media. The metal is transformed into solution in most often a RedOx-active form (see below), which offers the possibility to apply relatively low anodic potentials (below 3 V) close to the equilibrium values. The formation of most often insoluble alkoxides occurs via the interaction of halide complexes formed at the anode, with alkoxide ions generated at the cathode (see Lehmkuhl and Eisenbach[30]):

$$\text{Cathode}: \mathrm{ROH} + \mathrm{e} \rightarrow \mathrm{RO^-} + \tfrac{1}{2}\mathrm{H_2(g)} \quad [6]$$

$$\text{Anode}: \mathrm{Cu(s)} + 4\mathrm{Cl^-} - 2\mathrm{e} \rightarrow \mathrm{CuCl_4^{2-}} \quad [7]$$

$$\text{Solution}: \mathrm{CuCl_4^{2-}} + 2\mathrm{RO^-} \rightarrow \mathrm{Cu(OR)_2} + 4\mathrm{Cl^-} \quad [8]$$

The yields of the processes are often challenged by cathodic reduction of the solution species to pure metals again, and the approach is, thus, efficient in principle only for the synthesis of insoluble products. The latter are, to a considerable extent, contaminated with halides and require repeated washing with alcohols or other polar solvents to produce a good purity product.[31] The application of amines, providing insoluble and highly stable metal complexes (dipiridyl, phenanthroline), has been reported to be helpful in the electrochemical synthesis of alkoxides free from halide impurities.[32]

3. The most complex chemistry is observed on the anodic dissolution of early-transition metals. The dissolution itself occurs at the anode in one step:

$$\mathrm{M} + n\mathrm{RO^-} - n\mathrm{e} \rightarrow \mathrm{M(OR)}_n \quad [9]$$

The required anodic potentials are normally truly high (30–100 V), being due to the energy loss associated with the destruction of the surface oxide layer. This results in parallel partial oxidation of halide anions at the anode with the formation of active halide radicals and, as a result, on the one hand, halogenation and oxidation of the solvent, producing oxo-alkoxides as byproducts, and, on the other hand, generation of lithium alkoxide that can lead to the formation of bimetallic complexes involving lithium atoms.[33,34] For obtaining pure products, further purification steps, including either distillation (in vacuum) or recrystallization, are prerequisite. The attempts to develop anodic oxidation techniques on the industrial scale made in the middle of the 1980s have clearly failed, but they can be successfully used in laboratory practice for the preparation of Nb(OMe)$_5$[35] and Ta(OMe)$_5$,[36] molybdenum methoxides (mostly MoO(OMe)$_4$ with minor admixture of Mo(OMe)$_6$),[37,38] tungsten methoxides (mostly WO(OMe)$_4$),[38] and, especially, otherwise hardly accessible rhenium alkoxides, $\mathrm{Re_4O_2(OMe)_{16}}$,[39] $\mathrm{Re_4O_4(OEt)_{12}}$,[40] and $\mathrm{Re_4O_6(O^iPr)_{10}}$.[41]

2.16.2.3 Alcoholysis of Metal Hydrides, Metal Alkyls, and Metal Alkylamides

The alcohols, as acids, are able to replace the residues of extremely weak and, what is also very important, volatile acids, producing metal alkoxides as products. The reaction formula can be summarized as

$$\mathrm{MX}_n + n\mathrm{ROH} \longrightarrow \mathrm{M(OR)}_n + n\mathrm{HX}$$
$$\mathrm{X} = \mathrm{H, Alk, C} \equiv \mathrm{C, } \equiv \mathrm{N, NH_2, NR_2, N(SiR_3)_2, SH} \quad [10]$$

An important advantage of this approach lies in the possibility to apply stoichiometric amounts of alcohols, producing non-solvated alkoxides (not containing additional coordinated alcohol). The reaction is commonly carried out under very mild conditions, ensuring purity of the products from oxo-alkoxide admixtures common for other techniques of synthesis. The initial reagents, MX_n, are for transition metals mostly not available commercially, which limits this approach to laboratory practice. It has been successfully applied for obtaining Cr(OR)$_2$,[42] V(O^{t}Bu)$_4$,[43] and a broad variety of CuOR[44] from metal alkyls. Alcoholysis of metal alkyls is a standard approach in the synthesis of mixed-ligand alkyl alkoxide derivatives of zinc. Even bimetallic complexes, where all alkyl ligands are removed from an electropositive (alkaline at the other metal or alkaline-earth) metal center and only one of the two alkyls is replaced by alkoxide ligand, have been isolated[45]:

$$6\mathrm{Me_2Zn} + 2\mathrm{Me_2Mg} + 8\mathrm{ROH} \longrightarrow \mathrm{Mg_2Zn_6(OR)_8Me_6} + 8\mathrm{CH_4}$$
$$\mathrm{R} = \mathrm{Et}, n\mathrm{Pr}, n\mathrm{Bu} \quad [11]$$

The synthesis of both early-transition and heavy main-group alkoxide derivatives can be successfully carried out on the laboratory scale using metal bis-dialkyl-silylamides as reactants. The latter can be easily produced by reactions of metal chlorides with lithium amide in ether and then purified either by distillation used for heavy main-group metal complexes or by hydrocarbon extraction from LiCl byproduct for the early-transition metal complexes.[46–53]

$$\mathrm{MCl}_n + n\mathrm{LiN(SiR_3)_2} \longrightarrow \mathrm{M[N(SiR_3)_2]}_n + n\mathrm{LiCl} \quad [12]$$

$$\mathrm{M[N(SiR_3)_2]}_n + n\mathrm{R'OH} \longrightarrow \mathrm{M(OR)}_n + n\mathrm{HN(SiR_3)_2}$$
$$\mathrm{M} = \mathrm{Zn, Cd, Pb, Bi, In, Cr(II), Mn(II), Mo(III), and Mo(II)} \quad [13]$$

It has to be noted that the amide and silylamide derivates of late-transition metals are rather unstable, which, in practice, precludes application of this techniques for the preparation of alkoxides of Co, Ni, and Cu.[54]

2.16.2.4 Metathesis of Metal Halides

The interaction of metal halides with alcohols does not, in the majority of cases, lead to the formation of even partially substituted alkoxo complexes. Its products are usually alcohol solvates of halides or oxo-halides.[9,10,55]

Removal of the halide ligand is possible only in the form of a salt poorly soluble in the applied organic medium. Therefore, metathesis of metal halides with alkali alkoxides or with alcohols in the presence of ammonia or amine bases is the major route to metal alkoxides both in the laboratory and on the industrial scale:

$$MX_n + n\mathrm{ROH} + n\mathrm{R_3N} \longrightarrow \mathrm{M(OR)}n + n\mathrm{R_3NHX}$$
$$MX_n + n\mathrm{M^IOR} \longrightarrow \mathrm{M(OR)}_n + n\mathrm{M^IX},\ \mathrm{M^I} = \mathrm{Li, Na, K};\ \mathrm{X} = \mathrm{Cl, Br} \quad [14]$$

Easy formation of oxo species can result in drastically decreased yields of the target alkoxides or, when the tertiary[9,10] or aromatic[56] alcohols are used, can lead (often in not completely anhydrous conditions) even to the formation of oxides or hydrated oxides. To circumvent this difficulty, a number of different approaches have been elaborated, being aimed either at decreasing the Lewis acidity of the halide reactant or at avoiding its contact with alcohols. The first of these two approaches has been developed by Bradley, who proposed to use anionic halide complexes, such as $(PyH)_2ZrCl_6$,[57] instead of the metal chlorides. The approach turned out to be quite efficient and lies behind the processes industrially applied at present for the production of Zr and Hf alkoxides. It has to be mentioned, however, that these products, being essentially halide-free, contain quite high content of oxo-alkoxide byproducts. For example, $Zr(O^nPr)_4$ samples delivered in solution in parent alcohol consist of up to 10% of $Zr_4O(O^nPr)_{14}(^n\mathrm{PrOH})_2$.[58]

Another alternative in improving the efficiency of the metathesis pathway lies in the introduction of an alcohol-free solution of metal halide in an inert (hydrocarbon as hexanes or toluene) or donor solvent (eth., THF). Even in this case, there can be a risk of contamination. Thus, the application of alkali alkoxides may lead to stable bimetallic byproducts such as, for example, $NaZr_2(OR)_9$, that even distills in vacuum without decomposition.[59] When there is no stable bimetallic byproduct formed, the reaction stoichiometry may not be optimal for the formation of the expected alkoxide. Very often, the only stable and easily isolable product is not a homoleptic alkoxide, but an oxo-alkoxide or alkoxide halide. For example, $Y_3(O^tBu)_8Cl{\cdot}2THF$ or $Nd_6(O^iPr)_{17}Cl$ have been isolated as the major products in the reaction of the corresponding trichlorides with three equivalents of NaOR.[60,61] In many cases, larger halide ligands (Br or I instead of Cl) or larger alkaline metal atoms (K instead of Na or Li) can help to avoid the side reactions of this kind[62,63]:

$$\mathrm{FeCl_3} + 3\mathrm{NaOEt} - \mathrm{toluene/ethanol} \longrightarrow \mathrm{Fe_5O(OEt)_{13}} + \mathrm{Fe_5O(OEt)_{12}Cl} + \mathrm{Fe_5O(OEt)_{11}Cl_2} \quad [15]$$

$$\mathrm{FeBr_3} + 3\mathrm{NaOEt} - \mathrm{toluene/ethanol} \longrightarrow \mathrm{Fe_5O(OEt)_{13}\ (practically\ pure)} \quad [16]$$

$$5\mathrm{LnCl_3} + 15\mathrm{KO^iPr} + \mathrm{H_2O} \longrightarrow \mathrm{Ln_5O(O^iPr)_{13}} + 2\mathrm{^iPrOH} \quad [17]$$

2.16.2.5 Alkoxylation of Metal Salts

Metal salts other than halides can, in some cases, be used in the metathesis with alkali alkoxides. This approach has been proved to be successful for the preparation of heavy main-group metal derivatives, in particular, of alkoxides of Zn and Pb (see Papiernik et al.[48] and Turevskaya et al.[64]) using metal acetates as reagents. The reaction produces insoluble sodium acetate, which is removed on its completion by filtration or decantation. It has to be mentioned that, when carried out in toluene (on reflux), it can very easily produce oxo-alkoxide derivatives via ester or ether elimination side reactions.

Application of the nitrate complexes has been proposed in the metathesis-based approaches to the derivatives of Ce(IV) in the view of their much higher stability and commercial availability.[65] The synthesis of silver alkoxides has been achieved via the application of a less usual reactant, tetrafluoridoborate[66]:

$$\mathrm{MOR} + \mathrm{AgBF_4} - \mathrm{CH_2Cl_2} \longrightarrow \mathrm{AgOR} + \mathrm{MBF_4}$$
$$\mathrm{M} = \mathrm{Li\ or\ Na};\quad \mathrm{R} = \mathrm{C(CF_3)_3\ or\ SiPr^i_3} \quad [18]$$

It is necessary to mention that, during the development of metathetic approaches, a number of alkoxylating agents other than the alkali alkoxides have been tested for this purpose. For example, gas-phase co-condensation of volatile metal fluorides or chlorides with alkylsiliconalkoxides has been reported for the preparation of $M(OMe)_6$, M = Mo, W,[67] and Re.[68] This technique requires special equipment and provides rather small quantities of the products that can be obtained much more easily by anodic oxidation of corresponding metals. Another example of a different alkoxylating agent is the soluble $Mg(OMe)_2$, which has been used to produce methoxides from corresponding metal fluorides.[68] Even in this latter case, the stoichiometry can be tricky, as the byproducts encounter not only the insoluble MgF_2, but even a number of soluble magnesium alkoxide fluoride intermediates, such as, for example, $Mg_6F_2(OMe)_{10}(MeOH)_{14}$.[69]

2.16.2.6 Alcohol Interchange Reactions

The alkoxide ligands within a complex can, in many cases, be replaced by the introduction of an excess of a different alcohol. The equilibrium is shifted toward a new derivative if the introduced alcohol has a considerably higher boiling point than the one released, for example[70]:

$$\mathrm{MoO(OMe)_4} + \mathrm{excess\ ^iPrOH} \longrightarrow \mathrm{MoO(O^iPr)_4} + 4\mathrm{MeOH} \quad [19]$$

An alternative can be the formation of a derivative that is much less soluble in a new solvent[71]:

$$\mathrm{Zr(O^nPr)_4} + \mathrm{excess\ ^iPrOH} \longrightarrow \mathrm{Zr(O^nPr)(O^iPr)_3(^iPrOH)} \quad [20]$$

The same effect is achieved, of course, when the introduced alcohol displays much higher acidity or provides considerably higher complex stability via chelation[72]:

$$\mathrm{Ce(O^iPr)_4(^iPrOH)} + 4\mathrm{(CF_3)_2CHOH} - \mathrm{THF} \longrightarrow \mathrm{Ce(OCH(CF_3)_2)_4(THF)_2} \quad [21]$$

$$\mathrm{MoO_2(OC_2H_4OMe)_2} + \mathrm{excess\ EtOH} \longrightarrow \mathrm{recrystallization\ without\ substitution} \quad [22]$$

It has to be noted that the alcohol interchange is a stepwise process and, quite often, results in stable mixed-ligand alkoxide complexes, which are very difficult or completely impossible to convert further into a homoleptic derivative.

$$M(OR)_n + R'OH \rightleftharpoons M(OR)_{n-1}\left(OR'\right) + ROH \quad [23]$$

Thus, methoxides of niobium(V) and tantalum(V), on reaction with ethanol or iso-propanol, undergo the replacement of only 4 of 5 methoxide ligands, and conserve the fifth one independently of the excess of the new alcohol or repeated refluxing and evacuation procedures[8,71,73]:

$$M(OMe)_5 + \text{excess}\ {}^{i}PrOH \rightarrow M(OMe)(O^{i}Pr)_4 + 4MeOH \quad M = Nb, Ta \quad [24]$$

Even if alcohol interchange is carried out under relatively mild conditions, it can deliver oxo-alkoxides as products when only those that are more stable and/or crystallize more easily for a particular derivative; see, for example, Kusserow and Spandl[74]:

$$Fe_2(O^{t}Bu)_6 + \text{excess}\ {}^{i}PrOH \rightarrow Fe_5O(O^{i}Pr)_{13} \quad [25]$$

2.16.2.7 Self-Assembly Synthesis of Heteroleptic and Heterometallic Alkoxides

The predominantly electrostatic character of bonding in the metal alkoxide complexes opens perspectives for the facile preparation of complex derivatives, including both different ligands (heteroleptic) and different metal centers (heterometallic).

Thus, the addition of acids stronger than alcohols results, in the majority of cases, in immediate replacement of alkoxide groups by new anionic residues. The reaction can, in general, be written as follows:

$$M(OR)_n + mHZ \longrightarrow M(OR)_{n-m}Z_m + mROH \quad [26]$$

where HZ represents aminoalcohols or other functional alcohols, β-diketones, or carboxylic acids. These reactions have been rather thoroughly investigated for the derivatives of M(IV), such as titanium, zirconium, and hafnium, and are described in a number of detailed studies.[58,75,76] It is important to bear in mind that the structure and compositions of the produced species are governed by their relative thermodynamic stability and, thus, not all of the substitution intermediates are stable or even isolable. For, example, on the addition of symmetric β-diketones to zirconium or hafnium alkoxides, it is possible to obtain mono-, $Zr(OR)_3(\beta\text{-dik})$, tris-, $Zr(OR)(\beta\text{-dik})_3$, and tetrakis-β-diketonates, $Zr(\beta\text{-dik})_4$,[76] but no bis-substituted complexes are produced. The bis-substituted species $Zr(OR)_2L_2$ can, however, be isolated with β-ketoesterates,[77] stabilized supposedly by trans-effects in ligand packing.

Another important feature influencing the formation of heteroleptic alkoxide complexes is provided by the extreme basicity of the alkoxide ligand. Metal alkoxides are strong Brønsted bases in the alcohol media containing RO^- ligands, which are corresponding bases to the parent alcohol in their composition. They are strong Lewis bases as well. As a consequence, metal alkoxides form stable complexes only with neutral ligands that display not only electron-donor properties, but also appreciable Lewis acidity, for example, alcohols or mono- or dialkylamines. Trialkylamines, R_3N, do not form isolable complexes with alkoxides.[78,79]

The thermodynamic driving forces are governing even the formation of heterometallic alkoxide complexes. If a desired heteronuclear species is stable and the homometallic reactants are soluble, the simple mixing of reactants in an organic solvent will produce a heterometallic complex, for example,[35,80]

$$LiOR + Nb(OR)_5 \longrightarrow LiNb(OR)_6 \quad [27]$$

$$'La(OR)_3' + 2Nb(OR)_5 \longrightarrow LaNb_2(OR)_{13} \quad [28]$$

If at least one of the starting reagents is insoluble and poorly reactive, the synthetic strategy is put forward to avoid its formation and produce the desired heterometallic complex from another salt, removing its anion in the form of either an insoluble salt of other metal or a highly stable complex with another central atom, for example,[81,82]

$$NiCl_2 + 2NaAl(O^{t}Bu)_4 \longrightarrow NiAl_2(O^{t}Bu)_8 + 2NaCl(s) \quad [29]$$

$$Ni(acac)_2 + 4Nb(O^{i}Pr)_5 \longrightarrow NiNb_2(O^{i}Pr)_{12} + 2Nb(O^{i}Pr)_4(acac) \quad [30]$$

Even when the composition of the desired product is quite complex, it can most often be obtained with practically quantitative yields by providing the necessary metal centers and anions in a proper ratio[83,84]:

$$4CoCl_2 + 2Ta(OMe)_5 + 2NaOMe - CH_3CN \longrightarrow [Co_2Ta_2(OMe)_{12}(MeCN)_4]^{2+}\ [CoCl_3(MeCN)]_2^- + 2NaCl(s) \quad [31]$$

$$M^{II}(acac)_2 + 2Al(O^{i}Pr)_3 \longrightarrow \cdots + Hacac + HOAc \rightarrow M^{II}Al_2(acac)_3(O^{i}Pr)_4(OAc) + 2{}^{i}PrOH \quad M^{II} = Mn, Co, Zn \quad [32]$$

More details on the reaction mechanisms and conditions of such transformation can be found in Section 2.16.4.

2.16.3 Molecular and Crystal Structures of Metal Alkoxides

The predominantly electrostatic bonding in the structures of metal alkoxides leads to the formation of 'molecular' aggregates following common principles of dense packing for both metal cations and donor ligands. The structures can be rationalized as combinations of stable coordination polyhedra with geometry defined by the size relations between the cations and the ligands.[15] This means, in turn, that the alkoxide species display a strong trend to aggregation to complement the coordination of the metal centers and are found, at least in the solid state, most often as oligonuclear structures, sometimes erroneously described as 'clusters,' while they, with a few exceptions, do not contain any metal–metal bonds.[85]

2.16.3.1 Mononuclear Alkoxides

An alkoxide complex can remain non-aggregated only if the number of donor atoms in the ligands surrounding the metal

center is directly satisfying the requirements of dense packing and fit into a stable polyhedral geometry. This is possible for either hexa-alkoxides of transition elements, $M(OR)_6$, M = Mo, W, Re,[38] or when functional alkoxide ligands with several donor atoms are applied, like in $M^V(O_2C_2Me_4)_3H$, M^V = Nb, Ta,[86] see Figure 1.

In spite of the simple appearance of their molecules, the crystal structure of monometallic alkoxide complexes can be extremely difficult to determine using single-crystal X-ray diffraction. The reason for this lies in the highly symmetric topology of these objects that is close to spherical and results usually in highly symmetric packing, most often dense cubic packing (see Figure 2) associated with a high degree of disorder. Each molecule can have different orientations for its ligands to occupy the same space in the crystal structure.

2.16.3.2 Dinuclear Alkoxides

Metal centers in dinuclear aggregates can be connected via either alkoxide or oxide ligands. The alkoxide ligand bears an alkyl group, which results in an angle at the oxygen atom in the M–O(R)–M fragment being normally of about 110° or

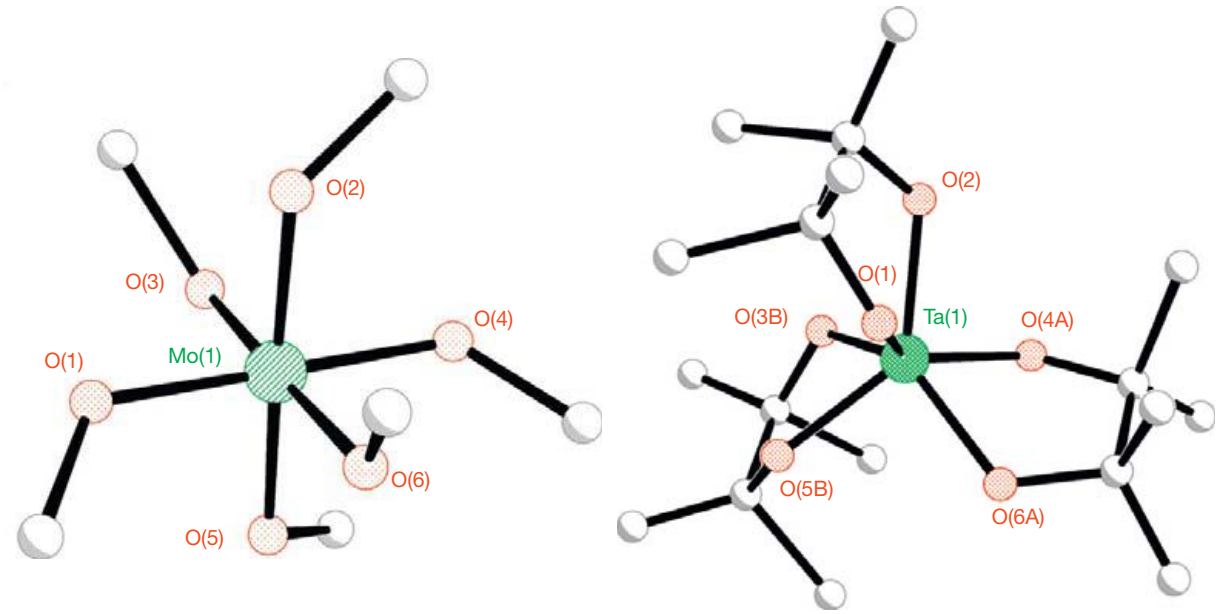

Figure 1 Molecular structures of mononuclear alkoxide complexes, $M(OMe)_6$, M = Mo, W, as described in Seisenbaeva et al.,[38] and $Ta(O_2C_2Me_4)_3H$, as described in Donat et al.[86]

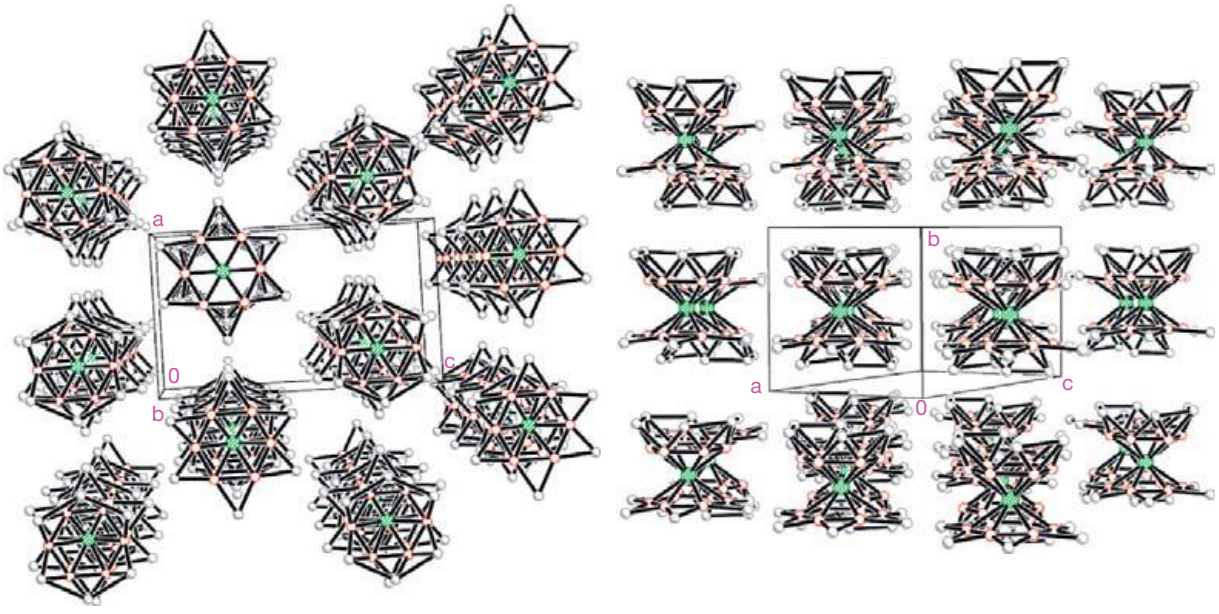

Figure 2 Cubic dense packing of the $M(OMe)_6$, M = Mo, W disordered molecules: hexagonal layers in the *ac* plane and vertical columns along the *b*-axis, as described in Seisenbaeva et al.[38]

smaller. This forces metal centers to a relatively short distance of 3.2–3.5 Å and forces at least one more alkoxide ligand to become bridging. This provides coordination geometry corresponding to two edge-sharing polyhedra common for higher oxidation state derivatives. If the metal centers are forced together even closer through the formation of a metal–metal bond, the formation of three alkoxide/oxide bridges can become preferential, with face-sharing octahedral geometry as a result (Figure 3).

Dinuclear species with a single oxo-bridge are extremely rare, because small oxide anions coordinate usually several, three or more, metal centers. The M–O–M chain in this exceptional case is practically linear, and the metal centers are normally protected by chelating functional ligands (Figure 4).

2.16.3.3 Trinuclear Alkoxides

Three metal centers can either form, with ligand donor atoms, a fragment of close hexagonal packing, where three octahedra share edges and a common vertex, or, in the case of bulky ligands, arrange into a chain of edge- or face-sharing polyhedra (see Figure 5). Tri-dentate ligand in the close packing motif is often an oxo-ligand. Triangular, closely packed fragments are common units in bigger aggregates. It is also rather common that the molecules of trinuclear alkoxide complexes involve other ligands than alkoxide ones (see Section 2.16.3.4).

2.16.3.4 Tetranuclear Alkoxides

Four metal centers provide already the possibility for, at least formally, a considerable variety of molecular structures. In the background, there is the presence, of course, of the same trend as in the structures of trinuclear complexes: smaller ligands lead to densely packed arrangements, while bigger ones result in the connection of coordination polyhedra into open or closed (ring-shaped) chains, with the connection of polyhedral units predominantly via sharing an edge. The five most common structural motifs for the tetranuclear species are (1) a planar fragment of dense hexagonal packing, so called M_4X_{16}

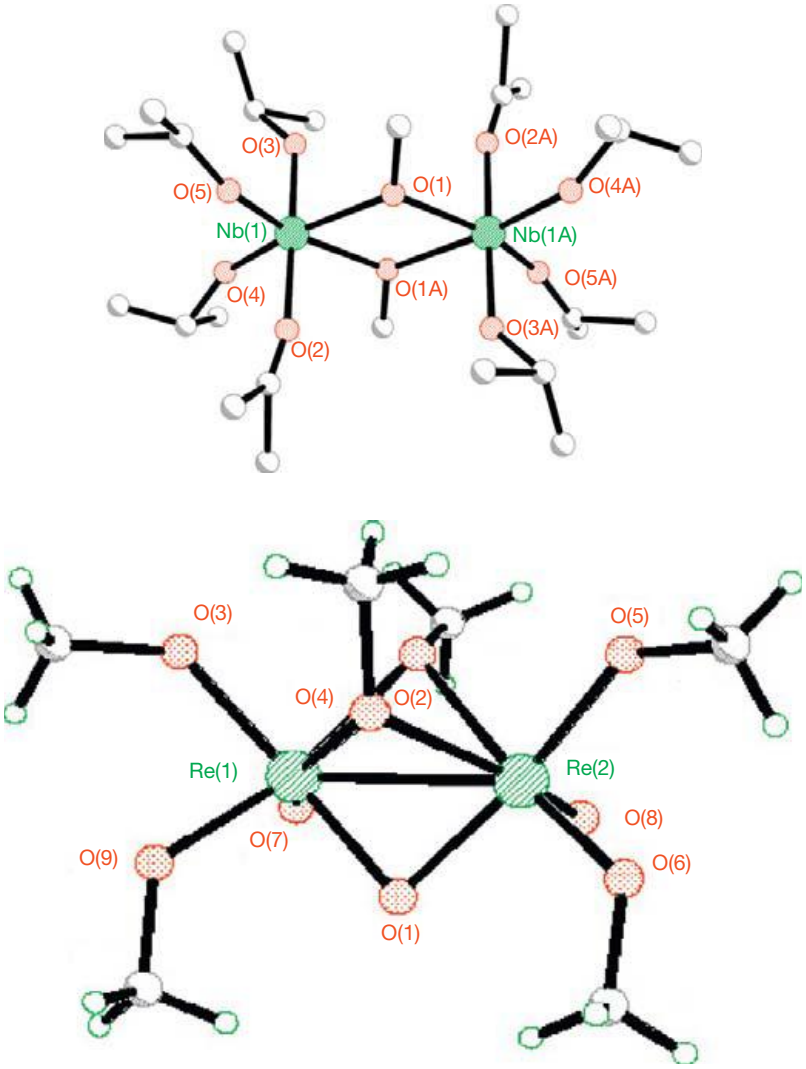

Figure 3 Examples of dinuclear alkoxide complexes, $[Nb(\mu\text{-}OMe)(O^iPr)_4]_2$, as described in Nunes et al.,[73] and $Re_2O_3(OMe)_6$, as reported in Seisenbaeva et al.[39]

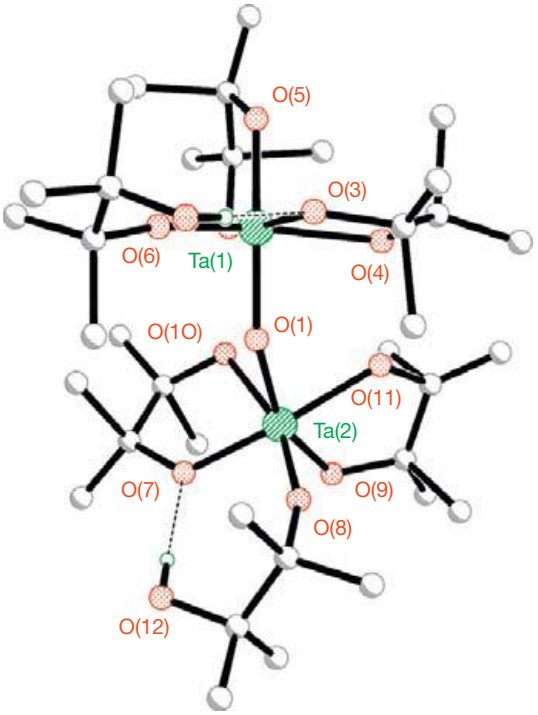

Figure 4 Molecular structure of $Ta_2O(O_2C_2Me_4)_6H_4$.[86]

or tetramolybdate type, which can, otherwise, be considered as two densely packed triangular units fused via a shared M–M side (sometimes erroneously referred to as 'defective double-cubane'); (2) a fragment of two-layer packing, often described as M_4O_4 cubane-like core, which can, otherwise, be considered as an M_4-tetrahedron capped by μ_3-ligands on each face; (3) a volume-centered M_4-fragment, most regularly a M_4O tetrahedron; (4) a combination of an octahedron, sharing edges with three tetrahedra, similar to the Mitsubishi logo; and (5) linear or ring-shaped chain of edge-sharing octahedra.

The M_4X_{16} type is, by far, the most common for both homo- and heterometallic species. The majority of heterometallic species with a 1:1 ratio between two metal atoms belong actually to this structure type. It is also very usual for mixed-ligand derivatives, alkoxide halides, late-transition 3d metal β-diketonates, functional alkoxides, etc., wherever the small size of ligands (primary alcohol derivatives are the typical case) facilitates dense packing.

For homometallic complexes, the arrangement of packing in a two-layer fragment is often practically as energetically advantageous as the formation of a planar single-layer packing (the M_4X_{16} type). Small changes in the size or ligand composition (in heteroleptic complexes) can result in a different structure type for the crystallizing compound (see Figure 6).

The volume-centered M_4-core has been mostly described for oxo-substituted alkoxide β-diketonate species, but it is present as a fragment in the structures of many both homo- and heteroleptic oxo-alkoxides. The realization of a type with a bigger central polyhedron and three smaller ones attached to it requires quite a large size for this central unit. It has been discovered in a limited number of compounds, with the first representative being $Al_4(O^iPr)_{12}$[90] and its analogs with an RE cation in the center.[91] The only representative of a structure with bigger peripheral units based on Nb-octahedra instead of Al-tetrahedra is $La(tea)_2\{Nb(O^iPr)_4\}_3$.[92]

Numerous representatives of linear M_4 chains have been described for heterometallic heteroleptic alkoxide species (Figure 7).

2.16.3.5 Oligonuclear Structures

The formation of bigger aggregates than tetranuclear complexes is, in fact, not unusual in the chemistry of metal alkoxides. They can be formed in coordination equilibria with non-oxo-alkoxides, but are especially typical for the oxo species, originating from hydrolysis or thermolysis (see Seisenbaeva et al.[85] or Eslava et al.[93] for recent examples).

The construction principle for non-oxo species is often the formation of ring-shaped structures with polyhedra connected via shared edges. Examples of such rings can be found in homoleptic species, such as $[Bi(OEt)_3]_8(EtOH)_{7+x}$,[94] homoleptic functional alkoxides, such as $M_{10}(OC_2H_4OMe)_{30}$, M = Y,[95] Dy,[96] and heteroleptic species $Fe_{10}(OEt)_{20}(OCOCH_2Cl)_{10}$[97] (Figure 8).

An alternative construction principle for larger aggregates is the formation of densely packed cores that have geometry often very close or identical to polyoxometallate structures formed in aqueous media, such as well-recognized Lindqvist, Anderson, and Keggin types (M.T. Pope). With functional alkoxide derivatives, even very large fragments of dense hexagonal packed layered structures have been reported, such as $Ca_9(OC_2H_4OMe)_{18}(HOC_2H_4OMe)_2$[98] and $Cd_9(OC_2H_4OMe)_{18}(HOC_2H_4OMe)_2$[47] (Figure 9).

2.16.4 Chemical Reactivity of Metal Alkoxides

The most fascinating feature of metal-alkoxide complexes is their truly high reactivity in a plethora of chemical processes, making them attractive as molecular precursors of materials and as homogeneous catalysts, but complicating their handling and application. Behind this reactivity lies the high contribution of the electrostatic component in the bonding: metal alkoxides are, in their nature, except possibly for noble-metal derivatives, actually not molecular complexes but close ion pairs. Their excellent solubility in many organic solvents, especially non-polar ones, and, in many cases, volatility in vacuum makes them resemble metal–organic compounds, being due to weak van-der-Waals interactions between the hydrocarbon tails of the alkoxide ligands with solvents and with each other. The chemical behavior of metal alkoxides is, however, very much like that of inorganic salts, being characterized by low activation energies for changes in coordination number and facile transformation in the geometry and even nuclearity of the species. That is, that type of chemical behavior which speaks against the contemporary trend to call all oligonuclear aggregates 'clusters.'[100] In the case of metal alkoxides, the cluster behavior (retention of nuclearity and geometry in chemical reactions) is very distinctly reserved for low-valent derivatives with well-defined metal–metal bonds.[85]

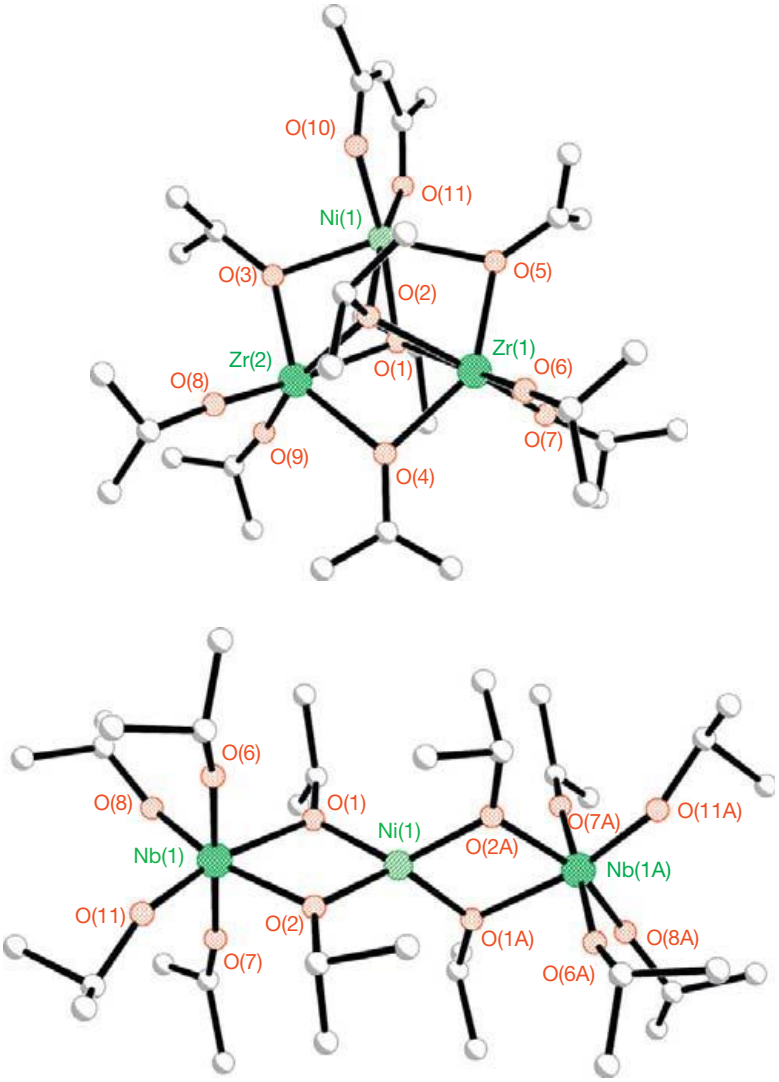

Figure 5 Molecular structures representing two principal motifs for trinuclear alkoxide complexes: dense packing for $NiZr_2(acac)(O^iPr)_9$, according to Seisenbaeva et al.,[87] and chain of edge-sharing polyhedra, as described in $NiNb_2(O^iPr)_{12}$.[82]

2.16.4.1 Ligand Exchange

The reactions of ligand exchange at a metal center or between metal centers have been studied intensively in the late 1980s and the first half of the 1990s. Fundamental contributions to the understanding of factors influencing the ligand-exchange mechanisms have been made by Wengrovius et al.[101] and Errington et al.,[75] who studied the heteroleptic derivatives of aluminum and titanium(IV), respectively. It was found that the activation energies for ligand transfer between the metal centers in hydrocarbon solvents at room temperatures (heteronuclear exchange!) are, for aluminum derivatives, on the order of magnitude of 10–40 kJ mol^{-1}, being relatively facile processes already at room temperature. The ligand exchange between the centers in an oligonuclear zirconium complex has also been studied in detail.[102] For the transfer of β-diketonate ligands between zirconium centers in different molecules in hydrocarbon solvents, the reaction half-time was found to be about 1 h.[58] It was also found that the addition of protolytes and protic solvents results in tremendous acceleration of the ligand exchange. Some species demonstrate, for example, quickly achieved ligand-exchange equilibria in solution[75]:

$$2Ti(O^iPr)_3(acac) \rightleftharpoons Ti(O^iPr)_4 + Ti(O^iPr)_2(acac)_2 \quad [33]$$

The reaction of metal alkoxides with acidic modifying ligands, such as carboxylic acids or β-diketones, results immediately in ligand exchange. There is no need for warming up the solution or waiting for some completion time. It is, however, important to keep the solution properly homogenized on addition of these reagents to ensure the uniformity of transformation. The mechanism of this process is in exploiting the

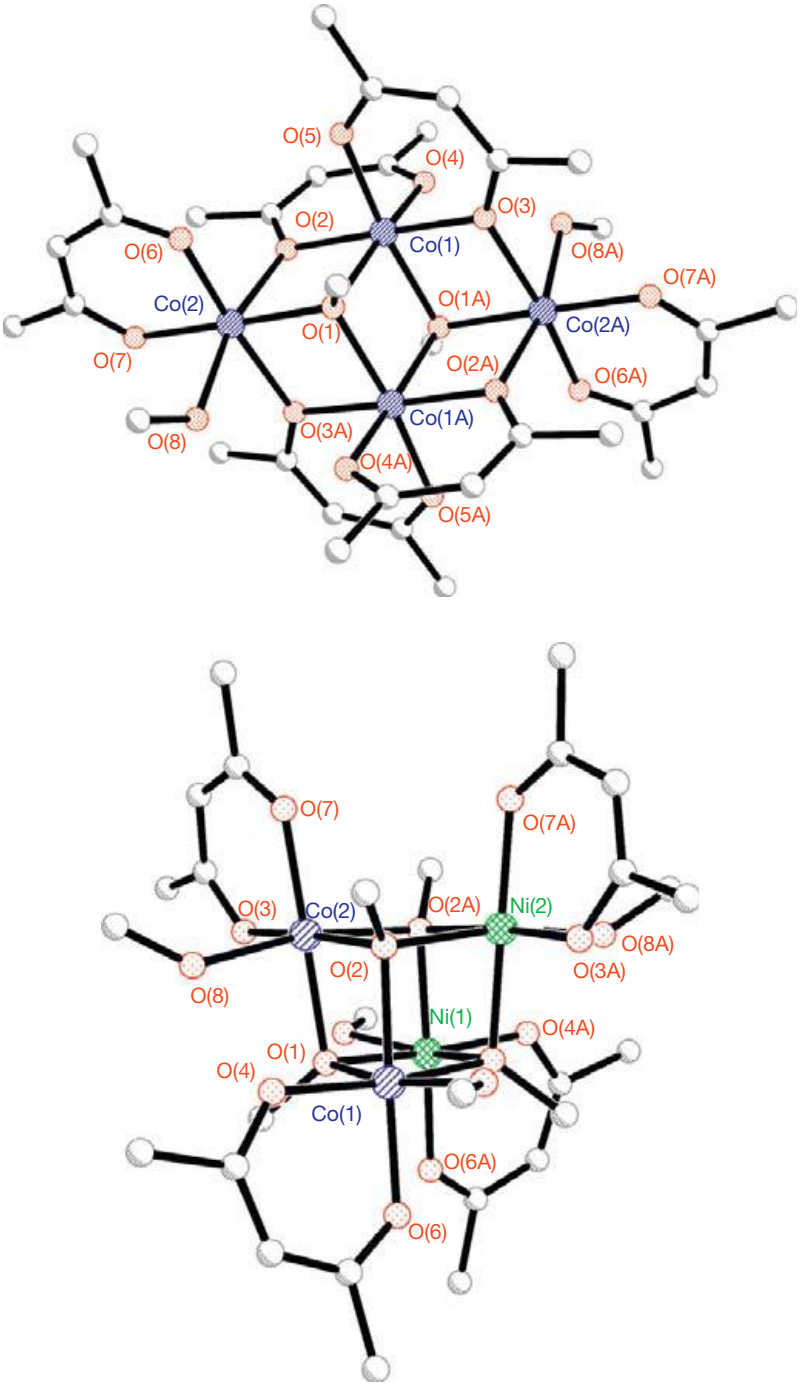

Figure 6 Representatives of cobalt methoxide β-diketonates following the single-layer packing, $Co_4(acac)_6(OMe)_2(MeOH)_2$, as described in Werndrup and Kessler,[88] and $Co_2Ni_2(acac)_4(OMe)_4(MeOH)_4$, according to Kessler et al.[89]

high Brønsted basicity of the alkoxide ligand, starting with protonation of the negatively charged oxygen atom.[103] The generated reactive cationic species then coordinates an additional donor ligand and releases an alcohol molecule (Scheme 1).

It should be noted that the reaction speed is determined, in the first hand, by the acidity of the HZ reactant, while the nucleophilic properties of the entering Z^- ligand have no influence on the ligand-exchange process.[104]

An important note is that, in many techniques applied for the synthesis of materials, the solutions of metal alkoxides in carboxylic acids, for example, $Ti(OPr)_4$ in acetic acid, do, thus, handle, in reality, not alkoxides, but, instead, the corresponding carboxylates of these metals.

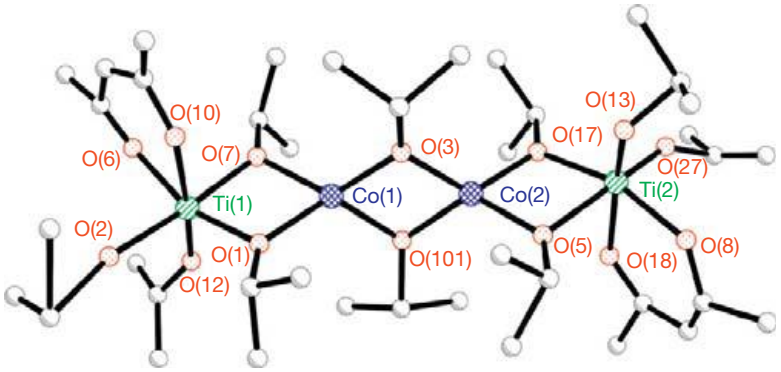

Figure 7 Molecular structure of $Co_2Ti_2(acac)_2(O^iPr)_{10}$, according to Kessler et al.[82]

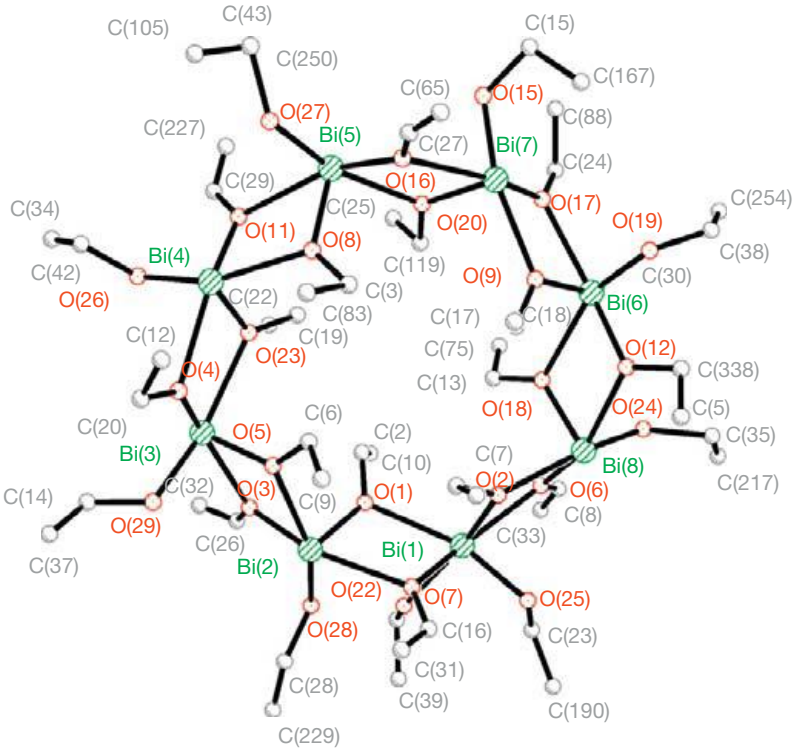

Figure 8 Molecular structure of the bismuth ethoxide, $[Bi(OEt)_3]_8$, according to Kessler et al.[94]

2.16.4.2 Hydrolysis and Condensation: Silicon Versus Metal Alkoxides

The hydrolysis and condensation of silicon alkoxides and metal alkoxides are highly interesting as initial steps in the preparation of, in the first hand, oxide materials in the sol–gel technology, a technique exploiting liquid–solid transformation in colloid systems.

Until recently, the understanding of the sol–gel transformation starting from metal–organic precursors, for example, metal alkoxides and chemically modified metal alkoxides, and even inorganic precursors, was dominated by the hypothesis of a kinetically controlled homogeneous hydrolysis–polycondensation process, which was thought to result in the reaction mechanisms analogous to the growth of true inorganic polymers, such as, for example, siloxanes.[105–107] Using insight into the reactivity of the alkoxides of silicon, which, however, is a non-metal and not a plausible analog, it was supposed that the metal alkoxide 'monomers' hydrolyze, forming, at the first step, hydroxo-alkoxide species like '$Ti(OR)_3(OH)$' or '$Zr(OR)_3(OH)$,' which can then either be hydrolyzed further or undergo condensation with the formation of oxo- (oxolation) or hydroxo (hydroxolation) bridges in independent kinetic regimes.[105] The sol–gel transition was attributed to the molecular percolation through polymeric condensation: it was supposed that the 'polymeric oxo-hydroxo molecules' are growing so big that they come into contact with each other and build up a solid framework. The stabilization of the colloid solutions, obtained from precursors modified with chelating ligands, was explained through a

supposition that the introduction of chelating moieties leads to slowing the hydrolysis and inhibits the condensation reaction.[108] The possibility to form sols and gels of complex oxides was attributed to 'adjusting' the speeds of hydrolysis and condensation between the species of different metals. The use of heterometallic precursors seemed to be the most reasonable tool for the solution of this problem.

The reality for metal alkoxides turned out to be drastically different[16]: while silicon alkoxides reveal low charge distribution and need catalysts to be activated for hydrolysis, the metal alkoxides, due to their extremely high Brønsted basicity, react with water – an acid much stronger than alcohols – immediately. The reactions produce not relatively stable hydroxide intermediates, but already condensed oxo-alkoxide species defined by coordination equilibria. The hydrolysis and condensation are, for metal alkoxides, not separate steps, but components in one and the same kinetic phenomenon. The chelating ligands are, in fact, increasing the reactivity of metal alkoxides toward hydrolysis–condensation. The products of this reaction are metal-oxide nanoparticles with structure related to polyoxometallate species. The role of chelating ligands in the stabilization of resulting colloids consists in reducing the surface energy through interactions of ligands expelled to the surface with the molecules of the solvent.[19]

The size of the primary colloid particles produced in the hydrolysis–condensation process is rather uniform and vary, dependent on the solvent and ligands applied, in a rather narrow interval of 2–5 nm. The gelation occurring through the interaction of these particles produces gels and, then, on removal of the solvent, dry gels xerogels, with closed irregular mesoporosity. Open pores can be produced applying amphiphylic modifying ligands, for example, aminoacids, opening approaches to materials with attractive applications in drug delivery and catalysis.[109]

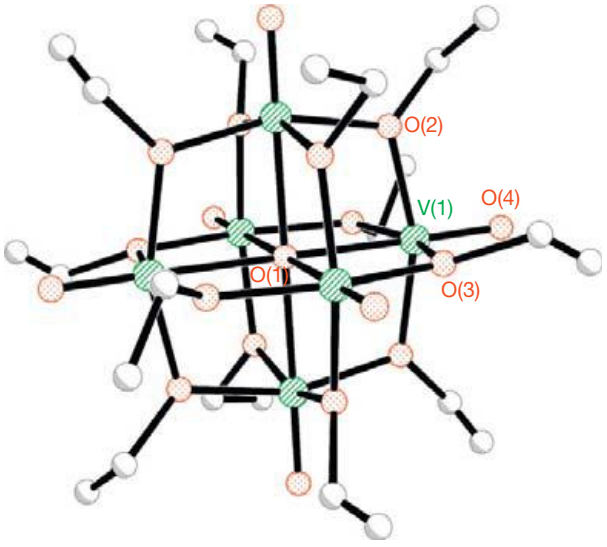

Figure 9 Molecular structure of the $V_6O_7(OEt)_{12}$ alkoxide, a representative of the Lindqvist structure type.[99]

2.16.4.3 Non-Hydrolytic Cleavage in Solution (Bradley Reaction; Guerbet Reaction)

The ether-elimination reaction that has received the name of Bradley, who studied it first in detail in the 1950s, is a spontaneous decomposition process characteristic of, in the first hand, high-valent early-transition elements, such as Mo, W, Re, Nb, and Ta. The reaction mechanism involves, at the first step, a redistribution of electron density, with a heterolytic cleavage of an O—C bond as a result. The liberated alkyl-cation is transferred to a neighboring terminal alkoxide group, forming an ether molecule (**Scheme 2**).

The reaction speed increases in the Figure 9series of homologs $Me < Et \ll {}^{i}Pr \ll {}^{t}Bu \ll C_6H_5CH_2 < CH_2{=}CH{-}CH_2$.[110] It is catalyzed by Brønsted acids (proton donors), neutralizing the negative charge, which appears at the oxygen atom due to heterolytic bond cleavage.[7,8] Molybdenum alkoxides, for example, are transformed into 'molybdenum blues' (reduced and often hydrated molybdenum oxides) on the action of water or organic acids. It is also accelerated by the basic (alkali, alkaline-earth) metal alkoxides, facilitating the departure of the liberated R^+ cation. Thus, the alkoxides of Mo(VI) and W(VI) are converted directly at room temperature into mixed-oxide nanoparticles (inorganic molybdates and tungstates) on the action of alkali or alkaline-earth metal alkoxides in excess.[111] The ether elimination reaction is also strongly accelerated by heating, opening perspectives for the synthesis of a broad variety of metal-oxide nanoparticles by applying this approach.[23,110,112,113] This approach is especially attractive in the preparation of nanoparticles doped with small concentrations of elements capable of providing them with attractive luminescent or magnetic characteristics.[23,110]

The Guerbet reaction, which is broadly used in the synthesis of ramified alcohols for cosmetic applications,[4] consists in the β-condensation of alkoxides in basic medium and is one of a number of β-hydrogen transfer processes typical for the high-temperature reactivity of metal alkoxides in solution. This family of processes includes two kinds of reactions: β-hydride transfer and β-proton transfer. The reaction of β-hydride transfer is typical for strongly electronegative high-valent metals such as V(V),[99,114] Mo(VI),[115] rhenium (detected even in the +III oxidation state[116] and precious metals and also Bi(III) and, probably, Sb(III), Pb(II)). It generates, at the first step, a metal hydride (which is then transformed into low-valent

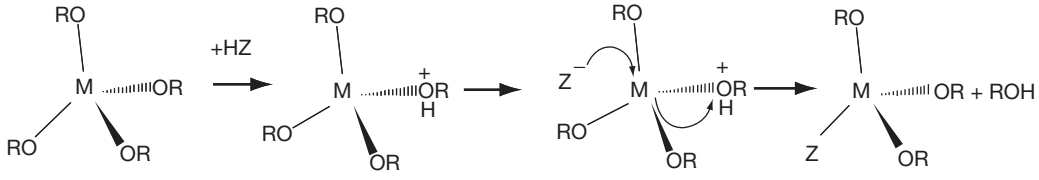

Scheme 1 Ligand exchange reaction mechanism for metal alkoxides.

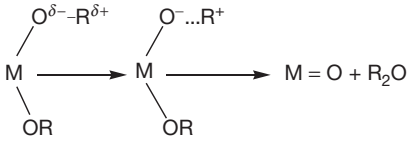

Scheme 2 The mechanism of ether elimination (Bradley) reaction.

(oxo)alkoxide or even elementary metal, offering an attractive approach to dispersions of uniform metal nanoparticles) and a carbonyl compound:

$$(RO)_mM-O-CH(R^1)R^2 \longrightarrow (RO)_mM-H + R^1R^2C=O \quad [34]$$

$$(RO)_mM-H + M(OR)_{m+1} \longrightarrow 2M(OR)_m + ROH \quad [35]$$

The β-hydride transfer often accompanies the other partial decomposition processes, such as hydrolysis[99] and ether elimination[115] (see Figure 9):

$$VO(OEt)_3 + H_2O \longrightarrow V_6O_7(OEt)_{12} + CH_3CHO + \cdots \quad [36]$$

$$6MoO(O^iPr)_4 \longrightarrow Mo_6O_{10}(O^iPr)_{12} + 2CH_3COCH_3 + 2^iPrOH + 4(^iPr)_2O \quad [37]$$

The reaction of β-proton transfer is well known in organic chemistry as the reaction of the dehydration of alcohols (especially typical for the ramified ones) :

$$(RO)_mM-O-CH(R^1)CH_2R^2 \longrightarrow (RO)_mM-OH^+ \quad [(R^1)CH=CHR^2] \quad [38]$$

$$(RO)_mM-O-CH(CH_3)_2 \longrightarrow (RO)_mM-OH + CH_3-CH=CH_2 \quad [39]$$

It is discussed in the majority of textbooks on organic chemistry, and is thought to be catalyzed by acidic reagents and may be the reason for the spontaneous decomposition of many alkoxides on microhydrolysis, with the formation of oxo species with much higher yield than that to be expected from the added amount of water.

2.16.4.4 Thermolysis in the Gas Phase

The gas-phase processes for metal alkoxides have been investigated for many species by mass-spectrometry. While electron impact as an ionization technique is an invasive method, providing strong energy input in itself producing decomposition, the revealed gas-phase reactions are, in their nature, closely analogous to processes otherwise observed in solution on heating. The most typical reactions involve ether elimination with the formation of oxo-alkoxide species, β-proton transfer with release of an olefin and the formation of a hydroxo group, and, of course, de-aggregation of oligonuclear species. Detailed descriptions of the cleavage and fragmentation of metal alkoxides in the mass spectra are available in particular for the derivatives of aluminum,[12] niobium and tantalum,[117] gallium,[118] and lanthanides.[23] Gas-phase thermolysis of metal alkoxides finds its application in the metal–organic chemical vapor deposition (MOCVD) technique for the production of thin oxide films from the gas phase.[119]

2.16.4.5 Thermolysis in a Melt and in Solid Phase: Metal–Organic Decomposition Versus Reaction Under Autogenic Pressure at Elevated Temperatures Technology

Facile thermal decomposition of metal alkoxides makes them attractive as precursors in the synthesis of oxide and metal nanomaterials by thermolysis in a condensed phase, known as the metal–organic decomposition (MOD) technique. The physical state of the phase undergoing decomposition plays an important role: while thermal cleavage in a liquid phase (a melt) can facilitate the formation of relatively well-shaped crystals with a size of several micrometers, the solid-state thermolysis offers normally small and uniform-size nanoparticles.[120] The aggregation of particles on decomposition can produce oxide materials with relatively regular small macropore arrangement.[121] A specific variety of the MOD approach is reaction under autogenic pressure at elevated temperatures (RAPET) technology.[122–124] It employs metal–organic precursors and is carried out in a pressure-stable stainless-steel Swagelok cell that is typically warmed up at a rate of 10–700°C min^{-1} and is kept at this temperature from 30 min to 1 h (Figure 10).

The typical reaction mechanism is that the precursor is decomposed thermally through ether elimination and β-hydrogen transfer reactions into metal oxide or metal nanoparticles, while the organic part is evaporated and then carbonized, forming a graphitic layer on the surface of the primary particles.[123] Even the production of multiwalled carbon nanotubes filled with metal oxides has been observed on specific reaction conditions.

2.16.5 Metal Alkoxides as Homogeneous Catalysts

The application of metal alkoxides as homogeneous catalysts is, in fact, as old as the chemistry of this class of compounds itself. In fact, Vyacheslav Tishchenko has discovered the Tishchenko reaction in the course of his studies of the chemical reactivity of aluminum alkoxides.[3] It consists in the transformation of aldehydes into esters in rather high yields; see, for example, Scheme 3.

An attractive technical advantage of this process is that it can be carried out in the aldehyde reactant as the solvent and driven practically until completion with facile further purification of the product by extraction etc. The reaction mechanism is analogous to the Bradley reaction in its initial step and involves the transformation of an aldehyde into a semiacetal via the attack of an alkoxide ligand as a Lewis base. The produced semiacetal then reduces another aldehyde molecule via α-hydride transfer. In addition to aluminum alkoxides, the alkoxides of other highly electropositive elements, especially alkali metals, can be successfully applied in this process (Scheme 4).

Another well-established industrial catalytic process exploiting both Lewis and Brønsted basicity of metal alkoxides is the Guerbet reaction: β-hydrogen abstraction from an alkoxide ligand with subsequent formation of a new C–C bond.[4] Originally, it was used to exploit partial oxidation by oxygen dissolved in solvents, but in the modern approaches, dehydrogenation iridium catalysts are also involved[125] (Scheme 5).

Modern applications of metal alkoxides in catalysis exploit their Lewis basicity for ring-opening polymerization of

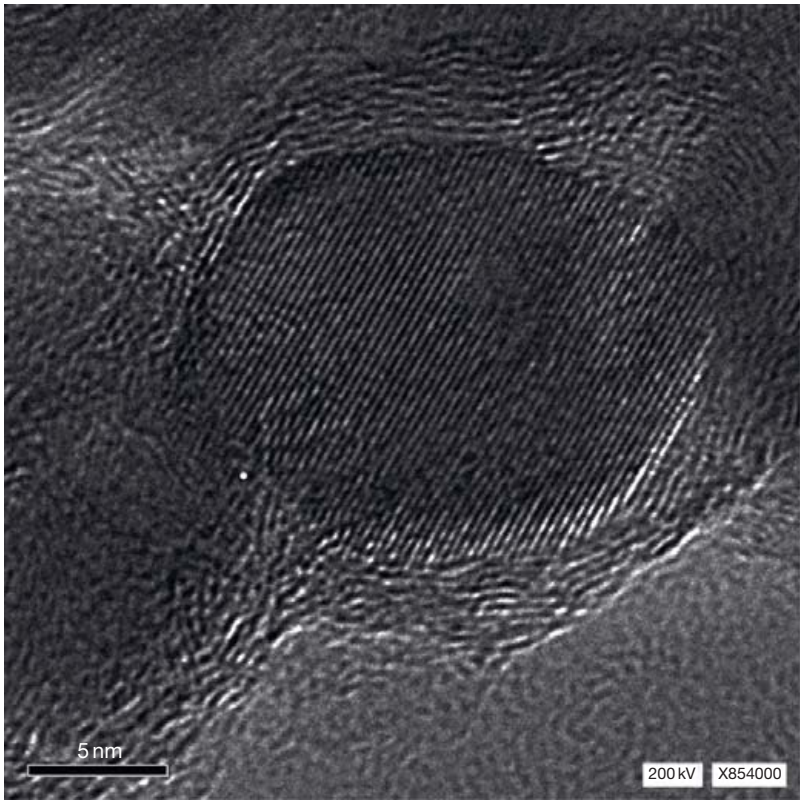

Figure 10 Tetragonal ZrO_2 single nanocrystal in a graphitic shell produced by RAPET of an alkoxide precursor. Reproduced from Pol, S. V.; Pol, V. G.; Seisenbaeva, G. A.; Kessler, V. G.; Gedanken, A. *Chem. Mater.* **2004**, *16*, 1793–1798, with permission.

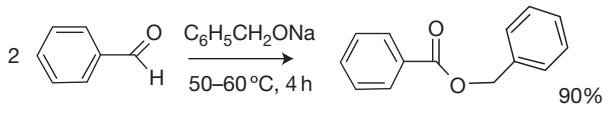

Scheme 3 Tishchenko reaction.

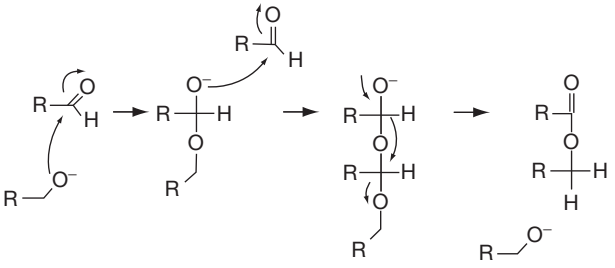

Scheme 4 Mechanism of the Tishchenko reaction.

lactides, lactones, and oxiranes.[126,127] A comprehensive review of the related chemistry with specific focus on achieving the formation of stereoregular polymers can be found in the thesis of ten Breteler from the University of Twente.[128]

2.16.6 Metal Alkoxide Complexes as Molecular Magnets

The interest in molecular magnetic materials as potential new-generation materials for computer memory has generated, in the middle of the 1990s, a real boom in the studies of the synthesis and chemistry, and, of course, magnetic characteristics of alkoxide complexes of 3d-transition elements, Mn,[129,130] Fe,[97] Co,[131,132] Ni,[133] Cu,[134] and of lanthanides, in the first hand, Gd and Dy.[96] The efforts were originally concentrated on increasing the size and controlling the molecular geometry of the species, among which the alkoxides, in the

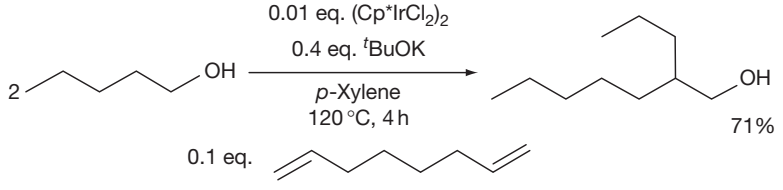

Scheme 5 Guerbet reaction.

view of their sensitivity to ambient atmosphere, were quickly losing ground to functional derivatives and alkoxide carboxylates. More recently, major interest has been shifted toward heterometallic 3d–4f complexes, with a hope for achieving higher magnetic susceptibility.[135]

2.16.7 Conclusion

The development of the chemistry of metal alkoxides as a long-time established and well-recognized field in synthetic inorganic chemistry has, of course, seen rises and falls. A tremendous explosion of interest in these compounds occurred in the beginning of the 1990s, being due to the intensive development in the sol–gel synthesis of functional ceramics, in the first hand, high-temperature superconductors. A new turn came about in the middle of the 2000s, with the interest turning to alkoxide β-diketonate derivatives for MOCVD and RAPET applications. The development of the synthesis of mixed-ligand and functional-alcohol complexes for molecular magnetism and for optical materials is still going strong.

Predicting the ways of future progress is always a tricky business, but it appears plausible that one more period of strong development can be associated in the near future with the growing field of metal–organic frameworks. These materials are, at present, produced almost exclusively in aqueous media through simple precipitation or hydrothermal synthesis. The tremendous potential of metal alkoxides as synthetic reagents and the chemical lability of the M–OR bond with its huge potential in catalysis appear to provide a good background for the synthesis of new hybrid metal–organic catalysts and possibly even optical and magnetic materials in nonaqueous media.

References

1. Lamy, A. *Compt. Rend.* **1862**, *55*, 836.
2. Demarcay, E. *Compt. Rend.* **1875**, *80*, 51.
3. Tishchenko, V. *J. Russ. Phys. Chem. Soc.* **1906**, *38*, 540–546.
4. Guerbet, M. *Compt. Rend.* **1909**, *149*, 129–132.
5. Bradley, D. C. *Chem. Rev.* **1989**, *89*, 1317–1322.
6. Bradley, D. C.; Hill, D. A. W. *J. Chem. Soc.* **1963**, 2101–2107.
7. Bradley, D. C.; Chakravarti, B. N.; Wardlaw, W. *J. Chem. Soc.* **1956**, 4439–4441.
8. Bradley, D. C.; Charkravarti, B. N.; Chatterjee, A. K.; Wardlaw, W.; Whitley, A. *J. Chem. Soc.* **1958**, 99–101.
9. Bradley, D. C.; Mehrotra, R. C.; Rothwell, I.; Singh, A. *Alkoxo and Aryloxo Derivatives of Metals*. Academic Press: London, 2001.
10. Turova, N. Ya.; Turevskaya, E. P.; Kessler, V. G.; Yanovskaya, M. I. *The Chemistry of Metal Alkoxides*. Kluwer: Boston, MA, 2002.
11. Caulton, K. G.; Hubert-Pfalzgraf, L. G. *Chem. Rev.* **1990**, *90*, 969–995.
12. Turova, N. Ya.; Turevskaya, E. P.; Yanovskaya, M. I.; Yanovsky, A. I.; Kessler, V. G.; Tcheboukov, D. E. *Polyhedron* **1998**, *17*, 899–915.
13. Hybert-Pfalzgraf, L. G. *Inorg. Chem. Commun.* **2003**, *6*, 102–120.
14. Day, V. W.; Eberspacher, T. A.; Klemperer, W. G.; Park, C. W. *J. Amer. Chem. Soc.* **1993**, *115*, 8469–8470.
15. Kessler, V. G. *Chem. Commun.* **2003**, 1213–1222.
16. Kessler, V. G.; Spijksma, G. I.; Seisenbaeva, G. A.; Håkansson, S.; Blank, D. H. A.; Bouwmeester, H. J. M. *J. Sol-Gel Sci. Tech.* **2006**, *40*, 163–179.
17. Turova, N. Ya. *Russ. Chem. Rev.* **2004**, *73*, 1041–1064.
18. Boyle, T. J.; Ottley, L. A. M. *Chem. Rev.* **2008**, *108*, 1896–1917.
19. Kessler, V. G. *J. Sol-Gel Sci. Tech.* **2009**, *51*, 264–271.
20. Lind, C.; Gates, S. D.; Pedoussaut, N. M.; Baiz, T. I. *Materials* **2010**, *3*, 2567–2587.
21. Caulton, K. G.; Chisholm, M. H.; Drake, S. R.; Streib, W. E. *Angew. Chem.* **1990**, *102*, 1492–1493.
22. Drake, S. R.; Streib, W. E.; Folting, K.; Chisholm, M. H.; Caulton, K. G. *Inorg. Chem.* **1992**, *31*, 3205–3210.
23. Pazik, R.; Seisenbaeva, G. A.; Gohil, S.; Wiglusz, R.; Kepinski, L.; Strek, W.; Kessler, V. G. *Inorg. Chem.* **2010**, *49*, 2684–2691.
24. Helgesson, G.; Jagner, S.; Poncelet, O.; Hubert-Pfalzgraf, L. G. *Polyhedron* **1991**, *10*, 1559–1564.
25. Evans, W. J.; Greci, M. A.; Ziller, J. W. *Inorg. Chem.* **1998**, *37*, 5221–5226.
26. Hubert-Pfalzgraf, L. G.; Daniele, S.; Bennaceur, A.; Daran, J. C.; Vaissermann, J. *Polyhedron* **1997**, *16*, 1223–1234.
27. Zöller, T.; Iovkova-Berends, L.; Dietz, C.; Berends, K.; Jurkschat, T. *Chem. Eur. J.* **2011**, *17*, 2361–2364.
28. Kovbasyuk, L. A.; Vassilyeva, O. Y.; Kokozay, V. N.; Linert, W.; Skelton, B. W.; Oliver, A. G. *New J. Chem.* **1998**, *22*, 931–932.
29. Turevskaya, E. P.; Turova, N. Ya.; Novoselova, A. V. *Russ. J. Inorg. Chem.* **1975**, *20*, 838–839.
30. Lehmkuhl, H.; Eisenbach, W. *Liebigs Ann.* **1975**, 672–691.
31. Hubert-Pfalzgraf, L. G.; Kessler, V. G.; Vaissermann, J. *Polyhedron* **1997**, *16*, 4197–4203.
32. Banait, J. S.; Pahil, P. K. *Synth. React. Inorg. Met. Org. Chem.* **1986**, *16*, 1217–1224.
33. Kessler, V. G.; Panov, A. N.; Turova, N. Ya.; Starikova, Z. A.; Yanovsky, A. I.; Dolgushin, F. M.; Pisarevsky, A. P.; Struchkov, Yu.T. *Dalton* **1998**, 21–29.
34. Tchebukov, D. E.; Turova, N. Ya.; Korolev, A. V.; Belokon, A. I. *Russ. J. Inorg. Chem.* **1997**, *42*, 1498–1501.
35. Turevskaya, E. P.; Turova, N. Ya.; Korolev, A. V.; Yanovsky, A. I.; Struchkov, Yu.T. *Polyhedron* **1995**, *14*, 1531–1542.
36. Turova, N. Ya.; Korolev, A. V.; Tchebukov, D. E.; Belokon, A. I.; Yanovsky, A. I.; Struchkov, Yu.T. *Polyhedron* **1996**, *15*, 3869–3880.
37. Kessler, V. G.; Mironov, A. V.; Turova, N. Ya.; Yanovsky, A. I.; Struchkov, Yu.T. *Polyhedron* **1993**, *12*, 1573–1576.
38. Seisenbaeva, G. A.; Kloo, L.; Werndrup, P.; Kessler, V. G. *Inorg. Chem.* **2001**, *40*, 3815–3818.
39. Seisenbaeva, G. A.; Shevelkov, A. V.; Tegenfeldt, J.; Kloo, L.; Drobot, D. V.; Kessler, V. G. *Dalton* **2001**, 2762–2768.
40. Nikonova, O. N.; Jansson, K.; Kessler, V. G.; Sundberg, M.; Baranov, A. I.; Shevelkov, A. V.; Drobot, D. V.; Seisenbaeva, G. A. *Inorg. Chem.* **2008**, *47*, 1295–1300.
41. Shcheglov, P. A.; Seisenbaeva, G. A.; Drobot, D. V.; Kessler, V. G. *Inorg. Chem. Commun.* **2001**, *4*, 227–229.
42. Chisholm, M. H.; Cotton, F. A.; Extine, M. W.; Rideout, D. C. *Inorg. Chem.* **1979**, *18*, 120–125.
43. Razuvaev, G. A.; Latayeva, V. N.; Drobotenko, V. V.; Linyova, A. N.; Vyshinskaya, N. I.; Cherkasov, V. K. *J. Organometal. Chem.* **1977**, *131*, 43–48.
44. Håkansson, M.; Lopes, C.; Jagner, S. *Organometallics* **1998**, *17*, 210–215.
45. Heitz, S.; Aksu, Y.; Merschjann, C.; Driess, M. *Chem. Eur. J.* **2011**, *17*, 3904–3910.
46. Goel, S. C.; Chiang, M. Y.; Buhro, W. E. *Inorg. Chem.* **1990**, *29*, 4646–4652.
47. Boulmaaz, S.; Papiernik, R.; Hubert-Pfalzgraf, L. G.; Vaisserman, J.; Daran, J. C. *Polyhedron* **1992**, *11*, 1331–1336.
48. Papiernik, R.; Hubert-Pfalzgraf, L. G.; Massiani, M. C. *Inorg. Chim. Acta* **1989**, *165*, 1–2.
49. Massiani, M. C.; Papiernik, R.; Hubert-Pfalzgraf, L. G. *Polyhedron* **1991**, *10*, 437–445.
50. Matchett, M. A.; Chiang, M. Y.; Buhro, W. E. *Inorg. Chem.* **1990**, *29*, 358–360.
51. Daniele, S.; Tcheboukov, D.; Hubert-Pfalzgraf, L. G.; Lecocq, S. *Inorg. Chem. Commun.* **2002**, *5*, 347–350.
52. Horvath, B.; Möseler, R.; Horvath, E. G. *Z. Anorg. Allg. Chem.* **1979**, *449*, 41–51.
53. Akiyama, M.; Chisholm, M. H.; Cotton, F. A. *Inorg. Chem.* **1977**, *16*, 2407–2411.
54. Bryndza, H. E.; Tam, W. *Chem. Rev.* **1988**, *88*, 1163–1188.
55. Turevskaya, E. P.; Turova, N. Ya. *Koord. Khim.* **1989**, *15*, 373–376.
56. Niederberger, M.; Bard, M. H.; Stucky, G. D. *J. Am. Chem. Soc.* **2002**, *124*, 13642–13643.
57. Bradley, D. C.; Abdelhalim, F. M.; Sadek, E. A.; Wardlaw, W. *J. Chem. Soc.* **1952**, 2032–2035.
58. Spijksma, G. I.; Seisenbaeva, G. A.; Bouwmeester, H. J. M.; Blank, D. H. A.; Kessler, V. G. *J. Sol-Gel Sci. Tech.* **2009**, *51*, 10–22.
59. Bartley, W. G.; Wardlaw, W. *J. Chem. Soc.* **1958**, 422–430.
60. Evans, W. E.; Sollberger, M. S.; Hanusa, T. *J. Am. Chem. Soc.* **1988**, *110*, 1841–1850.
61. Andersen, R. A.; Templeton, D. H.; Zalkin, A. *Inorg. Chem.* **1978**, *17*, 1962–1965.

62. Seisenbaeva, G. A.; Gohil, S.; Suslova, E. V.; Rogova, T. V.; Turova, N. Ya.; Kessler, V. G. *Inorg. Chim. Acta* **2005**, *358*, 3506–3512.
63. Kritikos, M.; Moustiakimov, M.; Wijk, M.; Westin, G. *J. Chem. Soc. Dalton Trans.* **2001**, 1931–1938.
64. Turevskaya, E. P.; Turova, N. Y.; Sudyin, E. V.; Novoselova, A. V. *Inorg. Mater.* **1982**, *18*, 222–226.
65. Gradeff, P. S.; Schreiber, F. G.; Brooks, K. S.; Sievers, R. E. *Inorg. Chem.* **1985**, *24*, 1110–1111.
66. Reisinger, A.; Himmel, D.; Krossing, I. *Angew. Chem. Int. Ed.* **2006**, *45*, 6997–7000.
67. Jacob, E. *Angew. Chem. Int. Ed.* **1982**, *21*, 142–143.
68. Bryan, J. C.; Wheeler, D. R.; Clark, D. L.; Huffman, J. C.; Sattelberger, A. P. *J. Am. Chem. Soc.* **1991**, *113*, 3184–3186.
69. Dimitrov, A.; Wuttke, S.; Troyanov, S.; Kemnitz, E. *Angew. Chem. Int. Ed.* **2008**, *47*, 190–192.
70. Johansson, A.; Kessler, V. G. *Polyhedron* **2000**, *19*, 1791–1798.
71. Seisenbaeva, G. A.; Gohil, S.; Kessler, V. G. *J. Mater. Chem.* **2004**, *14*, 3177–3190.
72. Daniele, S.; Hubert-Pfalzgraf, L. G.; Perrin, M. *Polyhedron* **2002**, *21*, 1985–1990.
73. Nunes, G. G.; Seisenbaeva, G. A.; Kessler, V. G. *J. Sol-Gel Sci. Tech.* **2007**, *43*, 105–109.
74. Kusserow, M.; Spandl, J. *Z. Anorg. Allg. Chem.* **2006**, *632*, 885–892.
75. Errington, R. J.; Ridland, J.; Clegg, W. *Polyhedron* **1998**, *17*, 659–674.
76. Spijksma, G. I.; Bouwmeester, H. J. M.; Blank, D. H. A.; Fischer, A.; Henry, M.; Kessler, V. G. *Inorg. Chem.* **2006**, *44*, 4938–4950.
77. Pothiraja, R.; Milanov, A.; Parala, H.; Winter, M.; Fischer, R. A.; Devi, A. *Dalton Trans.* **2009**, 654–663.
78. Bains, M. S.; Bradley, D. C. *Can. J. Chem.* **1962**, *40*, 2218–2221.
79. Fric, H.; Puchberger, M.; Schubert, U. *J. Sol-Gel Sci. Tech.* **2006**, *40*, 155–162.
80. Eichorst, D. E.; Payne, D. A.; Wilson, S. R.; Howard, K. E. *Inorg. Chem.* **1990**, *29*, 1458–1459.
81. Veith, M.; Valtchev, K.; Huch, V. *Inorg. Chem.* **2008**, *47*, 1204–1217.
82. Kessler, V. G.; Gohil, S.; Parola, S. *Dalton Trans.* **2003**, 544–550.
83. Nunes, G. G.; Kessler, V. G. *Inorg. Chem. Commun.* **2006**, *9*, 667–670.
84. Seisenbaeva, G. A.; Suslova, E. V.; Kritikos, M.; Rapenne, L.; Andrieux, M.; Parola, S.; Kessler, V. G. *J. Mater. Chem.* **2004**, *14*, 3150–3157.
85. Seisenbaeva, G. A.; Kessler, V. G.; Pazik, R.; Strek, W. *Dalton Trans.* **2008**, 3412–3421.
86. Donat, M.; Seisenbaeva, G. A.; Kessler, V. G. *J. Sol-Gel Sci. Tech.* **2008**, *48*, 61–65.
87. Seisenbaeva, G. A.; Gohil, S.; Kessler, V. G. *Inorg. Chem. Commun.* **2007**, *10*, 94–96.
88. Werndrup, P.; Kessler, V. G. *Dalton Trans.* **2001**, 574–579.
89. Kessler, V. G.; Gohil, S.; Kritikos, M.; Korsak, O. N.; Knyazeva, E. E.; Moskovskaya, I. F.; Romanovsky, B. V. *Polyhedron* **2001**, *20*, 915–922.
90. Turova, N. Ya.; Kozunov, V. A.; Yanovskii, A. I.; Bokii, N. G.; Struchkov, Yu.T.; Tarnopol'skii, B. L. *J. Inorg. Nucl. Chem.* **1979**, *41*, 5–11.
91. Wijk, M.; Norrestam, R.; Nygren, M.; Westin, G. *Inorg. Chem.* **1996**, *35*, 1077–1079.
92. Kessler, V. G.; Hubert-Pfalzgraf, L. G.; Halut, S.; Daran, J. C. *J. Chem. Soc. Chem. Commun.* **1994**, 705–706.
93. Eslava, S.; McPartlin, M.; Thomson, R. I.; Rawson, J. M.; Wright, D. S. *Inorg. Chem.* **2010**, *49*, 11532–11540.
94. Kessler, V. G.; Turova, N. Ya.; Turevskaya, E. P. *Inorg. Chem. Commun.* **2002**, *5*, 549–551.
95. Coan, P. S.; Hubert-Pfalzgraf, L. G.; Caulton, K. G. *Inorg. Chem.* **1992**, *31*, 1262–1267.
96. Westin, L. G.; Kritikos, M.; Caneschi, A. *Chem. Commun.* **2003**, 1012–1013.
97. Dutta, A. K.; Ghosh, R. *Inorg. Chem. Commun.* **2011**, *14*, 337–342.
98. Goel, S. C.; Matchett, M. A.; Chiang, M. Y.; Buhro, W. E. *J. Am. Chem. Soc.* **1991**, *113*, 1844–1845.
99. Kessler, V. G.; Seisenbaeva, G. A. *Inorg. Chem. Commun.* **2000**, *3*, 203–204.
100. Fromm, K. *Dalton Trans.* **2006**, 5103–5112.
101. Wengrovius, J. H.; Garbauskas, M. F.; Williams, E. A.; Goint, R. C.; Donahue, P. E.; Smith, J. F. *J. Am. Chem. Soc.* **1986**, *108*, 982–989.
102. Fric, H.; Schubert, U. *J. Sol-Gel Sci. Tech.* **2008**, *48*, 2–5.
103. Fortner, K. C.; Bigi, J. P.; Brown, S. N. *Inorg. Chem.* **2005**, *44*, 2803–2814.
104. Fornasieri, G.; Rozes, L.; Le Calvé, S.; Alonso, B.; Massiot, D.; Rager, M. N.; Evain, M.; Boubekeur, K.; Sanchez, C. *J. Am. Chem. Soc.* **2005**, *127*, 4869–4878.
105. Livage, J.; Henry, M.; Sanchez, C. *Progr. Solid State Chem.* **1988**, *18*, 259–341.
106. Sanchez, C.; Livage, J. *New J. Chem.* **1990**, *14*, 513–521.
107. Livage, J.; Sanchez, C. *J. Non-Cryst. Solids* **1992**, *145*, 11–19.
108. Sanchez, C.; Livage, J.; Henry, M.; Babonneau, F. *J. Non-Cryst. Solids* **1988**, *100*, 65–76.
109. Seisenbaeva, G. A.; Moloney, M. P.; Tekoriute, R.; Hardy-Dessource, A.; Nedelec, J. M.; Gun'ko, Y. K.; Kessler, V. G. *Langmuir* **2010**, *26*, 9809–9817.
110. Pazik, R.; Tekoriute, R.; Håkansson, S.; Wiglusz, R.; Strek, W.; Siesenbaeva, G. A.; Gun'ko, Y. K.; Kessler, V. G. *Chem. Eur. J.* **2009**, *15*, 6820–6826.
111. Turova, N. Ya.; Kessler, V. G.; Kucheiko, S. I. *Polyhedron* **1991**, *10*, 2617–2628.
112. Yanovskaya, M. I.; Turevskaya, E. P.; Kessler, V. G.; Obvintseva, I. E.; Turova, N. Ya. *Integr. Ferroelectr.* **1992**, *1*, 343–352.
113. Niederberger, M.; Pinna, N.; Polleux, J.; Antonietti, M. *Angew. Chem.* **2004**, *116*, 2320–2323.
114. Nabavi, M.; Sanchez, C.; Livage, J. *Eur. J. Solid State Inorg. Chem.* **1991**, *28*, 1173–1192.
115. Kessler, V. G.; Shevelkov, A. V.; Bengtsson-Kloo, L. A. *Polyhedron* **1998**, *17*, 965–968.
116. Hoffman, D. M.; Lappas, D.; Wierda, D. A. *J. Am. Chem. Soc.* **1989**, *111*, 1531–1533.
117. Hubert-Pfalzgraf, L. G.; Riess, J. G. *Inorg. Chem.* **1975**, *14*, 2854–2856.
118. Suslova, E. V.; Kessler, V. G.; Gohil, S.; Turova, N. Ya. *Eur. J. Inorg. Chem.* **2007**, 5182–5188.
119. Putkonen, M.; Niinistö, L. *Precursor Chemistry of Advanced Materials: CVD, ALD and Nanoparticles*. In *Topics in Organometallic Chemistry*; Fischer, R. A., Ed.; Springer: Boston, MA, 2010 pp 125–146.
120. Seisenbaeva, G. A.; Sundberg, M.; Nygren, M.; Dubrovinsky, L.; Kessler, V. G. *Mater. Chem. Phys.* **2004**, *87*, 142–148.
121. Nikonova, O. A.; Kessler, V. G.; Seisenbaeva, G. A. *J. Solid State Chem.* **2008**, *181*, 3294–3302.
122. Pol, S. V.; Pol, V. G.; Seisenbaeva, G. A.; Kessler, V. G.; Gedanken, A. *Chem. Mater.* **2004**, *16*, 1793–1798.
123. Pol, S. V.; Pol, V. G.; Kessler, V. G.; Gedanken, A. *New J. Chem.* **2006**, *30*, 370–376.
124. Pol, S. V.; Pol, V. G.; Gedanken, A.; Grinblat, Y.; Kalai Selvan, R.; Kessler, V. G.; Spijksma, G. I.; Seisenbaeva, G. A.; Gohil, S. *J. Phys. Chem. C* **2007**, *111*, 2484–2489.
125. Matsu-ura, T.; Sakaguchi, S.; Obora, Y.; Ishii, Y. *J. Org. Chem.* **2006**, *71*, 8306–8308.
126. Ouhadi, T.; Hamitou, A.; Jerome, R.; Teyssie, Ph. *Macromol.* **1976**, *9*, 927–931.
127. Kricheldorf, H. R.; Berl, M.; Scharnagl, N. *Macromol.* **1988**, *21*, 286–293.
128. ten Breteler, M. R. Stereoselective Polymerization of Lactones. Properties of Stereocomplexed PLA Building Blocks; University of Twente, Netherlands, 2010; http://doc.utwente.nl/71772/1/thesis_M_ten_Breteler.pdf
129. Stamatatos, T. C.; Christou, G. *Inorg. Chem.* **2009**, *48*, 3308–3322.
130. Pohl, I. A. M.; Westin, L. G.; Kritikos, M. *Chem. Eur. J.* **2001**, *7*, 3438–3445.
131. Stamatatos, T. C.; Boudalis, A. K.; Pringouri, K. V.; Raptopoulou, C. P.; Terzis, A.; Wolowska, J.; McInnes, E. J. L.; Perlepes, S. P. *Eur. J. Inorg. Chem.* **2007**, 5098–5104.
132. Seisenbaeva, G. A.; Kritikos, M.; Kessler, V. G. *Polyhedron* **2003**, *22*, 2581–2586.
133. Ilina, E.; Kessler, V. G. *Polyhedron* **2005**, *24*, 3052–3056.
134. Henkelis, J. J.; Jones, L. F.; de Miranda, M. P.; Kilner, C. A.; Halcrow, M. A. *Inorg. Chem.* **2010**, *49*, 11127–11132.
135. Zhao, X. Q.; Lan, Y.; Zhao, B.; Cheng, P.; Anson, C. E.; Powell, A. K. *Dalton Trans.* **2010**, *39*, 4911–4917.

2.17 Exothermic Metathesis Reactions

IP Parkin and A Kafizas, University College London, London, UK

2.17.1 Introduction

The conventional approach to the synthesis of solid-state materials is typically solvent free and involves the cyclic 'heat and beat' of starting materials that are cyclically ground, heated, and cooled until the solid-state diffusion barrier is overcome and the desired product is achieved.[1] However, unlike solutions that contain well-mixed components with high rates of diffusion, conventional solid-based reactions can often take days to progress even at extreme temperatures. Irrespective of such drawbacks, this conventional approach forms the basis of production in the ceramics industry. New approaches that aim to alleviate the time and the energy costs compared with conventional preparations have been developed over recent decades including sol–gel,[2] hydrothermal,[3] molecular precursor,[4] and self-propagating high-temperature synthesis (SHS).[5]

SHS is an exothermic elemental combination process where typically elements are reacted to form refractory materials. The process is rapid, requires a source of initiation, and can be used to make a wide range of ceramics and intermetallics. The technique was originally pioneered by Merzhanov and has been extensively studied particularly in former Soviet Union countries.[6] Examples of well-known SHS reactions are the thermite reaction ($Fe_2O_3 + 2Al \rightarrow Al_2O_3 + 2Fe$) and the Goldschmidt reaction ($Cr_2O_3 + 2Al \rightarrow Al_2O_3 + 2Cr$).

One avenue that has received great attention is a modification of the SHS process, termed solid-state metathesis (SSM).[7] Although both processes self-propagate due to the high level of exothermic energy released,[8] SSM reactions typically require less energy to initiate combustion (≈700–1400 °C) and specifically involve the reaction of an alkali or alkaline earth metal pnictide, chalcogenide, silicide, or boride with a metal halide:

$$M_xE_y + M'X_x \rightarrow M'E_y + xMX - \Delta H \qquad [1]$$

where M = Li, Na, K, Mg, Ca, Sr, Ba; E = B, Si, N, P, As, Sb, Bi, O, S, Se, Te; M′ = transition, main group, or actinide metal; X = halogen; and x and y are integers.

SSM reactions are highly exothermic. The driving force is the high lattice enthalpy that is released upon the co-formation of alkali or alkaline earth-metal halides. This energy release can account for up to 90% of the reaction enthalpy.[1] SSM reactions are typically initiated from a point source using a heated filament or flame where the reagents are often sealed in a bomb-type reactor. They can also be ignited in bulk by heating reagents sealed in an evacuated glass ampoule in either a furnace[9] or a microwave oven.[10] Care should be exercised with any sealed SSM reaction as large, potentially explosive gas pressures can build up. Less frequently, SSM reactions can self-initiate from the simple mixing[11] or grinding[12] of the reagents at room temperature, which is more common for low-melting-point reagents. When SSM reactions ignite, a propagating wave of exothermic energy is released local to the point of ignition. This wave rapidly engulfs the surrounding reactants, reaching temperatures ranging from 1000 to 4000 °C in a matter of seconds. The propagating wave can be quite intense and take the form of a bright solid flame that moves through the reactants at speeds of mm s^{-1} to cm s^{-1}. An example of this

rapidly propagating wave is shown for the reaction of $NbCl_5$ with Li_3N in the SSM formation of NbN (Figure 1). The rapid heating and cooling associated with SSM reactions leads to a high concentration of defects being present and a more easily sintered product.

The criteria for a reaction to self-propagate are related to the level of exothermicity, reagent and product heat capacities, as well as the density and the type of the containment vessel.[13] It has been empirically determined that an SSM reaction will self-propagate only if the exothermic energy release is high enough to melt the co-formed salt.[14] The energy release driven by the salt co-formation has major consequences on the maximum temperature reached during the reaction and hence the phases of product. Where alkali halides tend to have lower heats of formation than alkaline earth halides, reactions utilizing alkaline earth metals will generally produce higher reaction temperatures. Given that the upper limit of the reaction temperature is generally governed by the boiling point of the salt produced, the formation of alkaline earth salts, with their higher melting and boiling points, tends to increase this upper limit.[15] On the other hand, the reaction temperature generally decreases when a heavier halogen (X) is used, where careful selection of the halogen can promote the formation of thermally unstable, metastable, or thermodynamically favored products.

The maximum temperature (T_{ad}) for an adiabatic SSM reaction can be predicted by applying Hess's law and correlating this with the specific heat capacities of the reagents and products involved, with two assumptions: (1) the reaction is so rapid that all of the energy produced is transferred to heat the products and (2) the reactions go to completion (eqn [1]). The temperature can also be measured, either directly by placing a thermocouple at the heart of a reaction vessel or indirectly by optical pyrometry, where the color of the thermal flash associated with the reaction corresponds with a particular temperature. Unfortunately, significant deviations between the theoretical maximum temperature (T_{ad}) and those experimentally observed are typical and are primarily due to incomplete reactions, where yields of SSM reactions most commonly range between 50% and 90% depending on the scale of the reaction.[17] Despite the large formation enthalpies of SSM reactions, T_{ad} normally corresponds to the boiling point of the co-produced salt, thus limiting the maximum reaction temperature achieved compared with typical SHS reactions. Nevertheless, SSM reactions proceed on a similarly rapid timescale to SHS reactions, and are generally completed in less than 5 s after ignition. In addition, the lower temperatures of salt-mediated SSM reactions allow a different range of materials (with respect to composition, phase, and crystallinity) to be accessed compared with SHS. These properties can be further controlled by reducing the maximum temperature experienced in the reaction vessel through the use of heat sinks.[18] A similar tactic is used to reduce the temperature experienced in SSM reactions through the use of dilutants. When applied, dilutants provide a twofold inhibiting effect, as the diffusion path-length required for the SSM reaction to proceed is increased alongside thermal trapping. Such inhibition methods are particularly useful when trying to isolate more thermally unstable or metastable phases, reduce material crystallinity, or induce the formation of nanoscale powders and high surface area materials.

As SSM reactions complete so rapidly, it is difficult to precisely monitor local temperatures, let alone trace reaction pathways. Through investigating a range of SSM reactions by differential thermal analysis, it was suggested that reactions could proceed by either an ionic exchange or a reductive combination mechanism.[19] In the ionic exchange mechanism, the reaction proceeds via a transition state where the metal (M'^{y+}) that was contained on the initial salt and the anion (E^{-}) that was contained on the alkali/alkaline earth metal still carry their ionic charges:

$$M_xE_y + M'X_x \rightarrow \left[M'^{y+} + yE^{-} + xMX\right] \rightarrow M'E_y + xMX \qquad [2a]$$

In the reductive combination mechanism, the reaction proceeds via a transition state where the metal (M') that was contained on the initial salt becomes fully reduced and the anion (E) that was contained on the alkali/alkaline earth metal become fully oxidized to their elemental states:

$$M_xE_y + M'X_x \rightarrow [M' + yE + xMX] \rightarrow M'E_y + xMX \qquad [2b]$$

It is generally concluded in most SSM studies that the reactions contain some degree of both the ionic and reduction combination mechanisms. The resulting solid formed in SSM reactions is a composite of salt and product. Purification of the product by removing the salt is straightforward and simply involves trituration with the appropriate solvent (typically water). Nevertheless, trituration can alter the nature of the material, especially with solvent-sensitive products.[9]

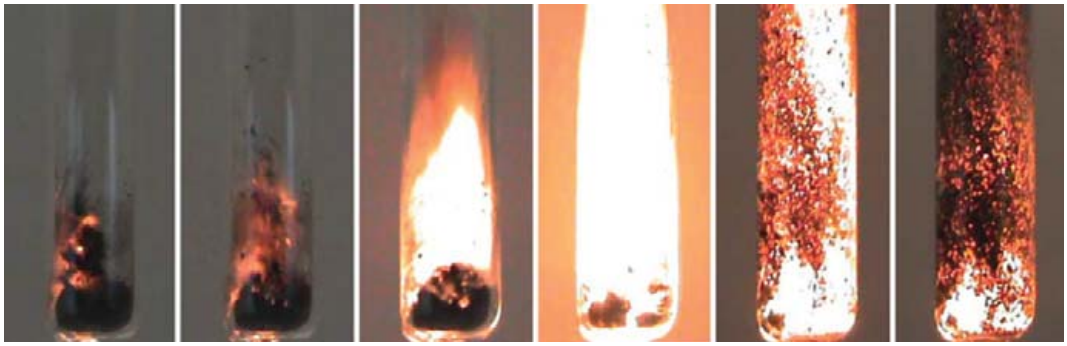

Figure 1 A sequence of photographs (0.04 s intervals) of the reaction of $NbCl_5$ with Li_3N in the SSM formation of NbN. The reaction was initiated through external heating using a hot plate. Reproduced from Meyer, H. -J. *Dalton Trans*. **2010**, *39*, 5973, with permission from Royal Society of Chemistry.

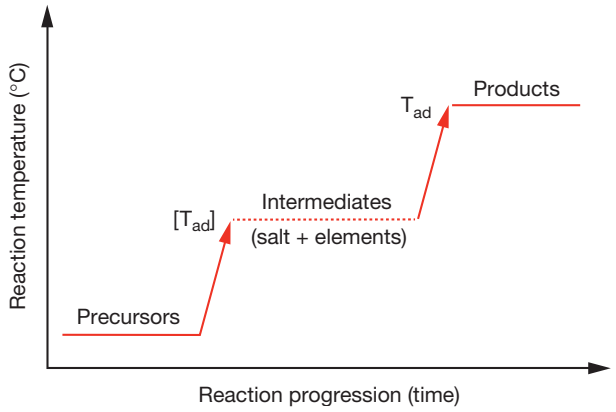

Figure 2 Reaction temperature as a function of reaction progression illustrating the criteria for self-propagation, where [T_{ad}] and T_{ad} represent the theoretical adiabatic maximum temperatures of the intermediate and product states, respectively, in an exothermic SSM reaction.

On the basis of the above observations, a general thermodynamic concept emerges relating the self-propagation of an SSM reaction to the temperature reached at the intermediate state. If the temperature at this point [T_{ad}] is high enough to melt the salt by-product, the solid-state diffusion barrier is overcome, the mobility of all species in the reaction is increased, and the reaction is rapid. On the other hand, if the salt by-product forms a solid, then self-propagation will be inhibited (Figure 2).

The development of SSM routes over the last two decades has revolutionized the way in which several industrially important refractory ceramics, intermetallics, and semiconductors are made.[17] In this chapter, the development of SSM routes in synthesizing a range of materials including metal borides and aluminides,[20–23] carbides and silicides,[24–29] nitrides,[30–44] phosphides, arsenides, and antimonides,[45–52] oxides and sulfides,[41,53–60] and selenides and tellurides[58,61–64] are covered. In addition, an overview of the new directions in metathesis, including carbon nanotube[65,66] and nanocrystal[67,68] formation, is presented.

2.17.2 Materials Synthesis

2.17.2.1 Metal Borides and Aluminides

2.17.2.1.1 Metal borides

Boron can be combined with a large number of transition metals to form borides.[69] These compounds form a class of super-hard materials with high melting points and excellent chemical stability. In addition, many metal borides show metal-like conductivity and/or unusual magnetic properties. Such materials are primarily applied as crucible materials for the melting of nonferrous metals; however, TiB_2 and ZrB_2 are also used as electrode materials for the electrolytic production of aluminum[70] and show the potential for applications in electronic devices.[71]

Metal borides are commonly formed from annealing the constituent elements at high temperatures and from a variety of thermal reduction processes. In the large-scale production of metal borides, metal oxides are reduced carbothermally at temperatures above 1400 °C and followed by a high-temperature purification stage. Recent synthetic approaches to metal borides have been aimed at controlling morphology and lowering the required reaction temperature. Some examples include solution phase reactions where metal borohydrides are produced and then decomposed to metal borides[72,73] and vapor phase reactions between metal halides and a reducing agent such as Na or H_2[74] and SHS.[75] A range of transition metal borides can also be produced through SSM routes.[19,23]

One such route was developed by Kaner et al., where MgB_2 was used as a boron precursor and reacted with a series of transition metal chlorides.[23] The SSM reaction with the group 4 chlorides did not self-propagate and required heating in an evacuated quartz tube at 850 °C for 18 h to react:

$$M'Cl_n + \frac{n}{2}MgB_2 \rightarrow M'B_2 + \frac{n}{2}MgCl_2 + (n-2)B \qquad [3]$$

where M′ = Ti, Zr, or Hf. A series of diborides were formed with hexagonal symmetry ($P_{6/mmm}$) that crystallized in the AlB_2 structure. However, some amorphous elemental boron by-product also formed that could not be removed by trituration. To eliminate this by-product, stoichiometric amounts of elemental transition metal can be added to the SSM process:

$$M'Cl_n + \frac{n}{2}MgB_2 + \frac{n-2}{2}M' \rightarrow \frac{n}{2}M'B_2 + \frac{n}{2}MgCl_2 \qquad [4]$$

or Mg metal to assist its removal:

$$M'Cl_n + MgB_2 + \frac{n-2}{2}Mg \rightarrow M'B_2 + \frac{n}{2}MgCl_2 \qquad [5]$$

forming $M'B_2$ products consisting of agglomerates of submicrometer particles. To make such SSM reactions self-propagating, additives such as NaN_3 or transition metal phosphides/nitrides can be included to enhance the exothermicity of the reaction. Nevertheless, this leads to the formation of inseparable metal boride/nitride composites.

Conversely, reactions of the group 5 chlorides produce self-propagating reactions with MgB_2 when ignited in a stainless steel bomb with a hot nichrome wire ($T < 850$ °C). A series of diborides were formed with crystal structure and topography analogous to their group 4 counterparts. According to their salt-balanced equations (eqn [3]), the reactions of the group 5 metals should have also produced excess elemental boron, especially for the high-valence precursors $NbCl_5$ and $TaCl_5$, but no presence of either crystalline or amorphous boron was observed:

$$M'Cl_n + \frac{n}{2}MgB_2 \rightarrow M'B_2 + \frac{n}{2}MgCl_2 \qquad [6]$$

where M = V, Nb, or Ta. Through the addition of $MgCl_2$ dilutant, the crystallinity of the group 5 diborides could be adjusted, where the average crystallite size determined through application of the Scherrer equation[76] to x-ray diffraction (XRD) patterns varied from 350 Å with no addition of salt to 100 Å with a 1: 1 addition of salt: group 5 metal chloride. Increased levels of salt dilutant lead to nonpropagating SSM reactions. Of further note, when group 5 solid-solution chlorides such as $Nb_{0.5}Ta_{0.5}Cl_5$ were reacted with MgB_2, a diboride solid solution was formed.

Although the SSM reactions of MgB_2 with the group 6 metal chlorides are also self-propagating, a variety of products

are formed. In the case of $CrCl_2$, the diboride CrB_2 is formed in majority alongside CrB. In the case of $MoCl_5$, three products form: MoB_2, MoB, and metallic Mo. In the case of WCl_6 also, three products form: W_2B_5, WB, and metallic W. The addition of $MgCl_2$ dilutant within these SSM reactions not only reduced product crystallinity but also encouraged the formation of the diboride up to a maximum ratio of 1: 2, transition metal: salt dilutant. The formation of late transition metal borides was demonstrated for the reaction of $FeCl_2$ with MgB_2 as an example. The reaction was also self-propagating and produced FeB.

From Kaner et al.'s dilutant studies with $MgCl_2$, it was found that an addition of excessive dilutant yielded an incomplete SSM reaction with the transition metal being present in its elemental form. This indicated that these SSM reactions proceeded via an intermediate, where the magnesium salt is first formed alongside elemental boron and transition metal (eqn [2]). The theoretical maximum temperature reached was determined through computation for each reaction (T_{ad}) and transition stage (T_{trans}). Interestingly, for all self-propagating reactions, T_{trans} was greater than 1013 K and for all nonpropagating reactions, T_{trans} was below 987 K; coinciding with the melting point of $MgCl_2$ (987 K). This confirmed that the prerequisite for rapid self-propagation hinged upon the melting of the salt product.

Additional work on actinide boride complexes for the potential storage of various radioactive wastes has also been undertaken by Abney et al. More compact than traditional borosilicate glasses, storing such materials would require less space with enhanced stability to moisture and a reduced likelihood of proliferation compared to traditional synthesis.[20,22] It has been demonstrated that several thorium, uranium, and plutonium borides can be synthesized by traditional routes; Abney et al. demonstrated the SSM reaction of uranium tetrachloride with MgB_2 as a proof of principle:

$$UCl_4 + 2MgB_2 \rightarrow UB_4 + 2MgCl_2 \qquad [7]$$

The reaction was initiated by oven heating at 850 °C for 24 h in a vacuum-sealed quartz tube and produced highly crystalline UB_4. Reaction of UCl_4 with substoichiometric amounts of the boron precursor yielded a mixture of crystalline phases including UB_4, UCl_3, and $MgCl_2$.

2.17.2.1.2 Metal aluminides

High-temperature intermetallic Ti–Al alloys have found application in aircraft and structural supports due to their light weight, and oxidation and heat resistance.[77] Nevertheless, one inhibiting feature is their ductility even at low temperatures.[78] Significant improvements in the material's mechanical properties can be achieved when fabricated in a fine-grained[79] or a nanocrystalline[80] form. Several SHS routes to titanium aluminides have been established, where the mechanical properties showed promise for industrial application.[81,82] In particular, highly crystalline and pure TiAl can be obtained through the SSM of $TiCl_3$ and LiAl[21]:

$$TiCl_3 + 3LiAl \rightarrow TiAl + 3LiCl \qquad [8]$$

The reaction is self-propagating after ignition with a nichrome wire and yields fine, gray powders after trituration. Scanning electron microscopy (SEM) analysis of the powders revealed spheroidal particles in the sub-micrometer size regime. Direct measurements of the reaction temperature profile showed how a maximum temperature of 1300 °C was reached 260 ms after ignition. After a rapid depletion of the reagents, the temperature dropped sharply to below 610 °C (the melting point of the LiCl by-product) within 8 s.

For ease of reference, the majority of the materials accessible from SSM reactions discussed in Sections 2.17.2.1–2.17.2.6 were amalgamated (Table 1).

2.17.2.2 Metal Carbides and Silicides

2.17.2.2.1 Metal carbides

Transition metal carbides show extremely high microhardness, elevated melting points, resistance to nonoxidizing acids, and good electrical and thermal conductivity.[83] These materials form a class of materials and abrasives where their properties of hardness and wear resistance combine to give outstanding cutting performance. Metal carbides have also demonstrated strong potential for use as diffusion barriers and hydrogen transfer catalysts.[84] The commercial manufacture of transition metal carbides exceeds 15 kilotons annually, where they are traditionally synthesized by reaction of the elements at 2300 °C in a hydrogen or an inert atmosphere.[29] Alternative synthetic routes to metal carbides have been developed, including sputtering and chemical vapor deposition (CVD) for coatings or SHS and molecular precursor routes for bulk materials.[25] Metal carbides have also been synthesized by the SSM route through either the use of CaC_2/SrC_2 or Al_4C_3 carbon precursors.[25,27–29]

It was demonstrated by Nartowski et al. that the group 4 transition metal carbides would adopt the face-centered cubic (FCC) rock-salt crystal phase when formed by the SSM reaction of either CaC_2 or Al_4C_3 with the metal halide.[27,29] Reactions with CaC_2 were self-propagating when heated above 220–350 °C by flame or by electric filament initiation, producing a transient red melt (>1100 °C) that turned into a black solid upon cooling. Reactions were rapid and over within 2–10 s of ignition. Such reactions could even be conducted on a ceramic tile in air and surprisingly incorporate no oxygen into the products. The overall reactions were as follows:

$$TiX_3 + \frac{3}{2}CaC_2 \rightarrow TiC + \frac{3}{2}CaX_2 + 2C \qquad [9a]$$

where X = Cl or I.

$$M'Cl_4 + 2CaC_2 \rightarrow M'C + 2CaCl_2 + 3C \qquad [9b]$$

where M′ = Zr or Hf. The excess carbon produced did not contaminate the carbide product and formed a separate black layer at the top of the reactant vessel. Trituration of the solid with either methanol or tetrahydrofuran removed both the coprecipitated salt and excess carbon. Reactions with Al_4C_3 required a constant high temperature to sustain propagation. By heating vacuum-sealed tubes with a temperature gradient from either 200 to 1000 °C for 2 days[27] or 800 to 1000 °C for 3 days[29] the formation of the co-produced aluminum halide was encouraged to sublime out of the carbide product:

$$3M'Cl_4 + Al_4C_3 \rightarrow 3M'C + 4AlCl_3 \qquad [10]$$

Table 1 Materials isolated from SSM reactions

		B/Al	*C/Si*	*N*	*P*	*As*	*Sb*	*O*	*S/Se/Te*
		MgB_2 LiAl	*CaC_2/Al_4C_3 $CaSi_2$: Mg_2Si/Li_2Si*	*LiN_3/Na_3N/Ba_2N_3/ Sr_2N Ca_3N_2/Mg_2N_3*	*Li_3P/Na_3P*	*Na_3As*	*Na_3Sb*	*Li_2O*	*Li_2S/NaS/Na_2S Na_2S_5 Li_2Se/Na_2Se Li_2Te/Na_2Te*
Group 3	YCl_3				*c* YP[48]	*c* YAs[50]	YSb[50]		
Group 4	$TiCl_3$	*t* TiAl[21]		*c* TiN[35–37]		*h* TiAs[50]	*t* $TiSb_2$, *h* TiSb[50]	TiO_2[57]	
	$TiCl_4$	*h* TiB_2[23]	*c* TiC[27]	*c* TiN[35–37]	*c* TiP[48]	*h* TiAs[50]	*h* TiSb[50]	TiO_2, $[Li_2TiO_3]$[57]	
	$ZrCl_4$	*h* ZrB_2[23]	*c* ZrC[27]	*c* ZrN[35–37]	*c* ZrP[48,52]	*h* ZrAs[50]		ZrO_2[57]	
	$HfCl_4$	*h* HfB_2[23]	*c* HfC[27]	*c* HfN[35–37]	*c* HfP[48,52]	*h* HfAs[50]		HfO_2[57]	
Group 5	VCl_3			*c* VN[37]	*h* VP, [*m* VP_2][48]	*o* VAs, [VAs_2][50]		V_2O_3, $[LiVO_2]$[57]	
	VCl_4	*h* VB_2[23]	*c* V_8C_7[27]	*h* β-V_2N[35]/*c* VN[33]	*h* VP[51]	*o* VAs[50]		VO_2, $[Li_3VO_4]$[57]	
	V_2O_5		VSi_2[26]						
	$NbCl_5$	*h* NbB_2[23]	*c* NbC[27]	*c* NbN[35]	*t* NbP[48]	*t* NbAs, *m* $NbAs_2$[50]	*m* $NbSb_2$[50]	$LiNbO_3$[57]	
	Nb_2O_5		$NbSi_2$[26]						
	$TaCl_5$	*h* TaB_2[23]	*c* TaC[27]	*c* TaN (45 kbar)[40]	*t* TaP[48]	*t* TaAs, [*m* $TaAs_2$][50]	*m* $TaSb_2$, [*t* Ta_5Sb_4] [50]	$LiTaO_3$[57]	
	Ta_2O_5		$TaSi_2$[26]						
Group 6	$CrCl_2$	CrB_2, [CrB] [23]	*o* Cr_3C_2		*o* CrP, [*h* $Cr_{12}P_7$][48]				
	$CrCl_3$			Cr_2N[30]/*h* CrN (49 kbar)[40]		*o* CrAs[50]		Cr_2O_3[57]	
	$MoCl_3$		*h* β-MoC_2[27]		*h* MoP[48]	MoAs, Mo_5As_4[50]		MoO_2[57]	
	$MoCl_5$	MoB_2, MoB, Mo[23]		*h* Mo_2N (57 kbar)[40]	*h* MoP[48]			MoO_2[57]	MoS_2[61]/$MoSe_2$[63]/ $MoTe_2$[63]
	MoO_3		*o* α-MoC_2[28]						
	WCl_4		*h* WC[27]/*c* WC[27]	*c* WN (LiCl)[36]	*o* WP[48]	WAs_2[50]		WO_2[57]	
	WCl_6	W_2B_5, WB, W[23]							WS_2[61]/WSe_2[63]/WTe_2[63]
Group 7	$MnCl_2$			*c* Mn_4N[38]					
	MnI_2				*o* MnP, [*h* Mn_2P][48]			MnO, $[Mn_3O_4]$ [57]	
Group 8	FeX_2	*o* FeB[23]						Fe_3O_4 $[Fe_2O_3]$	*c* FeS_2[64]
	$FeCl_3$				*o* FeP, [*h* Fe_2P][48]		*o* $FeSb_2$, [FeSb, Sb][50]		
Group 9	$CoCl_2$				*o* CoP[48]	*o* CoAs, *h* Co_2As[50]	*h* CoSb, [*m* $CoSb_2$][50]	CoO[57]	*c* CoS_2[64]/*h* CoS[64]
Group 10	$NiCl_2$				*h* Ni_2P[48]	$Ni_{11}As_8$, Ni_5As_2[50]	*h* NiSb, *o* $NiSb_2$[50]	NiO[57]	*c* NiS_2[64]
Group 11	CuI				*h* Cu_3P[48]	*h* Cu_3As, Cu[50]		Cu_2O[57]	
Group 12	ZnX_2				*t* Zn_3P_2[48]	*t* Zn_3As_2[50]	Zn_4Sb_3[50]	ZnO[57]	

(*Continued*)

Table 1 (Continued)

		B/Al	*C/Si*	*N*	*P*	*As*	*Sb*	*O*	*S/Se/Te*
		MgB_2 LiAl	*CaC_2/Al_4C_3 $CaSi_2$: Mg_2Si/Li_2Si*	*LiN_3/Na_3N/Ba_2N_3/ Sr_2N Ca_3N_2/Mg_2N_3*	*Li_3P/Na_3P*	*Na_3As*	*Na_3Sb*	*Li_2O*	*Li_2S/NaS/Na_2S Na_2S_5 Li_2Se/Na_2Se Li_2Te/Na_2Te*
Group III	AlX_3			*h* AlN[103]	AlP[46]	AlAs[46]	AlSb[46]		
	GaX_3			*h* GaN ($LiNH_2$: NH_4Cl)[34]	GaP (P)[46]	GaAs[46]	GaSb[46]		
	InX_3			*h* InN, In ($LiNH_2$: NH_4Cl)[34]	InP[46]	InAs, In[46]	InSb, Sb[46]		
Group IV	SnX_4			*s* Sn_3N_4 (2.5 GPa)[43]				SnO_2[58]	SnS_2/$SnSe_2$/ $SnTe_2$[58,64]
Lanthanides	MCl_3			MN[37] (M = La, Nd, Sm, Gd, Tb, Eu)	*c* MP[48] (M = La, Ce, Pr, Nd, Gd, Tb, Dy, Ho, Er, Yb) [45]	*c* MAs[49] (M = La, Pr, Nd, Sm, Gd, Tb, Dy, Er or Yb)	*c* MSb[49] (M = La, Ce, Pr, Nd, Sm, Gd, Tb, Dy, Ho or Er)/*o* Eu_2Sb_3/*t* Y_5Sb_4	M_2O_3 (M = La, Pr, Nd, Eu, Gd, Tb, Dy, Ho or Er)/CeO_2	
Actinides	MCl_4	MB_2[20,22] (M = Th, U, or Pu)		UN, α-U_2N_3[41]/ Th_3N_4, Li_2ThN_2[41]				MO_2 (M = U or Th)	

Forward slashes represent different syntheses. Commas separate multiple phases and square brackets encompass the minority phases produced. Single letters written before each phase represent the symmetry adopted (*c*, cubic; *h*, hexagonal; *m*, monoclinic; *o*, orthorhombic; *s*, spinel; *t*, tetragonal), omissions signify that the symmetry was not specified. Round brackets indicate a specific condition, other than conventional ignition, for the phase to be produced (pressure or dilutant).

where M′ = Ti, Zr, or Hf. Through the use of Hess's law, the exothermicities of reactions involving CaC_2 and Al_4C_3 were predicted. It was found that reactions involving CaC_2 were substantially more exothermic than those involving Al_4C_3 (by $\approx$400 kJ mol^{-1}), thus establishing the reason for the self-propagating nature of CaC_2 reactions over those involving Al_4C_3. SEM imaging of both sets of carbide products showed how agglomerates of particles ranging from 300 to 2000 nm in diameter of faulted flake-like structure had formed. The carbides formed from the aluminum precursor route were substantially more crystalline (average crystallites $\approx$100 nm) than those formed from the calcium precursor (average crystallites $\approx$20 nm) as they were annealed over a period of days.

Nartowski et al. also demonstrated how the group 5 transition metal carbides could be formed from either transition metal chloride[27,29] or oxide precursors.[28] In reacting the transition metal chlorides in a similar fashion to the group 4 chlorides with either CaC_2 or Al_4C_3, the rock-salt crystal phase was adopted. In cases involving Nb or Ta, the typical 1:1 stoichiometric carbide resulted whereas for cases involving V, a substoichiometric carbide formed:

$$8VCl_3 + 12CaC_2 \rightarrow V_8C_7 + 12CaCl_2 + 17\,C \qquad [11]$$

Transition electron microscopy (TEM) showed how the V_8C_7 grains formed regular polyhedrons as opposed to faulted flakes. Even when the vanadium chloride precursor was replaced with an oxide precursor such as V_2O_3 or $NaVO_3$, the substoichiometric vanadium carbide would form.[28] Such SSM reactions were not self-propagating and required annealing at 1000 °C for over 12 h to produce crystalline carbides. This was also apparent for reactions involving lithium niobate, tantalate, or transition metal oxide with the carbon precursor calcium/strontium dicarbide:

$$M'_2O_5 + 5MC_2 \rightarrow 2M'C + 5MO + 8C \qquad [12a]$$

$$2LiM'O_3 + 5MC_2 \rightarrow 2M'C + 5MO + Li_2O + 8C \qquad [12b]$$

where M′ = Nb or Ta and M = Ca or Sr. Within sealed flasks these oxide SSM reactions initiated at around 650 °C, causing some white residue to settle on the cooler regions of the vessel, whereas the solid at the hottest region of the vessel turned black over a period of 20s. The synthesis wave was not accompanied by a flash of light or flame, typical of most SSM processes,[1] but rather a distinct darkening of the product mixture from gray to black was observed. This was due to the lower exothermicity of the oxide metathesis reactions. After cooling and weak acid work-up, the single-phase metal carbides were isolated.

In the case of group 6 transition metal carbide formation, a variety of carbide crystal structures were achieved.[25,27–29] In reactions of $MoCl_3$ with either CaC_2 or Al_4C_3, the β-MoC_2 hexagonal close-packed (HCP) crystal arrangement was formed exclusively over cubic MoC.[25,27,29] However, for the oxide reactions of Li_2MoO_4 and MoO_3 with CaC_2, the orthorhombic α-MoC_2 phase would form.[28] For self-propagating reactions with $MoCl_3$ and CaC_2, elemental Mo contaminants were present in small yield (<10%). For reactions involving tungsten, either the cubic or the hexagonal phase could be achieved depending on the reagents and heating conditions used. In the reactions of WCl_4 and Al_4C_3 and Li_2WO_4 and CaC_2, the hexagonal WC phase would consistently form. However, in the self-propagating reaction of WCl_4 and CaC_2 either the hexagonal or the cubic phase could be formed in majority depending on the type of ignition.[27] In the case of gentle oven heating above 350 °C, cubic WC was isolated, whereas in the case of heated filament ignition, hexagonal WC was the majority phase. The SSM carbide chemistry of Cr was investigated solely for the annealed reaction of $CrCl_2/CrCl_3$ with Al_4C_3, where in either case orthorhombic Cr_3C_2 would form.[27]

Attempts at trying to extend the range of carbides to the latter transition metals failed, where only elemental metals were obtained. This was related to the so-called 'chromium enigma' in which the latter transition metal carbides are either unknown or have very low decomposition temperatures, making their formation by metathesis unfavorable.[85]

2.17.2.2.2 Metal silicides

The transition metal silicides form a class of super-hard and inert materials with high electrical and thermal stabilities.[86] For instance, $MoSi_2$ is a widely used high-temperature heating element, whereas other metal silicides have shown potential for interface diffusion barriers within integrated circuit technology.[87] The high temperature and chemical resistance of these materials is largely due to their protective oxide surface layer.[88] Transition metal silicides are traditionally prepared by a coreduction of SiO_2 with aluminum or carbon, or by direct elemental combination at high temperature. Although several SHS routes to transition metal silicides have been established,[89] SSM pathways are somewhat under-developed.[1] For instance, in their pursuit of a viable SSM route to $MoSi_2$, Kaner et al. reacted $MoCl_5$ with the silicon precursor Mg_2Si.[90] Although $MoSi_2$ was formed, Mo metal was also formed, which was difficult to remove from the product. Parkin et al. also investigated the reactions of $MgSi_2$ with a large range of transition metal chlorides (MCl_n, M = Y, Gd, Dy, Ho, Ti, Zr, Hf, Nb, Ta, Mo, W, Fe, Pt; n = 3, 4, 5).[24] However, the reactions were not self-propagating and even after heat treatment for 10 h at 850 °C single-phase metal silicide products were not formed.

In their experimentation of alternative SSM routes to transition metal silicides, Nartowski et al. found that the use of metal oxide precursors, as opposed to metal halide precursors, resulted in phase-pure silicides.[26] They demonstrated that this variant of the traditional SSM pathway was highly successful in producing phase-pure group 5 disilicides with a variety of silicon precursors ($CaSi_2$: Mg_2Si mixtures and Li_2Si). For reactions involving $CaSi_2$: Mg_2Si mixtures, the ratios were altered to encourage the formation of single-phase disilicide products:

$$M_2O_5 + 2Mg_2Si + CaSi_2 \rightarrow 2MSi_2 + 4MgO + CaO \qquad [13]$$

where M = V, Nb, or Ta. This proved to be a successful strategy for achieving the disilicide for reactions that were initiated by oven heating at 1000 °C in vacuum-sealed ampoules. This was also true for reactions with $LiNbO_3$. All reactions initiated between 450 and 600 °C in the oven and were accompanied by a bright yellow thermal flash. After annealing, the powders were isolated through triturations with dilute HCl (5%), rinses with water, and dryings in vacuo. Reactions that were initiated in air by either a flame (1000 °C) or a nichrome heating filament (800 °C) were also successful in reaching the disilicide

alone, with the exception of reactions with Nb_2O_5 and $LiNbO_3$ where small levels (≈10%) of hexagonal Nb_5Si_3 formed alongside $NbSi_2$. When the silicon precursor Li_2Si was used instead, the reactions were more vigorous and sometimes self-initiated upon grinding (Nb_2O_5, $LiNbO_3$, and $LiTaO_3$). Possibly because of the greater exothermicity of these reactions, phase-pure metal disilicides were consistently formed[26]:

$$M_2O_5 + 4Li_2Si \rightarrow 2MSi_2 + 4Li_2O + \frac{1}{2}O_2 \qquad [14]$$

The enthalpies of formation for reactions with either $CaSi_2$: Mg_2Si mixtures or Li_2Si with the group 5 oxides ranged between −300 and −500 kJ mol^{-1} and were self-sustaining (i.e., self-propagating once initiated). The driving force for each reaction was attributed to co-formation of the oxide by-product (MgO, CaO, and Li_2O). This was analogous to traditional SSM reactions that are driven by the co-formation of salt by-products. The temperature required to initiate a metathesis reaction often correlates with the melting of one of the reagents. However, this rule did not apply to this metal oxide variant of SSM. Nevertheless, the maximum temperatures reached in these reactions were ≈1000 °C (assessed by the color of the flame) and certainly high enough to surpass the solid-state diffusion barrier of the silicon precursors involved.

2.17.2.3 Metal Nitrides

The early transition metals (groups 4 and 5) all form highly stable nitrides.[35] These materials exhibit metallic conductivity and are hard and refractory, with melting points near 3000 °C.[91] They are also chemically resistant and stable at high temperatures in inert or reducing atmospheres[92] and are most commonly used as hard, protective coatings for cutting tools.[93] They are also used as vessels for melting metals and diffusion barriers in microelectronics.[94] Traditionally, nitrides are made by the direct reaction of metals with nitrogen or ammonia at temperatures near 1200 °C for extended periods of time.[95] However, they can be produced in thin-film form by physical[96] or CVD[97] routes at much lower temperatures. SHS routes have also been developed, where metal nitride powders can be formed by heating or igniting fine metal powders in the presence of high nitrogen pressures or by using sodium azide (NaN_3) as a solid nitriding source.[7] Nevertheless, SHS combustion reactions are often incomplete, leaving unreacted metal or lower nitrides in the product.[98] In contrast, SSM routes have recently been developed where a whole range of metal nitrides can be accessed in high yield with controllable physical properties including phase, composition, and microstructure.[30–44]

The group 4 metal nitrides (Ti, Zr, and Hf) have been accessed using a greater range of nitrogen precursors including Li_3N,[36] NaN_3,[35] Ba_2N_3 and Sr_2N,[31] and Ca_3N_2 and Mg_2N_3.[37] Reactions with Li_3N were conducted by Hector et al. by first grinding the nitrogen precursor with the anhydrous metal chloride source under a nitrogen/argon atmosphere, sealing the reagents within a quartz ampoule under vacuum, and then heating the container rapidly to 500 °C.[36] The self-propagating reactions took place between 300 and 400 °C, releasing a bright thermal flash upon initiation:

$$TiCl_3 + Li_3N \rightarrow TiN + 3LiCl \qquad [15a]$$

$$M'Cl_4 + \frac{4}{3}Li_3N \rightarrow M'N + 4LiCl + \frac{1}{2}N_2 \qquad [15b]$$

where M′ = Zr and Hf. Thermal measurements showed that temperatures inside the vessel reached 900–1100 °C. Upon cooling, the fused black solid products were purified by trituration with tetrahydrofuran or methanol and dried in vacuo. The group 4 nitrides adopted FCC rock-salt structures and were of high purity (>99% pure). It was first demonstrated by Kaner et al. that the group 4 nitrides could also be accessed in SSM reactions with NaN_3.[35] Finely ground metal chloride powders were reacted with NaN_3 after ignition with a heated nichrome wire (≈850 °C) inside bomb calorimeters:

$$TiCl_3 + 3NaN_3 \rightarrow TiN + 3NaCl + 4N_2 \qquad [16a]$$

$$M'Cl_4 + 4NaN_3 \rightarrow M'N + 4NaCl + \frac{11}{2}N_2 \qquad [16b]$$

where M′ = Zr and Hf. After cooling, the products were isolated through trituration with methanol, and then water, and subsequently dried in air. Although the rock-salt structure was adopted by all group 4 nitrides accessed by reactions with NaN_3, the crystallites formed were comparatively smaller than those formed through reactions with Li_3N. This was attributed to the increased level of N_2 released in reaction with NaN_3, causing the reactants to spread out, inhibiting thermal transfer.[1] It was also demonstrated by Parkin et al. that the Ti and Hf nitrides could be accessed through SSM reactions with Ca_3N_2 and Mg_3N_2.[37] Reactions were initiated by oven heating to either 500 or 900 °C or ignition from a heated filament. When $TiCl_3$ was reacted with Mg_3N_2 under thermal initiation at 500 °C only a partial reaction occurred, forming TiN in low yield. However, thermal initiation of the same reaction at 900 °C went to completion. Contrastingly, reactions of $TiCl_3$ and Ca_3N_2 went to completion when thermally initiated at either temperature. This difference was attributed to the greater exothermicity of reactions with Ca_3N_2 compared with Mg_3N_2:

$$TiCl_3 + \frac{1}{2}Mg_3N_2 \rightarrow TiN + \frac{3}{2}MgCl_2; \quad \Delta H_r^{\phi} = -345 \text{ kJ mol}^{-1} \qquad [17a]$$

$$TiCl_3 + \frac{1}{2}Ca_3N_2 \rightarrow TiN + \frac{3}{2}CaCl_2; \quad \Delta H_r^{\phi} = -588 \text{ kJ mol}^{-1} \qquad [17b]$$

This explained why reactions with Ca_3N_2 were self-propagating upon ignition with a heated filament whereas those with Mg_3N_2 were not. An SEM image displaying the particulate nature of the TiN powder formed is shown in **Figure 3**.

Forming group 5 mononitrides is certainly not as simple as forming group 4 nitrides as the tendency to form the nitrogen-deficient hexagonal β-M_2N phase increases.[35,37] It was demonstrated by Cai et al. that nanocrystalline VN can be prepared by a thermally initiated (600 °C) liquid–solid SSM reaction between VCl_4 and NaN_3.[33] In trying to avoid the use of VCl_4, a poisonous and corrosive liquid, it was demonstrated that cubic VN could also be accessed from the SSM reaction of VCl_3 with Mg_2N_3[37]:

$$VCl_3 + \frac{1}{2}Mg_3N_2 \rightarrow VN + \frac{3}{2}MgCl_2 \qquad [18]$$

By varying the initiation temperature from 500 to 900 °C, cubic VN with varying crystallinity would form. Contrastingly,

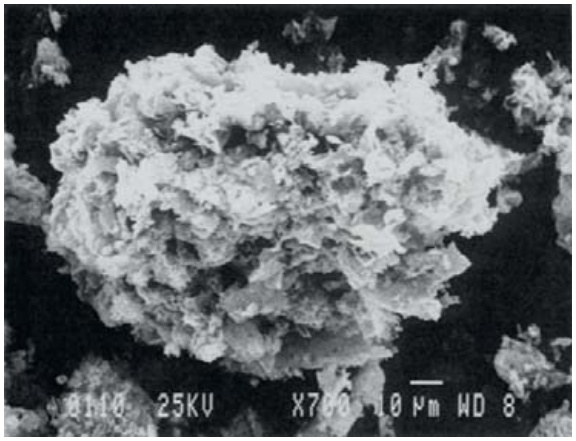

Figure 3 SEM micrograph of the purified TiN powder produced from the reaction of $TiCl_3$ and Ca_3N_2. These micrometer-sized agglomerates are typical of the powders formed from SSM reactions. Reproduced from Hector, A. L.; Parkin, I. P. *Chem. Mater.* **1996**, *7*, 1728, with permission from American Chemical Society.

reactions with Ca_2N_3,[37] Sr_2N,[31] or NaN_3[38] would always form some level of V_2N alongside the cubic VN phase, irrespective of the method of initiation (oven or filament). This was attributed to the greater overall exothermicity of such reactions, where lower maximum temperatures reached in SSM reactions with Mg_2N_3[37] allowed the metastable cubic VN phase to be accessed. However, this method for acquiring mononitrides did not carry forward for the heavier group 5 metals, where neither reaction of $NbCl_5$ or $TaCl_5$ with Ca_2N_3 or MgN_3 would yield the mononitride alone.[37] This was also observed by Gibson et al. for reactions with Li_3N.[19] Nevertheless, the problem of product mixtures in the route to a niobium mononitride was solved by Kaner et al. by mixing the two nitrogen precursors Li_3N and NaN_3 in a specific ratio (2 : 9) with $NbCl_5$ before initiating reactions with a heated nichrome wire (850 °C)[35]:

$$3NbCl_5 + 9NaN_3 + 2Li_3N \rightarrow 3NbN + 9NaCl + 6LiCl + 13N_2 \quad [19]$$

Irrespective of the ratio of Li_3N and NaN_3 used, reactions with $TaCl_5$ did not form the mononitride alone. This was again solved by Kaner et al. by conducting the SSM reaction of $TaCl_5$ and Li_3N under high pressure (45 kbar).[40]

With the exception of chromium, the formation of stable group 6 nitrides by SSM routes has posed a significant challenge. This is due to the 'chromium enigma' and is caused by the lower decomposition temperatures of the latter transition metal nitrides. Where the early transition metal nitrides (M′N = Ti, Zr, Hf, V, Nb, Ta, Cr) decompose at temperatures above 1900 °C, the latter transition metal nitrides typically show decomposition temperatures below 1000 °C. Therefore, accessing the latter transition metal nitrides has been particularly difficult through SSM routes as the high temperatures that are reached lead to the thermal decomposition of the nitride formed.

It was demonstrated that reaction of $CrCl_3$ with Li_3N in a vacuum-sealed vessel at 445 °C leads to the formation of phase-pure Cr_2N.[30] In an attempt to access solely the metastable CrN phase, two routes were developed. One route involved the reaction $CrCl_3$ with the less exothermic nitrogen precursor Mg_3N_2 in conjunction with a $MgCl_2$ dilutant (heat sink). Another route involved the reaction of Cr_2O_3 with Li_3N in a furnace at 500 °C for 2 h. This was the first case in which a nitride had been formed in an SSM reaction using an oxide starting material. Cubic CrN has also been accessed by the high-pressure SSM route, where the reaction of $CrCl_3$ with Li_3N was initiated by an electric current under 49 kbar of pressure.[40] A similar tactic did not produce the molybdenum mononitride but did allow the hexagonal Mo_2N phase to be accessed in the reaction of $MoCl_5$ and Ca_3N_2 under 57 kbar of pressure, where the Li_3N precursor was replaced with Ca_3N_2 as it self-detonated when put in contact with $MoCl_5$. Nevertheless, the tungsten mononitride could be accessed by reacting WCl_4 with Li_3N with an optimum level of LiCl dilutant.[36] Where reactions of WCl_4 with Li_3N produce tungsten metal, as the WN that forms decomposes (650 °C), diluting the reaction lowered the maximum temperature reached and inhibited decomposition. Reactions of $MnCl_2$ with NaN_3 yielded Mn_4N alongside some Mn metal side-product.[38] Replacing the nitrogen precursor for Li_3N led to the formation of Mn_4N only.

Aluminum nitride is an important material for the thermal management of silicon-based electronics, UV photo-detectors, pressure sensors, thermal radiation sensors, and field-effect transistors.[99,100] As traditional routes to AlN, such as ion beam evaporation and carbothermal reduction, are expensive and time consuming,[101] alternative routes have been investigated. Although SHS routes to AlN have been established,[102] the products are generally nitrogen deficient. To counter this, Kaner et al. developed a simple SSM route, where the reaction of $AlCl_3$ with Ca_3N_2 formed phase-pure AlN powders in a matter of seconds.[103] Reactions were conducted inside bomb calorimeters and initiated through ignition with a nichrome wire (850 °C):

$$2AlCl_3 + Ca_3N_2 \rightarrow 2AlN + 3CaCl_2 \quad [20]$$

Temperatures inside the reaction vessel reached 1673 K as quickly as 0.8 s after initiation. Upon substituting the Ca_3N_2 nitrogen precursor in the SSM reaction for Li_3N, a lower maximum temperature was reached, resulting in the incomplete formation of AlN alongside significant levels of Al and Al_2O_3 impurities.

Gallium nitride (GaN) and indium nitride (InN) form an important class of optoelectronic materials.[104] Traditionally, GaN is made by heating Ga metal, Ga_2O_3, or gallium halides at elevated temperatures in ammonia for prolonged periods.[105,106] However, materials synthesized in this manner are often poorly crystalline and display weakened functional properties. More recent synthetic methods include single-source and polymeric precursors, plasma-assisted nitridation, and microwave heating.[107] Conversely, indium nitride (InN) is a difficult material to prepare as it decomposes at a lower temperature.[108] Nevertheless, Kaner et al. demonstrated that both GaN and InN could be obtained through the SSM route.[34] When the reaction of just GaI_3 and Li_3N was ignited by a heated nichrome wire (850 °C) within their bomb calorimeter vessel, a mixture of both GaN and $LiGaN_2$ products resulted. As the maximum temperature observed from in situ measurements was shown to reach 1337 K, dilutants were added to encourage the formation of GaN alone. The SSM reaction of a series of combinations

of GaI_3, Li_3N and $LiNH_2$, and NH_4Cl dilutants was undertaken until the optimum ratio was found:

$$6GaI_3 + 6Li_3N + 3LiNH_2 + 4NH_4Cl \rightarrow 6GaN + 18LiI + \text{by-products} \quad [21]$$

At this optimum ratio, an almost 80% yield of crystalline HCP GaN was achieved. More surprisingly, crystalline InN could be formed by the same approach, where the optimum ratios of reagents were:

$$2InI_3 + Li_3N + 3LiNH_2 + NH_4Cl \rightarrow 2InN + 6LiI + 3NH_3 + HCl \quad [22]$$

This reaction produced crystalline InN in more than 83% yield. Converse to reactions with GaI_3, In metal formed as a side-product but could be removed with iodine in tetrahydrofuran (generating InI_3; see also **Chapter 1.31**).

Several SSM reactions have been carried out in an attempt to develop a simple, low-temperature route to silicon nitride.[109] Although repeated efforts were made by Anderson et al., they were unable to achieve the Si_3N_4 spinel compound by the SSM route. Nevertheless, Li_2SiN_2, a fast ion conductor material, was achieved instead through the reactions of $SiCl_4$/SiI_4 and Li_3N:

$$SiX_4 + 2Li_3N \rightarrow Li_2SiN_2 + 4LiX \quad [23]$$

where X = Cl or I. The reactions were initiated by microwave radiation and took anywhere between 1 and 3 min to activate and self-propagate. By adding $LiNH_2$ and NH_4Cl dilutants into these reactions, the formation of the unwanted $LiSi_2N_3$ side-product was avoided. On the other hand, the spinel Sn_3N_4 structure could be accessed by high-pressure SSM.[43] This was achieved by Petuskey et al. with the use of a piston-cylinder apparatus where SnI_4 was reacted with Li_3N and NH_4Cl dilutant at a pressure of 2.5 GPa and initiated at a temperature of 350 °C:

$$3SnI_4 + 4Li_3N + xNH_4Cl \rightarrow Sn_3N_4 + 12LiI + x\,NH_4Cl \quad [24]$$

The products were first washed and centrifuged in 3 M HCl to remove the residual Sn metal by-product, followed by rinsing with water and then methanol.

Substituted silicon nitrides have attracted attention as alternative thermal conductors, where $MgSiN_2$ has shown the most promise.[110,111] Traditionally, $MgSiN_2$ is reached through the heating of the spinel silicon nitride with either Mg_2Si or Mg_3N_2 at 1200 °C for several hours under nitrogen. Given the difficulty of acquiring the spinel silicon nitride used in this process, this route to the substituted silicon nitride is costly. It was found that the ternary nitride $MgSiN_2$ could be formed far more simply by the SSM route.[32] This was accomplished by initiating the self-propagating reaction of SiO_2 with Mg_3N_2 by a flame (1100 °C):

$$SiO_2 + Mg_3N_2 \rightarrow MgSiN_2 + 2MgO; \quad \Delta H_r^{\phi} = -141 \text{ kJ mol}^{-1} \quad [25]$$

When the reaction was initiated, the pellet glowed red and streams of gas were emitted. It was found that reacting the silica and nitrogen precursor in a 1: 2 ratio produced $MgSiN_2$ in highest yield (70%) with little silicon metal impurities. It was also found that initiating the reaction with hotter flames (2500–3300 °C) inhibited the silicon impurity from forming.

Many of the lanthanide nitrides have also been accessed by SSM routes. Hector et al. demonstrated that LaN and SmN could be accessed through reactions of the metal chloride ($LaCl_3$ and $SmCl_3$) with NaN_3.[38] Reactions were conducted within vacuum-sealed ampoules and then heated to between 300 and 400 °C to initiate the reaction. In both cases, the rock-salt structured mononitride was formed (LaN and SmN) where enthalpies of reaction approximated by Hess's law reached $\Delta_f^{\phi} \approx -900 \text{ kJ mol}^{-1}$. It was also shown by Gibson et al. that LaN could be achieved through the reaction of $LaCl_3$ and Li_3N when heated to 500 °C under a continuous flow of nitrogen[19]:

$$LaCl_3 + Li_3N \rightarrow LaN + 3LiCl \quad [26a]$$

Using either Ca_3N_2 or Mg_2N_2 nitrogen precursors, Hector et al. demonstrated that a series of lanthanide nitrides could be formed[37]:

$$2M'Cl_3 + M_3N_2 \rightarrow 2M'N + 3MCl_2 \quad [26b]$$

where M = Ca or Mg and M′ = Nd, Sm, Gd, Tb, or Eu. Reactions were initiated at 500 °C where Ca_3N_2 was used or at 900 °C where Mg_2N_2 was used. Reactions with Ca_3N_2 were exothermic and required lower ignition temperatures to self-propagate. However, greater activation energy for reactions with Mg_2N_2 was required as the enthalpies of formation were in fact slightly endothermic, although entropically favored.

Thorium and uranium nitrides could be formed through SSM reactions of the actinide chloride and Li_3N in vacuum-sealed ampoules at 500 °C.[41] The reactions were accompanied by a thermal flash lasting for 2–3 s, during which time the ampoule glowed orange–red in color as the reaction proceeded through the bulk of the solid. The reactions took less than 2 min to complete. The nitrides formed were purified through trituration with tetrahydrofuran or methanol, yielding particulate micrometer-sized agglomerates. The reaction of UCl_4 with Li_3N yields the nonstoichiometric sesquinitride phase (α-U_2N_3) as well as the mononitride (UN):

$$3UCl_4 + 4Li_3N \rightarrow U_2N_3 + UN + 12LiCl \quad [27a]$$

thus indicating partial reduction of the metal. The reaction of $ThCI_4$ and Li_3N produced two phases as well (Th_3N_4 and Li_2ThN_2), though no reduction of thorium was observed:

$$4ThCl_4 + 6Li_3N \rightarrow Th_3N_4 + Li_2ThN_2 + 16LiCl \quad [27b]$$

Transition metal nitride solid solutions can also be obtained through SSM reactions if there is a strong lattice match between components. For instance, solid solutions of Ti–V–N have been obtained through liquid–solid SSM reactions of $VCl_{4(l)}$, $TiCl_{4(l)}$, and $Li_3N_{(s)}$[11] or solid–solid reactions of VCl_3, $TiCl_3$, and Li_3N.[42] Similarly, solid solutions of lanthanide nitrides have also been achieved through SSM.[1] However, the criteria for solubility are mainly dependent upon the matching of the ionic radii of the lanthanides involved as opposed to lattice matching. It has been found that forming solid solutions through SSM reactions was best achieved by using miscible liquid-metal halides.

The α-polymorph of carbon nitride (C_3N_4) was accessed by Margrave et al. through the SSM reaction of cyanuric chloride

or its fluoro analog with lithium nitride under highly exothermic conditions.[112] This low-cost synthetic route to stoichiometric carbon nitride α-C_3N_4 in gram quantities facilitated the extensive studies of bulk processing and electromechanical properties, and high pressure/temperature transformation of this material into its super hard and highly inaccessible crystalline polymorphic phases (see also Chapter 7.14).

2.17.2.4 Metal Phosphides, Arsenides, and Antimonides

2.17.2.4.1 Metal phosphides

Metal phosphides are known for all the transition metal elements, adopting a variety of structures and stoichiometries.[113] They have been used as fumigants, phosphane release pesticides, flares, and for their semiconducting properties.[114] Transition metal phosphides have been made by a variety of methods, the most direct being the combination of the metal with elemental phosphorus at >1400 °C for several days. To alleviate such prolonged high-temperature syntheses, self-propagating SSM methods have been developed, covering almost all of the transition metals available (M′ = Y, La, Ti, Zr, Hf, V, Nb, Ta, Cr, Mo, W, Mn, Fe, Co, Ni, Cu, Zn).[48] This was achieved through the simple SSM reaction of the transition metal halide with stoichiometric levels of sodium phosphide (Na_3P). Reactions were contained in vacuum-sealed ampoules and initiated through thermal heating in a tube furnace at 550 °C (with the exception of those reactions that initiated upon contact) and annealed for a further 4 h to increase crystallinity. Upon cooling, the phosphides were separated from their salt by-products through triturations with methanol. All phosphides formed were agglomerates of micrometer-sized particles with rough, porous surface microstructures of high crystallinity, with average crystallite sizes ranging from 250 to 750 Å.

The group 3 and 4 transition metal phosphides were formed from reactions of the metal chloride and Na_3P:

$$M'Cl_3 + Na_3P \rightarrow M'P + 3NaCl \quad [28a]$$

where M′ = Y or La.

$$3M'Cl_4 + 4Na_3P \rightarrow 3M'P + 12NaCl + P \quad [28b]$$

where M′ = Ti, Zr, or Hf. All the group 3 and 4 metal phosphides formed adopted the cubic rock-salt structure. However, in the case of group 4 reactions, the metal was reduced from the +4 to the +3 state to form the mono-phosphide, which resulted in the co-formation of elemental phosphorus. This did not lead to a contaminated product as the phosphorus sublimed out due to the high temperatures reached (maximum temperature ≈ 1400 °C). It was also demonstrated by Kaner et al. that group 4 phosphides could be formed through reactions with Li_3P[52]:

$$3M'Cl_4 + 4Li_3P \rightarrow 3M'P + 12LiCl + P \quad [28c]$$

where M′ = Zr or Hf. It was also shown by Kaner et al. that the high temperatures reached in such SSM reactions were not responsible for the formation of the observed metastable cubic phase. By simply adding inert salt dilutants to the reaction mixtures before ignition, the maximum temperature reached during each SSM synthesis could be lowered in a controlled fashion. However, the formation of the cubic phase was still apparent, even with the heaviest of loadings despite the hexagonal phase being more thermodynamically stable. Templating was also ruled out by using lattice-mismatched KCl and hexagonal ZnS as additives. The direct synthesis of the high-temperature cubic phase was thought to be due to the nucleation of the metastable cubic form at high-temperature pockets, which is then trapped upon rapid cooling. The hexagonal phase could be reached by annealing the group 4 phosphides at 1000 °C for 18 h or carrying out SSM reactions in sealed ampoules at 1000 °C. However, liquid–solid metathesis reactions of $TiCl_4$ and Na_3P resulted in the direct formation of the thermodynamically stable hexagonal TiP phase.[51]

The group 5 phosphides were accessed through reactions of the metal chloride and Na_3P[48]:

$$VCl_3 + Na_3P \rightarrow VP + 3NaCl \quad [29a]$$

$$3M'Cl_5 + 5Na_3P \rightarrow 3M'P + 15NaCl + 2P \quad [29b]$$

where M′ = Nb or Ta. In the case of vanadium, the hexagonal phosphide was formed in addition to small amounts of the monoclinic side-product, VP_2. In the case of niobium and tantalum, tetragonal phosphides were formed. In addition to this phase difference, reactions involving niobium and tantalum self-initiated upon light grinding. Such reactions were accompanied by a bright white flash and the sublimation of the salt by-product, in addition to elemental phosphorus, onto the walls of the glovebox in which they were mixed. Liquid–solid metathesis reactions of VCl_4 and Na_3P avoided the formation of any VP_2 side-product and resulted in the sole formation of the thermodynamically stable hexagonal VP phase.[51]

The group 6 phosphides of chromium, molybdenum, and tungsten could also be formed in a similar manner. It was found in the reaction of $CrCl_2$ that orthorhombic CrP would form alongside trace amounts of hexagonal $Cr_{12}P_7$. The reaction of WCl_4 was self-initiating and led to the formation of the orthorhombic WP phase as well. However, both reactions of molybdenum chlorides yielded hexagonal MoP. Interestingly, it was found that the reaction of $MoCl_5$ with Na_3P would self-initiate; yet the reaction of $MoCl_3$ required ignition. This was attributed to the increased volatility of $MoCl_5$ over $MoCl_3$. In fact, all reactions that self-initiated could be ascribed to the comparatively greater volatility of the metal halide (this includes $NbCl_5$, $TaCl_5$, WCl_4, and $FeCl_3$). The reactions of the group 7 MnI_2 and the group 8 $FeCl_3$ resulted in the formation of the orthorhombic mono-phosphide (M′P) alongside low levels of a hexagonal dimetal phosphide (M'_2P). In the case of the reaction of the group 9 $CoCl_2$, solely the orthorhombic mono-phosphide formed. Group 10 $NiCl_2$ and group 11 CuI yielded hexagonal di and trimetal phosphides respectively, whereas group 12 $ZnCl_2$ formed a tetragonal Zn_3P_2 structure.

Hess law calculations of the SSM reaction of transition metal halides with Na_3P indicate that reactions were highly exothermic (Δ_f^o ranging from −300 to −600 kJ mol^{-1}). Upon initiation, a bright white flash was observed (≈1400 °C) for a few seconds before subsiding. Given that the phosphide-rich phases of the transition metals are known to decompose thermally to

the metal mono-phosphide and phosphorus, it was not surprising that most of the products generated in these SSM reactions were primarily composed of the mono-phosphide.

Lanthanide phosphides display enhanced optical, electronic, and magnetic properties in relation to other rock-salt cubic compounds.[115] They have been made in various ways, the most direct being the combination of a lanthanide with red phosphorus at 1400 °C, requiring several days to form crystalline products.[116] Other methods include reactions of phosphane with the metal or metal oxides, but again require high temperature for prolonged periods. To provide an alternative route to these prolonged syntheses, SSM pathways were developed for forming lanthanide phosphides to attain a whole host of highly crystalline materials.[45] This was achieved by reacting lanthanide chlorides mixed with stoichiometric amounts of Na_3P in vacuum-sealed ampoules at 700–800 °C in a tube furnace for 4 h:

$$LnCl_3 + Na_3P \rightarrow LnP + 3NaCl \quad [30]$$

where Ln = Ce, Pr, Nd, Gd, Tb, Dy, Ho, Er, Yb. The resulting phosphide was present as a fused black material at the base of the reaction vessel, whereas the salt by-product had largely sublimed onto the walls. Simple triturations with methanol allowed the two materials to be separated. All lanthanide phosphide materials consisted of FCC rock-salt structures with lattice constants similar to those in the literature. The SSM reactions initiated at ≈550 °C after which a self-propagating wave proceeded through the source. The initiation temperature also corresponded with the melting points of the lanthanide halides and suggests that this molten state is necessary to overcome the solid-state diffusion barrier for the reaction to self-propagate. This was corroborated by the failed attempts to initiate reactions through continuously milling. Hess law calculations demonstrated the exothermicity of reactions, where the reaction of $LaCl_3$ and Na_3P was predicted to have a formation enthalpy of ≈−300 kJ mol^{-1}.

Continued annealing at 700–800 °C was required to form crystalline lanthanide phosphide materials from the SSM reactions. By varying the length of annealing between 2 and 5 h, the average crystallite size of the phosphide formed could be controlled, ranging between ≈250 and 750 Å, respectively. It was also demonstrated by Kaner et al. that specifically GdP could be formed through the SSM reaction of GdI_3 with Na_3P.[47] In their study, a variety of initiation conditions and annealing temperatures were applied, and the physical and functional properties of the resulting antiferromagnetic phosphide material were compared. It was thus shown that GdP produced by SSM routes with as little as 12 h of postannealing could show properties analogous to GdP produced through traditional routes that required 100 h of annealing.

The group IIIb semiconductors are extensively applied in electronic and optoelectronic materials.[117] Early synthetic approaches to these materials resembled traditional solid-state methods where the respective elements were heated (typically above 1000 °C) in evacuated, sealed ampoules for long periods of time (typically several days). Frequently the products are inhomogeneous, the reactions are incomplete, and the products become fused with the silica ampoules. To alleviate these issues, SSM pathways to the group III phosphides were developed with the use of the phosphorus precursor, Na_3P.[46] Two distinct routes were examined: one in which the reactions were initiated inside a bomb calorimeter using a nichrome wire (≈850 °C) and another in which the reactions were vacuum-sealed inside glass ampoules and heated to a set temperature for several hours. The products were extracted after grinding and then washing in air with methanol, water, and diethyl ether to remove the sodium halide and unreacted starting reagents.

In their efforts to form AlP from AlI_3 and Na_3P, it was found that bomb ignition yielded a completely amorphous product. However, heating the reaction at 990 °C for 42 h yielded crystalline AlP:

$$AlI_3 + Na_3P \rightarrow AlP + 3NaI \quad [31a]$$

Attaining GaP was simpler, and could be reached through both bomb ignition and thermal initiation with GaF_3, $GaCl_3$, and GaI_3:

$$GaX_3 + Na_3P \rightarrow GaP + 3NaX \quad [31b]$$

where X = F, Cl, or I. Interestingly, it was found that the conditions for initiation changed with the halide used, where the more volatile chloride (mp = 78 °C) reacted upon stirring, the less volatile iodide (mp = 212 °C) reacted upon grinding, and the least volatile fluoride (mp > 900 °C) required ignition with a heated wire. Reactions were highly exothermic, reaching maximum temperatures near 1700 °C. Comparing the thermal reaction of GaI_3 with that of AlI_3, a lower thermal initiation (220 °C) and annealing time (8 h) was required to form crystalline GaP. Nevertheless, some level of Ga metal and red phosphorus would form and this was attributed to the decomposition of GaP. This could be circumvented by adding a red phosphorus dilutant into the reaction mixture, increasing insulation, and reducing the maximum temperatures reached inside the reaction vessel. It was also demonstrated that InP could be formed through reactions of Na_3P with either InF_3 or InI_3:

$$InX_3 + Na_3P \rightarrow InP + 3NaX \quad [31c]$$

where X = F or I. Incomplete reactions were observed for bomb-ignited reactions involving the iodide, where InI_2 side-products formed alongside In metal and red phosphorus. Thermally initiated reactions above 600 °C yielded crystalline InP alone.

2.17.2.4.2 Metal arsenides and antimonides

A range of transition metal pnictides (As and Sb) were synthesized through the exothermic self-propagating reactions of Na_3As/Na_3Sb with the metal chloride.[50] A range of transition metal arsenides M_xAs_y (M = Y, La, Ti, Hf, V, Nb, Ta, Cr, Mo, W, Mn, Fe, Co, Ni, Pt, Cu, and Zn) and antimonides M_xSb_y (M = Ti, V, Nb, Ta, Cr, Fe, Co, Ni, Pt, Cu, and Zn) were formed. Reactions would sometimes self-initiate but generally required heating (up to 550 °C) to surpass the activation energy for self-propagation.

Solid–liquid metathesis reactions of $TiCl_{4(l)}$ with Na_3As were also conducted.[51] The reactions would self-initiate upon contact producing a red–white flash and instant sublimation of the salt by-product (NaCl) and elemental As onto the sides of the flask. The room-temperature initiation was attributed to the high surface area solid–liquid contact between the

reagents as compared to analogous solid-state reactions that often require heating (400–600 °C) to overcome the solid-state diffusion barrier.[89] The reactions were highly exothermic with formation enthalpies of ≈ -600 kJ mol^{-1} predicted by Hess's law. In this solid–liquid metathesis reaction, the thermodynamically stable hexagonal phase of TiAs was formed. Similar reactions of the heavier pnictides (Na_3Sb and Na_3Bi) did not yield the Ti pnictide as the majority phase. In the case of Na_3Sb, some TiSb and $TiSb_2$ were observed in low yield; yet the main product was elemental Sb. In the case of Na_3Bi, only Bi metal formed alongside the chloride. Indeed, the voracity of the liquid–solid metathesis reactions visibly decreased from arsenide to bismuthide, where the decreased exothermicity of the heavier pnictide reactions resulted in little formation of the crystalline pnictide. It was suggested that additional annealing would be required to form the heavier Ti pnictides. Solid–liquid metathesis reactions of $VCl_{4(l)}$ with Na_3As were also examined by Parkin et al., leading to the exclusive formation of the hexagonal VAs phase.[51] Reactions with the heavier Na_3Sb and Na_3Bi pnictides resulted in the majority formation of elemental Sb (with trace VSb_2) or Bi. Given the simplicity of forming well-mixed reactions where metal precursors in liquid form are involved, several mixtures of $TiCl_{4(l)}$ and $VCl_{4(l)}$ were reacted with Na_3As to form $Ti_xV_{1-x}As$ solid solutions. In the case of $Ti_{0.25}V_{0.75}As$ and $Ti_{0.5}V_{0.5}As$, hexagonal structures were adopted. However, in the case of $Ti_{0.75}V_{0.25}As$ an orthorhombic structure was adopted.

Lanthanide pnictides (Ln_xE_y where E = As, Sb, Bi) are excellent phosphorescent materials and were used extensively in cathode-ray-tube television sets until the late 1990s as well as semiconducting devices. Such materials have traditionally been prepared by mixing the individual elemental components at high temperatures ($\approx$ 1200 °C) or by using extremely toxic compounds of arsine and antimony at lower temperatures. Low-temperature SSM pathways were developed to access these compounds more readily (550–900 °C, 2–4 h, 80% yield).[49]

A series of lanthanum arsenide compounds were synthesized by reaction of the lanthanum chloride with Na_3As in vacuum-sealed ampoules at 700–800 °C for 2–4 h:

$$LnCl_3 + Na_3As \rightarrow LnAs + 3NaCl \qquad [32a]$$

where Ln = Pr, Nd, Sm, Gd, Tb, Dy, Er, or Yb. The self-propagating reactions produced a fused black solid at the bottom of the ampoule (LnAs) that could be fully purified from the salt by-product (NaCl) that had partially sublimed onto the walls through triturations with methanol and dryings in vacuo. All arsenides adopted the cubic rock-salt structure with average crystallite sizes ranging from 150 to 400 Å. The magnetic moments of the compounds increased across the group from 3.8 μ_B at PrAs to 10 μ_B at ErAs in concordance with the literature.

The lanthanum antimonide compounds were accessed through reactions of the lanthanum chloride with Na_3Sb in vacuum-sealed ampoules at 550–900 °C for 3 h:

$$LnCl_3 + Na_3Sb \rightarrow LnSb + 3NaCl \qquad [32b]$$

where Ln = Y, La, Ce, Pr, Nd, Sm, Eu, Gd, Tb, Dy, Ho, Er, or Yb. The rock-salt structure was adopted by all antimonides formed, with the exception of Eu and Yb, forming the orthorhombic Eu_2Sb_3 and tetragonal Y_5Sb_4 structures, respectively. It is well known that Eu and Yb show anomalous chemistry within the lanthanides as they form comparatively stable M^{2+} complexes. However, the formation of Eu_2Sb_3 was somewhat surprising given that the reaction of Na_3P or Na_3As with $EuCl_3$ yields the cubic phases of EuP and EuAs, respectively.[45] The magnetic moment of Eu_2Sb_3 (7.6 μ_B) clarified the formation of a mixed-valence species (Eu^{2+} and Eu^{3+}). Similarly, the magnetic moment of the Yb_5Sb_4 phase (1.4 μ_B) confirmed the presence of a mixture of Yb^{2+} and some Yb^{3+} species. It was also demonstrated that ternary lanthanide pnictides could be formed containing either mixed pnictides or mixed metals. Solid solutions could only be formed where an analogous phase was observed between the two individual components being combined. In addition to this, the ionic radii should be of similar size. The reaction of these lanthanide halides with Na_3E (E = P, As, or Sb) was found to be exothermic through Hess law calculations ($\Delta_f^{\circ} = -130$ to -300 kJ mol^{-1}). Indeed, the SSM reactions could only occur at, or above, the melting points of the lanthanide halides involved (600–800 °C), indicating that a melt was required to overcome the solid-state diffusion barrier for the reaction.

The group III arsenides and antimonides were accessed by Kaner et al. through the SSM reactions of metal fluorides and iodides with either Na_3As or Na_3Sb, respectively[46]:

$$MX_3 + Na_3E \rightarrow ME + 3NaX \qquad [33]$$

where M = Al, Ga, or In, X = F or I and E = As or Sb. Two methods were used to achieve this, where either a bomb-type calorimeter was loaded with the material and ignited using a heated nichrome wire or the reagents were vacuum sealed in glass ampoules, and ignited and annealed through oven heating (220–950 °C). Products were purified by washing with methanol, water, and then diethyl ether.

Bomb ignition of $AlCl_3$ and Na_3As failed to produce any crystalline material. However, bomb ignition of $AlCl_3$ and Na_3Sb produced AlSb alongside elemental Al and Sb side-products. The thermal heating of both reactions above 550 °C for over 17 h produced crystalline AlAs and AlSb with only traces of elemental side-products. Bomb ignitions of GaI_3 with Na_3As and Na_3Sb resulted in the respective GaAs and GaSb materials; however, trace Ga metal was present as a side-product. By using GaF_3 instead of the iodide, the level of Ga metal side-product could be substantially reduced. Irrespective of this, annealing these reactions led to the formation of the purest product, where heating GaI_3 with Na_3As at 950 °C for 8 h produced pure GaAs. Bomb ignitions of InI_3 with Na_3As resulted in incomplete reactions that formed InAs alongside InI_2 and In metal. Replacing InI_3 for InF_3 countered this and resulted in the formation of InAs alongside In metal alone. Thermal reactions could not completely hinder In metal from forming alongside the arsenide product, even when heated for more than 12 h at 600 °C. An opposite effect was observed when trying to form the antimonide, where annealing InI_3 with Na_3Sb (550 °C for 12 h) resulted in the formation of InSb alongside elemental Sb as opposed to In metal (see also Chapter 2.05).

2.17.2.5 Metal Oxides

Metal oxides of various formulations are known for all of the transition metal elements.[118] They have widespread technological importance in catalysis,[119] as ceramics,[120] and functional

thin-film coatings.[121] More recently, interest in mixed-metal oxide materials for their high-temperature superconducting properties has increased.[122] Transition metal oxides have traditionally been made by heating in air, often at high temperatures. Given the refractory nature of some metal oxides, this often involves prolonged heating to produce crystalline, defect-free, materials. However, new developments in metal/mixed-metal oxide synthesis have reduced the temperature requirements for production, including molecular precursor chemistry,[123] sol–gel,[124] chemical vapor[125] and bath deposition,[126] and hydrothermal processes.[127] In addition to these routes, several SSM pathways have also been developed.[41,54–60] In fact, the earliest example of an SSM route to a metal oxide was demonstrated by Hilpert et al. in 1932, who reported the preparation of mixed-metal ferrates through the reaction of metal chlorides with lithium ferrate at 400–500 °C.[128] After the more recent developments in SHS chemistry, SSM routes to metal oxides experienced a renaissance. SSM pathways to most transition metal oxides,[56,57] some post-transition metal (Sn and Pb) oxides,[58] many lanthanide oxides,[53] and some actinide (U and Th) oxides[41] have been established where the use of the oxygen precursor Li_2O was used exclusively when reacted with the metal halide:

$$MX_n + \frac{n}{2}Li_2O \rightarrow MO_{n/2} + nLiX \quad [34]$$

where M = Ti, Zr, Hf, V, Nb, Ta, Cr, Mo, W, Mn, Fe, Ru, Os, Co, Rh, Ir, Ni, Pd, Pt, Cu, Zn, Hg, Sn, Pb, La, Ce, Pr, Nd, Eu, Gd, Tb, Dy, Ho, Er, U, or Th; X = Cl or I; n = 2, 3, 4, or 5. In each case, the metal chloride and oxygen precursor were first mixed by thorough grinding and then vacuum sealed in glass ampoules. After ultrasound sonication (10 min) the reactions were initiated by oven heating (400–500 °C) and annealed at that temperature for anywhere between 2 and 10 h. The reactions proceeded without an external thermal flash, forming a fused gray lump at the base of the vessel alongside the sublimed lithium halide by-product on the walls of the ampoule. Products were purified in a number of ways including triturations with water, dilute HCl, methanol, or tetrahydrofuran. In cases where some metal side-product formed, aqua regia work-up was necessary. Ceramic yields after purification ranged between 60% and 90%, depending on the sample (**Table 2**).

In most cases, the transition metal halides reacted with Li_2O to form the metal oxide without any observable redox chemistry at the metal. Exceptions were observed for reactions of $TiCl_4$, Na_3IrCl_6, $PdCl_2$, MnI_2, and the groups 5 and 8 chlorides where the lithium metallate, a more oxidized form (Mn_3O_4/

Table 2 A list of the metal oxide products formed (composition, color, yield, and reaction time) from the respective chloride in SSM reactions with Li_2O performed by Parkin et al.[41,53,56–58]

Group	*Metal chloride*	*Metal oxide*	*Color*	*Yield (%)*	*Reaction time (h)*
4	$TiCl_4$	TiO_2 (Li_2TiO_3)	White	60	2 (450 °C)[57]
	$TiCl_3$	TiO_2	White/gray	60	2
	$ZrCl_4$	ZrO_2	Gray	65	2
	$HfCl_4$	HfO_2	Gray	65	2
5	VCl_4	VO_2 (Li_3VO_4)	Black	55	2
	VCl_3	V_2O_3 ($LiVO_2$)	Black	60	2
	$NbCl_5$	$LiNbO_3$	Light gray	90	2
	$TaCl_5$	$LiTaO_3$	Gray	90	2
6	$CrCl_3$	Cr_2O_3	Gray	60	10
	$MoCl_5$	MoO_2	Brown	65	10
	$MoCl_3$	MoO_2	Black	70	10
	WCl_4	WO_2	Black	70	2
7	MnI_2	MnO (Mn_3O_4)	Brown	85	2
8	$FeCl_3$	Fe_3O_4 (Fe_2O_3)	Dark brown	80	2
	K_2RuCl_6	RuO_2, Ru	–	60–90	5 (400 °C)[56]
	K_2OsCl_6	OsO_2, Os	–	60–90	5
9	$CoCl_2$	CoO	Brown	85	10 (450 °C)[57]
	$RhCl_3$	$LiRhO_2$	–	60–90	5 (400 °C)[56]
	Na_3IrCl_6	IrO_2 (Ir)	–	60–90	5
10	$NiCl_2$	NiO	Light green	75	10 (450 °C)[57]
	$PdCl_2$	PdO (Pd)	–	60–90	5 (400 °C)[56]
	K_2PtCl_4	Pt_3O_4 (Pt)	–	60–90	5 (400 °C)[56]
11	CuI	Cu_2O	Yellow	40	2 (450 °C)[57]
12	$ZnCl_2$	ZnO	Light gray	90	2
	$HgCl_2$	HgO	Yellow	45	10
IV	SnI_4	SnO_2	White	–	5 (550 °C)[58]
	$PbCl_2$	Pb_2O_2Cl (Pb)	Orange	20	5
Lanthanides (La, Ce[a], Pr, Nd, Eu, Gd, Tb, Dy, Ho, Er)	$LnCl_3$	Ln_2O_3	White	–	10 (500 °C)[53]
Actinides (U, Th)	$AcCl_4$	AcO_2	White		2 (500 °C)[41]

[a]CeO_2 formed as opposed to the sesquioxide; minor phases are shown in brackets.

Fe_2O_3), or metallic impurities were produced alongside the metal oxide. Although metal impurities could be removed through aqua regia washings, the alternative oxide products were usually inseparable. For reactions of Li_2O with the group IV halides, SnI_4 formed SnO_2 alone; however, $PbCl_2$ formed Pb_2O_2Cl alongside some metal impurity in poor yield (20%) through disproportionation. In the lanthanide reactions, the sesquioxide Ln_2O_3 was formed in all cases except for CeO_2 and was attributed to the comparatively greater stability of the +4 oxidation state of Ce. Nevertheless, some reactions formed a competing side-product, LnOCl:

$$(x+y)\mathrm{LnCl} + \frac{z}{2}\mathrm{Li_2O} \rightarrow x\mathrm{LnOCl} + y\mathrm{Ln_2O_3} + z\mathrm{LiCl} \qquad [35]$$

where Ln = La, Pr, Nd, Eu, or Gd. The heats of formation, as predicted by Hess's law, ranged between −100 and −600 kJ mol^{-1}, depending on the metal. In situ temperature measurements revealed that the reactions were self-propagating after initiation at 250 °C. Attempts to produce mixed-metal oxides by reaction of Li_2O with a mixture of two anhydrous metal chlorides was unsuccessful, even when the temperature was raised from 450 to 900 °C.

Several alternative SSM routes to transition metal oxides were demonstrated by Kaner et al.[59] Using a variety of copper halide (CuCl, $CuCl_2$, K_3CuF_6, and CuF_2) and oxygen precursors (Na_2O_2, Na_2O, or KO_2), they demonstrated that either pure CuO or a variety of CuO: Cu_2O mixtures could be formed. The reactions were conducted in bomb calorimeters and ignited with a hot filament alone (no oven annealing) that was followed by a bright red propagation wave that engulfed the reagents in a matter of seconds. In the reactions of K_3CuF_6 or CuF_2 with Na_2O_2, purely CuO was formed. When CuF_2 was reacted with KO_2 or Na_2O, CuO:Cu_2O mixtures were formed in a 3:1 and 5:4 ratio, respectively. However, when CuCl or $CuCl_2$ was reacted with Na_2O_2, CuO:Cu_2O mixtures formed in a 3:2 and 2:1 ratio, respectively. SSM routes to alternative transition metal oxides were then examined using the oxygen precursor Na_2O_2. Kaner et al. found that the reactions of $ZrCl_4$, $CrCl_3$, $FeCl_3$, and $ZnCl_2$ yielded the oxide alone, without any redox chemistry. This was contrary to the finding of Hector et al., where the reaction of $FeCl_3$ with the oxygen precursor Li_2O would form the oxide in addition to Fe_3O_4 in small amounts.[57] However, reactions of NiF_2 with Na_2O_2 did not produce a crystalline product,[59] whereas the reaction of $NiCl_2$ with Li_2O formed crystalline NiO.[57] It was also demonstrated by Kaner et al. that the group 4 oxides of Zr and Hf could be formed from the SSM reaction of the metal halide with Na_2O.[60] Interestingly, it was shown how exothermic these oxide-forming SSM reactions could be, where temperatures of 1350 °C were reached (see also **Chapter 1.33**).

2.17.2.6 Metal Sulfides, Selenides, and Tellurides

Binary transition and main-group metal chalcogenides have varied technological application owing to their wide range of semiconducting properties.[129] Metal chalcogenides have been formed in bulk through a number of processes including organometallic precursor decomposition,[130] electro-deposition from solution,[131] and elemental combination at elevated temperatures.[132] Hydrogen sulfide and selenide have widely been employed in the synthesis of metal chalcogenides through reactions with aqueous metal cations, metal oxides, and sol–gel processing.[133] Most procedures require multiple steps, extended processing, carefully tailored precursors, and/or the use of highly toxic reagents.[1] To bypass some of the difficulties of traditional synthesis, new SSM methods were developed to access a number of transition metal chalcogenides.[61–63] This was first demonstrated in their synthesis of NiS_2 from the reactions of K_2NiF_6 with a range of sulfur precursors (NaS, Na_2S, and Na_2S_5).[61] They found that pure NiS_2 could be synthesized from reactions with hydrated Na_2S_5 when initiated through oven heating at 65 °C in vacuum-sealed glass ampoules:

$$\mathrm{K_2NiF_6} + 2\mathrm{Na_2S_5}.0.06\mathrm{H_2O} \rightarrow \mathrm{NiS_2} + 4\mathrm{NaF} + 2\mathrm{KF} + 8\mathrm{S} + 0.06\mathrm{H_2O} \qquad [36]$$

The product was purified by trituration with water, alcohol, and then ether. Any residual sulfur could also be removed with carbon disulphide washings. Increasing the hydration of the Na_2S_5 or lowering the oxidation state of the nickel precursor from Ni(IV) to Ni(III) led to a less crystalline product. In addition, SSM reactions with lower content sulfiding agents, such as NaS or Na_2S, led to NiS: NiS_2 mixtures. With this proof of principle, Kaner et al. applied their SSM approach to metal sulfide synthesis to form the industrially important materials MoS_2 and WS_2 through reactions with Na_2S[62]:

$$\mathrm{MoCl_5} + \frac{5}{2}\mathrm{Na_2S} \rightarrow \mathrm{MoS_2} + 5\mathrm{NaCl} + \frac{1}{2}\mathrm{S}; \quad \Delta H_r^{\phi} = -728 \text{ kJ mol}^{-1} \qquad [37a]$$

$$\mathrm{WCl_6} + 3\mathrm{Na_2S} \rightarrow \mathrm{WS_2} + 6\mathrm{NaCl} + \mathrm{S}; \quad \Delta H_r^{\phi} = -1055 \text{ kJ mol}^{-1} \qquad [37b]$$

Reactions were highly exothermic and required little thermal agitation (40–60 °C) to be ignited. This was accompanied by a bright thermal flash where maximum temperatures reached ≈1050 °C. In forming MoS_2, a mixture of the two polymorphs 2H and 3R resulted as opposed to traditional high-temperature synthesis where merely the 2H polymorph is formed. When the sulfur content of the precursor was increased (i.e., Na_2S was replaced with Na_2S_2 or Na_2S_5), a less crystalline product formed and was related to the increased formation of the sulfur by-product acting as a heat sink. It was found that the diselenides and ditellurides could be accessed in a similar fashion.[63] The diselenides could be formed through reactions of $MoCl_5$/WCl_6 with Na_2Se in a bomb calorimeter that was ignited using a heated filament. However, the ditellurides required much higher temperatures for extended periods to form, where the metal chloride was annealed at 1000 °C for 7 days with the tellurium source, Na_2Te. Attempts at forming the ditellurides through bomb activation instead led to the formation of Mo_3Te_4 in majority for the case of $MoCl_5$ and W metal in majority for the case of WCl_6. Products could be separated through triturations with water and methanol. By simply mixing the chalcogenide precursors (Na_2E, where E = S, Se, Te), they found that a range of ternary metal dichalcogenides could also be accessed.

Using a similar approach, Parkin et al. demonstrated that Sn and Pb chalcogenides could also be formed using SSM

chemistry.[58,64] Using lithium-based chalcogenide precursors instead of sodium (Li_2E, where E = S, Se, Te), single-phased tin dichalcogenide (SnE_2) or lead chalcogenide (PbE) materials were accessed:

$$SnI_4 + 2Li_2E \rightarrow SnE_2 + 4LiI \quad [38a]$$

where E = S or Se.

$$PbCl_2 + Li_2E \rightarrow PbE + 2LiI \quad [38b]$$

where E = S, Se, or Te. Reactions were conducted in vacuum-sealed glass ampoules after 10 min of sonication. Ignition was achieved through conventional oven heating (550 °C for 5 h). Higher temperatures were required to activate these SSM chalcogenide formation reactions compared with those of Kaner et al.,[61–63] as the associated formation enthalpies were far lower (-200 kJ mol^{-1} as opposed to less than -700 kJ mol^{-1}). The products were purified through triturations with either methanol or dilute HCl. The nanocrystalline powders (average crystallite sizes ranging from 300 to 600 Å) were composed of sub-micrometer agglomerates of particles. Several transition metal chalcogenides were also accessed through the SSM route by Parkin et al.[64] using sulfur precursors more familiar to Kaner et. al.'s synthesis of the Ni, Mo and W dichalcogenides.[61–63] Reactions were ignited by oven heating at a lower temperature (300 °C) for a longer period of time (48 h). The disulfides of Fe, Co, and Ni were formed through reactions of the metal chloride with Na_2S_2:

$$MX_2 + Na_2S_2 \rightarrow MS_2 + 2NaX \quad [39]$$

where $MX_2 = FeBr_2$, $CoCl_2$, or $NiCl_2$. The mono-sulfides of Co and Ag were formed through reactions of the metal chloride with Na_2S:

$$2AgF + Na_2S \rightarrow Ag_2S + 2NaF \quad [40a]$$

$$CoCl_2 + Na_2S \rightarrow Co_{1-x}S + 2NaCl + xCo \quad [40b]$$

where $x = 0.05$. In reactions [39] and [40], a dark wave passed through the reagents upon ignition (rather than a bright solid flame). This occurred once the surroundings reached ≈200 °C, irrespective of the metal halide used. The propagation of a dark wave was attributed to the comparatively low heats of formation (-200 to -250 kJ mol^{-1}) that could not sufficiently support a solid flame.[134] The black product that formed at the base of the ampoule was separated from the salt by triturations with water. Simply replacing the sulfur precursor with the selenide precursor Na_2Se led to the successful formation of a series of transition metal selenides, where interestingly, the mono-selenide formed in each case (M′Se, where M′ = Ag_2, Fe, or Ni). Replacing this precursor with the telluride precursor Na_2Te led to only partial success, forming the mono-telluride effectively for reactions with $NiCl_2$, $SnBr_2$, and AgF but forming a split product (the mono-telluride alongside elemental transition metal in a 1:1 ratio) for reactions with $FeBr_2$ and $CoCl_2$ (see also Chapter 1.32).

2.17.2.7 New Directions in Metathesis Reactions

Over the last decade, there have been several new developments in the field of metathesis, which can be separated into five distinct categories: solution-mediated metathesis,[135–139] carbon nanotube synthesis,[65,66] nanocrystal growth,[67,68] molecular precursor approaches,[140,141] and complex materials synthesis.[16]

2.17.2.7.1 Solution-mediated metathesis

One of the most interesting new directions in the field has been solution-mediated metathesis. In such procedures, the metathesis reaction is conducted within a liquid medium as opposed to the traditional solid state. This was first demonstrated by Dines et al. in the late 1970s, where a range of transition metal disulfide compounds were synthesized from reactions of tetravalent metal chlorides (Ti, Zr, Hf, V, and Mo) with Li_2S/Na_2S when refluxed in a range of organic media (THF, ethyl acetate, and acetonitrile).[135] The disulfides formed could be accessed at mild temperatures (25–100 °C) offering a distinct advantage over traditional preparation methods. Although the materials formed were primarily amorphous, some of the amorphous phases had never previously been observed. This new route paved the way for more economical routes to solid-state materials with physical properties (surface area, crystallinity, particle size, phase, and stoichiometry) that could be controlled by altering the preparation conditions (reflux temperature/time, solvent, reagent, and postcalcination). Their pioneering work was followed by Wells et al. in their solvent-mediated metathesis of group III pnictides (P and As).[142] In refluxing (2–12 h) the alkali metal pnictide with a soluble ligand-coordinated group III halide in a suitable solvent (toluene, monoglyme, and diglyme), nanoparticulate and monodisperse GaP, InP, and GaAs were formed. By simply changing the solvent and reaction time, the size of the nanoparticles could be altered. A series of ternary copper–indium chalcogenides were formed through the metathical reactions of $CuBr/CuCl_2$ and $InCl_3$ with a sodium chalcogenide (Na_2E, E = S, Se, Te) within a toluene medium (reflux, 72 h).[137] Applying this method further, a more extensive range of transition metal chalcogenides and pnictides was formed in a variety of media (toluene, ammonia, and *n*-butyl amine) and the reactions were termed solvent-based metathesis.[136,138,139]

2.17.2.7.2 Carbon nanotubes

Since the discovery of multiwalled and single-walled carbon nanotubes, there has been a great research effort in aid of understanding and applying their remarkable mechanical, thermal, and electrical properties.[143] To date, carbon nanotubes have only been commercially applied as additives in bulk resins and polymers to increase mechanical strength and in scanning tunneling and atomic force microscope tips. Nevertheless, the potential is there for future nanoscale electronic device[144] and hydrogen storage media[145] applications among others. Carbon nanotubes are typically synthesized by time, energy, and/or cost-intensive processes.[146] Kaner et al. demonstrated that carbon nanotubes could be made quite simply using the SSM route (**Figure 4**).[65,66] This was achieved through the reaction of hexachloroethane (C_2Cl_6) and lithium acetylide (Li_2C_2) in the presence of a 5 mol% $CoCl_2$ catalyst, producing a powder of mixed single and multiwalled nanotubes (7% nanotube yield)[66]:

$$C_2Cl_6 + 3Li_2C_2 \rightarrow 8C + 6LiCl \quad [41]$$

The reaction was highly exothermic ($\Delta_f^{\circ} = -2057$ kJ mol^{-1}) with a theoretical maximum reaction temperature (T_{ad}) of 2029 °C. The temperatures reached approached the

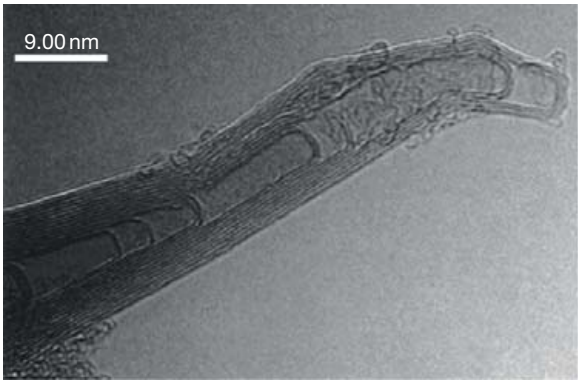

Figure 4 TEM image of a multiwalled carbon nanotube synthesized by the SSM reaction between C_2Cl_6, Li_2C_2, and 5 mol% $CoCl_2$ catalyst. Reproduced from Loughlin, J. L. O.; Kiang, C.; Wallace, C. H.; Reynolds, T. K.; Rao, L.; Kaner, R. B. J. Phys. Chem. B 2001, 105, 1921, with permission from American Chemical Society.

graphitization temperature of carbon (2300 °C) and explained why crystalline graphite could be formed in a matter of seconds from this reaction. As the $CaCl_2$ catalyst boils at 1049 °C, it was suggested that the nanotubes were catalyzed in the vapor phase. By decreasing the catalyst loading, lower levels of single-walled nanotubes were formed. When the catalyst loading was increased, the preference of graphite nanoparticle formation increased until no presence of nanotube growth was observed (>10 mol% $CaCl_2$). Alternative transition metal compounds such as CoS, $FeCl_2$, and $NiCl_2$ also served as effective carbon nanotube formation catalysts. However, a FeS catalyst (6 mol%) improved the synthetic yield more than threefold (25% nanotube yield).[66] In addition, the carbon precursor could be substituted by the cheaper alternative, CaC_2, without significantly affecting the yield. In these reactions, the theoretical maximum reaction temperature (T_{ad}) increased to 3550 °C with a heat of formation of −1992 kJ mol^{-1} (see also Chapter 9.34).

2.17.2.7.3 Nanocrystals

The development of novel methods for the controlled growth of materials at the nanoscale is of intense current interest. More recently, the SSM route has been utilized to form materials on the nanoscale (nanocrystals).[67,68] This was demonstrated by Xue et al. in their SSM synthesis of a range of nanocrystal materials.[67] By simply reacting hydrated transition metal salts or hydroxides with the appropriate precursor, a variety of nanoparticulate media could be formed outside of solution. Reactions would self-initiate upon mixing and could be carried out in air. Although the reactions were not vigorous (temperatures <80 °C), the nanocrystals would form rapidly (10 s to 30 min) in high yield (over 90%). For instance, nanocrystals of CuO could be formed in three ways through reactions of NaOH with hydrated copper (II) chloride, dinitrate, and tetra-amine. In each case, nanoparticulate and monodisperse CuO spheres were formed, ranging from 20 nm on average when $CuCl_2$ was used to 80 nm on average when $[Cu(NH_3)_4]SO_4$ was used. A series of metal sulfide nanoparticles (40–50 nm) were also formed by this route, where hydrated Na_2S is reacted with a transition metal dihydroxide:

$$M(OH)_2 + Na_2S.9H_2O \rightarrow MS + 2NaOH + 9H_2O \qquad [42]$$

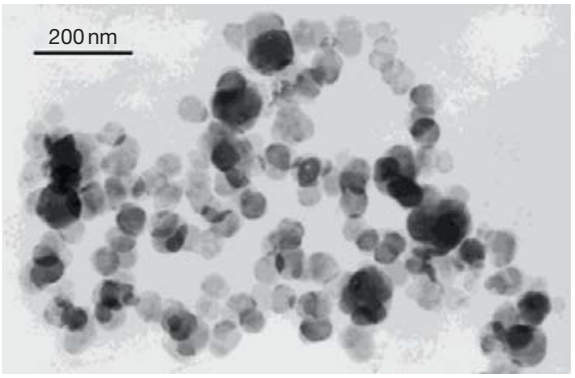

Figure 5 TEM image of CdS nanocrystals prepared by the one-step SSM reaction of $Cd(OH)_2$ and hydrated Na_2S in air at ambient pressure. Ye, X. R.; Jia, D. Z.; Yu, J. Q.; Xin, X. Q.; Xue, Z. *Adv. Mater.* **1999**, *11*, 941, with permission from Wiley.

where M = Cu, Zn, Cd, or Pb (Figure 5).

In addition, a series of oxalates, carbonates, and hydroquinoline nanoparticulate solids were formed. It was thus demonstrated that nanoparticulate materials, some being useful semiconductors, could be rapidly synthesized in air under ambient conditions without the requirement of pyrophoric/toxic chemicals and a broad scope for application and scale-up. It was also demonstrated by Cressey et al. that nanocrystals of Si and Ge could also be formed by the SSM route.[68] Their synthesis involved the SSM reaction of polyanionic Zintl phases of Si and Ge (Zintl NaA, where A = Si or Ge) with metal halides or ammonium salts. These Zintl phases contain tetrahedra of the group IV ions (i.e., Si_4^{4-}/Ge_4^{4-}) that are charge stabilized by four surrounding Na^+ ions. Metathesis reactions were conducted inside sealed glass tubes at temperatures ranging from 200 to 500 °C for periods ranging between 10 and 20 h. Nanocrystals could be formed through the reaction of a Zintl phase with CuBr:

$$CuBr + \text{zintl NaA} \rightarrow NaBr + A + Cu \qquad [43a]$$

where A = Si or Ge. In order to avoid acid work-up for removing metal by-products, ammonium salts could be used instead of metal halides:

$$NH_4Br + \text{Zintl NaA} \rightarrow NaBr + A + NH_{3(g)} + \frac{1}{2}H_{2(g)} \qquad [43b]$$

where the by-products of NH_3 and H_2 are expelled from the system during the course of the reaction and the salt could be easily washed from the semiconductor through trituration. TEM studies showed that the Si/Ge materials that formed were nanoparticulate. However, they were formed within a bulk Si/Ge matrix. Reactions conducted at lower temperatures (200–300 °C) led to a primarily amorphous product that became crystalline at higher reaction temperatures (400–500 °C). Given the industrial use of both crystalline and amorphous group IV semiconductors, this SSM route provides a convenient avenue to either material.

2.17.2.7.4 Molecular precursor approaches

Another interesting application of metathesis has been the development of pseudomolecular precursor approaches to forming ceramics. This was demonstrated by Rowley et al. in

their synthesis of transition metal nitrides from reactions of the metal halide with lithium amide (160–400 °C).[140,141] This produced a material that was rich in nitrogen, where gentle thermolysis yielded the metal nitride. As such reactions are less exothermic than those of lithium nitride (traditional SSM route), nitrogen-rich phases such as Ta_3N_5 could be isolated[141] as well as thermally sensitive phases such as Zn_3N_2.[140]

2.17.2.7.5 Complex materials

Wide-scale application of SSM routes to complex metal oxides is unlikely in preference to the number of other methods available, especially as the reactions have no clear advantage over traditional production methods. Circumventing this, more recent examples have been directed at forming more complex classes of mixed-metal oxide materials such as the perovskites[55] and hydroxyapatite[54], where the characteristics of SSM synthesis are exploited. For instance, Gopalakrishnan et al. devised SSM routes to perovskite oxides of current interest, exploiting the characteristic of SSM reactions in forming sub-micrometer-sized particles at temperatures lower than conventional routes. Lanthanum metallates were formed by reacting the lithium transition metal oxide with LaOCl at 810–850 °C for 12 h in air:

$$LiM'O_2 + LaOCl \rightarrow LaM'O_3 + LiCl \qquad [44a]$$

where M′ = Mn or Co. A series of other useful perovskite structures were formed through a more traditional SSM reaction with an alkaline earth-metal chloride:

$$Li_2M'O_3 + MCl_2 \rightarrow MM'O_3 + 2LiCl \qquad [44b]$$

where M′ = Ti or Mn and M = Ca, Sr, or Ba. In addition, the popular piezoelectric material lead zirconate titanate was also formed by the SSM route:

$$Li_2M'O_3 + PbSO_4 \rightarrow PbM'O_3 + Li_2SO_4 \qquad [45]$$

where M′ = Ti and/or Zr. In adapting SSM pathways to form hydroxyapatite, Ray et al. developed a novel microwave-initiated synthesis.[54] This was achieved by simply microwaving calcium chloride ($CaCl_2$) and sodium phosphate (Na_3PO_4) in air for 30 min:

$$10CaCl_2 + 6Na_3PO_4 + 2H_2O \rightarrow Ca_{10}(PO_4)_6(OH)_2 + 18NaCl + 2HCl \qquad [46]$$

They also demonstrated that when either Na_2CO_3 or NaF was added with $CaCl_2$ into the SSM reaction, a carbonate- or fluoride-substituted hydroxyapatite would result. This simple method demonstrated the versatility of SSM. It also presented an economical method for the potential large-scale production of nano-sized hydroxyapatite powders. Additional examples of complex materials synthesis include the formation of rare earth nitrido-borates,[147] cyanamides,[16] cyanoborates,[148] and carbon nitride nanotubes.[149]

2.17.3 Conclusion

SSM reactions enable a wide range of inorganic materials to be made in seconds, typically at far lower temperatures than traditional routes. Products of SSM reactions are easily purified and are usually very pure products with little chemical contamination. The inbuilt heat brake afforded by the co-produced alkali metal halide regulates the maximum reaction temperature and often allows metastable phases to be isolated where conventional SHS does not. In some cases, SSM reactions have provided routes to new phases. Furthermore, the co-produced salt can provide a template that promotes metathesis products of the same crystal structure. The use of dilutants (heat sinks) has also allowed metastable compounds to be accessed. The high-pressure SSM route has also been particularly useful in isolating crystalline materials where the adiabatic reaction temperature exceeds the decomposition temperature.

Traditional SSM reactions are performed on the gram scale and in many cases would be impractical for industrial scale-up, especially given the voracity of typical reactions and handling issues concerning some of the highly oxidizing reagents involved. Another limitation of SSM is the incomplete understanding of the reaction mechanism. Both ionic and reductive recombination pathways have been suggested (eqn [2]); however, the speed of the reaction has made elucidating the reaction pathway highly difficult. Nevertheless, current progress in the field has demonstrated how nanoscale materials such as nanoparticles and nanocrystals can be formed at low temperatures with the capacity for practical and economically viable scale-up.

References

1. Parkin, I. P. *Chem. Soc. Rev.* **1996**, *25*, 199.
2. Dimitriev, Y.; Ivanova, Y.; Iordanova, R. *J. Univ. Chem. Technol. Metallurgy* **2008**, *43*, 181.
3. Feng, S.; Xu, R. *Acc. Chem. Res.* **2001**, *34*, 239.
4. Corriu, R. J. P. *Angew. Chem.* **2000**, *39*, 1376.
5. Merzhanov, A. G. *Ceram. Int.* **1995**, *21*, 371.
6. Merzhanov, A. G. *J. Mater. Chem.* **2004**, *14*, 1779.
7. Yi, H. C.; Moore, J. J. *J. Mater. Sci.* **1990**, *25*, 1159.
8. Holt, J. B.; Dunmead, S. D. *Annu. Rev. Mater. Sci.* **1991**, *21*, 305.
9. Fitzmaurice, J. C.; Hector, A.; Parkin, I. P. *Polyhedron* **1993**, *12*, 1295.
10. Anderson, A. J.; Blair, R. G.; Hick, S. M.; Kaner, R. B. *J. Mater. Chem.* **2006**, *16*, 1318.
11. Hector, A.; Parkin, I. P. *J. Chem. Soc. Chem. Commun.* **1993**, 1095.
12. Treece, R. E.; Macala, G. S.; Kaner, R. B. *Chem. Mater.* **1992**, *4*, 9.
13. Bonneau, P. R.; Jarvis, R. F.; Kaner, R. B. *Nature* **1991**, *349*, 510.
14. Parkin, I. P. *Transit. Metal Chem.* **2002**, *27*, 569.
15. Blair, R. G.; Kaner, R. B. *Solid-State Synthesis. Aldrich Chemfiles* **2005**, *5*, 9.
16. Meyer, H.-J. *Dalton Trans.* **2010**, *39*, 5973.
17. Gillan, E. G.; Kaner, R. B. *Chem. Mater.* **1996**, *8*, 333.
18. Hu, J. Q.; Deng, B.; Zhang, W. X.; Tang, K. B.; Qian, Y. T. *Chem. Phys. Lett.* **2002**, *351*, 229.
19. Gibson, K.; Ströbele, M.; Blaschkowski, B.; Glaser, J.; Weisser, M.; Srinivasan, R.; Kolb, H.-J.; Meyer, H.-J. *Z. Anorg. Allg. Chem.* **2003**, *629*, 1863.
20. Lupinetti, A. J.; Fife, J.; Garcia, E.; Abney, K. *AIP Conference Proceedings* **2000**, *532*, 127–129.
21. Blair, R. G.; Gillan, E. G.; Nguyen, N. K. B.; Daurio, D.; Kaner, R. B. *Chem. Mater.* **2003**, *15*, 3286.
22. Lupinetti, A. J.; Fife, J. L.; Garcia, E.; Dorhout, P. K.; Abney, K. D. *Inorg. Chem.* **2002**, *41*, 2316.
23. Rao, L.; Gillan, E. G.; Kaner, R. B. *J. Mater. Res.* **1995**, *10*, 353.
24. Fitzmaurice, J. C.; Hector, A. L.; Parkin, I. P.; Rowley, A. T. *Phosphorus, Sulfur, Silicon Relat. Elem.* **1995**, *101*, 47.
25. Parkin, I. P.; Nartowski, A. T. *J. Mater. Sci. Lett.* **1999**, *18*, 267.
26. Nartowski, A. M.; Parkin, I. P. *Polyhedron* **2002**, *21*, 187.
27. Nartowski, A. M.; Parkin, I. P.; Mackenzie, M.; Craven, A. J.; Oaj, W. C. H. *J. Mater. Chem.* **1999**, *9*, 1275.
28. Nartowski, A. M.; Parkin, I. P.; Craven, A. J.; Oaj, W. C. H. *J. Mater. Chem.* **2001**, *11*, 3116.

29. Nartowski, A. M.; Parkin, I. P.; Craven, A. J.; Mackenzie, M. *Adv. Mater.* **1998**, *10*, 805.
30. Aguas, M. D.; Nartowski, A. M.; Parkin, I. P.; MacKenzie, M.; Craven, A. J. *J. Mater. Chem.* **1998**, *8*, 1875–1880.
31. Ali, S.; Aguas, M. D.; Hector, A. L.; Henshaw, G.; Parkin, I. P. *Polyhedron* **1997**, *16*, 3635.
32. Blair, R. G.; Anderson, A.; Kaner, R. B. *Chem. Mater.* **2005**, *17*, 2155.
33. Cai, P.; Yang, Z.; Wang, C.; Xia, P.; Qian, Y. *Mater. Lett.* **2006**, *60*, 410.
34. Cumberland, R. W.; Blair, R. G.; Wallace, C. H.; Reynolds, T. K.; Kaner, R. B. *J. Phys. Chem. B* **2001**, *105*, 11922.
35. Gillan, E. G.; Kaner, R. B. *Inorg. Chem.* **1994**, *33*, 5693.
36. Hector, A. L.; Henshaw, G.; Komarov, A. V.; Parkin, I. P. *J. Mater. Process. Technol.* **1998**, *77*, 103.
37. Hector, A. L.; Parkin, I. P. *Chem. Mater.* **1996**, *7*, 1728.
38. Hector, A. L.; Parkin, I. P. *Polyhedron* **1995**, *14*, 913.
39. Janes, R. A.; Low, M. A.; Kaner, R. B. *Inorg. Chem.* **2003**, *42*, 2714.
40. O'Loughlin, J. L.; Wallace, C. H.; Knox, M. S.; Kaner, R. B. *Inorg. Chem.* **2001**, *40*, 2240.
41. Parkin, I. P.; Fitzmaurice, J. C. *J. Mater. Sci. Lett.* **1994**, *13*, 1185.
42. Parkin, I. P.; Hector, A. *J. Mater. Sci. Lett.* **1993**, *12*, 1856.
43. Shemkunas, M. P.; Wolf, G. H.; Leinenweber, K.; Petuskey, W. T. *J. Am. Ceram. Soc.* **2004**, *85*, 101.
44. Treece, R. E.; Gillan, E. G.; Kaner, R. B. *Comm. Inorg. Chem.* **1995**, *16*, 313.
45. Rowley, A. T.; Parkin, I. P. *J. Mater. Chem.* **1993**, *3*, 689.
46. Treece, R. E.; Macala, G. S.; Rae, L.; Franke, D.; Eckert, H.; Kaner, R. B. *Inorg. Chem.* **1993**, *32*, 2745.
47. Treece, R. E.; Conklin, J. A.; Kaner, R. B. *Inorg. Chem.* **1994**, *33*, 5701.
48. Hector, A. L.; Parkin, I. P. *J. Mater. Chem.* **1994**, *4*, 279.
49. Fitzmaurice, J. C.; Parkin, I. P.; Rowley, A. T. *J. Mater. Chem.* **1994**, *4*, 285.
50. Hector, A. L.; Parkin, I. P. *Z. Naturforsch. B: J. Chem. Sci.* **1994**, *49*, 477.
51. Hector, A. L.; Parkin, I. P. *Inorg. Chem.* **1994**, *33*, 1727.
52. Jarvis, R. F.; Jacubinas, R. M.; Kaner, R. B. *Inorg. Chem.* **2000**, *39*, 3243.
53. Rowley, A. T.; Parkin, I. P. *Inorg. Chim. Acta* **1993**, *211*, 77.
54. Parhi, P.; Ramanan, A.; Ray, A. *Mater. Lett.* **2004**, *58*, 3610.
55. Mandal, T. K.; Gopalakrishnan, J. *J. Mater. Chem.* **2004**, *14*, 1273.
56. Hector, A. L.; Parkin, I. P. *J. Mater. Sci. Lett.* **1994**, *13*, 219.
57. Hector, A.; Parkin, I. P. *Polyhedron* **1993**, *12*, 1855.
58. Parkin, I. P.; Rowley, A. T. *Polyhedron* **1993**, *12*, 2961.
59. Wiley, J. B.; Gillan, E. G.; Kaner, R. B. *Mater. Res. Bull* **1993**, *28*, 893.
60. Gillan, E. G.; Kaner, R. B. *J. Mater. Chem.* **2001**, *11*, 1951.
61. Bonneau, P. R.; Shibao, R. K.; Kaner, R. B. *Inorg. Chem.* **1990**, *29*, 2511.
62. Bonneau, P. R.; Jarvis, R. F.; Kaner, R. B. *Nature* **1991**, *349*, 510.
63. Bonneau, P. R.; Jarvis, R. F.; Kaner, R. B. *Inorg. Chem.* **1992**, *31*, 2127.
64. Shaw, G. A.; Morrison, D. E.; Parkin, I. P. *J. Chem. Soc. Dalton Trans.* **2001**, *1872*.
65. Loughlin, J. L. O.; Kiang, C.; Wallace, C. H.; Reynolds, T. K.; Rao, L.; Kaner, R. B. *J. Phys. Chem. B* **2001**, *105*, 1921.
66. Mack, J. J.; Tari, S.; Kaner, R. B. *Inorg. Chem.* **2006**, *45*, 4243.
67. Ye, X. R.; Jia, D. Z.; Yu, J. Q.; Xin, X. Q.; Xue, Z. *Adv. Mater.* **1999**, *11*, 941.
68. McMillan, P. F.; Gryko, J.; Bull, C.; Arledge, R.; Kenyon, A. J.; Cressey, B. A. *J. Solid State Chem.* **2005**, *178*, 937.
69. Levine, J. B.; Tolbert, S. H.; Kaner, R. B. *Adv. Funct. Mater.* **2009**, *19*, 3519.
70. Wendt, H.; Reuhl, K.; Schwarz, V. *J. Appl. Electrochem.* **1992**, *22*, 161.
71. Su, K.; Sneddon, L. G. *Chem. Mater.* **1991**, *3*, 10.
72. Bates, S. E.; Buhro, W. E.; Frey, C. A.; Sastry, S. M. L.; Kelton, K. F. *J. Mater. Res.* **1995**, *10*, 2599.
73. Axelbaum, R.; Bates, S.; Buhroi, W.; Frey, C.; Kelton, K.; Lawton, S.; Rosen, L.; Sastry, S. *Nanostruct. Mater.* **1993**, *2*, 139.
74. Weimer, A. W. *Carbide Nitride and Boride Materials Synthesis and Processing*. Chapman and Hall: London, 1997; p. 671.
75. Khanra, A.; Pathak, L. C.; Mishrab, S. K.; Godkhindia, M. M. *Mater. Lett.* **2004**, *58*, 733.
76. Patterson, A. *Phys. Rev.* **1939**, *56*, 978.
77. Dimiduk, D. M. *Mater. Sci. Eng. A* **1999**, *263*, 281.
78. Fleischer, R. L. *J. Mater. Sci.* **1987**, *22*, 2281.
79. Han, W. B.; Wang, Z. J.; Wu, D. Z.; Wang, G. F. *Mater. Sci. Forum* **2007**, *551–552*, 467.
80. Calderón, H. A.; Garibay-Febles, V.; Cabrera, A. F.; Cabañas-Moreno, J. G.; Umemoto, M. *J. Metast. Nanocryst. Mater.* **2001**, *10*, 229.
81. Kopit, Y. *Intermetallics* **2001**, *9*, 387.
82. Hardt, A. P.; Holsinger, R. W. *Combust. Flame* **1973**, *21*, 91.
83. Oyama, S. T. *Catal. Today* **1992**, *15*, 179.
84. Lee, J. S. In *Encyclopedia of Catalysis*; Horváth, I., Ed.; John Wiley and Sons: Hoboken, NJ, 2002.
85. Craevn, A. J. *J. Microsc.* **1995**, *180*, 250.
86. Topor, L.; Kleppa, O. J. *Metall. Trans. A* **1986**, *17*, 1217.
87. Chandrasekharaiah, M. S.; Margrave, J. L.; O'Hare, P. A. G. *J. Phys. Chem. Ref. Data* **1993**, *22*, 1459.
88. Weaver, J.; Franciosi, A.; Moruzzi, V. *Phys. Rev. B* **1984**, *29*, 3293.
89. Yi, H.; Moore, J. J. *J. Mater. Sci.* **1990**, *25*, 1159.
90. Wiley, J. B.; Kaner, R. B. *Science* **1992**, *255*, 1093.
91. Toth, L. E. *Transition Metal Carbides and Nitrides (Refractory Materials Monograph)*; Academic Press: New York, 1971.
92. Blocher, J. M. In *High Temperature Technology*; Campbell, I. E., Ed.; John Wiley and Sons: New York, 1956; p 171.
93. Buhl, R.; Pulker, H. K.; Moll, E. *Thin Solid Films* **1981**, *80*, 265.
94. Wang, S.-Q.; Raaijmakers, I.; Burrow, B. J.; Suthar, S.; Redkar, S.; Kim, K.-B. *J. Appl. Phys.* **1990**, *68*, 5176.
95. Weimer, A. W., Ed.; In *Carbide, Nitride, and Boride Materials Synthesis and Processing*; Chapman and Hall: London, 1997.
96. Aronson, A. J.; Chen, D.; Class, W. H. *Thin Solid Films* **1980**, *72*, 535.
97. Kafizas, A.; Hyett, G.; Parkin, I. P. *J. Mater. Chem.* **2009**, *19*, 1399.
98. Deevi, S.; Munir, Z. A. *J. Mater. Res.* **1990**, *5*, 2177.
99. Fuflyigin, V.; Salley, E.; Osinsky, A.; Norris, P. *Appl. Phys. Lett.* **2000**, *77*, 3075.
100. Djurisic, A. B.; Bundaleski, N. K.; Li, E. H. *Semicond. Sci. Tech.* **2001**, *16*, 91.
101. Zhu, Q.; Jiang, W. H.; Yatsui, K. *J. Appl. Phys.* **1999**, *86*, 5279.
102. Munir, Z. A.; Holt, J. B. *J. Mater. Sci.* **1987**, *22*, 710.
103. Janes, R. A.; Low, M. A.; Kaner, R. B. *Inorg. Chem.* **2003**, *42*, 2714–2719.
104. Ponce, F. A.; Bour, D. P. *Nature* **1997**, *386*, 351.
105. Elwell, D.; Feigelson, R. S.; Simkins, M. M.; Tiller, W. A. *J. Cryst. Growth* **1984**, *66*, 45.
106. Addamiano, A. *J. Electrochem. Soc.* **1961**, *108*, 1072.
107. Hwang, J.-W.; Campbell, J. P.; Kozubowski, J.; Hanson, S. A.; Evans, J. F.; Gladfelter, W. L. *Chem. Mater.* **1995**, *7*, 517.
108. Krukowski, S.; Witek, A.; Adamczyk, J.; Jun, J.; Bockowski, M.; Grzegory, I.; Lucznik, B.; Nowak, G.; Wroblewski, M.; Presz, A.; Gierlotka, S.; Stelmach, S.; Palosz, B.; Porowski, S.; Zinn, P. *J. Phys. Chem. Solids* **1998**, *59*, 289.
109. Anderson, A. J. *Metathesis routes to binary and ternary silicon nitrides*. UCLA: Los Angeles, CA, 2005.
110. Slack, G. *J. Phys. Chem. Solids* **1973**, *34*, 321.
111. Bruls, R. J.; Hintzen, H. T.; Metselaar, R.; Cees van Miltenburg, J. *J. Phys. Chem. B* **1998**, *102*, 7871.
112. Khabashesku, V. N.; Zimmermann, J. L.; Margrave, J. L. *Chem. Mater.* **2000**, *12*, 3264.
113. Ertl, G., Knozinger, H., Schoth, F., Weitkamp, J., Eds.; In *Handbook of Heterogeneous Catalysis*; Wiley-VCH Verlag: Weinheim, 2008.
114. Aronsson, B.; Lundström, T.; Rundqvist, S. *Borides Silicides, and Phosphides – A Critical Review of Their Preparation, Properties and Crystal Chemistry*. Wiley: London, 1995.
115. Rogers, E.; Dorenbos, P.; Kolk, E.v.d. *New J. Phys.* **2011**, *13*, 093038.
116. Ono, S.; Nomura, K.; Hayakawa, H. *J. Less Common Met.* **1974**, *38*, 119.
117. Sze, S. M.; Ng, K. K. *Physics of Semiconductor Devices*, 3rd ed.; Wiley-Blackwell: New Jersey, 2006; p. 832.
118. Wulfsberg, G. *Inorganic chemistry*. University Science Books: Sausalito, CA, 2000; p. 978.
119. Jackson, S. D., Hargreaves, J. S. J., Eds.; In *Metal Oxide Catalysis*; Wiley-VCH: Weinheim, 2008.
120. Ryshkewitch, E.; Richerson, D. W. *Oxide Ceramics*. American Ceramic Society: Westerville, OH, 1985.
121. Ramanathan, S. *Thin Film Metal-Oxides: Fundamentals and Applications in Electronics and Energy*, 1st ed.; Springer: New York, 2010.
122. Vacquier, G.; Nadifi, H.; Ouali, A.; Grigorescu, C.; Monnereau, O.; Tortet, L.; Boulesteix, C. *J. Optoelectron. Adv. Mater.* **2000**, *2*, 676.
123. Banger, K. K.; Yamashita, Y.; Mori, K.; Peterson, R. L.; Leedham, T.; Rickard, J.; Sirringhaus, H. *Nat. Mater.* **2011**, *10*, 45.
124. Vioux, A. *Chem. Mater.* **1997**, *9*, 2292.
125. Jones, A. C., Hitchman, M. L., Eds.; In *Chemical Vapour Deposition: Precursors, Processes and Applications*; Royal Society of Chemistry: Cambridge, 2009.
126. Pawar, S. M.; Pawar, B. S.; Kim, J. H.; Joo, O.-S.; Lokhande, C. D. *Curr. Appl. Phys.* **2011**, *11*, 117.
127. Adschiri, T.; Hakuta, Y.; Arai, K. *Ind. Eng. Chem. Res.* **2000**, *39*, 4901.
128. Hilpert, S.; Wille, A. *Z. Physik. Chemie* **1932**, *18B*, 291.
129. Lopez, A.; Ortiz, A. *Semicond. Sci. Tech.* **1994**, *9*, 2130.
130. Nomura, R.; Konishi, K.; Futenma, S.; Matsuda, H. *Appl. Organomet. Chem.* **1990**, *4*, 607.
131. Massaccesi, S.; Sanchez, S.; Vedel, J. *J. Electroanal. Chem.* **1996**, *412*, 95.
132. Coustal, R. *J. Chim. Phys.* **1931**, *31*, 277.

133. Sriram, M. A.; Kumta, P. N. *J. Mater. Chem.* **1998**, *8*, 2453.
134. Crider Ceramic, J. F. *Eng. Sci. Proc.* **1982**, *3*, 519.
135. Chianelli, R. R.; Dines, M. B. *Inorg. Chem.* **1978**, *17*, 2758.
136. Carmalt, C. J.; Morrison, D. E.; Parkin, I. P. *Polyhedron* **2000**, *19*, 829.
137. Carmalt, C. J.; Morrison, D. E.; Parkin, I. P. *J. Mater. Chem.* **1998**, *8*, 2209.
138. Shaw, G. A.; Parkin, I. P. *Inorg. Chem.* **2001**, *40*, 6940.
139. Shaw, G.; Parkin, I. P. *Main Group Metal Chem.* **2001**, *24*, 195–203.
140. Parkin, I. P.; Rowley, A. T. *J. Mater. Chem.* **1995**, *5*, 909.
141. Parkin, I. P.; Rowley, A. T. *Adv. Mater.* **1994**, *6*, 780.
142. Kher, S. S.; Wells, R. L. *Chem. Mater.* **1994**, *6*, 2056.
143. Thostenson, E. T.; Ren, Z.; Chou, T.-W. *Compos. Sci. Technol.* **2001**, *61*, 1899.
144. Chico, L.; Crespi, V. H.; Benedict, L. X.; Louie, S. G.; Cohen, M. L. *Phys. Rev. Lett.* **1996**, *76*, 971.
145. Ye, Y.; Ahn, C. C.; Witham, C.; Fultz, B.; Liu, J.; Rinzler, A. G.; Colbert, D.; Smith, K. A.; Smalley, R. E. *Appl. Phys. Lett.* **1999**, *74*, 2307.
146. Jorio, A.; Dresselhaus, G.; Dresselhaus, M. S. *Carbon Nanotubes: Advanced Topics in the Synthesis, Structure, Properties and Applications*. Springer: Berlin, 2008.
147. Blaschkowski, B.; Jing, H.; Meyer, H.-J. *Angew. Chem.* **2002**, *114*, 3468.
148. Bernhardt, E.; Finze, M.; Willner, H. *Z. Anorg. Allg. Chem.* **2003**, *629*, 1229.
149. Tragl, S.; Gibson, K.; Glaser, J.; Duppel, V.; Simon, A.; Meyer, H.-J. *Solid State Commun.* **2007**, *141*, 529.

2.18 New Chemistry of Noble Metals

MS Wickleder and C Logemann, University of Oldenburg, Oldenburg, Germany

2.18.1 Introduction and Scope

The group of noble metals consists of the elements ruthenium, osmium, rhodium, iridium, palladium, and platinum, the so-called platinum metals, and the two coinage metals silver and gold. These metals are known to be chemically quite inert but nevertheless a large number of compounds have been prepared for each of the metals and there is still considerable interest in the chemistry of these elements. This interest is strongly triggered by the properties of the metals and their compounds making them suitable for various applications, for example, in electronics or in catalysis. Especially in the field of catalysis, important investigations have been performed throughout the past 30 years, and the ruthenium-based catalysts for olefin metathesis (e.g., the so-called Grubbs catalysts) as well as the observation that elemental gold is able to catalyze oxidation reactions may illustrate the importance of noble metals for homogeneous and heterogeneous catalysis. The surprising observation of the catalytic activity of elemental gold has to do with the dramatic expansion of nanochemistry throughout the last years, which is clearly driven by the improvement of analytic tools for studying nanoscaled objects. In order to account for these two important topics, the present edition of *Comprehensive Inorganic Chemistry* devotes special volumes (especially Volume VI and parts of Volume VII) to the item of catalysis. Moreover, different areas of research where also noble metals play an important role are discussed in breadth in further chapters. For example, because Volume VIII deals with the important aspects of coordination and organometallic chemistry, this chapter does not address organometallic compounds. Instead, this chapter emphasizes in its first section the special peculiarities of noble metals, such as the wide span of oxidation states they might adopt, with special focus on negative oxidation states where spectacular progress has been made. In a second section, metal–metal-bonded systems are discussed with a focus on more recent structural investigations. Finally, there is a larger section dealing with selected inorganic noble metal compounds. The selection is restricted in the sense that no compounds of organic acids (carboxylates) are considered and, as mentioned above, no organometallic chemistry is included. For all compounds under discussion structural data as far as they have been reported are provided in respective tables. These tables may also contain entries which are not explicitly mentioned in the text but which make the discussion more comprehensive. Nevertheless, also the table entries are based on the (subjective) selections of the authors.

2.18.2 Oxidation States

2.18.2.1 Relativistic Effects

Although it was well known since the early days of quantum mechanics that the theory of relativity has to be considered for a detailed understanding of the electronic structure of atoms,[1] it was only in the late 1970s that relativistic effects were also correlated with chemical properties and up to now there are continuous reports on that topic.[2–11] In a first approximation, the relativistic effects are due to the high velocity of inner electrons in close proximity to highly charged nuclei. According to the laws of relativity, this leads to an increasing mass of

these electrons, and in turn to decreasing Bohr radii. In terms of orbital theory, those orbitals bearing high probability densities for the electrons near to the nucleus are affected most strongly. These are the s and p orbitals and their shrinking is named 'direct relativistic effects.' The expansion and destabilization of d and f orbitals are referred to as 'indirect relativistic effects.' They occur because the contracted s and p orbitals provide a stronger screening of the nuclear charge for those electrons having low probability densities near the nucleus, that is, d and f electrons. As the influence of relativistic effects necessarily increases with the nuclear charge, that is, Z, their consequences are especially observed for elements with $Z > 50$. Thus, concerning the noble metals it should be the chemistry of osmium, iridium, platinum, and gold that is significantly stamped by relativistic effects, and indeed some peculiarities for these elements can be emphasized:

- Due to the destabilized d orbitals, Os, Ir, Pt, and Au adopt quite easily high oxidation states.
- Due to the stabilization of the 6s orbital, platinum and gold have extraordinarily high electron affinities (EAs) of −2.128 eV (Pt) and −2.308 eV (Au). These are much higher than those of the lighter group congener Ag (−1.303 eV) and Pd (−0.602 eV), and fall in the range of typical nonmetal values (S: −2.077 eV, I: −3.059 eV). Thus, these metals can adopt even negative oxidation states.
- Catalytic activity of platinum and gold species in the gas phase has been correlated to relativistic effects as well as the rapidly growing area of heterogeneous catalysis of metal nanoparticles.

Another typical example of gold chemistry, the so-called aurophilicity, that is, the closed shell Au(I)—Au(I) interactions, can obviously not be attributed to relativistic effects.[12]

2.18.2.2 High Oxidation States

The noble metals show a large variety of different oxidation states, being the highest known in the periodic table (cf. also Chapter 2.08). According to the presence of relativistic effects, there is a clear trend that the stability of high oxidation states increases with the nuclear charge Z, that is, the heavier elements Os, Ir, Pt, and Au adopt much easier high oxidation numbers than their lighter congeners. However, even for the lighter elements high oxidation states can be achieved compared to the non-noble metals of the respective groups, that is, Fe, Co, Ni, and Cu. Figure 1 illustrates the highest available oxidation states for the d-block elements of this period. The highest oxidation state for which compounds can be prepared is +VIII. They occur in the form of the tetroxides MO_4 (Os, Ru) which are obtained in the form of molecular orange-colored compounds of high volatility.[13,14] In the solid state, the MO_4 molecules might be arranged in two different ways, leading to a monoclinic and a cubic modification, respectively.[14] The oxidation number +VIII has recently also been observed for iridium and the oxide IrO_4 could be investigated spectroscopically at low temperature in a noble gas matrix.[15] There is also theoretical evidence that oxidation of IrO_4 leading to the cation IrO_4^+, that is, the oxidation number +IX, should be possible.[16] However, there is no experimental proof up to now. The same is true for the heptafluoride IrF_7, for which a molecular pentagonal bipyramidal structure has been predicted based on high-level calculations.[17] The fluoride of iridium with the highest oxidation state that is experimentally characterized is IrF_6.[18] It has the same molecular structure as the hexafluorides of osmium and platinum.[19,20] The latter is also the only binary representative for the highest oxidation state of platinum (the formally hexavalent oxide PtO_3 is in fact a platinum(IV) oxide peroxide). The highest oxidation state that can be gained in the group of the coinage metals is +V, as found for the fluoride AuF_5,[21] while an earlier report on the existence of AuF_7[22] has been shown to be certainly wrong.[23,24] AuF_5 has a dimeric structure consisting of two edge-connected $[AuF_6]$-octahedra (Figure 2).[21] Thus, it is remarkably different from the well-known noble metal pentafluorides MF_5 (M = Ru,[25] Os,[26] Rh,[27,28] Ir,[29] Pt[30,31]) which crystallize with tetrameric structures according to $(MF_5)_4$. The highest oxidation states that can be realized for the elements palladium and silver are +IV, for example, in PdF_4[32] and Cs_2AgF_6[33] (Table 1).

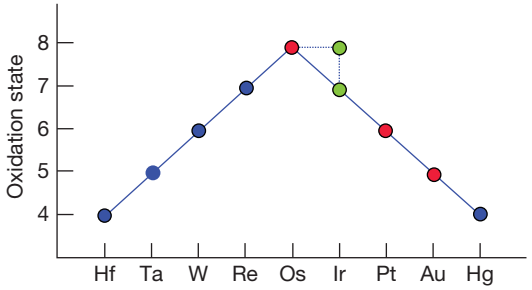

Figure 1 The highest known oxidation states of the elements of the 5d row. The red circles represent the noble metal for which well-defined compounds have been prepared. For iridium (green circle), the oxidation state +VII is only theoretically predicted to exist in the fluoride IrF_7, and there is spectroscopical evidence for the existence of IrO_4 in an argon matrix at low temperature.[15] Also the tetravalent oxidation state for mercury is based on spectroscopy in an argon matrix on HgF_4.[34]

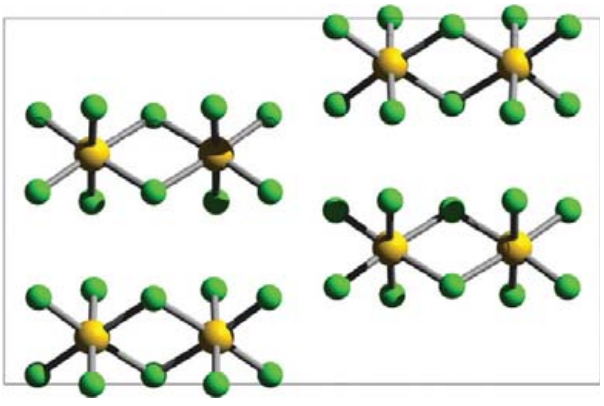

Figure 2 $[Au_2F_{10}]$ dimers of edge-connected $[AuF_6]$ octahedra in the crystal structure of AuF_5 (Au: yellow, F: green). The orthorhombic crystal structure is shown as projection onto the (001) plane.

Table 1 Structural data of noble metal compounds in high oxidation states

Compound	*Space group*	*Lattice parameters*				*References*
		a (*Å*)	b (*Å*)	c (*Å*)	β (°)	
OsO_4	*C*2/*c*	9.379	4.515	8.63	116.58	13
RuO_4-I	*C*2/*c*	9.302	4.397	8.454	116.82	14
RuO_4-II	*P*−43*n*	8.509				14
IrF_6	*Pnma*	9.411	8.547	4.952		18
OsF_6	*Pnma*	9.387	8.544	4.944		18
RhF_6	*Pnma*	9.323	8.474	4.910		18
PtF_6	*Pnma*	9.282	8.461	4.896		20
AuF_5	*Pnma*	9.366	15.052	4.84		21
RuF_5	$P2_1/c$	5.4967	9.946	12.528	99.96	35
OsF_5	$P2_1/c$	5.403	9.866	12.336	99.13	36
RhF_5	$P2_1/c$	12.3376	9.917	5.5173	100.42	27
PtF_5	$P2_1/c$	5.523	9.942	12.43	99.98	31
PdF_4	*Fdd*2	9.339	9.24	5.828		32
Cs_2AgF_6	*Fm*−3*m*	8.907				33

2.18.2.3 Low Oxidation States

As mentioned above, the stabilization of the 6s orbitals of gold and platinum leads to EAs of these metals as high as those of typical nonmetals such as sulfur or iodine. For this reason, these two elements may also adopt negative oxidation numbers, according to the formation of an electronic $6s^2$ configuration. This occurs especially in combination with very electropositive metals and the cesium auride CsAu was the first described example.[37,38] The yellow and transparent compound has a typical salt-type structure (CsCl type) and can be dissolved in liquid ammonia to give a nearly colorless solution showing high conductivity. The resulting solutions are transparent and are of a very pale yellow color. From this solution other aurides can be gained, for example, $[N(Me)_4]Au$.[39] Various physical investigations, for example, Mößbauer and x-ray absorption near-edge structure (XANES) spectroscopy, have clearly proved the anionic behavior of gold in these compounds. Complexing the alkali cations in the ammonia solutions with crown ethers has opened another field in auride chemistry, and examples that have been prepared are Cs([18]crown-6)Au·$8NH_3$[40] and [Rb([18]crown-6)$(NH_3)_3$]Au·NH_3.[41] The latter is especially remarkable, since it is the first experimental manifestation of the Au^- anion acting as an acceptor in a hydrogen bond. If the initial cesium auride is crystallized from liquid ammonia, the unique deep blue solvate CsAu·NH_3 is obtained.[42] Its structure consists of essentially intact blocks of CsAu, separated by layers of NH_3 molecules (**Figure 3**). However, a remarkable difference in the structure of CsAu is the occurrence of significantly shorter Au–Au distances. They are as short as 302 pm compared to the 426 pm observed in CsAu. Furthermore, Mößbauer spectroscopy revealed a reduced charge for the gold atom. In this way, excess electrons are gained which are delocalized over the entire Cs–NH_3 sublattice. This situation is comparable to the delocalization of electrons in the so-called electride solutions (e.g., sodium metal in liquid NH_3) and leads to the deep blue color of the compound (**Table 2**).

The auride ion may also be part in mixed anionic compounds. A striking quite recent example are the oxide aurides

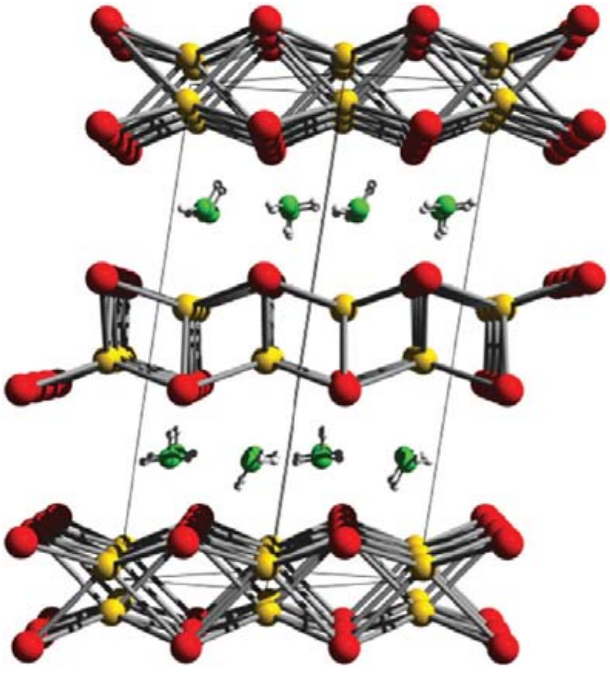

Figure 3 The crystal structure of CsAu·NH_3 (viewed along the [110] direction) consists of CsAu-type slabs separated by NH_3 molecules. Compared to CsAu shorter distances Au—Au are observed, which is explained by a reduced charge of the auride anion with delocalization of the excess electrons over the Cs–NH_3 sublattice. This delocalization leads to the blue color of the compound (Au: dark yellow, Cs: red, N: green, H: white).

M_3AuO (Cs, Rb, K) which adopt inverse perovskite type of structures.[43–49] Also in these compounds, the oxidation state-I has been unambiguously identified by XANES spectroscopy. Interestingly, the bandgap energy decreases remarkably when in the row Cs–Rb–K. While the yellow Cs_3AuO is a semiconductor ($\Delta E_g = 2.32(2)$ eV) the bandgap vanishes for M = Rb, K, and the compounds appear as black shiny crystals. Also in these cases the 'normal' halide congeners, that is, M_3XO

Table 2 Structural data of noble metal compounds in negative oxidation states

Compound	Space group	Lattice parameters				References
		a (Å)	b (Å)	c (Å)	β (°)	
CsAu	*Pm*−3*m*	4.262				38
$(NMe_4)Au$	*P*4/*nmm*	7.599		5.433		39
$CsAu{\cdot}NH_3$	*C*2/*c*	7.211	7.036	16.826	102.37	42
K_3AuO	*Pm*−3*m*	5.240				44
Rb_3AuO	*Pm*−3*m*	5.501				44
Cs_3AuO	$P6_3/mmc$	7.830		7.060		44
Ca_3AuN	*Pm*−3*m*	4.822				50
$Cs_7Au_5O_2$	*Immm*	5.999	9.572	17.261		59
Cs_2Pt	$P6_3/mmc$	5.676		9.471		55
BaPt	$P6_3/mmc$	5.057		5.42		56
Ba_2Pt	*R*−3*m*	4.564		22.091		58
Ba_3Pt_2	*R*3	9.624		18.606		57

(X = I, Br), can be prepared and the isotypic structure proves once more the similarity of Au^- and halide anions. Interestingly, also an auride nitride with the perovskite type of structure has been prepared.[50,51] However, Ca_3AuN is a metallic compound so that an electron count is not as simple as for the auride oxides.

The relationship of gold and halogens is not restricted to their crystal chemical behavior; it also has a nice chemical analogy. According to the reaction given in eqn [1], the reaction of elemental gold in a basic environment leads to its disproportionation to Au^{-1} and Au^{+1}, analogously to the well-known reaction of Cl_2 in basic media under formation of Cl^- and hypochlorite.[52–54] The resulting mixed-valent gold compound $Cs_7Au_5O_2$ can be seen as an auride–aurate according to $[CsAu]_4[Cs_3AuO_2]$, in line with the structural findings which show typical CsAu slabs separated by Cs_3AuO_2-type layers with linear coordinated Au^+ ions (**Figure 4**):

$$3Cs + 5Au^{\pm 0} + 2Cs_2O - \left[CsAu^{-1}\right]_4\left[Cs_3Au^{+1}O_2\right] \qquad [1]$$

Even if gold is certainly the noble metal for which a negative oxidation state is most easily to access, for platinum this should be possible when judged from its high EA. Indeed, the reaction of platinum with cesium led to the salt-like platinide Cs_2Pt.[55] The deep red compound adopts the Ni_2In-type structure, which is a high-temperature polymorph of CaF_2. It turned out that the reduction in platinum can also be achieved by barium as the electropositive reaction partner and the platinides BaPt, Ba_2Pt, and Ba_3Pt_2 emerged from these investigations.[56–58] Although BaPt crystallizes in a typical salt-like structure type (NiAs), there is no complete transfer of valence electrons from barium to platinum. Instead, infinite chains according to $^1_\infty[Pt]^-$ are found with Pt—Pt bonds as short as 2.7 Å. This feature can be rationalized in terms of the Zintl concept, that is, the transfer of one valence electron to the platinum atom leading to a $6s^1$ configuration followed by the formation of the polyanion. If more electrons are offered by increasing the barium concentration in the reaction, a stronger reduction of the platinum atoms is observed leading to a splitting of the $^1_\infty[Pt]^-$ chain into $[Pt_2]$ dumbbells as found for Ba_3Pt_2 ($=Ba_{1.5}Pt$) and finally to the formation of distinct Pt^{2-} anion in Ba_2Pt. The latter shows the $CdCl_2$ type of structure and has to be formulated according to

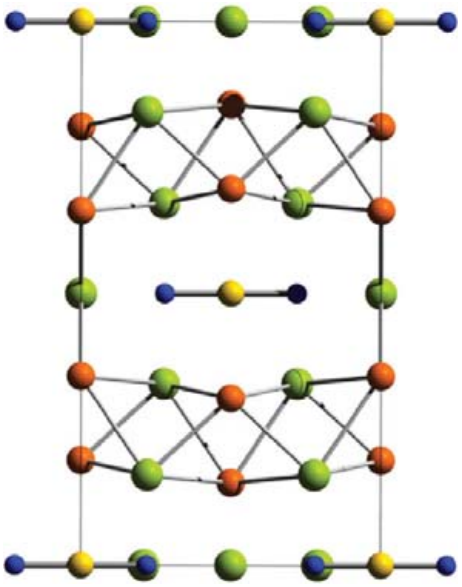

Figure 4 $Cs_7Au_5O_2$ can be obtained from the reaction of elemental gold with Cs and Cs_2O. The reaction is the analogon for the well-known Cl_2 disproportionation in basic medium (Au^{+I}: dark yellow, Au^{-I}: orange, Cs: green, O: blue). The orthorhombic structure is shown as projection onto the (100) plane.

$(Ba^{2+})_2(Pt^{2-})(e^-)_2$, in line with the observed metallic behavior of the compound. **Figure 5** compares the three barium platinides.

2.18.3 Metal–Metal Bonds

2.18.3.1 Generalities

The heavier noble metals have a tendency to form metal–metal bonds. This observation is in accordance with the findings for other metals of the second and third transition rows, for example, Mo, W, and Re.[60] The reason that these bonds occur more frequently between the heavier atoms compared to their respective lighter group congeners is that the larger expansion of the 4d and 5d orbitals allows for a better orbital overlap, that

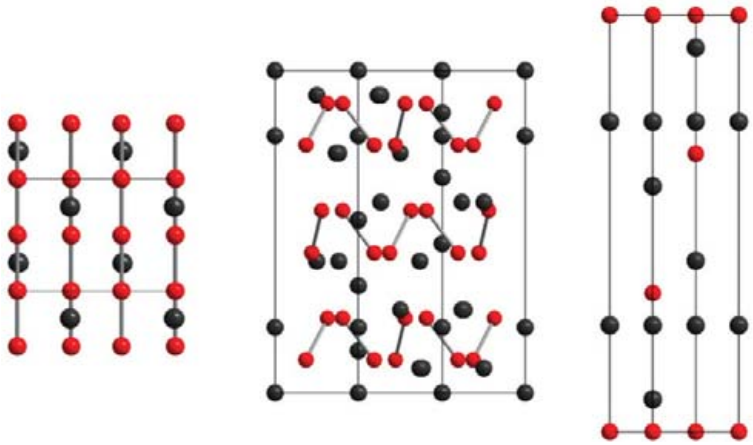

Figure 5 The platinides BaPt, Ba_3Pt_2, and Ba_2Pt as examples of anionic platinum. In BaPt (left), an anionic $^1_\infty[Pt]^-$ chain occurs which is split into anionic $[Pt_2]$ dumbbells in Ba_3Pt_2 (middle). A typical ionic structure, the anti-$CdCl_2$ type of structure, is found for Ba_2Pt (right).

is, a stronger bond. However, appropriate synthetic strategies and suitable ligand systems may lead to metal–metal bonds also for the 3d transition-metal elements, as might be nicely seen by recent findings for chromium that can even adopt bond orders up to five.[61]

In noble metal compounds, the metal–metal bonds are often stabilized by four chelating ligands that bridge the $[M_2]$ dumbbells, and especially carboxylates have been frequently used for that purpose. The resulting structural motif is often referred to as a 'paddlewheel' or a 'Chinese lantern' type of structure. The latter term is especially striking if the terminal positions of the $[M_2]$ dumbbells are occupied by additional ligands, usually neutral species such as solvent molecules. These ligands can be easily exchanged leading to a great interest in these complexes as catalysts. Besides carboxylate anions, other chelating ligands have been used to stabilize $[M_2]$ fragments, for example, sulfate and phosphate groups. The distances within the metal dumbbells do not alter significantly with the nature of the ligands, but depend strongly on the bond order between the metal atoms, that is, their electron configuration (cf. Chapter 9.11). Typical distances of single-bonded atoms are in the range between 2.4 and 2.6 Å, while a decrease of the distances is observed for the bond orders two (2.3–2.4 Å) and three (2.2–2.3 Å). It is worthwhile mentioning that the paddlewheel motif can even be obtained if no bonds are formed between the respective metal ions, that is, the bond order is zero. The structure of silver acetate is a striking example for the occurrence of this structure for a closed shell d^{10} metal ion.[62] In the paddlewheel structure, an octahedral coordination arises for both of the two metal atoms (Figure 6). Thus, for electronic configurations that favor other coordination geometries, the structure is not longer retained. For example, in gold(II) compounds bearing a $[Au_2]^{4+}$ dumbbell, the gold atoms are surrounded in a square planar fashion.

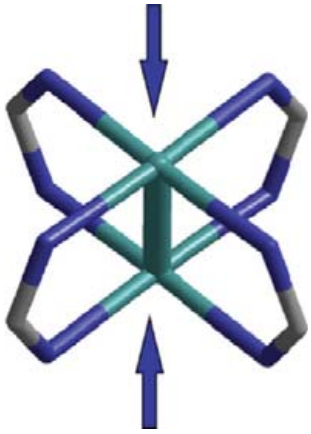

Figure 6 Scheme of the paddlewheel type of structure for metal–metal-bonded systems with chelating ligands. The coordination sphere of the metal atoms is usually completed by ligand molecules at the terminal positions of the $[M_2]$ dumbbell (arrows).

2.18.3.2 Examples

With respect to the long-known and well-established carboxylate representatives of metal–metal-bonded systems, we focus here on compounds stabilized by sulfate ligands (Table 3). The connection of two Pt^{3+} ions with formal d^7 configuration to dinuclear Pt_2^{6+} dumbbells was observed for the first time in the sulfate $K_2[Pt_2(SO_4)_4(H_2O)_2]$.[63,64] Within the anion $[Pt_2(SO_4)_4(H_2O)_2]^{2-}$ the four sulfate groups act as chelating ligands, and the H_2O molecules occupy the terminal positions of the Pt_2^{6+} dumbbell, leading to the lantern-type structure. This motive has been extensively varied, for example, by the replacement of the SO_4^{2-} ions by phosphate ligands, or by substitution of the terminal H_2O molecules for other donors.[65–68] Recently, it was also possible to replace the terminal ligands of the dumbbell even by further sulfate groups. In the crystal structure of $K_4[Pt_2(SO_4)_5]$, which has been obtained by the reaction of $K_2[PtCl_4]$ with concentrated H_2SO_4 as orange crystals, terminal monodentate sulfate ions connect the $[Pt_2(SO_4)_4]$ units to infinite chains according to the formulation $^1_\infty[Pt_2(SO_4)_{4/1}(SO_4)_{2/2}]^{4-}$ and charge compensation for chains is achieved by the K^+ ions.[69] A linkage of $[Pt_2(SO_4)_4]$ units to layers is observed in the crystal structure of Cs $[Pt_2(SO_4)_3(HSO_4)]$ which is formed in the reaction of

Table 3 Structural data of sulfates of platinum and gold with metal–metal bonds

Compound	Space group	Lattice parameters						References
		a (Å)	b (Å)	c (Å)	α (°)	β (°)	γ (°)	
$K_2[Pt_2(SO_4)_4(H_2O)_2]$	$P\bar{1}$	7.453	7.524	7.593	102.01	111.45	99.8	63
$K_4[Pt_2(SO_4)_5]$	$P\bar{1}$	9.754	13.318	14.910	101.16	96.28	102.849	69
$Cs[Pt_2(SO_4)_3(HSO_4)]$	$P2_1/c$	17.248	8.813	9.351		100.40		69
$Pt_2(SO_4)_2(HSO_4)_2$	$P2_1/c$	8.686	8.262	9.218		116.32		70
$(NH_4)_4[Pt_{12}O_8(SO_4)_{12}]$	$R\bar{3}$	11.897		27.897				71
$Cs_2K_2[Pt_{12}O_8(SO_4)_{12}]$	$R\bar{3}$	11.989		27.680				72
$Au_2(SO_4)_2$	*Pbca*	8.549	8.249	10.011				73
$K_3[Pt_2(SO_4)_3H(HSO_4)]$	*C2/c*	18.094	9.571	12.330		107.23		76
$Rb[Pt_2(SO_4)_3(HSO_4)]$	*Pnma*	9.231	17.629	8.436				77
$Gd(HSO_4)_2[Pt_2(SO_4)_4(HSO_4)_2]$	$P\bar{1}$	8.440	9.085	9.395	107.73	112.10	103.53	78

$Cs_2[PtCl_4]$ and concentrated H_2SO_4. The red single crystals of $Cs[Pt_2(SO_4)_3(HSO_4)]$ are extremely moisture sensitive and turn immediately cloudy when exposed to air.[69] As described for $K_4[Pt_2(SO_4)_5]$ in this compound, the Pt_2^{6+} dumbbells are also coordinated by four bidentate-bridging and two monodentate tetrahedra. In contrast to $K_4[Pt_2(SO_4)_5]$, the axial sulfate groups do not act as 'monodentate' but as 'bidentate-bridging' ligands for further Pt_2^{6+} ions and, vice versa, two of the bidentate-bridging tetrahedra are monodentate to neighboring Pt_2 dumbbells. The remaining two bidentate-bridging tetrahedra are not bonded to further platinum atoms. The connection leads to two different layers; one has to be formulated according to $^2_\infty[Pt_2(SO_4)_{4/2}(SO_4)_{2/1}]^{2-}$ while for the second one half of the tetrahedra can be clearly assigned as hydrogen sulfate ions leading to neutral sheets of the composition $^2_\infty[Pt_2(SO_4)_{4/2}(HSO_4)_{2/1}]$. The assignment as HSO_4^- ions can be done unambiguously with respect to the S–O distances. Interestingly, the structural characteristic of the neutral $^2_\infty[Pt_2(SO_4)_{4/2}(HSO_4)_{2/1}]$ sheets is identical to the one recently reported for $Pt_2(SO_4)_2(HSO_4)_2$.[70] Thus, the structure of $Cs[Pt_2(SO_4)_3(HSO_4)]$ might be described as a composite of $Pt_2(SO_4)_2(HSO_4)_2$ and the hitherto unknown sulfate $Cs_2[Pt_2(SO_4)_4]$. The above-mentioned $Pt_2(SO_4)_2(HSO_4)_2$ is the only 'binary' platinum sulfate known so far. It forms in the reaction of finely divided elemental platinum with concentrated sulfuric acid at 300 °C. In the structure of the compound, the terminal positions of the $[Pt_2]$ dumbbell are occupied by monodentate SO_4^{2-} ions. The latter are connected to further Pt_2^{6+} ions in a chelating way leading to layers of the composition $^2_\infty;[Pt_2(SO_4)_{4/2}(HSO_4)_{2/1}]$. As can be seen from Figure 7, the hydrogen bonds are needed to keep the $^2_\infty[Pt_2(SO_4)_{4/2}(HSO_4)_{2/1}]$ layers together.

The $[Pt_2]$ dumbbells occur also in the oxide sulfate $(NH_4)_4[Pt_{12}O_8(SO_4)_{12}]$ that has been obtained as dark red crystals in the reaction of $Pt(NO_3)_2$ with concentrated sulfuric acid at 350 °C in sealed glass ampoules.[71] The compound can be seen as a polyoxometalate and contains as the characteristical structural feature the unprecedented cluster anion $[Pt_{12}O_8(SO_4)_{12}]^{4-}$.[72] Within the anion, the 12 Pt^{III} ions are arranged in the form of an icosahedron which is remarkably distorted due to the formation of the $[Pt_2]$ dumbbells (Figure 8). The Pt–Pt distance within the dumbbells is 253 pm; the distances to the other neighboring platinum

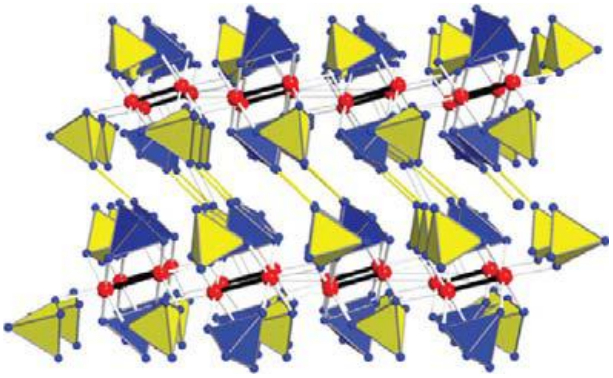

Figure 7 Crystal structure of $Pt_2(SO_4)_2(HSO_4)_2$ viewed along the [010] direction. The SO_4^{2-} ions (blue) link the $[Pt_2]$ dumbbells (red) into layers. The HSO_4^- groups (yellow) act also as chelating ligands for the dumbbells and take care for the connection of the layers by hydrogen bonds (yellow lines).

atoms are enlarged and range from 344 up to 346 pm. The six Pt_2 dumbbells of the icosahedron are connected by eight O^{2-} ions leading to an almost perfect trigonal planar coordination of the oxide ions by three platinum atoms. In this way, 8 of the 20 triangular faces of the icosahedron are centered by oxide ions. Above the remaining 12 triangular faces tridentate coordinating SO_4^{2-} groups are situated. Each sulfate ion acts as a chelating ligand to one Pt_2 dumbbell and as a monodentate ligand to the next. Thus, one oxygen atom of the tetrahedron is not attached to a platinum atom. The $[Pt_{12}O_8(SO_4)_{12}]^{4-}$ clusters are arranged in the trigonal body-centered unit cell in a way that their centers are situated in the origin of the cell (Wyckoff site 3a) leading to S_6 symmetry for the anions.

A metal dumbbell was surprisingly also found in the crystal structure of $Au_2(SO_4)_2$, which was obtained by the reaction of $Au(OH)_3$ and sulfuric acid, which interestingly runs under reduction of Au^{3+} and formation of oxygen.[73] It was thought for a long time that this sulfate is a mixed-valent compound containing Au(I) and Au(III) ions, analogously to most of the formally divalent gold compounds. However, the determination of the crystal structure showed recently that the compound is not mixed valent according to $Au^IAu^{III}(SO_4)_2$, but represents the first simple inorganic compound known so far containing the cation Au_2^{4+}. The distance between the gold

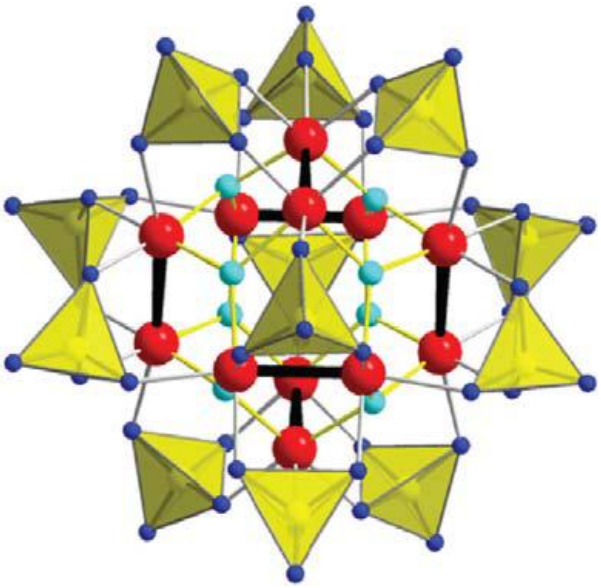

Figure 8 The unique cluster anion $[Pt_{12}O_8(SO_4)_{12}]^{4-}$ consisting of six O^{2-} (turquoise colored) linked $[Pt_2]$ dumbbells. The 12 Pt^{3+} ions are arranged in form of an icosahedron which is remarkably distorted due to the metal–metal bonds. The triangular faces of the icosahedron are capped by the SO_4^{2-} ions (yellow tetrahedra).

atoms of 249 pm is much shorter than the distances observed for the dinuclear complexes known so far which range from 258 to 275 pm.[74,75] The Au^{2+} ions in the Au_2^{4+} cation have d^9 configuration; thus, the coordination of the dumbbell leads not to paddlewheel structure but to square planar coordination of both the metal atoms. This is achieved by two chelating and two monodentate SO_4^{2-} ions (Figure 9). Each monodentate sulfate group is a chelating ligand to one further Au_2^{4+} ion and each chelating sulfate ion is monodentate to an adjacent Au_2^{4+} dumbbell. The linkage of Au_2^{4+} ions and SO_4^{2-} groups leads to infinite layers according to $^2_\infty[(Au_2)(SO_4)_{4/2}]$ which are stacked in the [001] direction.

2.18.4 Selected Compounds

2.18.4.1 The Unique Xenono Gold Complexes

One of the certainly most exciting recent discoveries in gold (and also noble gas, cf. Chapter 1.25) chemistry is the ability of xenon atoms to function as ligands for gold atoms. The first complex, $[AuXe_4]^{2+}$, has been obtained by reduction of AuF_3 with elemental xenon in a superacidic HF/SbF_5 medium.[79] The key for this reaction is the extreme Brønsted acidity of the medium, making Au^{3+} a strong oxidizer that might even oxidize xenon to the Xe_2^+ cation; the latter can be separated in the form of $Xe_2[Sb_4F_{21}]$. The complex $[AuXe_4]^{2+}$ ion has a square planar shape and was stabilized with $Sb_2F_{11}^-$ as counter-anions. The respective salts crystallize with two different modifications exhibiting triclinic(I) and tetragonal(II) symmetry. In both the modifications, the complex cations show gold–xenon bond lengths of about 274 pm (Table 4). The bonding between gold and xenon is of the σ donor type,

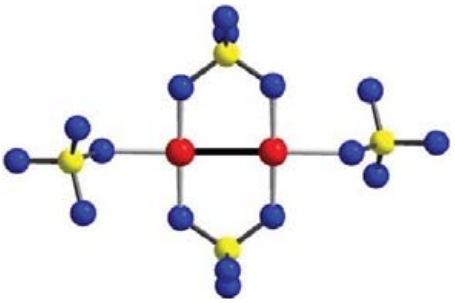

Figure 9 Coordination of the $[Au_2]^{4+}$ cation in the crystal structure of $Au_2(SO_4)_2$. Two chelating and two monodentate SO_4^{2-} lead to a square planar surrounding of each metal ion, in accordance with their d^9 configuration. In the crystal structure, each sulfate group is attached to two $[Au_2]$ dumbbells according to $^2_\infty[(Au_2)(SO_4)_{4/2}]$.

Table 4 Distances Au–Xe in gold–xenono complexes

Compound	*Oxidation state (Au)*	*Distance Au–Xe (Å)*
$[AuXe_4][Sb_2F_{11}]_2$-I	+II	2.733, 2.749, 2.728, 2.746
$[AuXe_4][Sb_2F_{11}]_2$-II	+II	2.737, 2 × 2.759, 2.670
cis-$[AuXe_2][Sb_2F_{11}]_2$	+II	2.658, 2.671
trans-$[AuXe_2][SbF_6]_2$	+II	2.709
$[Au_2Xe_2F][SbF_6]_3$	+II	2 × 2.647
trans-$[AuXe_2F][SbF_6][Sb_2F_{11}]$	+III	2.593, 2.619
$[(F_3As)AuXe][Sb_2F_{11}]$	+I	2.607; (Au–As: 2.315)

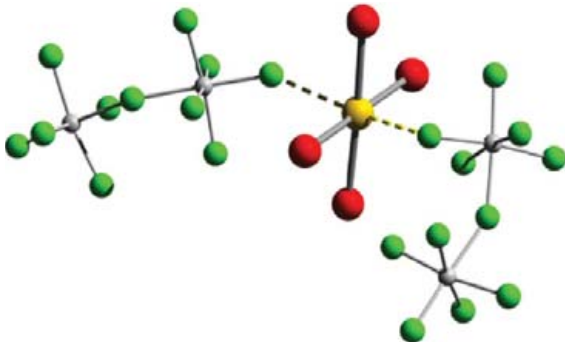

Figure 10 Structure of the cation $[AuXe_4]^{2+}$ in $[AuXe_4](Sb_2F_{11})_2$. Important distances are (in pm): Au–Xe: 273.30(6), 274.98(5), 272.79 (6), 274.56(5); Au–F: 267.1(4), 295.0(4).

resulting in a charge of approximately +0.4 per xenon atom (Figure 10).

Subsequently, variation of the acid strength and the internal xenon pressure resulted in further xenono gold complexes, for example, *cis*-$[AuXe_2][Sb_2F_{11}]_2$ and *trans*-$[AuXe_2][SbF_6]_2$.[80] Both compounds contain the Au^{2+} ions in square planar coordination of two xenon atoms and two fluoride atoms from the fluoridoantimonate anions; however, the xenon ligands are in *cis* orientation in the first example and *trans* in the other. In both the compounds, the distances Au–Xe are slightly shorter compared to the tetraxenono complex (Table 4). At low xenon pressure, $[Au_2Xe_2F][SbF_6]_3$ could be gained in the form of

green crystals. It contains the remarkable $[Au_2Xe_2F]^{3+}$ cation with two Au^{2+} ions bridged by a fluoride anion.[80] It is worthwhile mentioning that the oxidation state of gold in the above-mentioned complexes is always +II, a rather uncommon oxidation state for this element, especially if no metal–metal-bonded systems are considered. However, there is one example for a gold(III)–xenon species that was obtained under reduced acidity, the ochre-colored *trans*-$[AuXe_2F][SbF_6][Sb_2F_{11}]$ (**Table 5**).[80] The gold Au(III) ions are coordinated by two xenon atoms in *trans* orientation, one terminal fluoride anion and F atom from the SbF_6^- anion. The higher oxidation state can be clearly seen from the distance Au–Xe that decreased to 260 pm compared to the Au(II) complexes. In SbF_5-rich HF/SbF_5 solution also a Au(I)complex could be prepared, if AsF_3 is added to the solution.[81] The compound $[(F_3As)AuXe][Sb_2F_{11}]$ contains the Au^+ ion in linear coordination of the xenon atom and one AsF_3 molecule. The formation of bonds between gold and the noble gas xenon seems surprising on first sight. Again, the strong relativistic effects that are typical for gold are the driving force for the stability of these bonds. In this context, it is understandable that stable xenono complexes have also been observed for mercury which belongs also to the strongly relativistic elements.[81]

2.18.4.2 Polyoxometalates

Polyoxometalates are an important and rapidly growing class of compounds. In most cases, they consist of a rigid framework of condensed metal–oxygen polyhedra (predominantly molybdates and tungstates) incorporating further metal ions. A large number of compounds have been prepared where these ions are noble metals. A comprehensive recent review gives a concise discussion of these compounds and also a chapter of this book deals with polyoxometalates (Volume II, **Chapter 2.10**).[82] In contrast to noble metal incorporation into polyoxometalates, examples with noble metal being the constituents of the framework, that is, part of the condensed polyhedral, are extraordinarily limited, and shall be emphasized here.

In principle, the $[Pt_{12}O_8(SO_4)_{12}]^{4-}$ ion described above (**Section 2.18.3.2**) is already a polyoxometalate, however, with dinuclear Pt_2^{6+} metal ions. For divalent palladium, three polyoxometalates could be obtained from aqueous solution by the reaction of various Pd(II) salts with either As_2O_5, $PhAsO_3H_2$, or SeO_2 at pH values between 4.8 and 7.5. They have the general formula $[Pd_{13}O_8(LXO_3)_8]^{n-}$ (X=As^V, L=O, Ph; X=Se^{IV}, L=lone pair) and the palladium atoms are arranged in the form of a Pd-centered $[Pd_{12}]$ cuboctahedron. The 12 palladium atoms are linked by oxygen atoms and tridentate complex anions. The central palladium atoms have the unusual coordination numbers of 6 and 8 in the selenium and arsenic derivatives, respectively.[83–89]

Polyoxometalates exclusively composed of gold have been described in the form of the anions $[Au_4O_4(SeO_3)_4]^{4-}$ and $[Au_4O_4(AsO_4)_4]^{8-}$.[87,88] The compounds were obtained as complex potassium or sodium salts and characterized by single-crystal x-ray diffraction (XRD), elemental and thermogravimetric analyses, and infrared (IR) spectroscopy, as well as ^{77}Se nuclear magnetic resonance (NMR) spectroscopy in aqueous solution. The stability of $[Au_4O_4(SeO_3)_4]^{4-}$ was further investigated by mass spectrometry. In the sodium compound of the gold–arsenate complex, two $[Au_4O_4(AsO_4)_4]^{8-}$ anions are pair wise connected via a belt of five Na^+ ions (**Figure 11**, **Table 6**).

2.18.4.3 Compounds with Oxoanions

2.18.4.3.1 Selenates and selenites

It is well known that concentrated selenic acid is able to oxidize even noble metals, and in fact Mitscherlich was the first who reported this on the example of gold as early as 1827.[90] However, it was only in the early 1980s when it could be shown that selenites of gold form in these reactions, namely the oxide-selenite $Au_2O(SeO_3)_2$ and the selenite–diselenite $Au_2(SeO_3)_2(Se_2O_5)$.[91,92] Both compounds show the Au^{3+} ions in a typical square planar coordination of oxygen atoms. Recently, it has been shown that at high acid concentrations also the selenite–selenate $Au_2(SeO_3)_2(SeO_4)$ can be obtained by the reaction of elemental gold and selenic acid in Teflon-lined steel autoclaves as orange–yellow single crystals.[93] In the crystal structure, Au^{3+} is surrounded by four oxygen atoms of just as many monodentate SeO_3^{2-} ions in a square planar manner. The linkage of the polyhedra leads to double chains $^1_\infty[Au_2(SeO_3)_2]^{2+}$ in the [001] direction which are connected to puckered layers by SeO_4^{2-} groups. The noncentrosymmetric symmetry of the compound leads to the observation of a second harmonic generation (SHG) effect which shows an efficiency of 40% compared to a KH_2PO_4 (KDP) reference. The presence of selenite and selenate groups in the compound is also obvious in solid-state NMR spectra that reveal the different surroundings of the selenium atoms (**Table 7**).

Interestingly, the gold–neighbor platinum does not react under similar conditions with selenic acid. Its congener palladium, however, can be readily oxidized by H_2SeO_4 at 350 °C in

Table 5 Structural data of gold–xenono complexes

Compound	*Space group*	*Lattice parameters*						*References*
		a (Å)	b (Å)	c (Å)	α (°)	β (°)	γ (°)	
$[AuXe_4](Sb_2F_{11})_2$-I	$P\bar{1}$	7.9403	9.1775	17.391	99.539	92.64	94.656	79
$[AuXe_4](Sb_2F_{11})_2$-II	$Pna2_1$	14.519	7.8094	18.572				80
cis-$[AuXe_2][Sb_2F_{11}]_2$	$P4_32_12$	9.4415		27.631				80
trans-$[AuXe_2][SbF_6]_2$	$P\bar{1}$	5.605	7.306	8.075	90.991	91.244	97.895	80
$[Au_2Xe_2F][SbF_6]_3$	$P\bar{1}$	6.6156	8.5282	9.2514	72.114	79.274	67.929	80
trans-$[AuXe_2F][SbF_6][Sb_2F_{11}]$	$P2_1/c$	7.9525	9.9589	22.068		97.113		80
$[(F_3As)AuXe][Sb_2F_{11}]$	$Pna2_1$	15.8867	8.1333	10.9446				81

sealed glass tubes leading to the red crystals of $Pd(SeO_3)$, and to yellow–orange crystals of $Pd(SeO_4)$ at high H_2SeO_4 concentrations.[94,95] If SeO_3 was added to the reaction mixture yellow–orange crystals of the diselenite $Pd(Se_2O_5)$ were obtained. $Pd(SeO_3)$ consists of layers that are formed by square planar coordinated Pd^{2+} ions and pyramidal SeO_3^{2-} groups. The layers are held together by weak interactions involving the lone electron pairs of the selenium atoms. In the crystal structure of $Pd(SeO_4)$, square planar $[PdO_4]$ units are linked by tetrahedral SeO_4^{2-} ions into a three-dimensional (3D) network. In $Pd(Se_2O_5)$, the Pd^{2+} ions are coordinated by two chelating diselenite ions. The $Se_2O_5^{2-}$ ion links the palladium ions to corrugated chains which are held together by weak interactions only.

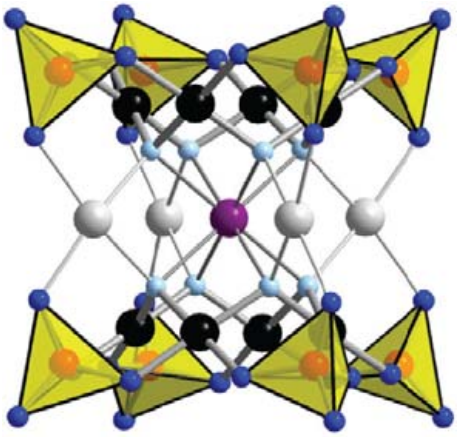

Figure 11 In the gold polyoxometalate anion $[Au_4O_4(AsO_4)_4]^{8-}$ four Au^{3+} ions (black) are connected by four oxide ions (light blue) and four arsenate ions (yellow tetrahedra) to the cyclic polyanion. In the crystal structure, two of these anions are pairwise connected by the charge-balancing sodium ions (gray and violet).

The second of the platinum metals that has been successfully reacted with selenic acid is rhodium.[96] At 350 °C in a sealed glass tube the reaction led to the deep red diselenite $Rh_2(Se_2O_5)_3$. The compound is isotypic with $Cr_2(Se_2O_5)_3$[97] and built up from $[ReO_6]$ octahedra and $Se_2O_5^{2-}$ groups. The latter act as monodentate ligands but are bridging to four further rhodium atoms according to $^3_\infty[Rh(Se_2O_5)_{6/4}]$ (Figure 12).

2.18.4.3.2 Sulfates

As discussed in Section 2.18.3, the sulfates $Pt_2(SO_4)_2(HSO_4)_2$ and $Au_2(SO_4)_2$ exhibit metal–metal-bonded $[M_2]$ dumbbells. Both compounds are the only binary sulfates of these two elements known so far, that is, the probably expected sulfates $Pt(SO_4)$ or $Au_2(SO_4)_3$ are still elusive. While for platinum also the ternary sulfates are exclusively based on the $[Pt(SO_4)_4]$ paddlewheel motif, $Au_2(SO_4)_2$ is the only sulfate showing a $[Au_2]$ dumbbell and all of the ternary sulfates known so far are Au(III) compounds. They are obtained from reactions of $Au(OH)_3$ in concentrated sulfuric acid in the presence of alkaline metal counter cations.[98,99] Independent of the specific cation, all of the sulfates contain infinite chains according to $^1_\infty[Au(SO_4)_{4/2}]^-$ with square planar $[AuO_4]$ units linked by bidentate-bridging SO_4^{2-} ions, except for Cs where layers according to $^2_\infty[Au(SO_4)_{4/2}]^-$ occur.

If the reactions are carried out with fuming sulfuric acid (containing 65% SO_3), the unique bis-disulfato-aurates $M[Au(S_2O_7)_2]$ (M = Li, Na) form as yellow crystalline

Table 6 Structural data of polyoxometalates of gold and palladium

Compound	Space group	Lattice parameters						References
		a (Å)	b (Å)	c (Å)	α (°)	β (°)	γ (°)	
I	*P*−1	12.748	13.163	14.454	105.07	109.73	105.81	83
II	*Cc*	19.666	18.674	36.386		99.48		89
III	*P*−1	13.357	13.936	15.044	65.15	84.73	63.97	87
IV	*P*−1	9.562	11.360	14.456	89.87	73.275	71.181	88

I: $Na_8(Pd_{13}AsO_8O_{34}(OH)_6)(H_2O)_{42}$.
II: $Na_{14}(H_3O)_6[Pd_{15}(\mu_3\text{-}SeO_3)_{10}(\mu_3\text{-}O)_{10}Na]_2(SeO_3)\cdot 27H_2O$.
III: $Na_{13}((H_2O)_4(NO_3)_2Na_5(Au_4As_4O_{20})_2)(H_2O)_{39}$.
IV: $K_4[Au_4O_4(SeO_3)_4]\cdot 0.4KNO_3\cdot 0.6CH_3COOK\cdot 6H_2O$.

Table 7 Structural data of noble metal selenates and selenites

Compound	Space group	Lattice parameters				References
		a (Å)	b (Å)	c (Å)	β (°)	
$Au_2O(SeO_3)_2$	*Pba*2	6.592	11.837	3.998		91
$Au_2(SeO_3)_2(Se_2O_5)$	*C*2/*c*	20.344	4.130	13.254	115.88	92
$Au_2(SeO_3)_2(SeO_4)$	*Cmc*2_1	16.891	6.301	8.862		93
$PdSeO_3$	*C*2/*m*	6.788	7.030	7.008	118.09	94,95
$PdSeO_4$	*C*2/*c*	8.171	5.286	8.115	94.54	95
$PdSe_2O_5$	*I*2/*a*	7.212	5.569	12.177	106.84	94,95
$Rh_2(Se_2O_5)$	*P*2_1/*n*	10.867	11.289	11.592	95.88	96

compounds.[100] They exhibit the unprecedented $[Au(S_2O_7)_2]^-$ anion with the gold atoms in square planar coordination of two chelating disulfate ions (Figure 13). For both compounds, the decomposition occurs via several steps and is finished at about 450 °C at the stage of elemental gold and the sulfates M_2SO_4 (M = Li, Na), as revealed by x-ray powder diffraction of the residues.

While no sulfate of divalent platinum is known to date, $Pd(SO_4)$ can be obtained as red crystalline material by oxidizing the metal with fuming sulfuric acid at 400 °C in sealed glass tubes. $Pd(SO_4)$ occurs in at least two different modifications, and both contain the Pd^{2+} ions in a typical square planar surrounding of oxygen atoms.[101,102] The $[PdO_4]$ moieties are connected by SO_4^{2-} tetrahedra according to $^3_\infty[Pd(SO_4)_{4/4}]$ and only the orientation of the polyhedra with respect to each other differs in the two modifications. Further oxidation of palladium to its tri- or even tetravalent state has not been observed up to now. Instead, attempts to achieve oxidation by sulfur trioxide, the anhydride of sulfuric acid, led to the disulfate $Pd(S_2O_7)$.[103] The compound can be prepared by the reaction of the noble metal with SO_3 at 120 °C and shows an unusual deep blue color. The latter can be attributed to the unique structure of the compound that shows the Pd^{2+} ions in octahedral coordination of oxygen atoms. The $[PdO_6]$ octahedron is essentially undistorted, that is, no Jahn–Teller effect is observable as might have been expected for an electronic d^8 configuration. The rare cases that this type of oxygen coordination has been observed for Pd^{2+} show that usually very rigid frameworks are necessary that force the metal into an octahedral surrounding. Examples are the oxides Ca_2PdWO_6[104] and $PdAs_2O_6$[105] which are closely related to the structures of perovskite and aluminum trichloride, respectively, and the above-mentioned polyoxometalates $[Pd_{13}(AsPh)_8O_{32}]^{6-}$ and $[Pd_{13}Se_8O_{32}]^{6-}$. By contrast, in $Pd(S_2O_7)$, the Pd^{2+} ion is found in an octahedral coordination of oxygen atoms that belong to six monodentate $S_2O_7^{2-}$ groups. All of the six disulfate groups bonded to the palladium atom are crystallographically equivalent, and the terminal oxygen atoms of the $S_2O_7^{2-}$ ion connect six Pd^{2+} ions with each other leading to a 3D structure according to the formulation $^3_\infty[Pd(S_2O_7)_{6/6}]$.

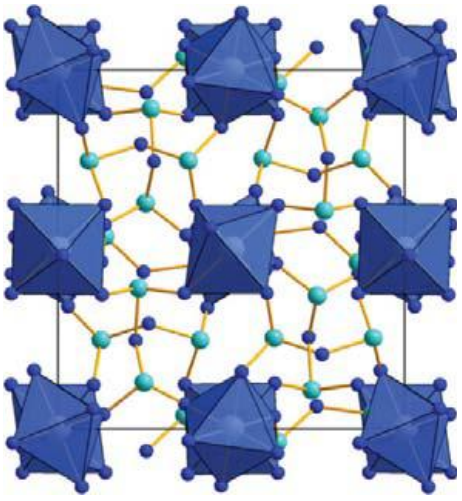

Figure 12 In the structure of $Rh_2(Se_2O_5)_3$ sixfold coordinated Rh^{3+} ions (blue octahedra) are linked by the $Se_2O_5^{2-}$ ions to a three-dimensional network $^3_\infty[Rh(Se_2O_5)_{6/4}]$.

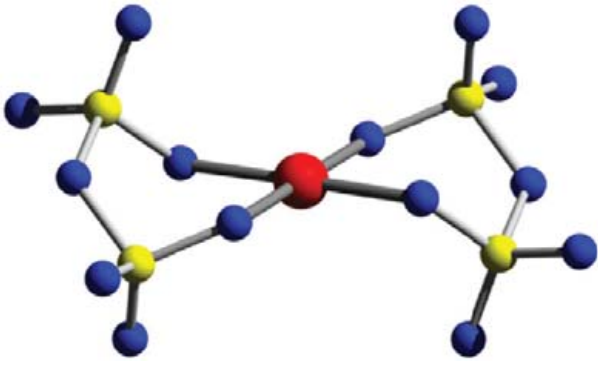

Figure 13 The bis-(disulfato)-aurate anion $[Au(S_2O_7)_2]^-$ shows the gold atom (red) in square planar coordination of two chelating disulfate groups.

The unusual Pd^{2+} coordination in $Pd(S_2O_7)$ leads to an electronic $t_{2g}^6e_g^2$ configuration of the palladium atom with two unpaired electrons bearing paramagnetic behavior of the compound. The temperature dependence of the magnetic and reciprocal magnetic susceptibility of $Pd(S_2O_7)$ is shown in Figure 14. The inverse magnetic susceptibility (χ^{-1} data) displays a linear Curie–Weiss behavior above 30 K leading to an effective magnetic moment of $\mu_{eff} = 2.89(1)\,\mu_B$/Pd atom (the theoretical spin-only value ($S = 1$) would be 2.83 μ_B) and a Weiss constant of $\theta_p = 11.6(2)$ K. The positive Weiss constant indicates ferromagnetic interactions and indeed $Pd(S_2O_7)$ is the first example that ferromagnetic ordering has been observed in an oxidic palladium compound. No hysteresis in the magnetization could be observed, classifying $Pd(S_2O_7)$ as a soft ferromagnet.

The oxidation of precious metals by sulfuric acid, oleum, or SO_3 does not work for the platinum metals ruthenium, osmium, and iridium. Besides palladium, only rhodium metal reacts with concentrated sulfuric acid, at least under harsh conditions as 400 °C in sealed glass ampoules.[106] Two sulfates could be gained, $Rh_2(SO_4)_3(H_2O)_2$ and $Rh_2(SO_4)_3$, which form red crystals and show the Rh^{3+} ions in octahedral coordination of oxygen atoms. In the hydrate, both water molecules are coordinated to metal atoms and form strong hydrogen bonds to noncoordinated oxygen atoms of the sulfate groups. The anhydrous rhodium(III) sulfate belongs to the to the large family of $M_2(SO_4)_3$-type sulfates that can be seen as corundum-type (Al_2O_3) varieties with complex anions. Thus, each Rh^{3+} ion is surrounded by six monodentate SO_4^{2-} anions which connect four metal ions with each other according to the formulation $^3_\infty[Rh(SO_4)_{6/4}]$. The decomposition of the compound occurs via Rh_2O_3 as an intermediate and leads to elemental rhodium finally.

The probably longest known noble metal sulfate is Ag_2SO_4 which has been investigated several times. A very exciting sulfate of silver is the recently described $Ag(SO_4)$ that has been obtained as black thermally labile (decomposition above 120 °C) powder from the reaction of AgF_2 with sulfuric acid.[107] In contrast to the above-mentioned $Au(SO_4)$, which has to be formulated as $Au_2(SO_4)_2$ according to the presence of

a $[Au_2]^{4+}$ ion, $Ag(SO_4)$ contains discrete Ag^{2+} ions in square planar coordination of oxygen atoms. The electronic d^9 configuration of the metal leads to antiferromagnetic ordering at low temperature. Furthermore, the bandgap of 0.82 eV indicates that $Ag(SO_4)$ is a semiconductor. It is worthwhile mentioning that $Ag(SO_4)$ behaves completely different from the copper(II) congener $Cu(SO_4)$[108] (Table 8).

2.18.4.3.3 Sulfate derivatives

The most important derivative of sulfuric acid is methanesulfonic acid (MSA), CH_3SO_3H. Because it has similar physical properties compared to H_2SO_4, but is much less oxidizing, it is strongly used in electroplating processes. However, the knowledge of noble metal methanesulfonates is very limited. This might have to do with the reduction power of MSA which leads often to the formation of the elemental metals when their compounds are reacted with the acid. In fact, besides $Ag(CH_3SO_3)$ only the ternary aurates $M[Au(CH_3SO_3)_4]$ (M = Li, Na, Rb) have been reported up to now.[109] They have been prepared by the reactions of $Au(OH)_3$, M_2CO_3 (M = Li, Na, Rb), and MSA at elevated temperatures in sealed glass ampoules. In the crystal structures of the tetragonal compounds $Li[Au(CH_3SO_3)_4]$ and $Rb[Au(CH_3SO_3)_4]$, the complex $[Au(CH_3SO_3)_4]^-$ anions are linked by the M^+ ions in three dimensions. Contrastingly, in the triclinic structure of $Na[Au(CH_3SO_3)_4]$, the complex anions linked into layers that are further connected by weak hydrogen bonds. The thermal decomposition of the compounds leads in a multistep process to elemental gold and the sulfates M_2SO_4.

Similar to the methanesulfonates also the 'triflates', that is, salts of trifluoromethanesulfonic acid (triflic acid), are only known for gold if $Ag(CF_3SO_3)$ is neglected. The ternary gold salts $M[Au(CF_3SO_3)_4]$ (M = Li, Na, K, Rb, Ag) exhibit the *tetrakis*-(triflato)-aurate anion, $[Au(CF_3SO_3)_4]^-$, with the gold atom in square planar coordination of four monodentate triflate ions.[110] Two different shapes of the complex anion occur in the crystal structures, which differ in the orientations of the $[CF_3]$ moieties with respect to each other. This can be

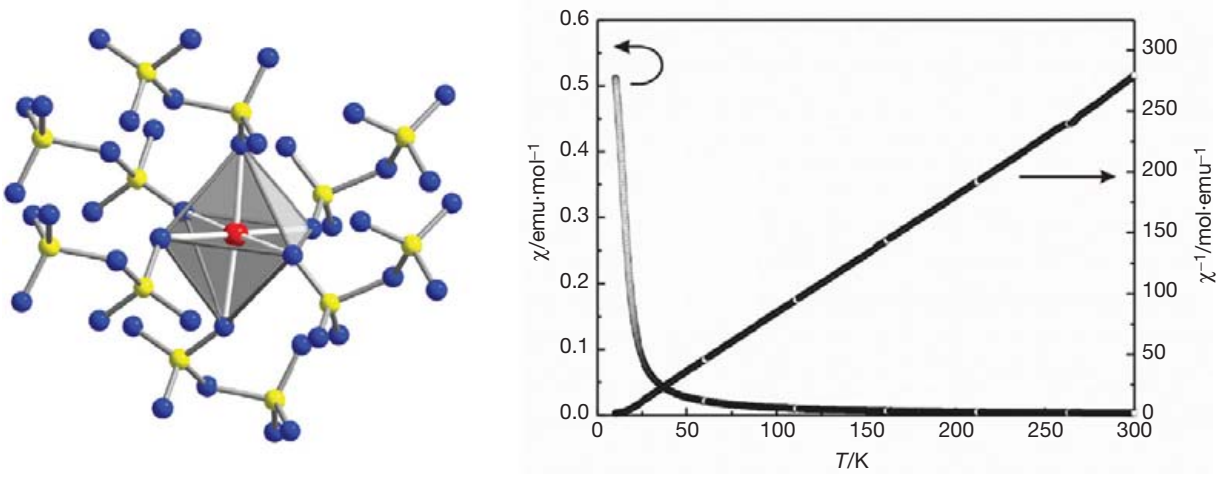

Figure 14 In the crystal structure of the deep blue disulfate $Pd(S_2O_7)$ the Pd^{2+} ion (red) exhibits unusual octahedral coordination by six monodentate disulfate groups (left). The octahedron is nearly undistorted and the high-spin d^8 configuration of the metal ion leads to the paramagnetism of the compound (right). Moreover, at low temperature $Pd(S_2O_7)$ orders ferromagnetically with an ordering temperature of 11.6 K.

Table 8 Structural data of noble metal sulfates

Compound	*Space group*	*Lattice parameters*						*References*
		a *(Å)*	b *(Å)*	c *(Å)*	α *(°)*	β *(°)*	γ *(°)*	
$Li[Au(S_2O_7)_2]$	*P*−1	5.322	6.497	8.367	107.98	90.17	102.58	100
$Na[Au(S_2O_7)_2]$	$P2_1/n$	5.331	11.934	9.077		98.55		100
$NaAu(SO_4)_2$	$P2_1/n$	4.691	8.459	8.312		95.69		99
$KAu(SO_4)_2$	*C*2/*c*	11.099	7.242	9.411		118.35		99
$RbAu(SO_4)_2$	*P*−1	4.236	4.975	8.890	76.36	88.44	73.53	99
$CsAu(SO_4)_2$	$P2_1/c$	10.297	8.934	9.010		111.08		98
$Pd(SO_4)$	*C*2/*c*	7.845	5.179	7.909		95.61		101
$Pd(S_2O_7)$	$P2_1/n$	5.022	12.805	8.043		91.41		103
Ca_2PdWO_6	*Fm*−3*m*	8.103						104
$PdAs_2O_6$	*P*−31*m*	4.820		4.665				105
$Rh_2(SO_4)_3(H_2O)_2$	*Pnma*	9.205	12.445	8.334				106
$Rh_2(SO_4)_3$	*R*−3	8.068		22.048				106
$AgSO_4$	*P*−1	4.692	4.753	8.013	103.40	76.48	118.08	107

most easily expressed by the angles C–Au–C which are 120° and 60°, respectively, for the one structure type and 90° for the other (Figure 15). In the first case a sandwich-type arrangement of the $[CF_3]$ groups results while otherwise a winged wheel type of structure occurs. The compounds turned out to be quite thermolabile and their decomposition leads in the course of complicated reactions to elemental gold and the respective alkaline metal sulfates. For M = Ag elemental silver is formed instead of an sulfate.

The sulfuric acid derivate that has been investigated most intensively is fluorosulfuric acid, HSO_3F. One reason is that the systems HSO_3F–$Au(SO_3F)_3$ and HSO_3F–$Pt(SO_3F)_4$ have been regarded as noble metal superacid systems.[111] In the course of the investigations of these systems cesium *tetrakis*-fluorosulfato-aurate, $Cs[Au(SO_3F)_4]$, and cesium hexakis-fluorosulfato-platinate $Cs_2[Pt(SO_3F)_6]$ were characterized. As expected, the aurate shows typical square planar gold coordination, and the Pt^{4+} ion in the platinate is in a nearly perfect octahedral surrounding of oxygen atoms from six monodentate anions. The most remarkable compound that arises from these reactions is gold(III)-fluorosulfate, $Au(SO_3F)_3$.[112] Single crystals were obtained by recrystallization from bis(fluorosulfuryl) peroxide, $S_2O_6F_2$, under O_2 pressure. The structure of the compound is dimeric according to $\{[Au(SO_3F)_{2/1}(SO_3F)_{2/2}]\}_2$ and shows the Au^{3+} ions in square planar coordination of four SO_3F^- groups, of which two are bridging to the second gold atom of the dimer. Structurally, $Au(SO_3F)_3$ is an analog of $AuCl_3$ with complex anions. $Au(SO_3F)_3$ can be reduced with either gold powder or carbon monoxide in fluorosulfuric acid to yield gold(II) fluorosulfate as a yellow–red solid. No structural data are known but based on magnetic measurements and vibrational spectra the compound is mixed valent according to $Au^{I}Au^{III}(SO_3F)_4$.

Very recently, the SO_3F^- anion has been successfully used to stabilize divalent silver. In $Ag(SO_3F)_2$, the Ag^{2+} ions are octahedrally coordinated by oxygen atoms with a severe Jahn–Teller distortion of the $[AgO_6]$ polyhedra.[113] The octahedra are linked by the fluorosulfate ions to a 3D network. $Ag(SO_3F)_2$ is a soft ferromagnet with a Curie temperature of 24.8 K and it shows a single broad electron spin resonance (ESR) with $g = 2.183$ at $T = 293$ K. Coulomb-corrected local spin density approximation (LSDA + U) calculations predict a direct electronic bandgap at the Fermi level of 1.05 eV. $Ag(SO_3F)_2$ is thermally unstable and at room temperature or in the presence of strong acids the dark brown crystals slowly decompose at the surface to the black mixed-valent $Ag_3(SO_3F)_4$. Very fast exothermic decomposition of $Ag(SO_3F)_2$ with emission of a fluorosulfuryl radical ($SO_3F^{\bullet}$) occurs above 120 °C as confirmed by thermoanalytical measurements, and evolved gas analyses. The mixed-valent $Ag_3(SO_3F)_4$ has to be formulated as $Ag^{I}{}_2Ag^{II}(SO_3F)_4$ and is one of the few Ag^{I}/Ag^{II} examples.[114] The monoclinic compound can be best written as $[Ag^{I}{}_2(SO_3F)]^+[Ag^{II}(SO_3F)_3]^-$. The Ag^{II} centers form 1D chains linked through O–S–O bridges that result in pronounced antiferromagnetic coupling with $T_N = 225$ K. The environments around Ag^{I} and Ag^{II} differ substantially, which suggests a genuine mixed- (i.e., localized) and not intermediate-valent (i.e., delocalized) character. Indeed, electronic absorption is not observed up to 7500 cm^{-1}, so the intervalence charge-transfer transition across the electronic bandgap must fall above 0.8 eV. The compound is stable up to about 75 °C, which marks the onset of its thermal decomposition to $Ag^{I}SO_3F$ and the $SO_3F^{\bullet}$ radical. $Ag_3(SO_3F)_4$ is, along with the above-mentioned $Ag(SO_4)$, the second known 1D antiferromagnetic semiconducting oxide derivative of Ag^{II} (Table 9).

2.18.4.3.4 Nitrates, perchlorates, and iodates

Besides the sulfates of noble metals, their respective nitrates have been investigated relatively intensively. Nevertheless, our knowledge is still limited, and for some of the metals no nitrates are known up to now, for example, for iridium and osmium. Again gold is the element which has been investigated best, although even for this element no simple binary nitrate is known. Gold nitrates occur as *tetrakis*-(nitrato)-aurates and the aristotype for these salts is the acid $(H_5O_2)[Au(NO_3)_4]\cdot H_2O$ that can be obtained as yellow crystalline material upon cooling of a solution of $Au(OH)_3$ in concentrated nitric acid.[116] The crystal structure contains the Au^{3+} ion in coordination of four monodentate NO_3^- ligands and the $[Au(NO_3)_4]^-$ units are linked by $H_5O_2^+$ ions. Significant hydrogen bonding is observed in the crystal structure between the $H_5O_2^+$ ions and the H_2O molecules. The same anion is found in a large number of compounds $M[Au(NO_3)_4]$, with M being a monovalent cation.

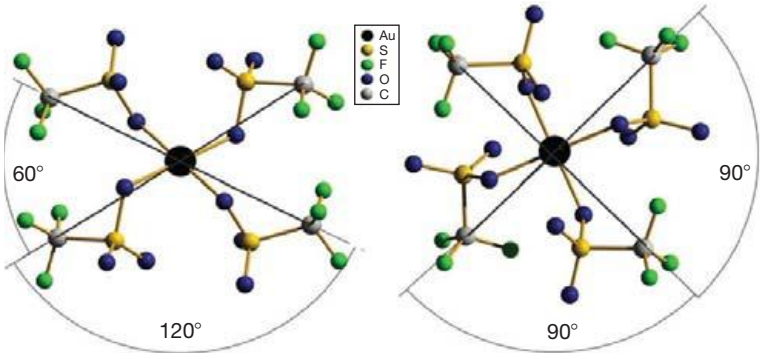

Figure 15 Sandwich-type structure of the observed $[Au(CF_3SO_3)_4]^-$ anion in the structures of $M[Au(CF_3SO_3)_4]$-type compounds (at left). An alternative structure would be the winged wheel type of structure (at right) that has been observed previously for the methanesulfonate analogs $[Au(CH_3SO_3)_4]^-$. Both structures differ in the orientations of the $[CF_3]$ moieties with respect to each other. This can be most easily expressed by the angles C–Au–C which are 120° and 60°, respectively, for the one structure type and 90° for the other.

Table 9 Structural data of sulfate derivatives of noble metals

Compound	*Space group*	*Lattice parameters*						*References*
		a (Å)	b (Å)	c (Å)	α (°)	β (°)	γ (°)	
$Ag(CH_3SO_3)$	$P2_1/c$	8.699	5.777	8.267		100.21		115
$Li[Au(CH_3SO_3)_4]$	$I-4$	9.386		9.170				109
$Na[Au(CH_3SO_3)_4]$	$P-1$	5.040	8.637	9.733	72.69	75.61	77.69	109
$Rb[AuCH_3(SO_3)_4]$	$P-42_1c$	9.467		8.899				109
$Li[Au(CF_3SO_3)_4]$	$P-1$	5.099	8.541	10.447	94.01	92.94	93.84	110
$Na[Au(CF_3SO_3)_4]$	$P-1$	5.254	9.021	10.803	104.37	93.60	90.716	110
$K[Au(CF_3SO_3)_4]$	*Pbcn*	9.043	10.506	21.207				110
$Rb[Au(CF_3SO_3)_4]$	$P21/n$	9.198	21.218	10.834		90.12		110
$Ag[Au(CF_3SO_3)_4]$	$C2/c$	22.188	4.992	17.517		104.74		110
$Cs[Au(SO_3F)_4]$	$C2/c$	17.725	5.822	14.624		102.12		111
$Cs_2[Pt(SO_3F)_6]$	*P*321	9.070		7.603				111
$Au(SO_3F)_3$	$P2_1/a$	9.700	9.222	10.810		94.43		112
$Ag(SO_3F)_2$	$P2_1/c$	10.513	7.752	8.937		117.87		113
$Ag_3(SO_3F)_4$	$P2_1/c$	5.3367	12.949	19.598		100.64		114

The $[Au(NO_3)_4]^-$ anion occurs also in the structures of $(NO_2)[Au(NO_3)_4]$ and $(NO)[Au(NO_3)_4]$.[117,118] These compounds are obtained by the reaction of elemental gold with N_2O_5, the anhydride of nitric acid, and contain NO^+ and NO_2^+ cations, respectively, for the charge balance. These nitrates can be used as precursor materials as they do not contain elements such as carbon or chlorine which may lead to a contamination of the deposited gold. Interestingly, the decomposition of the precursors can be initiated by an electron beam, which allows a simple 'writing' of gold structures. For that purpose solutions of $(NO_2)[Au(NO_3)_4]$ in N_2O_5 were applied onto a silica surface and decomposed at desired locations by the electron beam.[117]

N_2O_5 is also a suitable reagent for the oxidation of other noble metals. Thus, the oxidation of palladium leads to the red-colored complex nitrate $(NO)_2[Pd(NO_3)_4]$ that contains the square planar *tetrakis*-(nitrato)-palladate ion, $[Pd(NO_3)_4]^{2-}$,[118] which is already known for several alkali metal compounds $M_2[Pd(NO_3)_4]$.[119] Upon heating, the nitrate $(NO)_2[Pd(NO_3)_4]$ decomposes via $Pd(NO_3)_2$ and PdO to the elemental metal. The constitution of the binary nitrate $Pd(NO_3)_2$ is not known, but two modifications of the hydrate $Pd(NO_3)_2 \cdot 2H_2O$ have been reported.[120,121] They show the Pd^{2+} ion in square planar coordination of two nitrate groups and two water molecules which might be either in *cis* (modification I) or *trans* orientation (modification II) with respect to each other.

Similar to the findings for the sulfates also for the nitrates no platinum analogs of palladium are known. Unexpectedly elemental platinum does not react with N_2O_5, even if the metal is provided as fine powder. However, the reaction with $H_2[Pt(OH)_6]$ as starting material afforded at room temperature light yellow plates of $(NO)_2[Pt(NO_3)_6]$. The nitrylium nitrate is extremely hygroscopic and decomposes already at room temperature. $(NO)_2[Pt(NO_3)_6]$ contains the *hexakis*-(nitrato)-platinate anion which shows the central Pt^{4+} ion in coordination of six monodentate nitrate groups.[118]

The perchlorate anion is known as a weakly coordinating ligand and it is therefore often used if charge balance is needed to stabilize various complexes. By contrast, it is very difficult to obtain simple metal perchlorates, and this is especially true for noble metals. In fact, no binary perchlorate has been described up to now for these elements. A very elegant, however not trivial, way to perchlorates is the reaction of chlorine trioxide, Cl_2O_6, with metals or suitable metal compounds. It has been shown that this method works also for gold, and the respective reactions with Au metal, $AuCl_3$, or $HAuCl_4 \cdot nH_2O$ led to the chloryl salt, $(ClO_2)Au(ClO_4)_4$.[122] The structure of the perchlorate was solved by a Rietveld analysis of powder XRD data. The structure displays discrete ClO_2^+ ions lying in channels formed by $[Au(ClO_4)_4]^-$ stacks. The latter show the Au^{3+} ions in square planar coordination. It is remarkable that the distances Cl–O differ significantly in the anions. Those oxygen atoms which are bonded to the central atom show bond lengths of 153 pm while the respective terminal bonds are as short as 139 pm.

Compared to the perchlorates, a little bit more is known on noble metal iodates, even if also in this case gold, palladium, and platinum are the dominating metals. In all cases, the anion is IO_3^- which has achieved considerable attention because its pyramidal shape and the resulting polarity make it a suitable building unit for non-centrosymmetric compounds bearing potential for nonlinear optical effects, such as frequency doubling (SHG). Indeed, the *tetrakis*-(iodato)-aurate $K[Au(IO_3)_4]$ crystallizes with noncentrosymmetric symmetry (*P*1).[123] The compound has been prepared by the reaction of elemental gold with concentrated selenic acid and KIO_4 under mild hydrothermal conditions. Interestingly, the single crystals of $K[Au(IO_3)_4]$ grew directly off the surface of the gold metal. The *in situ* generation of iodate by the reduction of periodate by water is a critical feature of this reaction, because it allows for the slow introduction of the key reactant that controls solubility. Interestingly, the isotypic compound $Ba[Pd(IO_3)_4]$ with Pd^{2+} replacing Au^{3+} and Ba^{2+} replacing K^+ is also available by hydrothermal synthesis.[124] Furthermore, the $[Pd(IO_3)_4]^{2-}$ ion occurs in $K_{2.5}[Pd(IO_3)_4] \cdot H_{0.5}IO_3$ that has also been prepared hydrothermally.[124] The structure of this compound, however, bears inversion symmetry (space group $C2/m$). The square planar coordination of Pd^{2+} is also the characteristic feature of $AgPd(IO_3)_3$ and the binary $Pd(IO_3)_2$.[124] In contrast to the above-mentioned iodates in both compounds, the IO_3^- ions

act as bridging ligands leading to $^{1}_{\infty}[Pd(IO_3)_{2/2}(IO_3)_{2/1}]^-$ chains in the silver compound and to $^{2}_{\infty}[Pd(IO_3)_{4/2}]$ layers in $Pd(IO_3)_2$. Both compounds show inversion symmetry. For $Ba[Pd(IO_3)_4]$, SHG measurements have been performed. They prove the non-centrosymmetric structure of the compound and show a moderate SHG response of about $0.4 \times$ KTP (KTP = $KTiOPO_4$) as standard.

A much stronger SHG response is found for the unique Pt^{IV} iodate $Pb[Pt(IO_3)_6]\cdot H_2O$.[125] This compound contains $[Pt(IO_3)_6]^{2-}$ octahedra and has been obtained hydrothermally from I_2O_5, $Pt(acac)_2$, and $PbCl_2$. The iodate crystallizes with the non-centrosymmetric polar space group *R*3 and shows an SHG effect as strong as $8 \times$ KDP (KDP = KH_2PO_4 as standard). The unique parallel alignment of the stereoactive lone pairs on the Pb^{2+} cations and the iodate anions might strengthen the SHG response in a synergistic way (**Table 10**).

2.18.4.3.5 Phosphates and silicates

It is astonishing to see that for the most abandoned oxoanions in nature, that is, silicate (SiO_4^{4-}), phosphate (PO_4^{3-}), and carbonate (CO_3^{2-}), essentially no minerals containing noble metals occur. Laboratory work has meanwhile afforded a limited number of compounds but our knowledge is mainly restricted to phosphates which are known for all noble metals except osmium, while simple binary silicates and carbonates, for example, for gold or platinum, are still elusive.

The gold phosphate $Au(PO_4)$ has been characterized recently by x-ray powder diffraction.[129] It can be prepared from gold(III)–hydroxide and concentrated phosphoric acid at 130 °C as a yellow powder. The compound is isotypic with the above-mentioned $Pd(SO_4)$, that is, it contains a network of PO_4^{3-}-linked $[AuO_4]$ squares. The compound decomposes above 400 °C.

Reactions in highly concentrated H_3PO_4 have recently also provided access to the first binary iridium phosphates.[130] They have the composition $Ir(PO_3)_3$ and $(Ir_{1-x}Si_x)_3[Si_2O(PO_4)_6]$ and are *meta*-phosphates and silico-phosphates of trivalent and tetravalent iridium, respectively. The *meta*-phosphate $Ir(PO_3)_3$ crystallizes with two different modifications, both containing infinite phosphate chains and octahedral coordinated Ir^{3+} ions. One of these modification has been previously also found for rhodium in the phosphate $Rh(PO_3)_3$.[131,132] The respective phosphates could be also prepared for ruthenium, and furthermore a cyclohexaphosphate has been reported for this element, namely $Ru_2[P_6O_{18}]$.[132] The silico-phosphate exhibits the complex $[Si_2O(PO_4)_6]^{12-}$ anion with a central [Si–O–Si] moiety surrounded by six PO_4^{3-} tetrahedra.

Another preparative approach toward noble metal phosphates are reactions in reactive fluxes, for example, the hydrogen phosphates $M(H_2PO_4)$, with M being an alkaline metal. However, in these cases usually the M atom is incorporated into the structures, that is, ternary compounds are formed. Such ternary compounds can also be obtained if the metals M are introduced as oxides in the typical syntheses with H_3PO_4. The by far most ternary compounds have been described for palladium. They all have something in common, in that they contain the Pd^{2+} ions in square planar coordination of oxygen atoms which belong to $P_2O_7^{4-}$ groups.[133–135]

Silicates of noble metals are only known for silver if the above-mentioned silico-phosphates are neglected. The problems in the synthesis of noble metal silicates are caused on the one hand by the weak acidity of silica acids and on the other hand by the reduced thermal stability of noble metal oxides that prevents typical solid-state reactions. A possibility to overcome these problems is the application of high oxygen pressure during synthesis. In this way at least for silver a number of silicates have been prepared. According to the condensation tendency of $[SiO_4]$ tetrahedra, some of these silicates are rather complex like the red compounds $Ag_{10}[Si_4O_{13}]$, $Ag_{18}[SiO_4]_2[Si_4O_{13}]$, and $Ag_6[Si_2O_7]$.[136–138] However, also the simple *ortho*-silicate $Ag_4[SiO_4]$ which exhibits surprisingly a different

Table 10 Structural data of noble metal nitrates, perchlorates, and iodates

Compound	*Space group*	*Lattice parameters*						*References*
		a (Å)	b (Å)	c (Å)	α (°)	β (°)	γ (°)	
$(H_5O_2)[Au(NO_3)_4]\cdot H_2O$	*C*2/*c*	12.145	8.544	12.257		117.75		116
$K[Au(NO_3)_4]$	$P2_1/c$	9.21	7.14	10.04		128.6		126
$(NO)[Au(NO_3)_4]$	$P2_1/n$	8.270	7.264	9.092		111.91		118
$(NO_2)[Au(NO_3)_4]$	$P2_1/n$	7.751	8.102	8.987		112.67		117
$(NO)_2[Pd(NO_3)_4]$	$P2_1/c$	8.069	7.473	9.171		99.372		118
$Na_2[Pd(NO_3)_4]$	$P2_1/c$	7.093	7.782	8.994		91.67		127
$K_2[Pd(NO_3)_4]$	$P2_1/c$	7.864	7.532	9.441		99.49		128
$Rb_2[Pd(NO_3)_4]$	$P2_1/c$	7.843	7.97	9.725		100.39		119
$Cs_2[Pd(NO_3)_4]$	$P2_1/c$	10.31	10.426	11.839		108.17		119
$(NO)_2[Pt(NO_3)_6]$	$P2_1/c$	7.114	9.350	11.567		107.56		118
$Pd(NO_3)_2\cdot 2H_2O$	*Pbca*	5.004	10.607	11.722				120,121
$(ClO_2)[Au(ClO_4)_4]$	*C*2/*c*	15.047	5.294	22.202		128.33		122
$K[Au(IO_3)_4]$	*P*1	5.648	7.196	8.1377	105.26	93.59	111.84	123
$Ba[Pd(IO_3)_4]$	*P*1	5.753	7.33	8.119	105.49	94.39	112.42	124
$K_{2.5}[Pd(IO_3)_4]\cdot H_{0.5}IO_3$	*C*2/*m*	11.327	11.825	12.967		114.42		124
$AgPd(IO_3)_3$	*P*−1	7.315	7.991	8.575	63.75	76.59	82.27	124
$Pd(IO_3)_2$	*Pbca*	5.839	6.037	15.071				124
$Pb[Pt(IO_3)_6]\cdot H_2O$	*R*3	11.307		11.242				125

Table 11 Structural data of noble metal phosphates and silicates

Compound	Space group	Lattice parameters						References
		a (Å)	b (Å)	c (Å)	α (°)	β (°)	γ (°)	
$Au(PO_4)$	*C*2/*c*	7.792	5.458	7.725		97.01		129
$Ir(PO_3)_3$	*P*−1	5.003	6.971	10.305	98.48	92.43	92.56	130
$(Ir_{1-x}Si_x)_3[Si_2O(PO_4)_6]$	*R*−3	7.882		24.476				130
$Rh(PO_3)_3$	*C*/*c*	13.00	19.065	9.296		127.04		131
$Rh(PO_4)$	*Imma*	10.397	13.112	6.393				131
$Ru_2[P_6O_{18}]$	$P2_1/c$	6.292	15.276	8.365		106.54		132
Ru(PO3)3	*P*−1	6.957	10.324	5.03	92.45	92.31	98.61	132
$Ag_{10}[Si_4O_{13}]$	*P*−1	11.356	9.131	8.038	100.32	98.62	112.83	136
$Ag_{18}[SiO_4]_2[Si_4O_{13}]$	*C*2/*m*	12.725	9.714	10.73		106.8		137
$Ag_6[Si_2O_7]$	$P2_1$	5.304	9.753	15.928		91.17		138
$Ag_4[SiO_4]$	*P*42/*n*	7.317		4.960				139
$Ag_5[SiO_4]$	*Pnnm*	9.856	9.108	6.271				140
$Ag_9[SiO_4]_2[NO_3]$	*P*−1	5.768	6.768	8.843	107.03	99.87	94.16	141

structure from what is known for the alkaline metal orthosilicates could be gained as yellow crystals.[139] The most surprising compound is probably $Ag_5[SiO_4]$, a subvalent greenish black metallic compound.[140] An early report on the synthesis of $Ag_4[SiO_4]$ in the reaction of $Ca_2[SiO_4]$ with molten $AgNO_3$ turned out to be erroneous and in fact the silicate–nitrate $Ag_9[SiO_4]_2[NO_3]$ could be identified as the reaction product[141] (Table 11).

2.18.4.4 Halides

Halides are probably the best investigated class of compounds in noble metal chemistry. Nevertheless, there is still interest in these compounds and even nowadays new and sometimes unexpected discoveries are made. In the case of the fluorides, these new findings are often correlated with the search for high oxidation states, as pointed out in Section 2.18.2.2. Also, other halides have sometimes attracted renewed interest for several reasons. Some recent findings should be emphasized here, while Table 12 provides a more comprehensive overview.

2.18.4.4.1 Chlorides

One of the most important chemicals of gold is the so-called tetrachloroauric acid, usually written as $H[AuCl_4]$. The compound has been structurally characterized for the first time in 1971 and identified as a tetrahydrate.[142] However, it was only recently that a detailed investigation revealed that tetrachloroauric acid may occur with a variable amount of water and the hydrates $H[AuCl_4]\cdot xH_2O$ with $x = 2, 3, 4$ have been characterized.[143] The tetrahydrate was obtained from the reaction of elemental gold in *aqua regia*. At low temperature (233 K), the compound consists of square planar $[AuCl_4]^-$ anions, $H_5O_2^+$ cations, and water molecules. The latter two form infinite chains according to $^1_\infty[(H_5O_2)(H_2O)_{4/2}]^+$ established via strong hydrogen bonding. At higher temperature, the tetrahydrate adopts the structure reported in the literature which is stamped by a disorder of the $[AuCl_4]^-$ anions. Attempts to recrystallize the tetrahydrate from ethanol led to the trihydrate $H[AuCl_4]\cdot 3H_2O$ and reaction of the tetrahydrate with sulfuric acid at 200 °C gave the dihydrate $H[AuCl_4]\cdot 2H_2O$. Both the tri- and the dihydrate are closely related to the tetrahydrate and it is essentially the hydrogen bonding pattern that varies between the structures. In the trihydrate the observed $^1_\infty[(H_5O_2)(H_2O)_{4/2}]^+$ chain of the tetrahydrate is cut into $[(H_7O_3^+)]_2$ dimers by removing one H_2O molecule per formula unit. In the dihydrate, these dimers are further transformed to $H_5O_2^+$ ions by further removal of water molecules. According to these findings, the tetrachloroauric acids $H[AuCl_4]\cdot xH_2O$ should be written as $(H_5O_2)(H_2O)_2[AuCl_4]$ $(x=4)$, $(H_7O_3)[AuCl_4]$ $(x=3)$, and $(H_5O_2)[AuCl_4]$ $(x=2)$, respectively.

The chlorides of platinum have attracted recently renewed interest with respect to a detailed view on chemical bonding in these compounds.[144,145] This is especially true for the β-form of $PtCl_2$ which exhibits hexameric Pt_6Cl_{12} molecules. The Pt_6Cl_{12} molecules show the trigonally elongated structure of the classical M_6X_{12} type of clusters with square planar $PtCl_4$ fragments. However, in contrast to the M_6X_{12} type of clusters of early transition metals, it could be shown that no metal–metal bonds are formed in the in the Pt_6Cl_{12} molecules, as can be seen from the distances Pt—Pt of about 335 pm. Interestingly, the Pt_6Cl_{12} molecule was also part of the mixed-valent chloride $PtCl_3$ (Figure 16). The molecules are intersected by chains of edge-connected $[PtCl_{4/2}Cl_{2/1}]$ octahedra as they also occur in the crystal structure of $PtCl_4$. As it could be shown the two regions of the structure do not have remarkable interactions with each other. It should be noted that the same features have been found for $PtBr_3$.

A fascinating study has been undertaken for the iodopalladates Cs_2PdI_6 and $Cs_2PdI_4\cdot I_2$ which are structurally closely related.[146] Cs_2PdI_6 has the cubic K_2PtCl_6 type of structure while $Cs_2PdI_4\cdot I_2$ is a tetragonally distorted variety of this structure. This can be explained in terms of an internal solid-state redox reaction which might be initiated by pressure. At high pressure, the I_2 molecules in $Cs_2PdI_4\cdot I_2$ oxidize Pd^{2+} to Pd^{4+} and the square planar $[PdI_4]$ moiety is transformed to a $[PdI_6]$ octahedron with splitting of the I–I bond. Thus, $Cs_2PdI_4\cdot I_2$ represents an excellent example of a solid-state electron transfer reaction.

Table 12 Structural data of noble metal halides (for high-valent metals see also **Table 1**)

Compound	*Space group*	*Lattice parameters*						*References*
		a *(Å)*	b *(Å)*	c *(Å)*	α *(°)*	β *(°)*	γ *(°)*	
$H[AuCl_4]\cdot 4H_2O$-I	*C*2/*m*	11.78	4.62	8.89		101.9		142
$H[AuCl_4]\cdot 4H_2O$-II	*C*2/*c*	19.057	4.811	11.300		117.73		143
$H[AuCl_4]\cdot 3H_2O$	$P2_1/c$	8.0221	11.488	11.443		127.665		143
$H[AuCl_4]\cdot 2H_2O$	$P2_1/c$	4.1136	10.382	9.364		101.62		143
$PtCl_2$	*C*2/*m*	13.258	3.194	6.802		107.75		147
Pt_6Cl_{12}	*R*−3*m*	13.126	8.666					144
$PtCl_3$	*R*−3	21.213		8.6				145
$PtCl_4$	*Pa*−3	10.45						148
$PtBr_3$	*R*−3	22.318		9.034				145
Cs_2PdI_6	*Fm*−3*m*	11.332						146
$Cs_2PdI_4\cdot I_2$	*I*4/*mmm*	8.987		9.240				146
RuF_3	*R*−3*c*	5.410			54.68			35
RuF_4	$P2_1/n$	5.607	4.946	5.413		121.27		35
RhF_3	*R*−3*c*	4.873		13.55				149
PdF_2	$P4_2/mnm$	4.954		3.385				150
PdF_3	*R*−3*c*	5.523			53.025			151
AgF	*P*−3*m*1	2.977						152
AgF_2	*Pbca*	5.568	5.831	5.101				153
AgF_3	$P6_122$	5.078		15.452				154
Ag_2F_5	*P*−1	4.999	11.087	7.357	90.05	106.54	90.18	155
Ag_3F_8	$P2_1/n$	5.046	11.054	5.449		97.17		156
OsF_5	$P2_1/c$	5.403	9.866	12.336		99.13		157
IrF_3	*R*−3*c*	4.943		13.82				158
IrF_4	*Fdd*2	9.64	9.25	5.67				159
PtF_4	*Fdd*2	9.59	9.284	5.712				31
AuF_3	$P6_122$	5.151		16.264				154
Au_3F_8	*P*21/*n*	5.272	10.708	5.735		90.63		160
$RuCl_3$	*P*63/*mcm*	6.121		5.655				161
$RhCl_3$	*C*2/*m*	5.95	10.3	6.03		109.2		162
$PdCl_2$	*R*−3	13.040		8.601				163
$OsCl_4$	*Cmmm*	7.930	8.326	3.56				164
$OsCl_5$	$P2_1/c$	9.17	11.5	11.97		109		165
$IrCl_3$	*Fddd*	6.95	9.81	20.82				166
AuCl	$I4_1/amd$	6.734		8.674				167
$AuCl_3$	$P2_1/c$	6.57	11.04	6.44		113.3		168
Au_4Cl_8	*P*−1	7.015	6.83	6.684	94.4	107.5	88.4	169
$RuBr_3$	$P6_3/mcm$	6.522		5.885				161
$RhBr_3$	*C*2/*m*	6.27	10.85	6.35		109		170
$PdBr_2$	$P2_1/c$	6.59	3.96	24.22		92.6		171
$OsBr_4$	*Pbca*	6.340	12.109	14.615				172
$IrBr_3$	*C*2/*m*	6.3	10.98	6.34		108.7		173
AuBr	$P4_2/ncm$	4.296		12.146				174
$AuBr_3$	$P2_1/c$	6.831	20.41	8.105		119.74		175
PdI_2	$P2_1/c$	6.69	8.6	6.87		103.5		176
PtI_2	$P2_1/c$	6.588	8.715	6.889		102.76		177
PtI_4	*Pbca*	12.9	15.64	6.9				178
Pt_2I_6	*C*2/*c*	6.735	12.061	13.313		101.25		179
Pt_3I_8	$P4_12_12$	11.664		10.682				180
AuI	$P4_2/ncm$	4.35		13.73				181

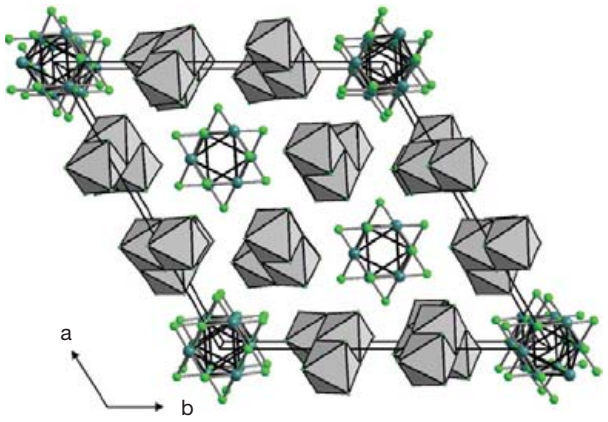

Figure 16 Crystal structure of $PtCl_3$, a mixed-valent chloride according to $Pt^{IV}Pt^{II}Cl_6$. The compound is composed of chains of edge-connected $[Pt^{IV}Cl_6]$ octahedra (drawn as gray polyhedra running along the *c*-axis) and $[Pt^{II}_6Cl_{12}]$ molecules as they are well known from the structure of β-$PtCl_2$. It is interesting to see that the different parts of the structure are nearly independent from each other and do not intersect.

2.18.5 Conclusion

The noble metals are still a fascinating object for chemists from all disciplines. Recent research has afforded interesting new insights in the structural chemistry of these elements and the properties of noble metal compounds. The chapter presents a selection of these newer results with a strong focus on inorganic compounds, their preparation, and their structural features. Moreover, comprehensive tables provide an overview of essential data of inorganic noble metal compounds.

References

1. Dirac, P. A. M. *Proc. R. Soc. Lond. Ser. A* **1929**, *123*, 714–733.
2. Pyykkö, P. *Adv. Quantum Chem.* **1978**, *11*, 353–409.
3. Pitzer, K. S. *Acc. Chem. Res.* **1979**, *12*, 271–276.
4. Pyykkö, P.; Desclaux, J.-P. *Acc. Chem. Res.* **1979**, *12*, 276–281.
5. Pyykkö, P. *Chem. Rev.* **1988**, *88*, 563–594.
6. Pyykkö, P. *Chem. Rev.* **1997**, *97*, 597–636.
7. Pyykkö, P. *Angew. Chem. Int. Ed.* **2004**, *43*, 4412–4456.
8. Pyykkö, P. *Annu. Rev. Phys. Chem.* **2012**, *63*, 45–64.
9. Pyykkö, P. *Chem. Rev.* **2012**, *112*, 371–384.
10. Kaltsoyannis, N. *J. Chem. Soc. Dalton Trans.* **1997**, *1997*, 1–11.
11. Schwerdtfeger, P. *J. Am. Chem. Soc.* **1989**, *111*, 7261–7262.
12. O´Grady, E.; Kaltsoyannis, N. *Phys. Chem. Chem. Phys.* **2004**, *6*, 680–687.
13. Krebs, B.; Hasse, K. *Acta Crystallogr.* **1976**, *B32*, 1334–1337.
14. Pley, M.; Wickleder, M. S. *J. Solid State Chem.* **2005**, *178*, 3206–3209.
15. Gong, Y.; Zhou, M.; Kaupp, M.; Riedel, S. *Angew. Chem. Int. Ed.* **2009**, *48*, 7879–7883.
16. Himmel, D.; Knapp, C.; Patzschke, M.; Riedel, S. *Chemphyschem* **2010**, *11*, 865–869.
17. Riedel, S.; Kaupp, M. *Angew. Chem. Int. Ed.* **2006**, *45*, 3708–3711.
18. Drews, T.; Supeł, J.; Hagenbach, A.; Seppelt, K. *Inorg. Chem.* **2006**, *45*, 3782–3788.
19. Craciun, R.; Picone, D.; Long, R. T.; Li, S. G.; Dixon, D. A.; Peterson, K. A.; Christe, K. O. *Inorg. Chem.* **2010**, *49*, 1056–1070.
20. Marx, R.; Seppelt, K.; Ibberson, R. M. *J. Chem. Phys.* **1996**, *104*, 7658–7664.
21. Hwang, I.-C.; Seppelt, K. *Angew. Chem. Int. Ed.* **2001**, *40*, 3690–3693.
22. Timakov, A. A.; Prusakov, V. N.; Drobyshevskii, Y. V. *Dokl. Akad. Nauk SSSR* **1986**, *291*, 125–128.
23. Himmel, D.; Riedel, S. *Inorg. Chem.* **2007**, *46*, 5338–5342.
24. Riedel, S.; Kaupp, M. *Inorg. Chem.* **2006**, *45*, 1228–1234.
25. Holloway, J. H.; Peacock, R. D.; Small, R. W. H. *J. Chem. Soc.* **1964**, *1964*, 644–648.
26. Mitchell, S. J.; Holloway, J. H. *J. Chem. Soc. A* **1971**, *1971*, 2789–2794.
27. Morrell, K.; Zalkin, A.; Tressaud, A.; Bartlett, N. *Inorg. Chem.* **1973**, *12*, 2640–2644.
28. Holloway, J. H.; Rao, P. R.; Bartlett, N. *Chem. Commun.* **1965**, *1965*, 306–307.
29. Bartlett, N.; Rao, P. R. *Chem. Commun.* **1965**, *1965*, 252–253.
30. Bartlett, N.; Lohmann, D. H. *J. Chem. Soc.* **1964**, *1964*, 619–626.
31. Müller, B. G.; Serafin, M. *Eur. J. Solid State Inorg. Chem.* **1992**, *29*, 625–633.
32. Wright, A. F.; Fender, B. E. F.; Bartlett, N.; Leary, K. *Inorg. Chem.* **1978**, *17*, 748–749.
33. Sorbe, P.; Grannec, J.; Portier, J.; Hagenmüller, P. *C. R. Seances Acad. Sci. Ser. C* **1977**, *1977*, 284–288.
34. Wang, X.; Andrews, L.; Riedel, S.; Kaupp, M. *Angew. Chem. Int. Ed.* **2007**, *46*, 8371–8375.
35. Casteel, W. J., Jr.; Wilkinson, A. P.; Borrmann, H.; Serfass, R. E.; Bartlett, N. *Inorg. Chem.* **1992**, *31*(14), 3124–3131.
36. Darriet, J.; Soubeyroux, J. L.; Touhara, H.; Tressaud, A.; Hagenmuller, P. *Mat. Res. Bull.* **1982**, *17*, 315–324.
37. Biltz, W.; Weibke, F. *Z. Anorg. Allg. Chem.* **1938**, *236*, 12–23.
38. Tinelli, G. A.; Holcomb, D. F. *J. Solid State Chem.* **1978**, *25*, 157–165.
39. Dietzel, P. D. C.; Jansen, M. *Chem. Commun.* **2001**, *2001*, 2208–2209.
40. Nuss, H.; Jansen, M. *Z. Naturforsch.* **2006**, *61b*, 1205–1208.
41. Nuss, H.; Jansen, M. *Angew. Chem. Int. Ed.* **2006**, *45*, 4369–4371.
42. Mudring, A.-V.; Jansen, M.; Daniels, J.; Krämer, S.; Mehring, M.; Ramalho, J. P.; Humberto Romero, A.; Parrinello, M. *Angew. Chem. Int. Ed.* **2002**, *41*, 120–124.
43. Feldmann, C.; Jansen, M. *Angew. Chem. Int. Ed Engl.* **1993**, *32*, 1049–1050.
44. Feldmann, C.; Jansen, M. *Z. Anorg. Allg. Chem.* **1995**, *621*, 201–206.
45. Feldmann, C.; Jansen, M. *Z. Anorg. Allg. Chem.* **1995**, *621*, 1907–1912.
46. Mudring, A.-V.; Jansen, M. *Z. Kristallogr. New Cryst. Struct.* **2001**, *216*, 325.
47. Feldmann, C.; Jansen, M. *Z. Naturforsch.* **1996**, *51b*, 607–608.
48. Feldmann, C.; Jansen, M. *J. Chem. Soc. Chem. Commun.* **1994**, *1994*, 1045–1046.
49. Pantelouris, A.; Küper, G.; Hormes, J.; Feldmann, C.; Jansen, M. *J. Am. Chem. Soc.* **1995**, *117*, 11749–11753.
50. Jäger, J.; Stahl, D.; Schmidt, P. C.; Kniep, R. *Angew. Chem. Int. Ed Engl.* **1993**, *32*, 709–710.
51. Boca, R.; Kniep, R. *Solid State Commun.* **1993**, *88*, 391–394.
52. Mudring, A.-V.; Jansen, M. *Angew. Chem. Int. Ed.* **2000**, *39*, 3066–3068.
53. Mudring, A.-V.; Nuss, J.; Wedig, U.; Jansen, M. *J. Solid State Chem.* **2000**, *155*, 29–36.
54. Mudring, A.-V.; Jansen, M. *Z. Naturforsch.* **2001**, *56b*, 433–436.
55. Karpov, A.; Nuss, J.; Wedig, U.; Jansen, M. *Angew. Chem. Int. Ed.* **2003**, *42*, 4818–4821.
56. Karpov, A.; Nuss, J.; Wedig, U.; Jansen, M. *J. Am. Chem. Soc.* **2004**, *126*, 14123–14128.
57. Karpov, A.; Wedig, U.; Jansen, M. *Z. Naturforsch.* **2004**, *59b*, 1387–1394.
58. Karpov, A.; Wedig, U.; Jansen, M. *Angew. Chem. Int. Ed.* **2005**, *44*, 770–773.
59. Mudring, A. V.; Jansen, M. *Z. Anorg. Allg. Chem.* **2002**, *628*, 2200.
60. Cotton, F. A., Murillo, C. A., Walton, R. A., Eds.; In *Multiple bonds between metal atoms*, 3; Springer: New York, 2005.
61. Nguyen, T.; Sutton, A. D.; Brynda, M.; Fettinger, J. C.; Long, G. J.; Power, P. P. *Science* **2005**, *4*, 844–847.
62. Olson, L. P.; Whitcomb, D. R.; Rajeswaran, M.; Blanton, T. N.; Stwertka, B. J. *Chem. Mater.* **2006**, *18*, 1667–1674.
63. Muraveiskaya, G. S.; Orlova, V. S.; Evstaf'eva, O. N. *Russ. J. Inorg. Chem.* **1974**, *19*, 1030.
64. Muraveiskaya, G. S.; Kukina, G. A.; Orlova, V. S.; Evstaf'eva, O. N.; Porai-Koshits, M. A. *Dokl. Akad. Nauk SSSR* **1976**, *226*, 596.
65. Bancroft, D. P.; Cotton, F. A.; Falvello, L. R.; Han, S.; Schwotzer, W. *Inorg. Chim. Acta* **1984**, *87*, 147–153.
66. Cotton, F. A.; Falvello, L. R.; Han, S. *Inorg. Chem.* **1982**, *21*, 2889–2891.
67. Conder, H. L.; Cotton, F. A.; Falvello, L. R.; Han, S.; Walton, R. A. *Inorg. Chem.* **1983**, *22*, 1887–1891.
68. Orlova, V. S.; Muraveiskaya, G. S.; Evstaf'eva, O. N. *Russ. J. Inorg. Chem.* **1975**, *20*, 753.
69. Pley, M.; Wickleder, M. S. *Eur. J. Inorg. Chem.* **2005**, *2005*, 529–535.
70. Pley, M.; Wickleder, M. S. *Z. Anorg. Allg. Chem.* **2004**, *630*, 1036–1039.
71. Pley, M.; Wickleder, M. S. *Z. Angew. Chem. Int. Ed.* **2004**, *43*, 4168–4170.
72. Pley, M.; Wickleder, M. S. *Z. Naturforsch.* **2006**, 912–915.
73. Wickleder, M. S. *Z. Anorg. Allg. Chem.* **2001**, *627*, 2112–2114.
74. Schmidbaur, H.; Mandl, J. R.; Huttner, G.; Frank, A. *Chem. Ber.* **1976**, *109*, 466–472.

75. Laguna, A. In *Gold, Progress in Chemistry, Biochemistry and Technology*; Schmidbaur, H., Ed.; Wiley: Chichester, **1999**; p 401.
76. Pley, M.; Wickleder, M. S. *Z. Anorg. Allg. Chem.* **2005**, *631*, 592–595.
77. Wickleder, M. S.; Pley, M. *Z. Anorg. Allg. Chem.* **2004**, *630*, 1769.
78. Arndt, A.; Wickleder, M. S. *Z. Anorg. Allg. Chem.* **2008**, *634*, 369–372.
79. Seidel, S.; Seppelt, K. *Science* **2000**, *290*, 117–118.
80. Drews, T.; Seidel, S.; Seppelt, K. *Angew. Chem. Int. Ed.* **2002**, *41*, 455–456.
81. Hwang, I.-C.; Seidel, S.; Seppelt, K. *Angew. Chem. Int. Ed.* **2003**, *42*, 4392–4395.
82. Izarova, N. V.; Pope, M. T.; Kortz, U. *Angew. Chem. Int. Ed.* **2012**, *51*, 9492–9510.
83. Chubarova, E. V.; Dickman, M. H.; Keita, B.; Nadjo, L.; Miserque, F.; Mifsud, M.; Arends, I. W. C. E.; Kortz, U. *Angew. Chem. Int. Ed.* **2008**, *47*, 9542–9546.
84. Goloboy, J. C.; Klemperer, W. G. *Angew. Chem. Int. Ed.* **2009**, *48*, 3562–3564.
85. Izarova, N. V.; Dickman, M. H.; Ngo Biboum, R.; Keita, B.; Nadjo, L.; Ramachandran, V.; Dalal, N. S.; Kortz, U. *Inorg. Chem.* **2009**, *48*, 7504–7506.
86. Barsukova, M.; Izarova, N. V.; Ngo Biboum, R.; Keita, B.; Nadjo, L.; Ramachandran, V.; Dalal, N. S.; Antonova, N. S.; Carb, J. J.; Poblet, J. M.; Kortz, U. *Chem. Eur. J.* **2010**, *16*, 9076–9085.
87. Izarova, N. V.; Vankova, N.; Heine, T.; Ngo Biboum, R.; Keita, B.; Nadjo, L.; Kortz, U. *Angew. Chem. Int. Ed.* **2010**, *49*, 1886–1889.
88. Xiang, Y.; Izarova, N. V.; Schinle, F.; Hampe, O.; Keita, B.; Kortz, U. *Chem. Commun.* **2012**, *48*, 9849–9851.
89. Delferro, M.; Graiff, C.; Elviri, L.; Predieri, G. *Dalton Trans.* **2010**, *39*, 4479–4481.
90. Mitscherlich, E. *Pogg. Ann.* **1827**, *9*, 623.
91. Jones, P. G.; Sheldrick, G. M.; Schwarzmann, E.; Vielmäder, A. *Z. Naturforsch.* **1983**, *38b*, 10–11.
92. Jones, P. G.; Schwarzmann, E.; Sheldrick, G. M.; Timpe, H. *Z. Naturforsch.* **1981**, *36b*, 1050–1051.
93. Wickleder, M. S.; Büchner, O.; Wickleder, C.; el Sheik, S.; Brunklaus, G.; Eckert, H. *Inorg. Chem.* **2004**, *43*, 5860–5864.
94. Ling, J.; Albrecht-Schmitt, T. E. *Inorg. Chem.* **2007**, *46*, 5686–5690.
95. Arndt, A.; Wickleder, M. S. *Eur. J. Inorg. Chem.* **2007**, *2007*, 4335–4339.
96. Fischer, A.; Wickleder, M. S., unpublished.
97. Lafront, A. M.; Bonvoisin, J.; Trombe, J. C. *J. Solid State Chem.* **1996**, *122*, 130–138.
98. Wickleder, M. S.; Esser, K. *Z. Anorg. Allg. Chem.* **2002**, *628*, 911–912.
99. Wickleder, M. S.; Büchner, O. *Z. Naturforsch.* **2001**, *56b*, 1340–1343.
100. Logemann, C.; Wickleder, M. S. *Inorg. Chem.* **2011**, *50*, 11111–11116.
101. Dahmen, T.; Rittner, P.; Boeger-Seidl, S.; Gruehn, R. *J. Alloys Compd.* **1994**, *216*, 11–19.
102. Bruns, J.; Fischer, A.; Wickleder, M. S. unpublished.
103. Bruns, J.; Eul, M.; Pöttgen, R.; Wickleder, M. S. *Angew. Chem. Int. Ed.* **2012**, *51*, 2204–2207.
104. Fu, Z. M.; Li, W. X. *Sci. China* **1996**, *A39*, 981–990.
105. Orosel, D.; Jansen, M. *Z. Anorg. Allg. Chem.* **2006**, *632*, 1131–1133.
106. Schwarzer, S.; Fischer, A.; Wickleder, M. S. unpublished; cf.: Stefan Schwarzer, PhD Thesis, University of Oldenburg, 2010.
107. Malinowski, P. J.; Derzsi, M.; Mazej, Z.; Jagličić, Z.; Leszczyński, P. J.; Michałowski, T.; Grochala, W. *Angew. Chem. Int. Ed.* **2010**, *49*, 1683–1686.
108. Derzsi, M.; Stasiewicz, J.; Grochala, W. *J. Mol. Model.* **2011**, *17*, 2259–2264.
109. Logemann, C.; Wickleder, M. S. *Z. Anorg. Allg. Chem.* **2012**, *638*, 1468–1472.
110. Logemann, C.; Klüner, T.; Wickleder, M. S. *Eur. J. Inorg. Chem.* **2013**, submitted.
111. Zhang, D.; Rettig, S. J.; Trotter, J.; Aubke, F. *Inorg. Chem.* **1996**, *35*, 6113–6130.
112. Willner, H.; Rettig, S. J.; Trotter, J.; Aubke, F. *Can. J. Chem.* **1991**, *69*, 391–396.
113. Malinowski, P. J.; Derzsi, M.; Mazej, Z.; Jagličić, Z.; Leszczyński, P. J.; Michałowski, T.; Grochala, W. *Eur. J. Inorg. Chem.* **2011**, *2011*, 2499–2507.
114. Malinowski, P. J.; Derzsi, M.; Mazej, Z.; Jagličić, Z.; Leszczyński, P. J.; Michałowski, T.; Grochala, W. *Eur. J. Inorg. Chem.* **2011**, *2011*, 2507–2516.
115. Charbonnier, F.; Faure, R.; Loiseleur, H. *Acta Crystallogr.* **1977**, *33b*, 824–2826.
116. Büchner, O.; Wickleder, M. S. *Z. Anorg. Allg. Chem.* **2004**, *630*, 1079–1083.
117. Wickleder, M. S.; Büchner, O.; Gerlach, F.; Necke, M.; Al-Shamery, K.; Wich, T.; Luttermann, T. *Chem. Mater.* **2008**, *20*, 5181–5185.
118. Wickleder, M. S.; Gerlach, F.; Gagelmann, S.; Bruns, J.; Fenske, M.; Al-Shamery, K. *Angew. Chem. Int. Ed.* **2012**, *51*, 2199–2203.
119. Khranenko, S. P.; Baidina, I. A.; Gromilov, S. A.; Belyaev, A. V. *J. Struct. Chem. (USSR)* **2005**, *46*, 1063–1065.
120. Laligant, Y.; Férey, G.; Le Bail, A. *Mater. Res. Bull* **1991**, *26*, 269–275.
121. Khranenko, S. P.; Baidina, I. A.; Gromilov, S. A. *J. Struct. Chem. (USSR)* **2007**, *48*, 1152–1155.
122. Cunin, F.; Deudon, C.; Favier, F.; Mula, B.; Pascal, J. L. *Inorg. Chem.* **2002**, *41*, 4173–4178.
123. Jie, L.; Albrecht Schmitt, T. E. *Eur. J. Inorg. Chem.* **2007**, *5*, 652–655.
124. Sun, C.-F.; Hu, C.-L.; Xu, X.; Mao, J.-G. *Inorg. Chem.* **2010**, *49*, 9581–9589.
125. Sun, C.-F.; Hu, C.-L.; Mao, J.-G. *Chem. Commun.* **2012**, *48*, 4220–4222.
126. Garner, C. D.; Wallwork, S. C. *J. Chem. Soc. A* **1970**, *1970*, 3092–3095.
127. Khranenko, S. P.; Baidina, I. A.; Gromilov, S. A.; Belyaev, A. V. *J. Struct. Chem. (USSR)* **2000**, *41*, 709–712.
128. Khranenko, S. P.; Baidina, I. A.; Gromilov, S. A. *J. Struct. Chem. (USSR)* **2009**, *50*, 361–364.
129. Panagiotidis, K.; Glaum, R. *Phosphorus Res. Bull.* **2005**, *19*, 77–82.
130. Panagiotidis, K.; Glaum, R.; Hoffbauer, W.; Weber, W.; Schmedt auf der Guenne, J. *Z. Anorg. Allg. Chem.* **2008**, *634*, 2922–2932.
131. Rittner, P.; Glaum, R. *Z. Kristallogr.* **1994**, *209*, 162–169.
132. Fukuoka, H.; Imoto, H.; Saito, T. *J. Solid State Chem.* **1995**, *119*, 107–114.
133. Panagiotidis, K.; Hoffbauer, W.; Glaum, R. *Z. Anorg. Allg. Chem.* **2009**, *635*, 1969–1978.
134. Panagiotidis, K.; Glaum, R. *Acta Crystallogr.* **2008**, *E64*, i84–i85.
135. Li, K.-H.; Wang, S. L.; Liao, F. L. *Inorg. Chem.* **2004**, *43*, 2499–2502.
136. Jansen, M.; Keller, H. L. *Angew. Chem. Int. Ed. Engl.* **1979**, *91*, 464.
137. Heidebrecht, K.; Jansen, M. *Z. Anorg. Allg. Chem.* **1991**, *597*, 79–86.
138. Linke, C.; Jansen, M. *Z. Anorg. Allg. Chem.* **1996**, *622*, 486–493.
139. Klein, W.; Jansen, M. *Z. Anorg. Allg. Chem.* **2008**, *634*, 1077–1081.
140. Linke, C.; Jansen, M. *Z. Anorg. Allg. Chem.* **1994**, *33*(12), 2614–2616.
141. Jansen, M.; Heidebrecht, K. *Z. Kristallogr.* **1987**, *179*, 347–356.
142. O'Reilly, D. E.; Peterson, E. M.; Scheie, C. E.; Williams, J. M. *J. Chem. Phys.* **1971**, *55*, 5629–5635.
143. Büchner, O.; Wickleder, M. S. *Z. Kristallogr.* **2005**, Suppl. 22, 143; cf. Oliver Büchner, PhD Thesis, University of Oldenburg, 2005.
144. von Schnering, H. G.; Chang Jenhui, ; Peters, K.; Wagner, F. R.; Grin, Y.; Thiele, G. *Z. Anorg. Allg. Chem.* **2003**, *629*, 516–522.
145. von Schnering, H. G.; Chang Jenhui, ; Freiberg, M.; Peters, K.; Peters, E. M.; Ormeci, A.; Schroeder, L.; Thiele, G.; Roehr, C. *Z. Anorg. Allg. Chem.* **2004**, *630*, 109–116.
146. Schüpp, B.; Heines, P.; Savin, A.; Keller, H. L. *Inorg. Chem.* **2000**, *39*, 732–735.
147. Krebs, B.; Brendel, C. J.; Schaefer, H. *Z. Anorg. Allg. Chem.* **1988**, *561*, 119–131.
148. Falqui, M. T. *Ann. Chim.* **1958**, *48*, 1160–1167.
149. Grosse, L.; Hoppe, R. *Z. Anorg. Allg. Chem.* **1987**, *552*, 123–131.
150. Bachmann, B.; Mueller, B. G. *Z. Anorg. Allg. Chem.* **1993**, *619*, 387–391.
151. Hepworth, M. A.; Jack, K. H.; Peacock, R. D.; Westland, G. J. *Acta Crystallogr.* **1957**, *10*, 63–69.
152. Williams, A. *J. Phys. Condens. Matter* **1989**, *1*, 2569–2574.
153. Jesih, A.; Lutar, K.; Zemva, B.; Bachmann, B.; Becker, S.; Mueller, B. G.; Hoppe, R. *Z. Anorg. Allg. Chem.* **1990**, *588*, 77–83.
154. Zemva, B.; Lutar, K.; Jesih, A.; Casteel, W. J., Jr.; Wilkinson, A. P.; Cox, D. E.; von Dreele, R. B.; Borrmann, H.; Bartlett, N. *J. Am. Chem. Soc.* **1991**, *113*, 4192–4198.
155. Fischer, R.; Mueller, B. G. *Z. Anorg. Allg. Chem.* **2002**, *628*, 2592–2596.
156. Graudejus, O.; Wilkinson, A. P.; Bartlett, N. *Inorg. Chem.* **2000**, *39*, 1545–1548.
157. Darriet, J.; Soubeyroux, J. L.; Touhara, H.; Tressaud, A.; Hagenmuller, P. *Mater. Res. Bull* **1982**, *17*, 315–324.
158. Hector, A. L.; Hoppe, E. G.; Levason, W.; Weller, M. T. *Z. Anorg. Allg. Chem.* **1998**, *624*, 1982–1988.
159. Bartlett, N.; Tressaud, A. *C. R. Seances Acad. Sci. Ser. C* **1974**, *278*, 1501–1504.
160. Schmidt, R.; Mueller, B. G. *Z. Anorg. Allg. Chem.* **1999**, *625*, 605–608.
161. Hillebrecht, H.; Ludwig, T.; Thiele, G. *Z. Anorg. Allg. Chem.* **2004**, *630*, 2199–2204.
162. Baernighausen, H.; Handa, B. K. *J. Less Common Met.* **1964**, *6*, 226–231.
163. Belli Dell'Amico, D.; Calderazzo, F.; Marchetti, F.; Ramello, S. *Angew. Chem. Int. Ed.* **1996**, *35*, 1331–1333.
164. Cotton, F. A.; Rice, C. E. *Inorg. Chem.* **1977**, *16*, 1865–1867.
165. Burns, R. C.; O'Donnell, T. A. *Inorg. Chem.* **1979**, *18*, 3081–3086.
166. Babel, D.; Deigner, P. *Z. Anorg. Allg. Chem.* **1965**, *339*, 57–66.
167. Janssen, E. M. W.; Folmer, J. C. W.; Wiegers, G. A. *J. Less Common Met.* **1974**, *38*, 71–76.
168. Clark, E. S.; Templeton, D. H.; MacGillavry, C. H. *Acta Crystallogr.* **1958**, *11*, 284–288.
169. Dell'amico, D. B.; Calderazzo, F.; Marchetti, F.; Merlino, S. *J. Chem. Soc.* **1982**, *1982*, 2257–2260.
170. Brodersen, K.; Thiele, G.; Recke, I. *J. Less Common Met.* **1968**, *14*, 151–152.
171. Brodersen, K.; Thiele, G.; Gaedcke, H. *Z. Anorg. Allg. Chem.* **1966**, *348*, 162–167.

172. Thiele, G.; Wochner, H.; Wagner, H. *Z. Anorg. Allg. Chem.* **1985**, *530*, 178–186.
173. Brodersen, K.; Thiele, G.; Ohnsorge, H.; Recke, I.; Moers, F. *J. Less Common Met.* **1968**, *15*, 347–354.
174. Janssen, E. M. W.; Wiegers, G. A. *J. Less Common Met.* **1978**, *57*, 58–67.
175. Loercher, K. P.; Straehle, J. *Z. Naturforsch.* **1975**, *30b*, 662–664.
176. Thiele, G.; Brodersen, K.; Kruse, E.; Holle, B. *Chem. Ber.* **1968**, *101*, 2771–2775.
177. Thiele, G.; Weigl, W.; Wochner, H. *Z. Anorg. Allg. Chem.* **1986**, *539*, 131–153.
178. Brodersen, K.; Thiele, G.; Holle, B. *Z. Anorg. Allg. Chem.* **1969**, *369*, 154–160.
179. Thiele, G.; Steiert, M.; Wagner, D.; Wochner, H. *Z. Anorg. Allg. Chem.* **1984**, *516*, 207–213.
180. Thiele, G.; Weigl, W.; Wochner, H. *Z. Anorg. Allg. Chem.* **1986**, *539*, 141–153.
181. Jagodzinski, H. *Z. Kristallogr.* **1959**, *112*, 80–87.

This page intentionally left blank